

**GROUNDWATER PURIFICATION USING FUNCTIONALISED MAGNETIC  
NANOPARTICLES (ELECTROMAGNETIC SEPARATION)**

by

**UYIOSA OSAGIE AIGBE**

submitted in accordance with the requirement for  
the degree of

**DOCTOR OF PHILOSOPHY**

in the subject area

**PHYSICS**

at the

**UNIVERSITY OF SOUTH AFRICA**

**SUPERVISOR: PROF VIJAYA SRINIVASU VALLABHAPURAPU**

**CO-SUPERVISOR: PROF WEI HUA HO/ PROF ARJUN MAITY**

**JANUARY 2018.**

## DECLARATION

Name: Uyiosa Osagie Aigbe

Student Number: 50796151

Degree: PhD in Physics

Groundwater Purification Using Functionalised Magnetic Nanoparticles (Electromagnetic

Separation)

I declare that the above thesis is my own work and that all the sources that I have used or quoted have been indicated and acknowledged by means of complete references.

**Signature:** \_\_\_\_\_

**Date:** 29/01/18

Mr Uyiosa Osagie Aigbe

## **DEDICATION**

This thesis is dedicated to God almighty, my lovely wife (Vivian), my kids (Eghosa and Esosa) and my siblings for their endless love, support, understanding and encouragement.

## **ACKNOWLEDGEMENT**

I am highly grateful to my PhD supervisors, Prof Vijaya Srinivasu Vallabhapurapu, Prof Wei Hua Ho and Prof Arjun Maity for their financial and technical support, valuable advice and expert guidance throughout this program. Thanks also go to the entire staffs of Physics and Mechanical and Industrial Engineering Department of the University of South Africa, most especially the chair of both departments for their support.

I would like to thank the National Centre for Nanostructured Materials, Council for Scientific and Industrial Research for providing and allowing me to use their facility. I would like to acknowledge Dr M. Bhaumik and Dr M. Khenfouch for their help and guidance.

My sincere gratitude to my wife (Chineye) and kids (Eghosa and Esosa) for their prayers, the long nights they had to stay awake waiting for me to come back from school and their continuous support in all aspects. You all are such amazing figures in my life. Many thanks for being there for me always and your patience. I love you all.

To my family, I am so indebted to you all for your prayers, financial support and advice throughout this program most especially Prof Harrison Atagana and my siblings. To my Friends, most especially Ubani and Robert, I say a big thank you for the support throughout this program. God bless you all, Amen.

## ABSTRACT

Most developing countries are faced with drinking water problems, with conditions becoming more severe due to water pollution. Meeting the growing demands for clean water in most countries, there are difficult challenges as the availability and supply of drinkable water are diminishing. Due to economic and environmental concerns, development of additional physical means for the removal of organic compounds from wastewater using permanent magnets, electromagnetic coils, electrodes and ultrasonic pretreatment is desirable. Improving the adsorption and separation process, magnetic field exposure method has progressively drawn consideration. Magnetic field exposure method has demonstrated its capacity for increasing the adsorptive elimination of contaminants from water as static magnetization is suitable, simple and cost-effective.

The polypyrrole magnetic nanocomposite use for adsorption experiments influenced by external magnetic field was prepared using the in-situ polymerization method, which was characterized using TEM, SEM, EDX, XRD, BET, FTIR, VSM, and ESR spectrophotometers. The magnetic nanocomposite (PPy/Fe<sub>3</sub>O<sub>4</sub>) was observed to have an average particle size of 10 nm with the elementary composition of carbon, oxygen, nitrogen, chloride and iron. The magnetic nanocomposite had a crystalline structure of face-centred cubic lattice of Fe<sub>3</sub>O<sub>4</sub>, an adsorption-desorption isotherm shape indicating a typical type-IV mesoporous material with a surface area of 28.77 m<sup>2</sup>/g. Characteristic peaks of Fe<sub>3</sub>O<sub>4</sub> and PPy were also observed using FTIR spectrophotometer. From the VSM and ESR characterization, the synthesized superparamagnetic material was shown to have a saturation magnetization of 23 emu/g and an effective g-value of 2.25 g which was attributed to Fe<sup>3+</sup> spin interaction.

An enhanced removal of Cr(VI), fluoride and congo red dye were observed under the influence of magnetic field, with parameters like pH, adsorbent dosage, the initial concentration of adsorbate, magnetic field and magnetic exposure time been varied. The enhanced adsorption of contaminants using magnetic field is attributed to the increase in the magnetic field induced on the particles over a magnetic exposure time, resulting in the rotating particles forming aggregates due to the increased magnetic force and torque on the particles from the PSV results. This leads to increase in the chain collision and area of particle interaction with the aqueous solution of hexavalent chromium, fluoride and congo red dye.

**Keywords:** Magnetic nanoparticles, magnetic field, water treatment, velocimetry, adsorption; congo red, hexavalent chromium, fluoride, three-phase, induction motor, aggregation, velocity magnitude, velocity field, wall channel, kinetics, isotherm.

## TABLE OF CONTENTS

<b>TITLE PAGE .....</b>	<b>I</b>
<b>DECLARATION.....</b>	<b>II</b>
<b>DEDICATION.....</b>	<b>III</b>
<b>ACKNOWLEDGEMENT .....</b>	<b>IV</b>
<b>ABSTRACT.....</b>	<b>V</b>
<b>TABLE OF CONTENTS .....</b>	<b>VII</b>
<b>LIST OF TABLES.....</b>	<b>XIII</b>
<b>LIST OF FIGURES.....</b>	<b>XIV</b>
<b>NOMENCLATURE.....</b>	<b>XX</b>
<b>CHAPTER ONE.....</b>	<b>1</b>
1.1 Introduction.....	1
1.2 Water Pollution by Heavy Metals and Dyes.....	3
1.2.1 Chromium Six.....	4
1.2.2 Fluoride.....	5
1.2.3 Congo Red.....	8
1.3 Nanotechnology (Nanoscale, Nanoscience) .....	9
1.4 Nanoparticles and Magnetic Behaviour of Nanoparticles.....	11
1.5 Magnetism and Superparamagnetism.....	13
1.6 Statement of Problem.....	20
1.7 Objectives of this Study.....	21
1.8 References.....	23

<b>CHAPTER TWO.....</b>	<b>31</b>
2.1 Remediation Methods Using Nanoparticles.....	31
2.2 Literature Review on Magnetic Field Effect on Adsorption Process.....	32
2.3 Three Phase Induction Motor.....	37
2.4 Structures of a Three-Phase Induction Motor.....	38
2.4.1 Stationary Stator.....	39
2.4.2 Rotating Rotor.....	40
2.5 Working Principle of Three-Phase Induction Motor.....	41
2.6 Rotating Magnetic Field Creation Due to Three Phase Currents.....	44
2.7 Particle Shadow Velocimetry (PSV).....	47
2.8 References.....	54
<b>CHAPTER THREE.....</b>	<b>61</b>
3.0 Experimental Methods.....	61
3.1 Materials.....	61
3.2 Polypyrrole Magnetic Nanocomposite Synthesis and Characterization.....	61
3.3 Experimental Method.....	62
3.3.1 Experimental Setup: Magnetic Adsorption Device.....	62
3.3.2 Preparation of Cr(VI), Fluoride and Congo Red Wastewater.....	63
3.3.3 Batch Adsorption Experiment Influence by Rotating Magnetic Field for Cr(VI) Adsorption using 8-Pole Three-Phase Induction Motor.....	64
3.3.4 Desorption Experiment.....	65
3.3.5 Adsorption Experiment under the Influence of Magnetic Field for Cr(VI) Adsorption using 2-Pole Three-Phase Induction Motor.....	65

3.3.6	Adsorption Experiment under the Influence of Magnetic Field for Fluoride Adsorption using 8-Pole Three-Phase Induction Motor.....	66
3.3.7	Adsorption Experiment under the Influence of Magnetic field for Congo Red Adsorption.....	67
3.3.8	Adsorption-Desorption Experiment.....	68
3.4	Particle Shadow Velocimetry Materials and Methods.....	69
3.4.1	Apparatus and Measurements .....	69
3.4.2	Particle Shadow Velocimetry Measurement.....	70
3.5	References.....	72
<b>CHAPTER FOUR A Novel Method for Removal of Cr(VI) using Polypyrrole Magnetic Nanocomposite in the Presence of Unsteady Magnetic Fields.....</b>		<b>73</b>
4.0	Results and Discussion.....	73
4.1	Introduction.....	73
4.2	Results and Discussion.....	75
4.2.1	PPy/Fe <sub>3</sub> O <sub>4</sub> Characterization.....	75
4.3	Equilibrium Adsorption Studies of Cr(VI).....	80
4.3.1	Influence of Solution pH.....	80
4.3.2	Effect of Adsorbent Dosage.....	81
4.3.3	Effect of Initial Cr(VI) Concentration on Adsorption Studies.....	82
4.3.4	Effect of Magnetic Field and Exposure Time.....	82
4.4	Adsorption Isotherms.....	84
4.5	Adsorption Kinetics.....	88
4.6	Regeneration Study.....	91
4.7	Conclusion.....	92

4.8	References.....	94
<b>CHAPTER FIVE Removal of Fluoride Ions from Wastewater Influenced by Rotating Magnetic Field.....98</b>		
5.1	Results and Discussion.....	98
5.1.1	Characterization of Adsorbent.....	98
5.2	Results and Discussion.....	104
5.2.1	pH Effect on Adsorption of Fluoride.....	104
5.2.2	Adsorbent Dosage Effect on Fluoride Adsorption.....	105
5.2.3	Initial Concentration Effect on Fluoride Adsorption.....	105
5.2.4	Effect of Magnetic Field on Fluoride Adsorption at Magnetic Exposure Time.....	105
5.3	Adsorption Isotherms.....	107
5.4	Adsorption Kinetics.....	108
5.5	Conclusion.....	111
5.6	References.....	112
<b>CHAPTER SIX Removal of Hexavalent Chromium from Wastewater using PPy/Fe<sub>3</sub>O<sub>4</sub> Magnetic Nanocomposite Influenced by Rotating Magnetic Field from Two Pole Three-Phase Induction Motor.....115</b>		
6.1	Introduction.....	115
6.2	Results and Discussion.....	116
6.2.1	Characterization of PPy/Fe <sub>3</sub> O <sub>4</sub> .....	116
6.2.2	Effect of pH on Adsorption of Hexavalent Chromium under the Influence of Magnetic Field.....	122
6.2.3	Effect of Adsorbent Dosage on Adsorption of Hexavalent Chromium under the Influence of Magnetic Field.....	124

6.2.4	Effect of Magnetic Field on Adsorption of Hexavalent Chromium.....	125
6.3	Conclusion.....	126
6.4	References.....	128
<b>CHAPTER SEVEN Congo Red Dye Removal Under the Influence of Rotating Magnetic Field by Polypyrrole Magnetic Nanocomposite.....131</b>		
7.1	Introduction.....	131
7.2	Results and Discussion.....	134
7.2.1	Characterization of PPy/Fe <sub>3</sub> O <sub>4</sub> Magnetic Nanocomposite.....	134
7.2.2	Effect of pH on Congo Red Adsorption Influenced by Magnetic Field.....	141
7.2.3	Effect of Adsorbent Dosage on Congo Red Adsorption under Magnetic Field Influence.....	142
7.2.4	Effect of Initial Concentration on Congo Red Adsorption under Magnetic Field Influence.....	142
7.2.5	Effect of Magnetic Field and Exposure Time on Congo Red Adsorption.....	143
7.3	Adsorption Isotherms.....	145
7.4	Adsorption Kinetics.....	148
7.5	Reuse of Pre-Treated PPy/Fe <sub>3</sub> O <sub>4</sub> .....	151
7.6	Conclusion.....	152
7.7	References.....	153
<b>CHAPTER EIGHT Velocity Measurement of Rotating Particles in Cylindrical Channel Using Particle Shadow Velocimetry.....157</b>		
8.1	Introduction.....	157
8.2	Results and Discussion.....	160

8.3	Conclusion.....	167
8.4	References.....	169
<b>CHAPTER NINE.....</b>		<b>171</b>
9.1	Conclusion.....	171
9.2	Future Research.....	172
<b>Appendix I.....</b>		<b>173</b>
<b>Appendix II.....</b>		<b>177</b>

## LIST OF TABLES

<b>Table 1.1:</b>	Effect of Chromium(VI) on Human Health at Different Concentration.....	5
<b>Table 1.2:</b>	Aesthetic and Human Health at Different Concentration due to Fluoride Effect.....	7
<b>Table 1.3:</b>	Single Domain Radius $r_c$ for Different Spherical Particles.....	19
<b>Table 3.1:</b>	Three-Phase Induction Motor Specification.....	63
<b>Table 4.1:</b>	Langmuir and Freundlich Constants for Adsorption of Cr(VI) Ions.....	86
<b>Table 4.2:</b>	Comparison of Maximum Adsorption Capacity of PPy/Fe <sub>3</sub> O <sub>4</sub> Against Other Adsorbent for Removal of Cr(VI) Ion.....	87
<b>Table 4.3:</b>	Kinetics Parameters for Adsorption of Cr(VI) Ions from Aqueous Medium.....	91
<b>Table 5.1:</b>	Langmuir and Freundlich constants for adsorption of Cr(VI) Ions.....	108
<b>Table 5.2:</b>	Estimated Values of the Kinetic Parameters of the Pseudo-First-Order and Pseudo-Second-Order Models for the Adsorptive Removal of Fluoride Ions Onto Polypyrrole Magnetic Nanocomposite at Different Initial Fluoride Concentrations. Other Experimental Parameters are T = 301 K, pH = 6, and magnetic field = 18.99 mT.....	110
<b>Table 7.1:</b>	Surface Parameters of PPy/Fe <sub>3</sub> O <sub>4</sub> Nanocomposite Sample.....	139
<b>Table 7.2:</b>	Langmuir and Freundlich Isotherm Constants for Adsorption of Congo Red Dye on 0.15 g PPy/Fe <sub>3</sub> O <sub>4</sub> Nanocomposite.....	147
<b>Table 7.3:</b>	Comparison of Congo Red Adsorption Capacity of PPy/Fe <sub>3</sub> O <sub>4</sub> Nanocomposite with Other Reported Adsorbents.....	148
<b>Table 7.4:</b>	Kinetics Parameters for Adsorption of Congo Red Ions from Aqueous Medium.....	151

## LIST OF FIGURES

<b>Figure 1.1</b>	Distribution of Earth's Water.....	2
<b>Figure 1.2</b>	Congo Red Dye Chemical Structure (Molecular Formula of Congo Red Dye: $C_{32}H_{22}N_6Na_2O_6S_2$ ).....	9
<b>Figure 1.3</b>	Representation of Magnetite Crystalline Structure ( $Fe_3O_4$ ).....	12
<b>Figure 1.4</b>	Schematics Showing the Arrangement of the Magnetic Dipoles for Five Different Types of Materials in the Absence or Presence of External Magnetic Field ( $H$ ).....	15
<b>Figure 1.5</b>	The Schematics Describing Diamagnetic, Paramagnetic, Ferromagnetic And Superparamagnetic Materials Behaviour in External Magnetic Field.....	16
<b>Figure 1.6</b>	Schematic Illustration of the Change in the Coercivity Field $H_C$ as a Function of Particle Size.....	18
<b>Figure 2.1</b>	Cutaway Diagram of Squirrel-Cage Three-Phase AC Motor.....	39
<b>Figure 2.2</b>	Stator Winding of a Three-Phase Induction Motor.....	40
<b>Figure 2.3</b>	Squirrel Cage Rotor of a Three-Phase Induction Motor.....	41
<b>Figure 2.4</b>	The Relationship Between Three-Phase Currents and Rotating Magnetic Field over 360 Electrical Degrees in Time.....	45
<b>Figure 2.5</b>	Particle Shadow Velocimetry Setup Direct Inline LED Volume Illumination.....	50
<b>Figure 2.6</b>	Description of Areas Associated with the Interaction of Plane Wave Associated with a Hard Sphere, S-Deep Shadow, a-Particle Radius, $\beta$ -Size Parameter, $\gamma$ -Penumbra Width.....	51
<b>Figure 2.7</b>	Schematics of Cross-Correlation Procedure.....	53
<b>Figure 3.1</b>	Schematics of the Magnetic Adsorption Device.....	63
<b>Figure 3.2</b>	(a) Schematic of Eight-Pole Three-Phase Induction Motor, (b) PSV Experimental Setup Showing Inline Excitation by LED.....	71
<b>Figure 4.1</b>	(a) FTIR and (b) XRD Pattern of (I) PPy, (II) $Fe_3O_4$ , PPy/ $Fe_3O_4$ (III) Before and (IV) After Adsorption of Cr(VI) Ions.....	76

<b>Figure 4.2</b>	(a) SEM and (b) HR-TEM Image of PPy/Fe <sub>3</sub> O <sub>4</sub> Nanocomposite.....	77
<b>Figure 4.3</b>	N <sub>2</sub> Adsorption-Desorption Isotherms for PPy/Fe <sub>3</sub> O <sub>4</sub> .....	78
<b>Figure 4.4</b>	(a) First Derivative ESR Adsorption Signals Versus Magnetic field (H) for (A) PPy/Fe <sub>3</sub> O <sub>4</sub> Nanocomposite Before and (B) PPy/Fe <sub>3</sub> O <sub>4</sub> Nanocomposite After Adsorption (b) ESR Spectra of PPy/Fe <sub>3</sub> O <sub>4</sub> Nanocomposite Before Adsorption and Simulation using Gaussian fitting and (c) ESR Spectra of PPy/Fe <sub>3</sub> O <sub>4</sub> Nanocomposite Before Adsorption and Simulation using Lorentzian fitting.....	79
<b>Figure 4.5</b>	M-H Curve at Room Temperature for PPy/Fe <sub>3</sub> O <sub>4</sub> Nanocomposite Before and After Cr(VI) Adsorption.....	80
<b>Figure 4.6</b>	Effect of (a) pH, (b) Adsorbent Dosage and (c) Initial Cr(VI) Concentration on the Adsorption of Cr(VI) Onto PPy/Fe <sub>3</sub> O <sub>4</sub> Nanocomposite.....	82
<b>Figure 4.7</b>	Effect of (a) Magnetic Field Strength and (b) Magnetic Exposure Time on the Adsorption of Cr(VI) Onto PPy/Fe <sub>3</sub> O <sub>4</sub> Nanocomposite.....	84
<b>Figure 4.8</b>	Adsorption Isotherm for Cr(VI) Removal by PPy/Fe <sub>3</sub> O <sub>4</sub> (a) Langmuir and (b) Freundlich Isotherm Model.....	86
<b>Figure 4.9</b>	(a) Kinetics for Cr(VI) Adsorption Onto PPy/Fe <sub>3</sub> O <sub>4</sub> , (b) Pseudo-First-Order (c) Pseudo-Second-Order and (d) Intraparticle Diffusion Model for Cr(VI) Adsorption Onto PPy/Fe <sub>3</sub> O <sub>4</sub> .....	90
<b>Figure 4.10</b>	Cr(VI) Adsorption-Desorption Cycles.....	92
<b>Figure 5.1</b>	XRD of (a) Magnetite (Fe <sub>3</sub> O <sub>4</sub> ), (b) Polypyrrole and (c) Magnetic Nanocomposite Before and After Adsorption.....	99
<b>Figure 5.2</b>	FTIR Spectra of (a) PPy and Fe <sub>3</sub> O <sub>4</sub> and (b) Polypyrrole Magnetic Nanocomposite Before and After Adsorption of Fluoride.....	100
<b>Figure 5.3</b>	(a) TEM Image of Polypyrrole Magnetic Nanocomposite (Inset: Histogram Showing the Size Distribution of the Nanocomposite using ImageJ Software), (b) TEM Image Showing the Core-Shell Structure of Polypyrrole Magnetic Nanocomposite and (c) EDX Spectrum of PPy/Fe <sub>3</sub> O <sub>4</sub> Nanoadsorbent.....	101
<b>Figure 5.4</b>	N <sub>2</sub> Adsorption-Desorption Isotherms for PPy/Fe <sub>3</sub> O <sub>4</sub> Nanoadsorbent.....	102
<b>Figure 5.5</b>	ESR Spectra of PPy/Fe <sub>3</sub> O <sub>4</sub> (a) Before and After Adsorption of Fluoride, (b) Simulation of ESR Spectra of PPy/Fe <sub>3</sub> O <sub>4</sub> After Induced Adsorption of Fluoride	

	using Gaussian Function and (c) Simulation of ESR Spectra of PPy/Fe <sub>3</sub> O <sub>4</sub> After Induced Adsorption of Fluoride using Lorentzian Function.....	103
<b>Figure 5.6</b>	Magnetisation Curve of Magnetic Nanocomposite at Room Temperature....	104
<b>Figure 5.7</b>	Effect of (a) pH, (b) Adsorbent Dosage, (c) Initial Fluoride Concentration and (d) Magnetic Field Strength and Magnetic Exposure Time on the Adsorption of Fluoride Onto PPy/Fe <sub>3</sub> O <sub>4</sub> Nanocomposite.....	106
<b>Figure 5.8</b>	Adsorption Isotherm for Fluoride Removal by PPy/Fe <sub>3</sub> O <sub>4</sub> (a) Langmuir and (b) Freundlich Isotherm Model.....	108
<b>Figure 5.9</b>	(a) Kinetics for Fluoride Adsorption Onto PPy/Fe <sub>3</sub> O <sub>4</sub> , (b) Pseudo-First-Order and (c) Pseudo-Second-Order.....	110
<b>Figure 6.1</b>	(a) HR-TEM Image of Polypyrrole Magnetic Nanocomposite (b) SEM Image of Polypyrrole Magnetic Nanocomposite (c) EDX Spectrum of PPy/Fe <sub>3</sub> O <sub>4</sub> Nanocomposite Before Hexavalent Chromium Adsorption and (d) EDX Spectrum of PPy/Fe <sub>3</sub> O <sub>4</sub> Magnetic Nanocomposite After Hexavalent Chromium Adsorption.....	117
<b>Figure 6.2</b>	N <sub>2</sub> Adsorption-Desorption Isotherms for PPy/Fe <sub>3</sub> O <sub>4</sub> Nanocomposite.....	118
<b>Figure 6.3</b>	XRD Pattern of (a) Polypyrrole, (b) Magnetite (Fe <sub>3</sub> O <sub>4</sub> ), and (c) Polypyrrole Magnetic Nanocomposite Before and After Adsorption of Hexavalent Chromium Using 2-Pole Three-Phase Induction Motor.....	119
<b>Figure 6.4</b>	FTIR Spectra of (a) PPy, (b) Fe <sub>3</sub> O <sub>4</sub> and (c) Polypyrrole Magnetic Nanocomposite Before and After Adsorption of Hexavalent Chromium using 2-Pole Three-Phase Induction Motor.....	120
<b>Figure 6.5</b>	ESR Spectra of PPy/Fe <sub>3</sub> O <sub>4</sub> (a) Before and After Adsorption of Hexavalent Chromium, (b) PPy/Fe <sub>3</sub> O <sub>4</sub> Nanocomposite After Cr(VI) Adsorption (b) ESR Spectra of PPy/Fe <sub>3</sub> O <sub>4</sub> Nanocomposite After Hexavalent Chromium Adsorption Fitted with Gaussian Function and (c) ESR Spectra of PPy/Fe <sub>3</sub> O <sub>4</sub> Nanocomposite After Hexavalent Chromium Adsorption Fitted with Lorentzian Function.....	121
<b>Figure 6.6</b>	Magnetization Curve of Polypyrrole Magnetic Nanocomposite at Room Temperature.....	122
<b>Figure 6.7</b>	Point of Zero Charge of Polypyrrole Magnetic Nanocomposite.....	124

<b>Figure 6.8</b>	Effect of (a) pH on the Adsorption of Hexavalent Chromium Onto PPy/Fe <sub>3</sub> O <sub>4</sub> Nanocomposite, (b) Adsorbent Dosage on the Adsorption of Hexavalent Chromium Onto PPy/Fe <sub>3</sub> O <sub>4</sub> Nanocomposite, (c) Magnetic Field Strength on the Adsorption of Hexavalent Chromium Onto PPy/Fe <sub>3</sub> O <sub>4</sub> Nanocomposite (Anti-clockwise Direction) and (d) Magnetic Field Strength on the Adsorption of Chromium Onto PPy/Fe <sub>3</sub> O <sub>4</sub> Nanocomposite (Clockwise Direction).....	126
<b>Figure 7.1</b>	XRD Diffraction Pattern of (a) Fe <sub>3</sub> O <sub>4</sub> , (b) PPy and (c) PPy/Fe <sub>3</sub> O <sub>4</sub> Nanocomposite Before and After Congo Red Adsorption.....	134
<b>Figure 7.2</b>	FTIR Spectra of PPy/Fe <sub>3</sub> O <sub>4</sub> Nanocomposite Before and After Adsorption, (Inset (a) Fe <sub>3</sub> O <sub>4</sub> , and (b) PPy).....	135
<b>Figure 7.3</b>	(a) TEM Image of Polypyrrole Magnetic Nanocomposite, with Histogram Obtained from TEM Showing the Size Distribution of the MNC Fitted with a Gaussian Fitting (b) SEM Image of Polypyrrole Magnetic Nanocomposite, with Histogram Obtained from TEM Showing the Size Distribution of the MNC Fitted with Gaussian Fitting and (c) EDX spectra of PPy/Fe <sub>3</sub> O <sub>4</sub> Nanocomposite Before Adsorption.....	137
<b>Figure 7.4</b>	N <sub>2</sub> Adsorption-Desorption Isotherms Of Polypyrrole Magnetic Nanocomposite.....	138
<b>Figure 7.5</b>	(A)(a) ESR Spectra of PPy/Fe <sub>3</sub> O <sub>4</sub> Nanocomposite After Congo Red Adsorption and (b) Before Congo Red Adsorption, (B)(a) ESR Spectra of PPy/Fe <sub>3</sub> O <sub>4</sub> Nanocomposite After Congo Red Adsorption Fitted to Gaussian Fitting and (b) ESR Spectra of PPy/Fe <sub>3</sub> O <sub>4</sub> Nanocomposite After Congo Red Adsorption and (C)(a) ESR Spectra PPy/Fe <sub>3</sub> O <sub>4</sub> Nanocomposite After Congo Red Adsorption Fitted to Lorentzian Fitting and (b) ESR Spectra PPy/Fe <sub>3</sub> O <sub>4</sub> Nanocomposite After Congo Red Adsorption.....	140
<b>Figure 7.6</b>	M-H Curve at Room Temperature for PPy/Fe <sub>3</sub> O <sub>4</sub> Nanocomposite.....	141
<b>Figure 7.7</b>	(a) pH Effect on Congo Red Adsorption under the Influence of MF (b) Adsorbent Dosage Effect on CR Adsorption under MF Influence (c) Initial Concentration Effect on CR Adsorption under MF Influence (d) Effect of Magnetic Field Intensity on the Adsorption of CR and (e) Effect of Magnetic Exposure Time on Adsorption of CR.....	144

<b>Figure 7.8</b>	(a) Fit of Equilibrium Data to Langmuir Isotherm Model and (b) Fit of Equilibrium Data to Freundlich Isotherm Model.....	147
<b>Figure 7.9</b>	(a) Kinetics Data for CR Adsorption Onto PPy/Fe <sub>3</sub> O <sub>4</sub> , (b) Pseudo-First-Order Model for Adsorption of CR Onto PPy/Fe <sub>3</sub> O <sub>4</sub> , and (c) Pseudo-Second-Order Model for Adsorption of CR Onto PPy/Fe <sub>3</sub> O <sub>4</sub> .....	150
<b>Figure 7.10</b>	Adsorption-desorption Cycles.....	152
<b>Figure 8.1</b>	Description of the Regions Associated with the Plane Wave Interaction with Hard Sphere, S-Deep Shadow, $\alpha$ -Particle Radius, $\beta$ -Size Parameter, $\gamma$ -Penumbra Width.....	160
<b>Figure 8.2</b>	Sequence of Inverted Image of Particles in Chromium Six Solution at Magnetic Field of 15.48 (a) No Field is Applied, (b) 3.01 s (RMF),(c) 6 s (RMF), (d) 15 s (RMF) and (e) 19.99 s (RMF).....	161
<b>Figure 8.3</b>	Sequence of Inverted Image of Particles in Chromium Six Solution at Magnetic Field of 25.54 mT (a) No Field is Applied, (b) 3.01 s (RMF), (c) 6 s (RMF), (d) 15 s (RMF) and (e) 19.99 s (RMF).....	161
<b>Figure 8.4</b>	Aggregation of Particles in Magnetic Field of (a) 11.84 mT in Fluoride Solution, (b) 19 mT in Fluoride Solution, (c) 11.84 mT in Hexavalent Chromium Solution and (d) 19 mT in Hexavalent Chromium Solution.....	163
<b>Figure 8.5</b>	Instantaneous and Mean Velocity Measurement of Particles in Fluoride Solution at Magnetic Field of 15.48 mT (a) Instantaneous Velocity of Particles at Time Interval of 3.06 s (b) Resulting Instantaneous Velocity of Particles at Time Interval of 6.01 s, (c) Resulting Instantaneous Velocity of Particles at Time Interval of 13 s, (d) Resulting Instantaneous Velocity of Particles at Time Interval of 14 s, and (e) Resulting Average Velocity Field of Particles.....	165
<b>Figure 8.6</b>	Instantaneous and mean velocity measurement of particles in fluoride solution at magnetic field of 25.54 mT (a) instantaneous velocity of particles at time interval of 3.06 s (b) resulting instantaneous velocity of particles at time interval of 6.01 s, (c) resulting instantaneous velocity of particles at time interval of 13 s, (d) resulting instantaneous velocity of particles at time interval of 14 s, and (e) resulting average velocity field of particles resulting average velocity field of particles.....	166
<b>Figure 8.7</b>	Aggregation of Particles in the Magnetic Field of (a) 16.55 mT and (b) 25.54 mT.....	167

<b>Figure S4.1</b>	EDX Spectra of PPy/Fe <sub>3</sub> O <sub>4</sub> (a) Before and (b) After Cr(VI) Adsorption.....	173
<b>Figure S4.2</b>	Zeta Potential of Adsorbent (PPy/Fe <sub>3</sub> O <sub>4</sub> ) at Different pH.....	174
<b>Figure S4.3</b>	Images of Particles Aggregation of PPy/Fe <sub>3</sub> O <sub>4</sub> Nanocomposite at Different Magnetic Field of (a) 10.80, (b) 11.84, (c) 13.20, (d) 16.46 and (e) 19.01 mT .....	175
<b>Figure S4.4</b>	Effect of Magnetic Field on Particle Aggregation for Cr(VI) Adsorption.....	176

## NOMENCLATURE

<b>Cr(VI)</b>	Chromium Six
<b>NP's</b>	Nanoparticles
<b>BET</b>	Brunauer-Emmett-Teller
<b>CR</b>	Congo Red
<b>FTIR</b>	Fourier Transform Infrared Spectroscopy
<b>SEM</b>	Scanning Electron Microscope
<b>TEM</b>	Transmission Electronic Microscopy
<b>XRD</b>	X-ray Diffraction
<b>VSM</b>	Vibrating Sample Magnetometer
<b>ESR</b>	Electron Spin Resonance
<b>MF</b>	Magnetic Field
<b>AC</b>	Alternating Current
<b>DC</b>	Direct Current
<b>IM</b>	Induction Motor
<b>NEMA</b>	National Electrical Manufactures Association
<b>S</b>	Slip
<b>PSV</b>	Particle Shadow Velocimetry
<b>PIV</b>	Particle Image Velocimetry
<b>LED</b>	Light Emitting Diode
<b>fsPIV</b>	Forward Scatter Particle Image Velocimetry
<b>DOF</b>	Depth of Field
<b>NaF</b>	Sodium Fluoride
<b>PPy</b>	Polypyrrole
<b>Fe<sub>3</sub>O<sub>4</sub></b>	Magnetite
<b>PPMS</b>	Physical Property Measurement System
<b>EDX</b>	Energy Dispersive X-ray
<b>UV</b>	Ultra-Violet
<b>Vis</b>	Visible
<b>mT</b>	Millitesla
<b>FFT</b>	Fast Fourier Transform
<b>nm</b>	Nanometer
<b>emf</b>	Electromotive Force

# CHAPTER ONE

## 1.1 Introduction

The earth is covered with 75% water, with only 3% being fresh water. In addition, only 1% of fresh water is available for humans and industrial purpose (Figure 1.1) [1-2]. People's health and a distinguished way of life are centred on access to clean water and proper sanitation. Providing clean water that is inexpensive to meet human needs is a key challenge of the 21st century, as access to clean water is viewed as one of the basic needs. Worldwide, there is a struggle to keep up water supply with the increasing demand, which is heightened by growth in population, change in global climate, and declining water quality [3-4].

For the larger part of human history, water has been in abundant supply in most areas of the world and therefore was an available resource for most of humanity. The situation in most developing countries is sad, as an estimated one billion people dearth access to safe drinking water, with an additional 2.6 billion people lacking access to appropriate sanitation. In addition to the result of the well-documented economic, social and environmental impact on poor water supply and sanitation, the health and welfare of frail groups like children, the elderly and the poor are closely associated with the availability of acceptable, safe and affordable water supply [5-6].

According to the World Health Organization (WHO) and United Nations Children's Fund (UNICEF) report, an estimated 82% of the world's population is projected to have access to adequate water supply, with improvement in the number of people around the world having proper sanitation growing from 49% - 58% in 1990 and 2002. But, approximately one out of six which represents 1.1 billion people lack access to acceptable water supply, with two out of five which represents 2.6 billion people without appropriate sanitation services, with half of the population of people living in Asia lacking suitable sanitation facilities. In Africa, it is estimated that two out of five people lack access to appropriate water supply and sanitation. This is particularly alarming in most rural areas where fifty percent of the population lack access to suitable sanitation and water supply services [7-11]. The principal single cause of deaths in the world is linked to water consumption, with an estimated five to seven million deaths per year. At this rate, it is estimated that 75 million people would die of preventable water-related diseases each year by 2020. Most of these deaths will be caused by infectious diseases and

secondary diarrhoea. Yet, several deaths may occur secondary to consuming non-pathogen water contaminants [12].

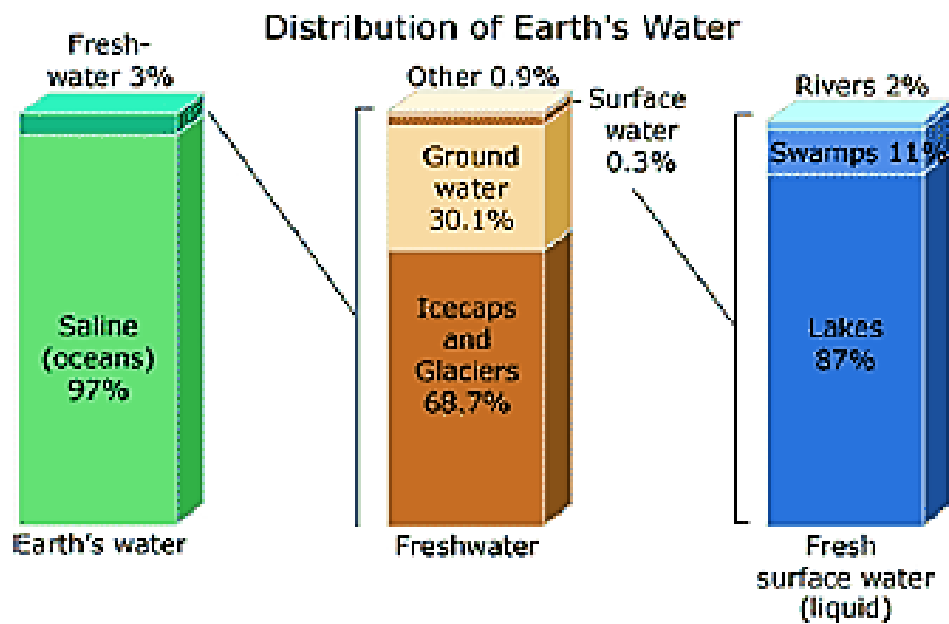


**Figure 1.1** Distribution of earth's water [13]

The most critical environmental problem is water pollution. This leads to a change in water colour and increases in harmful microscopic living organisms count, which causes the spread of dangerous diseases. The effects of discarding of solid and liquid waste products containing heavy metals stemming from industrial processes have received massive attention around the world, with legislation for the environmental protection increasingly becoming more rigid each day [14-15].

Most developing countries are faced with drinking water problems, with conditions becoming more severe. Meeting the rising demands for clean water in most countries, there are formidable challenges as the availability and supply of drinkable water are diminishing due to continued droughts, growth in population, sterner health-based regulations and contending demands from a diversity of users. With increasing demand for natural resources, the key problems in industrial applications are contaminated water treatment, power production, and water supply. With the increase in water, demand joined with the escalating cost of energy today, the world cannot afford to waste energy in the processes of water treatment as significant savings in production time and costs can be saved by effective water treatment. Thus, the demand for

effective water treatment is to ensure the minimum environmental pollution attainable and that is economical is increasing [16-17].

## **1.2 Water Pollution by Heavy Metals and Dyes**

Water contamination is due to any chemical, biological, or physical change in water quality that has a negative effect on living organisms. This makes water unhealthy for the desired usage. Heavy metal pollution is an issue worldwide, with the levels and severity of pollution differing from place to place. With half of the metals emitted into the environment being classified as toxic, they pose great risks to human health. Heavy metals contamination of water has turned out to be a stern problem due to their adversative effects on human health and ecological systems. Natural or human-induced activities are the main cause of contaminants released into the environment [5, 18-20]. The fundamental cause of heavy metals are wastewaters from contemporary chemical industries. In recent years, industrial development has significantly contributed to the heavy metal released into the environment [21].

Heavy metals are metallic elements having a high relative density when related to water density [22-23]. Due to their non-biodegradable and toxic nature, heavy metals persist in wastewater. The main concern about heavy metals is their capacity to accumulate in the environment which leads to water contamination [24-26]. Heavy metals with their corresponding relative density consist of cadmium ( $8.65 \text{ gcm}^{-3}$ ), chromium ( $7.19 \text{ gcm}^{-3}$ ), cobalt ( $8.90 \text{ gcm}^{-3}$ ), copper ( $8.95 \text{ gcm}^{-3}$ ), lead ( $11.34 \text{ gcm}^{-3}$ ), mercury ( $13.53 \text{ gcm}^{-3}$ ), nickel ( $8.91 \text{ gcm}^{-3}$ ) and zinc ( $7.14 \text{ gcm}^{-3}$ ). In their ionic state, these metals are in their extreme toxic form, they react with the body's bio-molecules to form very stable biotoxic compounds, which are difficult to separate at their stable oxidation states [27-28]. Heavy metal toxicity is defined by a "toxic level". Contaminants in water are regularly measured in parts per million or milligrams per litre (PPM or mg/L) or parts per billion or micrograms per litre (PPB or  $\mu\text{g/L}$ ) [27-29].

One of the major water pollutants is organic compounds like pesticides, organochlorines, polychlorinated biphenyls, polycyclic aromatic hydrocarbons and organic dyes. Organic compounds that contain single or more benzene rings are known as dyes. Due to their toxicity and late hydrolysis, such materials cause irreversible damage to the environment and humans, namely cancer, mutagenesis, etc. Among the various wastewater contaminants, the most important known contaminant is dye waste as their existence in water is highly visible even at

very low concentration. Dyes are known to have an artificial origin and complex aromatic molecular structures manufactured to impart strong and persistent colour that does not degrade when they are exposed to sunlight [5, 30-32].

Due to the toxic effects of dyes to humans, animals, plants and aquatic organisms, the mobility and distribution of dyes in water have been studied extensively. The presence of contaminants like heavy metals and dyes in the environment is a serious risk to human life as they enter domestic water sources like rivers, lakes, ponds etc. Their presence in water leads to bioaccumulation in living organisms triggering health problems in humans [33-34].

### **1.2.1 Chromium Six**

Chromium is a component of the 6th group of the IUPAC periodic table existing primarily in  $\text{Cr}^{3+}$  and  $\text{Cr}^{6+}$  states in the environment. Because of the non-toxic nature of  $\text{Cr}^{3+}$ ,  $\text{Cr}^{3+}$  is a vital specie that helps the body to regulate trace concentrations of blood sugar-levels when present in trace concentration. but are toxic when the concentration of  $\text{Cr}^{3+}$  in water exceeds 5.0 mg/L. Hexavalent chromium occurs naturally at high concentration in ultramafic rocks like igneous and meta-igneous rocks. The reoccurring appearance of chromium in surface and groundwater shows its use as a vital industrial metal in a variety of various processes. Chromium is characterized by a lustrous silver-grey metal, which is hardly found in the earth's crust as an element or metal but only in compound forms or ions in water. The main source of chromium is chromite ( $\text{FeCr}_2\text{O}_4$ ), with chromium been the main product, mined [35-36].

Chromium is a major pollutant in water resources around the world due to their use in metal plating, mining operations and tanneries industries [37]. Chromium exists in trivalent (Cr(III)) and hexavalent forms in the environment. Chromium six poses a great health risk to humans, as it is toxic, soluble and mobile in the environment when compared to Cr(III). Generally, there is added concern about Cr(VI) due to its toxicity, which is 100 times higher than that of Cr(III). Due to the teratogenicity, mutagenicity and carcinogenicity of Cr(VI) in biological systems, the health of humans is seriously affected [38-39]. Studies have shown that drinking water contaminated with hexavalent chromium leads to high chromium levels in tissues mainly the gastrointestinal tract, blood, liver, kidneys, spleen and increased toxicity in animals and humans [40].

Hexavalent chromium is not recyclable and is insoluble in aqueous solutions. Hexavalent chromium has the property to bio-accumulate in the environment and can greatly accumulate in

living bodies [41]. Hexavalent chromium is tremendously mobile in the environment, accumulates in the food chain. Ingestion of Cr(VI) causes skin irritation, lung cancer, as well as kidney, liver and gastric damage. The tolerance border for Cr(VI) discharge into the inland surface water and potable water is 0.1 mg/L and 0.05 mg/L [42-44]. Table 1.1 shows the effect of chromium(VI) on human health at different concentration:

**Table 1.1:** Effect of chromium(VI) on human health at different concentration [45].

Chromium Six (Cr(VI)) Range (mg/L)	Effects
Target Water Quality Range (TWQR) 0-0.050	Risk of cancer induction insignificant. No toxic or aesthetic.
As a precautionary measure, it is recommended that the TWQR not be exceeded due to the potentially acute and/or irreversible effects of chromium six (Cr(VI)) on human health.	
0.05-1.0	Possible risk of induction of gastrointestinal cancer following long-term exposure.
1.0-5.0	Undesirable taste, slight nausea and increasing risk of cancer induction.
> 5.0	Risk of acute toxicity.

### 1.2.2 Fluoride

The most electronegative element distributed all over the earth crust as fluoride in nature is fluorine. The most highly reactive elements of the halogen family is fluoride. Fluoride is observed to behave differently from other halogen elements, which is evident in its reaction in

natural water. 0.06-0.09% of the earth's crust is made up of fluoride elements found naturally in the environment [46-48].

In minerals, geochemical deposits and in natural water systems, fluoride occurs naturally as an element. It enters the food chain either via drinking water or eating plants and cereals having a high level of fluoride. The fluoride contamination of water resources arises from the contact of water with mineral sediments and the discharge of wastewaters from several manufacturing industries like fertilizer, glass, ceramics, bricks, iron works and electroplating [49-50]. The strengthening of bones and prevention of tooth decay in the human body is among the useful effects of fluoride in humans. It is estimated that in 25 countries in both developed and developing nations by the United Nations Environmental Program (UNEP) that the numbers of individuals affected by fluorosis are in tens of millions. In low concentration of up to 1 mg/L in drinking water, fluoride is useful in the reduction of dental caries. The tolerance level for fluoride in drinking water by the World Health Organization (WHO) is 1.5 mg/L [51-52].

Fluoride level in drinking water is a vital physicochemical feature which must be considered when evaluating water quality for human ingesting. It is well known that low fluoride concentration as well as its excess causes health problems in humans. A range of disorders and diseases are associated with the excess ingestion of fluoride ions. Dental fluorosis is detected in the human population when drinking water with a fluoride level greater than 4 mg/L is ingested. The continuous consumption of water holding high levels of fluoride between 4 and 15 mg/L incites skeletal fluorosis that is associated with serious bone anomalies. Long-term digestion of high fluoride ions in drinking water are causes of fluorosis, an enduring disease shown by the mottling of teeth in a minor case, softening of bones ossification of tendons, ligaments and neurological damage in severe cases [50, 53-54]. Table 1.2 shows the effect of fluoride on Aesthetic and human health at different concentration:

**Table 1.2:** Aesthetic and human health at different concentration due to fluoride effect [45].

Fluoride Range (mg/L)	Effects
Target Water Quality Range (TWQR) 0-1.0	The concentration in water necessary to meet requirement for healthy tooth structure is a function of daily water intake and hence varies with annual maximum daily air temperature. A concentration of approximately 0.75 mg/L corresponds to a maximum daily temperature of approximately 26-28°C. No adverse health effects or tooth damage occurs.
1.0-1.5	Slight mottling of dental enamel may occur in sensitive individuals. No other health effects are expected.
1.5-3.5	The threshold for marked dental mottling with associated tooth damage due to softening of enamel is 1.5 mg/L. Above this, mottling and tooth damage will probably be noticeable in most continuous users of the water. No other health effects occur.
3.5-4.0	Severe tooth damage especially in infants temporary and permanent teeth: softening of the enamel and dentine will occur on continuous use of water. Threshold for chronic effects of fluoride exposure, manifested as skeletal effects. Effects at this concentration are detected mainly by radiological examination rather than overt.
4.0-6.0	Severe tooth damage especially to the temporary and permanent teeth of infants; softening of the enamel and dentine will occur on continuous use of water. Skeletal fluorosis occurs on long-term exposure.
> 8.0	Severe tooth damage as above. Crippling skeletal fluorosis is likely to appear on long-term exposure.
> 100	Threshold for onset of acute fluoride poisoning, marked by vomiting and diarrhoea.
> 2000	The lethal concentration of fluoride is approximately 2000 mg/L.

### 1.2.3 Congo Red

Waste products released into the environment around the world is an immense problem. This waste product can include coloured organic dyes which are produced by many industries. Water contamination ensuing from the release of coloured wastes from the textile dye industry and colouring mills are of environmental concern. Though dyes impact good-looking colours to textile fibres, foodstuffs, etc., these strong colours impacted by dyes tend to pose aesthetic and ecological snags to the aquatic ecosystem [55-56]. A lot of dye contents are discharged as wastes from textile, paper, leather and cosmetics industries, which mix with water bodies to cause severe complications such as an increase in the chemical oxygen demand (COD), reduced light penetration and visibility [36, 57].

The various dyes types include acid dyes, basic dye, azo dyes, mordant dyes, plastic dyes etc. Azo dyes are the most common dye used and account for 65-70% of the total dyes produced. Azo dyes are artificial organic pigments employed in colour productions worldwide. These coloured compounds are visually unpleasant and deterring sunlight penetration into water bodies (e.g. streams, rivers etc.). Furthermore, coloured wastes also affect photosynthetic processes of aquatic plants, in most case reducing oxygen levels in water, leading to the suffocation of aquatic flora and fauna. [58-64].

The largest group of synthetic dyes known are azo dyes. This has given rise to many water and soil environmental snags. Congo red (CR) is the most widely azo dye used in the textile industry [5, 65]. A known human carcinogen is congo red dye [1-naphthalenesulfonic acid, 3, 3'-(4,4'-biphenylene bis (azo)) bis (4-amino-) disodium salt] which is a benzidine-based anionic diazo dye and known to break down to benzidine [66]. Congo red dyes are acknowledged to have a synthetic source and a complex aromatic molecular structure which make them more stable and hard to biodegrade and photodegrade, making its treatment hard. A small amount of dyes present in water (less than 1 ppm) is extremely visible and unwanted, as excessive ingestion of congo red dye causes skin irritation, allergic, dermatitis, mutations and cancer. Therefore, it is crucial for the dye to be removed before the wastewater can be discharged into the environment [62, 67-70]. Congo red chemical structure is shown in Figure 1.2.

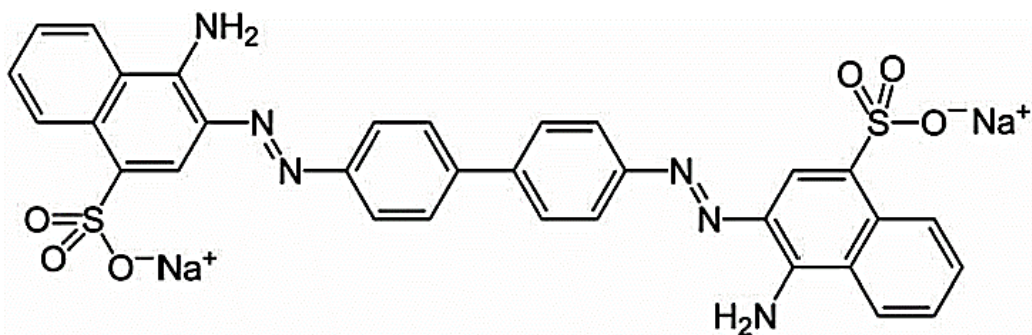


**Figure 1.2** Congo red dye chemical structure (molecular formula of congo red:  $C_{32}H_{22}N_6Na_2O_6S_2$ ) [63]

### 1.3 Nanotechnology (Nanoscale and Nanoscience)

The word 'nanotechnology' yet new has existed for a long-time providing prospects for the development of materials for medical applications, where conventional methods may reach their limits. Small objects that act as a unit are termed a particle in nanotechnology, in terms of its transport and properties. Particles are classified by its size in terms of its diameter with fine particles covering a range of 100 and 2500 nanometer. For ultrafine particles, the size range is between 1 and 100 nm. The nanoparticle has a size range of the ultrafine particles (1-100 nm). Nanoparticles might or might not show size-related properties that vary meaningfully from those observed in fine particles or bulk materials [71-72].

The understanding matter at the scale of atoms was discovered by Ancient Indian scholars like Kanada in 600 BC and Democritus of Greece in 400 BC. Kanada described atoms as composing of everything in the world. The word "atom" was also coined by Democritus to mean "not cleavable in Greek", that individual matter was made up of atoms and that atoms are invisible. Huge contributions to nanoscience and nanotechnology fields were made by three scientists. Contributions from Richard Feynman, Norio Taniguchi, and Eric Drexler led to modern nanoscience and nanotechnology. The whole field of nanotechnology was foretold in 1959 by an American physicist and Noble Laureate Richard Feynman. In Feynman paper titled "There is plenty of room at the bottom: an invitation to enter a new field of physics, Feynman encouraged scientists to think small and indicated that the ability to manipulate matter at very fine and atomic scale, several breakthroughs can be made. Norio Taniguchi (1974) is recognized for

inventing the term "nanotechnology", where the term nanotechnology was used in his lecture on ultra-precision machining. But the first technical paper on molecular nanotechnology was published by Eric Drexler. A complete description of the molecular computer was presented in 1983, with subsequent publication of a book in 1986 published on molecular nanotechnology, Engines of Creation. The effects of nanoscale mainly include:

- I. In the nanoscale system, small length scales influenced directly the energy band structures and leads indirectly to the change in the associated atomic structure. These effects are termed quantum confinement, which changes the total energy of the system.
- II. The chemical reactivity of any system may be changed by the reduction of the system size. This is a function of the structure and occupation of the outermost electronic energy levels. Physical properties like electrical, thermal, optical and magnetic characteristics all depend on the outermost energy levels arrangement, which can be changed due to size reduction and
- III. Size reduction may also affect the mechanical strength, and this depends on the electronic structure. The transport properties of materials at the nanoscale may exhibit quantized rather than continuous behaviours owing to the change of electron energy levels [73].

Substances can be altered with different properties been developed when compared to the substance in bulk or micro atom when these substances are manipulated at an atomic level. Nanotechnology is acknowledged as a new generation of technology with the possibility to transform several areas of the world we live in. Virtually all aspect of our daily life including health and healthcare, manufacturing and the use of materials and equipment, the environment and protection are included. It's an enabling technology that could possibly lead to a cost-effective and high-performance in water treatment [74].

The massive increase in the ratio of the surface area to the volume present at nanoscale materials is an exclusive feature of nanotechnology, which open possibilities in surface-based sciences. The prospect to improve the environment through the direct applications of nanoscale materials in detecting, preventing and removing contaminants, as well as the indirectly use of nanotechnology to design cleaner industrial processes and creating environmentally responsible products is through nanoscale materials. A crucial natural application of nanotechnology is

in the water sector. Nanotechnology is applied in three core areas in the environmental field, which are classified namely as;

- I. Restoration (remediation) and purification of contaminated material,
- II. Pollution detection (sensing and detection) and
- III. Pollution prevention. With the fast increase of pollutant species and concentration, the development of devices that can treat and prevent pollution is needed [75-76].

The application of nanotechnology in the purification and treatment of wastewater have revolutionised water treatment procedures potentially. Nanotechnology exploits phenomenon and properties of matter at atomic and molecular levels that are novel. Nanomaterials display an array of novel properties that can be used to develop new technologies and improve current technologies due to their size effect. Features of the large surface area, self-assembly potential, high specificity, high reactivity, and catalytic potential makes nanoparticles outstanding contenders for applications in water treatment [77]. Advancement in nanoscale science and engineering offers that many of the current problems involving water quality could be fixed or significantly reduced using nano-absorbents, nano-catalysts, bioactive nanoparticles, nanostructured catalytic membranes, submicron, nanopowder, nanotubes, magnetic nanoparticles, granules, clusters, micromolecules, nanoparticles, colloids, flake with distinctive length scales of 9-10 nm have a substantial influence on water quality in the natural environment [16, 78].

#### **1.4 Nanoparticles and Magnetic Behaviour of Nanoparticles**

A nanoscale particle with a size range from 1-100 nm is termed nanoparticle. An innovation in the field of nanotechnology is the synthesis of nanoparticles exhibiting magnetic properties, as they can be influenced using a magnetic field. They are generally composed of iron, nickel, cobalt and their chemical compounds. Nanoparticles have applications in fields such as biomedicine, environmental remediation, magnetic resonance imaging and optical fibres. Nanoparticles are made up of porous media, colloids, gels and polymers in combination with a nano-dimensional magnetic particle [79-80]. Owing to their important and unique surface to mass ratio features, which is higher than that of bulk particles and materials, allows for the catalytic promotion of reactions, as well as the ability of nanoparticles to adsorb and transport other compounds such as drugs, probes, and proteins due to their large (functional) surface, nanoparticles (NP) has attracted much consideration [72, 81-82].

Iron oxide nanoparticles occur in the earth's crust as volcanoes and fires [83]. In nature, iron oxides are common and can readily be made in the laboratory. Among the eight iron oxides known, hematite ( $\alpha$ - $\text{Fe}_2\text{O}_3$ ), magnetite ( $\text{Fe}_3\text{O}_4$ ) and maghemite ( $\gamma$ - $\text{Fe}_2\text{O}_3$ ) are very promising and common materials due to their polymorphism involving temperature-induced phase transition. Each of these three iron oxides has unique biochemical, magnetic, catalytic, and other properties which provide suitability. The crystalline structure of magnetite ( $\text{Fe}_3\text{O}_4$ ) having a face-centred cubic spinel structure, based on 32  $\text{O}^{2-}$  ions and close-packed along the [111] direction is shown in Figure 1.3. Half of the octahedral sites are occupied by  $\text{Fe}^{2+}$  ions and the  $\text{Fe}^{3+}$  ions are split evenly across the remaining octahedral sites and the tetrahedral sites.  $\text{Fe}_3\text{O}_4$  differs from other iron oxides in that it comprises both divalent trivalent iron [84-85].

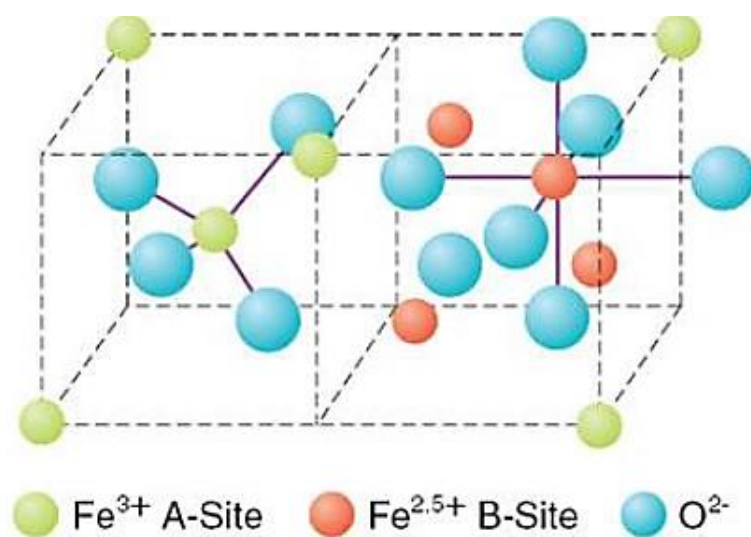


**Figure 1.3** Representation of magnetite crystalline structure ( $\text{Fe}_3\text{O}_4$ ) [86].

Magnetite ( $\text{Fe}_3\text{O}_4$ ) particles have been found in several studies to be of vital scientific and technological importance because of their intrinsic magnetic features and outstanding applications in magnetic fluids, catalysis, electronic devices, information storage, sensors, drug-delivery technology, biomedicine, magnetic recording devices, and environmental remediation [87-88]. Magnetic nanoparticles presence in adsorbent's structure leads to a chemical stability, decreases toxicity and excellent recyclability of the adsorbent. High surface area and dispersibility are the two important factors that can improve interfacial interaction between the adsorbent and heavy metal ions to guarantee high adsorption performance of  $\text{Fe}_3\text{O}_4$  nanoparticles [89-91].

When the surface of iron oxide nanoparticles is changed with a variety of functional groups, these functionalized iron oxide nanoparticles are observed to be promising in heavy metals ions elimination from water. Iron oxide nanomaterials as a sorbent, also have a great potential application in wastewater treatment technology due to its capability to react with the different functional group via stabiliser, electrostatic surfactant, and steric polymers to facilitate nonmaterial with specific, group-specific or highly specific ligands [83].

## **1.5 Magnetism and Superparamagnetism**

Magnetism date back to the early Greeks, where its name (magnetism) was derived from. The etymological origin of the word “magnet” meaning “the stone from Magnesia” was derived from Magnesia, a Greek town. This stone contained magnetite and a piece of iron was acknowledged to become magnetized when rubbed with magnetite. Smaller pieces of magnetic materials combined into a larger magnetic body were found to have a large lifting power in the 18th century. After Oersted discovery in 1820 that magnetic field could be produced by an electric current, progress in magnetism was made. This knowledge was effectively used by Sturgeon in 1825 to produce the first electromagnet. Although several famous scientists tackled the phenomenon of magnetism from the theoretical viewpoint (Gauss, Maxwell, and Faraday), the right explanation of magnetic materials and the foundations of modern technology is credited to the 20th-century physicist. Curie and Weiss succeeded in describing the phenomenon of spontaneous magnetization and its temperature dependence. The reality of magnetic domains was postulated by Weiss to explain how a material could be magnetized and yet have a net magnetization of zero [92].

The magnetic behaviour of solids is hinged on the magnetic moments of the atoms or ions in the solids. The quantized angular momenta associated with the orbital motion of electrons about the nucleus and the spins of the electrons about their own axes of rotation are related to the atomic and ionic-magnetic moments. In quantum theory, the Wolfgang Pauli exclusion principle states that no two electrons in each structure can have the same set of a quantum number when applied to an atom or ion. The principle postulates that only two electrons with opposite spins can occupy each possible electron orbital. The orbits are arranged in shells around the nucleus, with the magnetic moments of opposite spins pairs cancelling each other out. Thus, the net angular momentum and magnetic moments of the filled shell are equivalent to zero. The net magnetic moment of an atom or ion resulting from incomplete filled shells contains unpaired spins. The atoms or ions in a solid are not randomly distributed but occupy

fixed positions in a regular lattice, which reflects the symmetry of the crystalline structure and controls the interactions between the ions. Thus, the different magnetic behaviour types observed in solids depends not only on the presence of ions with unpaired spins but on the lattice symmetry and cell size also [93].

A magnetic material placed in a magnetic field of strength ( $H$ ), the individual atomic moments in the material contributes to its overall response. The magnetic induction is given by equation 1.1:

$$\mathbf{B} = \mu_0(\mathbf{H} + \mathbf{M}) \quad \mathbf{1.1}$$

where  $\mu_0$  is the permeability of vacuum and the magnetization is the magnetic moment per unit volume represented by  $M = m/V$ , where  $m$  is the magnetic moment on a volume ( $V$ ) of the material). To some degree all materials are magnetic, but their response depends on their atomic structure and temperature. Magnetic materials are classified in terms of their magnetic susceptibility ( $\chi$ ), which is defined by equation 1.2 [94-95]:

$$\mathbf{M} = \chi\mathbf{H} \quad \mathbf{1.2}$$

The arrangement of magnetic dipoles for five different materials in the absence or presence of an external magnetic field ( $H$ ) is shown in Figure 1.4. Diamagnets are materials showing weak repulsion (negative susceptibility, with  $\chi$  in the range  $10^{-6}$ - $10^{-3}$ ). Diamagnets lack magnetic dipoles in the absence or presence of external magnetic field and weakly induced dipole in the presence of the field. When the materials show small positive susceptibility ( $\chi$ ) in the range of  $10^{-1}$ - $10^{-6}$ ) and randomly oriented dipoles in the material can be aligned in an external magnetic field, are termed paramagnets. The magnetic interactions resulting from the above two types of materials are very weak since the thermal agitation at room temperature can make the magnetic moments to flip over nonstop. Ferromagnet materials tend to exhibit a positive susceptibility. The magnetic dipoles permanently exist in the absence and presence of an external field and exhibit long-range order. if the external magnetic field is removed the magnetic properties of the first classes of magnetic materials do not continue, while ferromagnetic materials have a stable magnetic property even after the magnetic field is removed. A ferromagnet become a paramagnet above a temperature called the Curie temperature ( $T_c$ ): a temperature at which there is a change of the direction of the intrinsic magnetic moment. Below  $T_c$ , the atoms lose their ordered magnetic moments and the material is paramagnetic. For diamagnets and

paramagnets, the relationship  $M = \chi H$  is generally linear, but for ferromagnets, there is no linear relationship between  $H$  and  $M$  [95, 96].

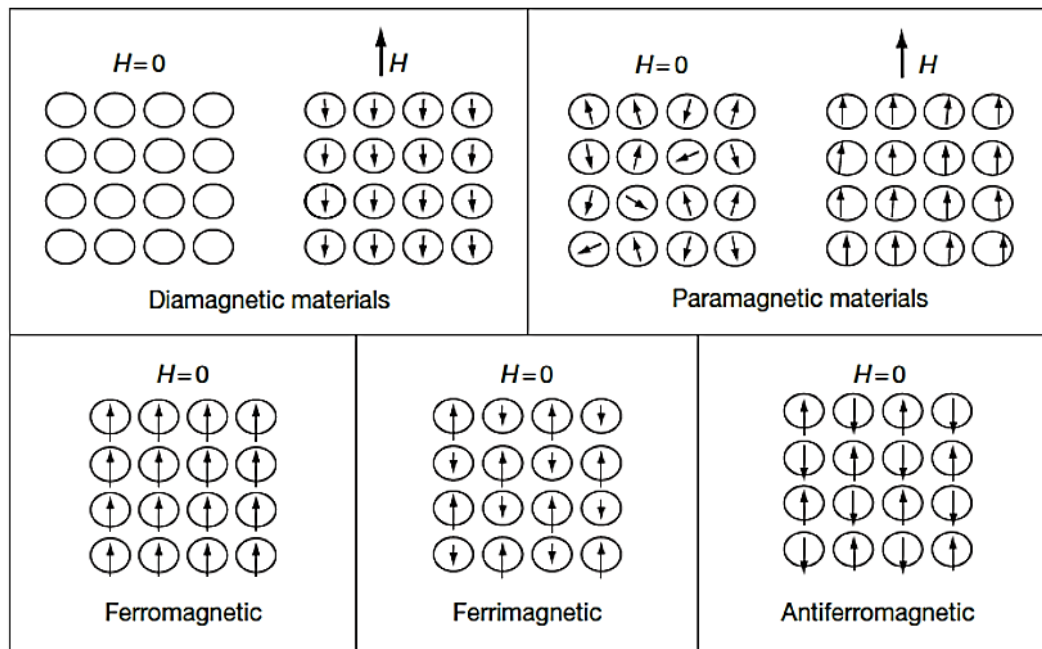


**Figure 1.4** Schematics showing the arrangement of the magnetic dipoles for five different types of materials in the absence or presence of external magnetic field ( $H$ ) [95].

The diagrams in Figure 5.1 describes the diamagnetic, paramagnetic, ferromagnetic and superparamagnetic materials behaviour in the external magnetic field such that high external magnetic field applied ( $H$ ), leads to lower the magnetization ( $M$ ) for diamagnetic material (Figure 1.5(a)). High external magnetic field applied ( $H$ ), leads to higher magnetization ( $M$ ) for paramagnetic material (Figure 1.5(b)). For ferromagnetic material, a hysteresis loop is observed and for the multi-domain particle, the loop is narrower (dashed line) (Figures 1.5(c)), and for superparamagnetic material, no hysteresis loop is observed, (a single-domain particle) superparamagnetic material have a sigmoidal shape (Figure 1.5(d)).

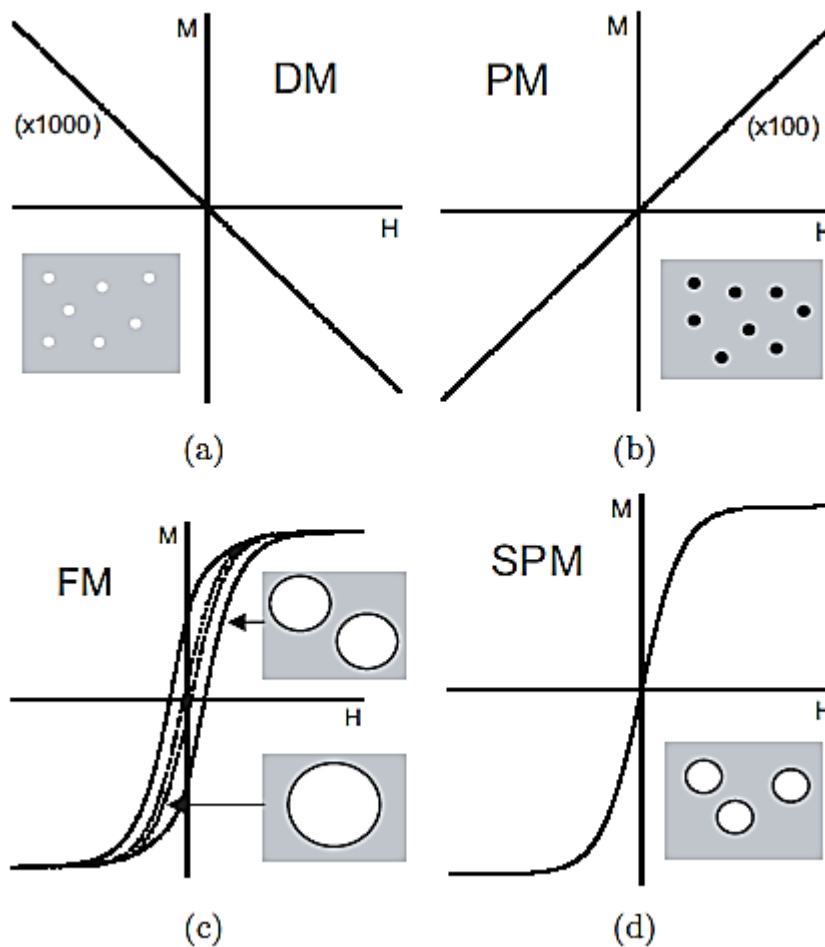


**Figure 1.5** The schematics describing (a) diamagnetic, (b) paramagnetic, (c) ferromagnetic and (d) superparamagnetic materials behaviour in the external magnetic field [97].

Magnetic nanoparticles have shown remarkable new phenomena such as high field irreversibility, high saturation field, superparamagnetism, extra anisotropy contributions, or shifted loops after field cooling. The narrow finite-size effects and surface effects that govern the magnetic behaviour of individual nanoparticles arises from these phenomena. Below a critical particle size, Frenkel and Dorfman were first to show that particles of ferromagnetic materials (<15 nm for the common materials) were found to have a single magnetic domain, i.e., at any field, the particles were in a state of fixed magnetization. The magnetization behaviour of particles above a certain temperature, i.e., the blocking temperature was identical to that of atomic

paramagnets (superparamagnetism), but large susceptibilities and extremely large moment were involved [98-101].

When magnetic materials show a behaviour like paramagnetism at temperatures below the Curie or the Neel temperature is known as Superparamagnetism. Superparamagnets comprise of individual (single) magnetic domains of elements (or compounds) that have ferromagnetic properties in bulk. Lately, increased attention has been received by superparamagnetic magnetite nanoparticles (MNPs) owing to their characteristics, i.e. magnetic moments been induced in the presence of an external magnetic field [102-103].

Superparamagnetism is linked with a phenomenon characteristic at the nanoscale, attributed to the unusual behaviour shown by nanometer-sized grains of magnetic materials such as cobalt, nickel, iron and some alloys and oxides, among others. Below a critical particle size of the magnetic material,  $D_c$ , the normal microscopic multi-domain ferromagnetic (*FM*) structure is energetically unfavourable and thus it contains only a single magnetic domain. This means that such a particle will pose a uniform magnetization. This critical particle size can be calculated easily accounting for the intrinsic properties of the material such as its saturation magnetization, their crystalline anisotropy or the exchange stiffness contributions. As particle size decreases in the single domain range, another critical threshold is reached,  $D_{SP}$ , at which the remanence and coercivity go to zero and the particle falls into the superparamagnetic (*SP*) state. A sketch illustrating this transition is provided in Figure 1.6. In this state, for a sufficiently small magnetic particle, the energy required to reverse its magnetization is smaller than the thermal energy. Then, the magnetic dipole randomly rotates changing its orientation [104].

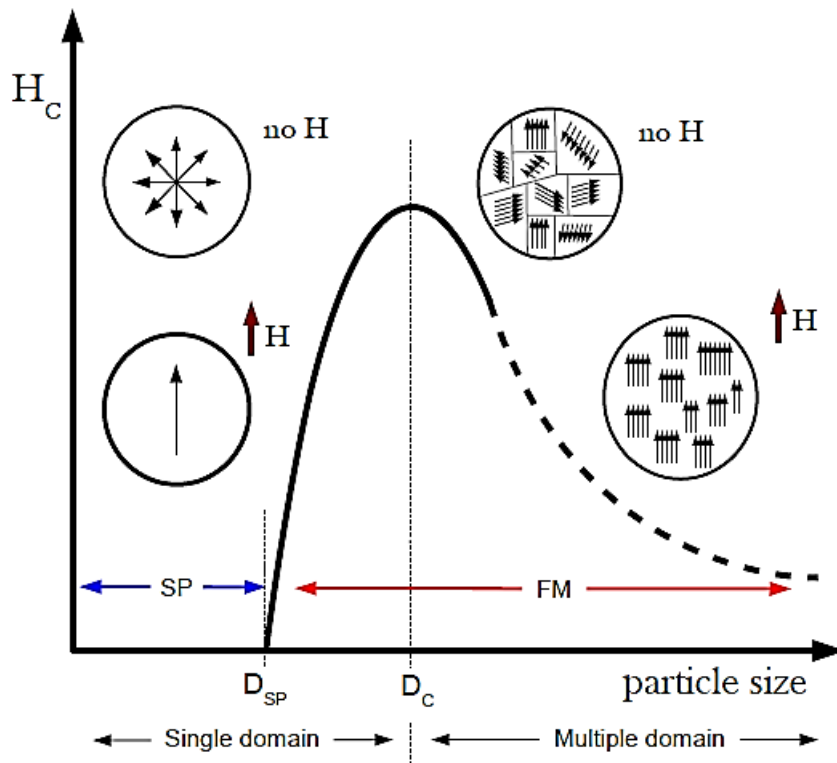


**Figure 1.6** Schematic illustration of the change in the coercivity field  $H_C$  as a function of particle size.

The finite size effects of nanoparticles are studied through the single domain and the superparamagnetic limits. In large magnetic particles having multi-domain structure, the regions of uniform magnetization are separated by the domain walls [105-106]. The domain walls formation is a process driven by the balance between the magnetostatics energy ( $\Delta E_{MS}$ ), which increases proportionately to the volume of the materials and the domain wall energy ( $E_{dw}$ ) which increases proportionately to the interfacial area between domains. When the size of a magnetic particle is reduced, a critical volume below which more energy is used to create a domain wall than to support the external magnetostatics energy (stray field) of the single domain state is reached. This is influenced by the contribution from various anisotropy energy terms. The critical radius  $r_c$  below which a particle acts as a single domain particle is given by equation 1.3 [96, 107-109].

$$r_c = 9 \frac{(AK_u)^{\frac{1}{2}}}{\mu_0 M_s^2} \quad 1.3$$

where  $A$  is the exchange constant,  $K_u$  is the uniaxial anisotropy constant,  $\mu_0$  is the vacuum permeability and  $M_s$  is the saturation magnetization. Characteristic  $r_c$  values are given in Table 1.3. The higher the particle magnetic moment, the lower the magnetic field  $H_s$  that is required to observe the magnetization saturation phenomenon. In a rough approximation, the  $H_s$  saturation field value can be estimated from the formula in equation 1.4, where  $\mu_{ef}$  is the effective magnetic moment of the particle [110]:

$$\mu_{ef}H_s \approx k_B T \quad 1.4$$

**Table 1.3:** Single domain radius  $r_c$  for different spherical particles [111].

Material	$r_c$ (nm)
Hcp $C_o$	8
FCC $C_o$	4
Fe	8
Ni	28
FePt	28
$C_oPt$	30
$Fe_2O_3$	45
$C_o Fe_2O_4$	50
$Fe_3O_4$	64
$SmC_{o5}$	375

The magnetic properties of non-interacting magnetic nanoparticles are strongly influenced by superparamagnetic relaxation at finite temperature. For a nanoparticle with uniaxial anisotropy and magnetic anisotropy energy is given by the expression in equation 1.5:

$$E_a = KV \sin^2 \theta \quad 1.5$$

At  $\theta = 0^\circ$  and  $\theta = 180^\circ$ , the energy is minimal and are separated by an energy barrier  $KV$ , where  $K$  is the anisotropy constant,  $V$  is the particle volume and  $\theta$  is the angle between the magnetization vector and an easy direction of magnetization. Nanoparticles often show a certain preference for the direction along which magnetization aligns to. Nanoparticles are said to have an anisotropy in these directions and if it is mainly one preferred direction (uniaxial anisotropy). Nanoparticles with uniaxial anisotropy flip the direction of their magnetization randomly. This effect of uniaxial anisotropy is induced by thermal energy. At finite temperature, the thermal energy may be sufficient to induce superparamagnetic relaxation. The superparamagnetic relaxation time is specified by the Neel-Brown expression given in equation 1.4:

$$\tau = \tau_o \exp\left(\frac{KV}{k_B T}\right) \quad 1.6$$

where  $k_B$  represents the Boltzmann's constant,  $T$  represents the temperature and  $\tau_o$  is in order of  $10^{-13}$  -  $10^{-9}$  s and temperature dependent [97, 112].

The non-interaction of single-domain particles occurs at temperatures greater than the blocking temperature known as the superparamagnetic behaviour. In the absence of magnetic field, magnetization is observed to disappears in superparamagnetic materials ( $T > T_B$ ). The mechanism of electrical relaxation is the Brownian relaxation mechanism, ( $\tau_B$ ), given by equation 1.7. This involves the rotation of the particles against the viscous force and the time constant describing this motion surges with the particle volume.

$$\tau_B = \frac{3V_H \eta}{k_B T} \quad 1.7$$

where  $\eta$  is the viscosity of the liquid containing the particles and  $V_H$  is the hydrodynamic volume of the particle. The total magnetic relaxation time is given by equation 1.8;

$$\frac{1}{\tau_{eff}} = \frac{1}{\tau_N} + \frac{1}{\tau_B} \quad 1.8$$

When  $\tau_B < \tau_N$  (for large nanoparticles with radius greater than 15 nm), the viscous component dominates the magnetic relaxation [113-114].

## 1.6 Statement of Problem

The consequence of the high concentration of heavy metals in water has severe effects on humans, plants, and animals. Contaminants like chromium, lead, copper, mercury, cadmium, nickel, fluoride, arsenic and congo red dye are released into groundwater and wastewater daily

through industrialization and urbanization from human activities in the environment, which result in reduced growth and development in humans, cancer, organ damage, nervous system damage and in extreme case death in humans. The actual costs of meeting growing demand for all water users at an environmentally acceptable quality level is increasing dramatically in the developing world. Owing to declining funding needed to meet the rising cost of producing clean water at specific standards in developing and developed countries around the world, there is need to provide a sustainable way of servicing the growing population of developing countries serviced by the water and sanitation sector during the next era. There is an urgent need for techniques that are cheap, effective and durable and environment-friendly to remove heavy metals from groundwater and wastewater, to meet the rising demand for water supply in around the world is unavoidable. The requirement for an effective and cheap way of decontaminating polluted groundwater necessitated this study, using nanotechnology and magnetic field to treat or remediate groundwater and wastewater source contaminated by heavy metals in-situ or ex-situ, to increase the reliable source of water available to the African continent and the world.

### **1.7 Objectives of this Study**

The basic objectives of this study are:

- I. To investigate the capability of synthesizing a functionalized magnetic nanoparticle (sorber) for the remediation of water contaminated by heavy metals and dye (chromium six, fluoride and congo red) using electromagnetic excitation/torque technology.
- II. To investigate the methodology for removing heavy metals and dye using functionalized magnetic nanocomposite as a function of the magnetic field strength, magnetic exposure time, solution pH, adsorbent dosage, the initial concentration of adsorbate, sorption kinetics, sorption isotherms and desorption experiments.
- III. To establish appropriate adsorbent dosage for the decontamination of wastewater with heavy metals and dye in water works, municipal and industrial waste using electromagnetic excitation/torque technology.
- IV. To determine the velocity field of rotating polypyrrole magnetic nanocomposite in an aqueous solution of Cr(VI) and fluoride using particle shadow velocimetry method and the effect of the increased magnetic field on the particles during the adsorption process.

- V. Using velocity field profile generated from the PIVLab analysis to check for the effect of particles aggregation and other factors on the adsorption process with the increased induced magnetic field on the particles.

## 1.8 References

- [1] R. Sivashankar, A. B. Sathya, K. Vasantharaj, and V. Sivasubramanian, **2014**, *Environmental Nanotechnology, Monitoring and Management*, 1-2, 36-49.
- [2] S. P. Kamble, S. B. Sawant, J. C. Schouten, and V. G. Pangarkar, **2003**, *J. of Chemical Technology and Biotechnology*, 78, 865-872.
- [3] D. Mara, J. Lane, B. Scott, and D. Trouba, **2010**, *PLOS Medicine*, 7, e1000363.
- [4] X. Qu, P. J. J. Alvarez, and Q. Li, **2013**, *Water Research*, 47, 3931-3946.
- [5] A. M. Al-Sabagh, Y. M. Moustafa, A. Hamdy, H. M. Killa, R. T. M. Ghanem and, R. E. Morsi, **2017**, *Egyptian J. of Petroleum*.
- [6] World Health Organization, **2006**, *Meeting the MDG Drinking Water and Sanitation Target: The Urban and Rural Challenge of the Decade*.
- [7] World Health Organization (WHO, & UNICEF), **2000**, *Global Water Supply and Sanitation Assessment 2000 Report*, World Health Organization (WHO).
- [8] UNICEF, **2004**, *Meeting the MDG Drinking Water and Sanitation Target: A Mid-Term Assessment of Progress*
- [9] J. Theron, J. A. Walker, and T. E. Cloete, **2008**, *Critical Reviews in Microbiology*, 34, 43-69.
- [10] F. Ferrarini, L. R. Bonetto, J. S. Crespo and M. Giovanela, **2016**, *Water Science, and Technology*, 73, 2132-2142.
- [11] E.W. Boulware, **2013**, McGraw-Hill Education.
- [12] S. J. Wimalawansa, **2013**, *International J. of Emerging Technology and Advanced Engineering*, 13, 75-89.
- [13] USGS, **2016**, Retrieved March 9, 2017, from <http://water.usgs.gov/edu/earthwhere-water.html>.
- [14] M. M. K. Alkhazan and A. A. N. Saddiq, **2010**, *J. of Evolutionary Biology Research*, 2, 7-14.

- [15] M. S. Slimani, H. Ahlafi, H. Moussout, R. Chfaira, and O. Zegaoui, **2014**, International J. of Advanced Research in Chemical Science (IJARCS), 1, 17-29.
- [16] D. K. Tiwari, J. Behari, and P. Sen, **2008**, World Applied Science J., 3, 414-433.
- [17] C. J. Quinn, T. C. Molden, and C. H. Sanderson, **1997**, Iron and Steel Engineer, 74, 47-52.
- [18] B. Kavitha, P. Jothimani, S. Ponmani, and R. Sangeetha, **2013**, Int. J. Res. Studies in Biosci, 1, 17-23.
- [19] O. B. Akpor and M. Muchie, **2010**, International J. of Physical Science, 5, 1807-1817.
- [20] J. Gomez-Pastora, E. Bringas, and I. Ortiz, **2014**, Chemical Engineering J; 256, 187-204.
- [21] A. Abbas, A. M. Al-Amer, T. Laoui, M. J. Al-Marri, M. S. Nasser, M. Khraisheh, and M. A. Atieh, **2016**, Separation and Purification Technology, 157, 141-161.
- [22] S. E. Ghazy and S. M. El-Morsy, **2009**, African J. of Biotechnology, 8, 4140-4148.
- [23] P. B. Tchounwou, C. G. Yedjou, A. K. Patlolla, and D.J. Sutton, **2012**, Springer Basel, 133-164.
- [24] O. B. Akpor, G. O. Ohiobor and T. D. Olaolu, **2014**, Advances in Bioscience and Bio-engineering, 2, 37-43.
- [25] R. Khandanlou, M. B. Ahmad, H. R. F. Masoumi, K. Shameli, M. Basri and K. Kalantari, **2015**, PLOS ONE, 10
- [26] J. Sharma and B. Janveja, **2008**, Rasayan J. Chem, 1, 936-942.
- [27] M. R. Hadjmohammadi, M. Salary, and P. Biparva, **2010**, J. of Applied Science in Environmental Sanitation, 6, 1-13
- [28] M. A. Hashim, S. Mukhopadhyay, J. N. Sahu and B. Sengupta, **2011**, J. of Environmental Management, 92, 2355-2388.
- [29] L. Filipponi and D. Sutherland, **2010**, Interdisciplinary Nanoscience Centre (iNaNo), Aarhus University, Denmark, 4-26.

- [30] M. Tanzifi, M. Mansouri, M., Heidarzadeh, and K. Gheibi, **2016**, *J. of Water and Environmental Nanotechnology*, 1, 124-134.
- [31] M. B. Ibrahim and S. Sani, **2014**, *J. of Physical Chemistry*, 4, 139-146.
- [32] M. A. Ahmad, S. G. Herawan, and A. A. Yusof, **2014**, *ISRN Mechanical Engineering*, 2014.
- [33] G. Vijayakumar, R. Tamilarasan and M. Dharmendirakumar, **2012**, *J. Mater. Environs. Sci.*, 3, 2028-2508.
- [34] S. K. Bajpai, M. K. Armo, and M. Namdesh, **2009**, *Acta Chimica Slovenica*, 56, 254-261.
- [35] A. El-Sikaily, A. El-Nemr, A. Khaled, and O. Abdelwehab, **2007**, *J. of Hazardous Materials*, 148, 216–228.
- [36] R. Saha, R. Nandi and B. Saha, **2011**, *J. of Coordination Chemistry*, 64, 1784-1806.
- [37] C. M. Zvinowanda, J. O. Okonkwo, P. N. Shabalala and N. M. Agyei, **2009**, *International J. of Environmental Science and Technology*, 6, 425-434.
- [38] A. Amalraj, M. K. Selvi, A. Rajeswari, E. J. S. Christy and A. Pius, **2016**, *J. of Water Process Engineering*, 13, 88-99.
- [39] M. Muliwa and M.S. Onyango, **2014**, *International Conference on Sustainable Research and Innovation*, 5, 83-90.
- [40] M. R. Lasheen, I. Y. El-Sherif, D. Y. Sabry, S. T. El-Wakeela, and M. F. El-Shahat, **2014**, *Desalination and Water Treatment*, 52, 6464–6473.
- [41] M. R. Samarghandi, G. Asgari, A. Ahmadzadeh, A. Poormohammadi and M. Ahmadian, **2015**, *J. of Chemical and Pharmaceutical Research*, 7, 933-941.
- [42] S. Edeballi, **2015**, *J. of Nanomaterials*, 2015.
- [43] A. E. Chavez-Guajardo, J. C. Medina-Liomas, L. Maqueira, C. A. S. Andrade, K. G. B. Alves and C. P. De Melo, **2015**, *Chemical Engineering J.*, 281, 826-836.
- [44] Attia, S. A. Khedr, and S. A. Elkholy, **2010**, *Brazilian J. of Chemical Engineering*, 27, 183-193.

- [45] Department of Water Affairs and Forestry Report, **1996**, 1, Second Edition, 45-46.
- [46] R. Bhaumik, N. K. Mondal, B. Das, P. Roy, K. C. Pal, C. Das, A. Banerjee and J.K. Datta, **2012**, J. of Chemistry, 9, 1457-1480.
- [47] A. V. Jamode, V. S. Sapkal, and V. S. Jamode, **2004**, J. Indian Inst. Sci., 84, 163-171.
- [48] Sunitha and B. M. Reddy, **2014**, International J. of Current Research and Academic Review, 2, 159-166.
- [49] S. S. Tripathy, J. Bersillon, and K. Gopal, **2006**, Separation and Purification Technology, 50, 310-317.
- [50] D. Balarak, Y. Mahdavi, E. Bazrafshan, A. H. Mahvi and Y. Esfandyari, **2016**, Research Report, 49, 71-83.
- [51] A. Rafique, M. A. Awan, A. Wasti, I. A. Qazi and M. Arshad, **2013**, J. of Chemistry, 2013.
- [52] S. Tokalioglu, S. Kartal and U. Sahin, **2004**, Turk. J. of Chemistry, 28, 203-211.
- [53] N. Agnihotri, V. K. Pathak, N. Khatoon and M. Rahman, **2013**, International J. of Scientific & Engineering Research, 4, 106-110.
- [54] X. Zhao, J. Wang, F. Wu, T. Wang, Y. Cai, Y. Shi and G. Jiang, **2010**, J. of Hazardous Materials, 173, 102-109.
- [55] N. P. Bhagya, P. A. Prashanth, R. S. Raveendra and B. M. Nagabhushana, **2015**, International J. of ChemTech Research, 8, 1829-1835.
- [56] A. Mittal, L. Kurup and J. Mittal, **2007**, J. of Hazardous Materials, 146, 243-248.
- [57] R. Satheesh, K. Vignesh, M. Rajarajan, A. Suganthi, S. Sreekantan, M. Kang and B. S. Kwak, **2016**, Material Chemistry, and Physics, 180, 53-65.
- [58] H. Kaur, S. Kaur, and R. Kaur, **2014**, Chemical Science Transactions, 3, 1300-1309.
- [59] A. Shojamoradi, H. Abolghasemi, M. Esmaili, M. Foroughi-Dahr and H. Fatoorehchi, **2013**, J. of Petroleum Science and Technology, 3, 25-34.

- [60] J. M. Salman, A. R. Amrin, F. M. Hassan, and S. A. Jouda, **2015**, *Mesopotamia Environmental J.*, 1, 82-89.
- [61] W. C. Wanyonyi, J. M. Onyari, and P. M. Shiundu, **2014**, *Energy Procedia*, 50, 862-869.
- [62] M. S. Alam, R. Khanom, and M. A. Rahman, **2015**, *American J. of Environmental Protection*, 4, 207-213,
- [63] O. Paska, R. Ianos, C. Pacurariu, and A. Bradeanu, **2014**, *Water Science, and Technology*, 69, 1234-1240.
- [64] M. Bhaumik, R. I. McCrindle, and A. Maity, **2015**, *Chemical Engineering J*; 260, 716-729.
- [65] T. Liu, Y. Li, Q. Du, J. Sun, Y. Jiao, G. Yang, Z. Wang, Y. Xia, W. Zhang, and K. Wang, **2012**, *Colloids Surf. B Biointerf.* 90, 197–203.
- [66] S. Kaur, S. Rani, and R. K. Mahajan, **2013**, *J. of Chemistry*, 2012.
- [67] Z. Xu, W. Li, Z. Xiong, J. Fang, Y. Li, Q. Wang and Q. Zeng, **2016**, *Desalination and Water Treatment*, 57, 7054-7065.
- [68] H. Chen and J. Zhao, **2009**, *Adsorption*, 15, 381-389.
- [69] L. Wang and A. Wang, **2007**, *J. of Hazardous Materials*, 147, 979-985.
- [70] X. Yang, Z. Wang, M. Jing, R. Liu, L. Jin and X. Shen, **2014**, *Water Air Soil Pollut*, 225, 1819.
- [71] S. L. Pal, U. Jana, P. K. Manna, G. P. Mohanta and R. Manavalan, **2011**, *J. of Applied Pharmaceutical Science*, 1, 228-234.
- [72] M. Abhilash, **2010**, *International J. of Pharma and Bio Sciences*, 1, 1-12.
- [73] K. Varadan, A. Sivathanu Pillai, D. Mukherji, M. Dwivedi and L. Chen, **2010**, *World Scientific Publication*, 2-9.
- [74] F. Schutte and W. Focke, **2007**, *Report to the Water Research Commission*, 1-23.

- [75] G. A. Mansoori, T. Rohani Bastami, A. Ahmadpour, and Z. Eshaghi, **2008**, Annual Review of Nanoresearch, 2, 1-73.
- [76] S. Yunus, H. A. Kurniawan D. Adityawarman, and A. Indarto, **2012**, Environmental Technology Reviews, 1, 136-148.
- [77] K. Setshedi, M. S. Onyango, F. Otieno, G. Carja and S. Nichetus, **2012**, J. of Hazardous Materials, 61, 278-290.
- [78] P. Bhawana and M. H. Fulekar, **2012**, Research J. of Chemical Sciences, 2, 90-96.
- [79] A. Gurunathan, D. Viswanathan, S. Rajasekar, and G. B. George, **2016**, An International J; 27, 45-58.
- [80] M. I. Din and A. Rani, **2016**, International J. of Analytical Chemistry, 2016.
- [81] P. J. A. Borm, and W. Kreyling, **2004**, J. Nanosci. Nanotech; 4, 521–531,
- [82] S. Ghaderi, B. Ramesh, and A. M. Seifalian, **2011**, J. of Drug Targeting, 19, 475–486.
- [83] N. Neyaz, W. A. Siddiqui, and K. K. Nair, **2013**, International J. of Environmental Science, 4, 472-483.
- [84] W. Wu, Z. Wu, T. Yu, C. Jiang and W. Kim, **2015**, Science and Technology of Advanced Materials, 16, 023501.
- [85] A. Waleed, **2009**, Open Chemistry, 7. 884-899.
- [86] M. Kumari, **2015**, Doctoral Dissertation, 4.
- [87] H. Wang, Y. Shen, C. Shen, Y. Wen, and H. Li, **2012**, Desalination, 284, 122-127.
- [88] K. L. Palanisamy, V. Devabharathi, and N. M. Sundaram, **2013**, International Journal of Research in Applied, Natural and Social Sciences,1, 15-22.
- [89] A. Kakavandi, R. R. Kalantary, A. J. Jafari, S. Nasser, A. Ameri, A. Esrafil and A. Azari, **2015**, Clean-Soil, Air, Water, 43, 1157-1166.
- [90] L. Feng, M. Cao, X. Ma, Y. Zhu and C. Hu, **2012**, J. of Hazardous Materials, 217-218, 439-446.

- [91] S. A. Elhafez, H. A. Hamad, A. A. Zaatout, and G. F. Malash, **2017**, *Environmental Science and Pollution Research*, 24, 1397-1415.
- [92] K. H. J. Buschow and F. R. De Boer, **2004**, Kluwer Academic Publishers, 92, 1.
- [93] W. Lowrie, **1997**, Cambridge University Press, 237.
- [94] S. Laurent, S. Dutz, U. O. Hafeli and M. Mahmoudi, **2011**, *Advances in Colloid and Interface Science*, 166, 8-23.
- [95] R. Epherre, G. Goglio, S. Mornet, and E. Duguet, **2011**, *Comprehensive Biomaterials*, 4, 575-593.
- [96] J. Estelrich, E. Escribano, J. Quearlt and M. A. Busquets, **2015**, *International J. of Molecular Sciences*, 16, 8070-8101.
- [97] M. Benz, **2012**, Discussion, 3-27.
- [98] S. G. Grancharov, H. Zeng, S. Sun, S. X. Wang, S. O'Brien, C. B. Murray, J. R. Kirtley, and G. A. Held, **2005**, *The J. of Physical Chemistry B*, 109, 13030-13035.
- [99] Y. W. Jun, Y. M. Huh, J. S. Choi, J. H. Lee, H. T. Song, S. Kim, S. Kim, S. Yoon, K. S. Kim, J. S. Shin, and J. S. Suh, **2005**, *J. of the American Chemical Society*, 127, 5732-5733.,
- [100] T. Yavuz, J. T Mayo, W. Y. William, A. Prakash, J. C. Falkner, S Yean, L. Cong, H. J. Shipley, A. Kan, M. Tomson, and D. Natelson, **2006**, *Science*, 314, 964-967.
- [101] A. Akbarzadeh, M. Samiei, and S. Davaran, **2012**, *Nanoscale Research Letter*, 7, 144.
- [102] J. P. Vejpravova, V. Sechovsky, D. Niznansky, J. Plocek, A. Hutlov and J. L. Rehspringer, **2005**, *WDS'05 Proceedings of Contributed Papers*, 518–523.
- [103] Cheraghipour, S. Javadpour, and A. R. Mehdizadeh, **2012**, *J. of Biomedical Science and Engineering*, 5, 715-719.
- [104] J. A. Segura, **2013**, PhD Thesis in Materials Science, 3-5.
- [105] Z. Mosleh, P. Kameli, M Ranjbar, and H. Salamati, **2014**, *Ceramics International*, 40, 7279-7284.

- [106] N. I. Cuello, V. R. Elías, E. Winkler, G. Pozo-López, M. I. Oliva, and G. A. Eimer, **2016**, *J. of Magnetism and Magnetic Materials*, 407, 299-307.
- [107] Issa, I. M. Obaidat, B. A. Albiss, and Y. Haik, **2013**, *International J. of Molecular Sciences*, 14, 21266-21305.
- [108] T. Muthukumaran, and J. Philip, **2016**, *J. of Alloys and Compounds*, 689, 959-968.
- [109] A. H. Lu, E. L. Salabas, and F. Schuth, **2007**, *Angewandte Chemie International Edition*, 46, 1222-1244.
- [110] S. P. Gubin, Y. A. Koksharov, G. B. Khomutov and G. Y. Yurkov, **2005**, *Russian Chemical Reviews*, 74, 489-520.
- [111] K. H. J. Buschow, **2015**, *Elsevier*, 23, 6-7.
- [112] S. Morup, M. F. Hansen, and C. Frandsen, **2010**, *Beilstein J. of Nanotechnology*, 1, 182-190.
- [113] M. I. Obaidat, B. Issa, and Y. Haik, **2015**, *Nanomaterials*, 5, 63-89.
- [114] Issa, I. M. Obaidat, B. A. Albiss and Y. Haik, **2013**, *International J. of Molecular Science*, 14, 21266-21305.

## CHAPTER TWO

### 2.1 Remediation Methods Using Nanoparticles

For the evaluation and remediation of sites contaminated, a systematic approach is required to ease the process of remediation, to avoid pointless delays. The most significant feature of the systematic method is site characterization, assessment of risk and remedial action. In a polluted site remediation design, site characterization is often the first step. This involves the collection and data assessment, which represents the contaminants types and its distribution at the site under investigation. The results of a site characterization form the basis for decisions concerning the needs of remedial action and the results serve as a guide for design, implementation, and monitoring of the remedial system. Risk assessment is done when the site pollution is established through a sequence of site characterization. A complete approach for risk assessment is hazard identification, exposure assessment, toxicity assessment and risk characterization. To determine the potential risk detected contamination posed to human health and the environment under present and possible future conditions, systematic evaluation is used. If the risk assessment reveals an intolerable risk owing to the contamination, a remedial strategy is developed to evaluate the problem of contamination. When the action is needed, a remedial strategy must be developed to ensure that the planned method of remediation complies with all the technological, financial and regulatory considerations. The cost and benefits of the various remedial alternatives are repeatedly weighed by equating the flexibility, compatibility, speed and cost of each method. The remediation technique must be flexible in its application to ensure that it is adjustable to the specific site soil and groundwater characteristics [1]

Remediation is the process of removing, minimising or neutralising water contaminants that could cause harm to human health or ecosystems. Several treatment techniques and processes have been used to eliminate pollutants from contaminated water. To avoid the undesirable effects of heavy metals in wastewater, there is a need for acceptable treatment of wastes before it is discharged into receiving water bodies. The treatment goal is to remove any existing or potential threat to human health and the environment [2-4]. Progressively strict water quality standards compounded by evolving pollutants have brought new inspection to present water treatment and supply systems widely established in developed countries, as the rapidly growing worldwide population and the improvement of living standard continuously drive up the demand. Moreover, global climate change highlights the already uneven distribution of fresh wa-

ter, destabilizing the supply. Furthermore, current water and wastewater treatment technologies and infrastructure are reaching their limit for providing adequate water quality to meet human and environmental needs [5].

In the case of water remediation, biological, chemical and physical methods are generally employed. Biological treatment refers to the degradation of organic compounds by breaking and transformation of inorganic compounds by bio-aided reactions. Chemical treatment procedures include coagulation, oxidation, electron beam irradiation and sorption to organic/inorganic substrates, while Physical treatment methods include air sparging/air strapping and incineration [6]. Several treatment techniques have been explored for the removal of metals from wastewater using membrane filtration, reduction, adsorption/biosorption, ion-exchange, coagulation-flocculation, chemical precipitation, flotation and electrochemical methods. Most of them are significantly costly and incapable of removing trace levels of heavy metal ions. But, due to economic constraints in most countries, developing cost-effective procedures that are clean is desired. Adsorption has proved to be the most effective method specifically for effluents with moderate and low concentrations. The effectiveness of adsorption hinges on factors like surface area, pore size distribution, polarity, and functional groups of the adsorbent [7-8].

Adsorption method hitherto robust in nature suffers from immense mass transport resistance due to the size of the adsorbents. To overcome this limitation, advanced techniques in material design are required and can be realized through nanotechnology. The search for new technologies for the removal of toxic metals from aqueous waste has prompted attention directed at synthetic new materials with high capability of removal. Increased in the sorption capacity of these magnetic materials, are prepared by coating iron or metallic ions or ferromagnetic materials either with an organic polymer or ion-exchange resin. These coatings are observed to selectively isolated the contaminants on top of the particles due to their chemical nature. Once the particles are loaded with contaminants, a magnet is used to recover the particles from the waste stream. The magnetic particles are superparamagnetic; as they are not permanently magnetized after aggregate formation. The Stability of the polymeric coating and the covalent attachment of molecules contributes to the particles use and reuse [9-10].

## **2.2 Literature Review on Magnetic Field Effect on Adsorption Process**

The non-chemical water treatment devices were originally proposed as a means of scale control in 1865. A. T. Hay received the first US patent for a water treatment device that employed a

magnetic field in 1873. Theo Vermeiren of Belgium was the first to patent a practical magnetic device for water treatment [11-12]. Magnetism is an inimitable property that supports water purification as it influences contaminants physical and chemical properties in aqueous solution and suspensions [13-14].

Fiscal and environmental concerns have led to the development of additional physical means for the removal of organic compounds from wastewater using permanent magnets, electromagnetic coils, electrodes and ultrasonic pretreatment [15-17]. Improving the adsorption and separation process, magnetic field method has progressively drawn consideration. Magnetic field exposure method has demonstrated its capacity for increasing the adsorptive elimination of contaminants from water, as static magnetization is appropriate, simple and cost-effective. Essentially, the magnetic field has shown to influence the behaviour and physicochemical properties of water when applied to water. The magnetic field within changes the rates of chemical reactions owing to the existence of competing ions dissolution and precipitation of dissolved salts, which facilitates the formation and decomposition of colloidal complexes and improves electrocoagulation followed by sedimentation and crystallization of scaling salts of  $\text{Ca}^{2+}$ ,  $\text{Mg}^{2+}$ ,  $\text{Fe}^{2+}$  and  $\text{Fe}^{3+}$  [15, 18-19].

The efficiency of magnetic water treatment is strongly affected by the water chemical properties, the strength of the magnetic field and the characteristics of the fluid flow. The materials used and the equipment type utilized determines the magnetic field strength. Stronger magnetic field leads to greater number of dipoles pointing in the direction of the field [20].

In recent years, increase application of an electromagnetic field in different fields like therapeutic and diagnostic medicine, environment management and industrial procedures have been witnessed. The effect of magnetic field on scale prevention, [21-24], separation of the suspended particle [25], magnetic field effect on the adsorption of zinc, copper (II), industrial waste, colour removal, total suspended solids, chemical oxygen demand, pH and Uranium and Strontium have been reported [11, 26-30].

Brito et al [10] reported that the adsorption of methyl blue and phenol were significantly influenced by a magnetic field. In the presence of magnetic field, 97% and 51.12% removal were observed for low and high dye concentrations, while 87% and 71.6% removal were observed for low and high phenol concentrations. Without a magnetic field, the removal of low and high dye concentrations was observed to be 86.6% and 33.91% and 82.3% and 65.81% at low and

high phenol concentrations. The Langmuir isotherm model best describes the results of the adsorption process of phenol and methyl blue molecules in the presence of magnetic field and without magnetic field, with a significant difference observed among the adsorbed amounts per gram of adsorbent between the curves in the presence of magnetic field and without magnetic field. Improvement in the orientation of the molecules of the adsorbate towards the activated carbon pores assisted the adsorptive process and resulting in the adsorption time gain. This was attributed to the difference in the adsorption of methyl blue dye and phenol in the presence of magnetic field.

Duan et al [14] observed that the degree of Pb(II) adsorbed onto modified chitosan were affected by pH, the concentration of the ion solution, the exposure time and the strength of the magnetic field. Using adsorption isotherm and kinetics models, the adsorption capacity of modified chitosan for Pb(II) ions in a magnetic field when compared with the magnetically untreated samples was observed to be improved. The experimental data was best described using the Langmuir and Freundlich models, with a maximum adsorption capacity of 2.5040 mg/g using modified chitosan for Pb(II) adsorption under the influence of a magnetic field of 480 kA/m.

Hao et al [15] reported in their study that the properties of the adsorbent and adsorbate were observed to change, with the adsorbent surface morphology becoming less homogeneous under the magnetic field exposure. This led to an increase in the surface area of the organo-bentonite particles, hence enhancing the adsorption of methyl blue dye. Improved adsorption of methyl blue was also observed to increase with increased magnetic field intensity in this study. The adsorption data was observed to fit well to the Freundlich isotherm model, with the magnitude of the dimensionless exponent ( $n$ ) reflecting the surface heterogeneity of the adsorbent with a beneficial adsorption. The rate constants of the second-order-models showed that the adsorption increased with increasing magnetic field intensity.

Li et al [18] reported that the external magnetic field significantly improved the adsorption of methylene blue with a decrease in the dose of wheat straw biochar used. Enhancement of adsorption capacity under the effect of an external magnetic field was observed to increase with an initial dye concentration of 5-80 mg/L. The surface chemistry of wheat straw biochar and the positive charge molecules of MB were observed to be sensitive to the presence of the external magnetic field. The viscosity and surface tension of the solutions were observed to be

reduced by the magnetic treatment, which was attributed to the resonance effect. This resonance effect was observed to impart energy to the system, hence changing the structure and nature of the material involved. With and without an external magnetic field, the maximum adsorption capacity for dye adsorption was found to 46.6 and 62.5 mg/g.

Mohammed et al [26] study showed that colour, TSS and COD were effectively reduced using magnetic treatment, with a maximum degradation of 16.13%, 34.34% and 44.29% for colour, TSS and COD when the magnetic field was 200 mT. This was attributed to the contribution of atmospheric oxygen and the intensification of free radicals' formation. The adsorbed layer was observed to be thickened by the magnetic exposure, as efficient coagulation induced by the magnetic field may have positively influenced the bonding and removal of adsorbate.

Zhang et al [27] found that the equilibrium for the adsorption of copper onto Ca-rectorite was attained in the first hour under the influence of magnetic field. It was observed that Cu ions adsorbed increased progressively with increase in exposure time and magnetic flux density, with a maximum increment obtained at 30 min and 0.34 T. The zeta potential and diffusivity of the colloids were observed to be reduced by magnetic exposure and field effect, which was attributed mainly to particles rather than the bulk solution.

Yuan-Yuan et al [29] study showed that the fraction of copper (II) adsorbed was significantly improved using a magnetic field, with copper(II) adsorption by kaolinite increasing with increase in pH 2-6. Magnetic exposure time and the magnetic flux density were also observed to promote the fraction of copper(II) adsorbed onto Kaolinite.

Jiang et al [31] reported 99% of  $\text{Cu}^{2+}$  been sequestered by ZVI with the induction of weak magnetic field over a pH range of 3-6 for 30 min. It was observed in this study that the removal efficiency of  $\text{Cu}^{2+}$  dropped from 97.5-4.5% without weak magnetic field applied for 2 h, as ZVI corrosion resulted in the ingesting of hydrogen ion ( $\text{H}^+$ ). Uneven distribution of paramagnetic  $\text{Cu}^{2+}$  along a wire in a heterogeneous MF showed the magnetic field gradient force accelerated the paramagnetic  $\text{Cu}^{2+}$  transportation towards the surface of ZVI, which induced sharp decay of the magnetic flux intensity from the ZVI surface to bulk  $\text{Cu}^{2+}$  solution.

Li et al [32] reported improvement in the reactivity of ZVI towards Cr(VI) as the applied WMF with flux intensity increased from 0.2-20 mT. 80.9% of Cr(VI) was sequestered by ZVI in the presence of MF of 0.2 mT for 60 min. Rapid Cr(VI) removal was attained in MF of 2.0 mT, and subsequent increase in the MF flux density resulted in a drop in the Cr(VI) removal rate,

suggestive of the minor role of the Lorentz force. Without the application of MF, 69.4% of Cr(VI) was removed by ZVI in 120 min. It is also reported that decreases in ZVI particle size resulted in the improved removal of Cr(VI) under the influence of WMF. This is evident in the increase of the ratio of the Cr(VI) removal rate constant with MF of 2.0 mT to that without MF from 1.2 to 11.3 as the iron particles sizes decrease from 421.2 to 18.1 m.

Liang et al [33] reported in their study that small amount of Se(VI) (less than 4%) was removed by ZVI without the application of WMF for 72 hours. With the application of WMF, a remarkable improvement in Se(VI) sequestered by ZVI was observed, with a complete removal of 10 mg/L Se(VI) achieved with ZVI in 90 min. Se(VI) removal was also observed to increase with an increase in the ZVI dosage used in the presence of WMF, with a complete removal of Se(VI) using 2.5 g/L ZVI in 4 hours. The main portion of the kinetics of Se(VI) removed by ZVI in the presence of WMF was observed to follow a zero-order rate law, with the rate constant of Se(VI) sequestered increasing with ZVI dosage.

Khiadani et al [34] reported improved removal of turbidity, which increased from 90.8%-95.7% with the application of magnetic field. This was ascribed to colloidal stability influenced by the application of magnetic field, which lead to the reduction in the charge density within the Stern layer. The zeta potential of the colloidal particles was reduced by the magnetic field, thereby causing particle instability, aggregation and more rapid sedimentation. It was also reported that improvement in the removal efficiency of lead, zinc, and cadmium using nano iron oxide coated with sand increase to 89.5%, 79.9%, and 91.5% with the application of magnetic field. Due to the magnetic force resulting from the magnetic field, the increased electrostatic interaction between the positive charge ions such as lead, zinc and cadmium with the adsorbent surface was observed.

He et al [35] observed a significant amount of mercury captured using ash fly under the influence of electromagnetic field (15-25%), with opposing magnetic poles and like magnetic poles providing better mercury adsorption capacity when no magnetic field was used. Improvement in the removal efficiency using electromagnetic field was attributed to a likely change of mercury material or the fly ash. The interaction of the EMF with orbital angular momentum and the intrinsic spin angular momentum was observed to leads to a change in the energy of the mercury atom. Mercury atom induced by the EMF caused energy level splitting and the EMF motivates the occurrences of Zeeman or the Paschen-back effects that vary the electronic orbit of the vapour of mercury. The energy level splitting observed in both valence and conduction

bands enhance the chemical activity of mercury due to increasing the electron-transition probability.

Eskandarpour et al [36] reported a high efficiency of phosphate removed without the use of magnetic seeding at magnetic intensities of 1 Tesla. Shen et al [37] observed improvement in the rate of methylene blue dye removed with the introduction of acoustic field at frequencies of 50-300 Hz and a magnetic field strength of 334-485 mT. 50 Hz frequency and 485 mT magnetic field were recorded to give the best result indicating that the corresponding acoustic wave and magnetic field strength promote the movement of the molecules and increase the collision between the methylene blue molecules and the porous carbon thereby increasing the proportion of dye entering the pores.

### **2.3 Three-Phase Induction Motor**

The history of electric motors can be traced to the work of Charles Wheatstone in 1840. But then, Wheatstone's model was practically inept. In 1824, present rotating magnetic fields termed Arago's rotations were used manually to turn on and off switches. This was expressed by French physicist Francois Arago. In 1879, the effect of the first primitive induction motor was confirmed by Walter Baily. Fundamentally, AC induction motors were invented exclusively by Galileo Ferraris and Nikola Tesla. A model of a working motor was demonstrated by Galileo Ferraris in 1885 and by Nikola Tesla in 1887. Explanation of the basics of motor operation published by the Royal Academy of Science of Turin was because of Ferraris's research (April 1888) on alternating current polyphone motor. In 1889 and 1890, the cage rotor induction motor and the three-limb transformer were invented by Mikhail Dolivo-Dobrovolsky's. The development of the three-phase induction motors was started by the General Electric Company (GE) in 1891 and by 1896, General Electric and Westinghouse signed a cross-licensing contract for the bar-winding-rotor design which was later called the squirrel-cage rotor [38].

For over 100 years, Electric motors have been a central component of the industry. Electric motors are considered as the 'workhorse' of the industry because of their distinct features such as ruggedness, simplicity to control, very efficient, and environmentally friendly. They are extensively used in home and industrial appliances such as fans, air conditioners, machine tool technology, education, etc. [39-45]. Electric drive has advanced over the years, also with the method to control their speed and torque. In the 1980s, DC motor drives were largely used in

variable speed drives because of the effortlessness to control the DC motors, due to the decoupling between armature current and the field current. With numerous disadvantages like regular maintenance of commutator, brushes & brushes holder, limited current carrying capacity during high-speed applications of DC motors in most applications, AC machines were preferred over DC machines owing to their simple and robust construction without any mechanical commutators [46-47].

It is appraised that more than half of the world electric energy generated is consumed by electric machines. Improving the efficiency of electric drives is vital, chiefly for economic saving and reduction of environmental pollution. A rough approximation shows that nearly 80% of AC motors in the world are polyphase induction motors, while the rest are single-phase induction motors [41-45]. The name “induction motor” results from the method used for the formation of the rotor magnetic field. AC motor is an induction motor type, where power is provided to the rotor through means of electromagnetic induction, rather than a commutator or slips rings as in other types of motor [48-49]. To realize variable speed operations in an AC induction motor, an adjustable voltage and frequency need to be supplied to the motor. Due to their variable speed applications in a wide power range that covers from slight kilowatts power to multi-megawatts, the induction motor has been the workhouse in the industrial world [50-54].

The squirrel cage type of the induction motors is used extensively for single speed applications rather than variable speed applications owing to the intricacy of regulating the algorithm and IM high production cost. The induction motor describes the two characteristics in which this type of motor differs from DC motors and synchronous motors. Induction motors (IM) are very simple and cheap to manufacture due to no sliding contacts and permanent magnets needed to make IM work. The three-phase Induction motors are built according to the established National Electrical Manufacturers Association (NEMA) standards in myriad fractional, integral horsepower ratings and associated frame sizes [55-56].

#### **2.4 Structures of a Three-Phase Induction Motor**

In various industrial applications, three-phase induction motors are widely used due to their self-starting property, no starting device needed, high power factor, good speed regulation and robotics construction [57]. The two main types of induction motors are the squirrel-cage and wound-rotor. The rotor winding is the key difference between the squirrel-cage and wound-rotor type of induction motor. For the wound-rotor type of induction motor, the rotor winding

is accessible for control through slip rings and brushes, while in the squirrel-cage type of induction motor, the rotor winding is fixed and not accessible for control. The rotor winding is composed of a series of longitudinal conductors (bars) bounded or surface mounted in steel rings. The rotor bars are connected at each rotor end creating the rotor electrical circuit. The number of poles or the stator windings determines the speed of the rotating magnetic field or synchronous speed of the motor. If there is no load on the motor shaft, the rotor will turn at a speed that slightly lags the synchronous speed, which defines the slip of the induction motor. Figure 2.1 shows a cutaway diagram of squirrel-cage three-phase AC motor [58].

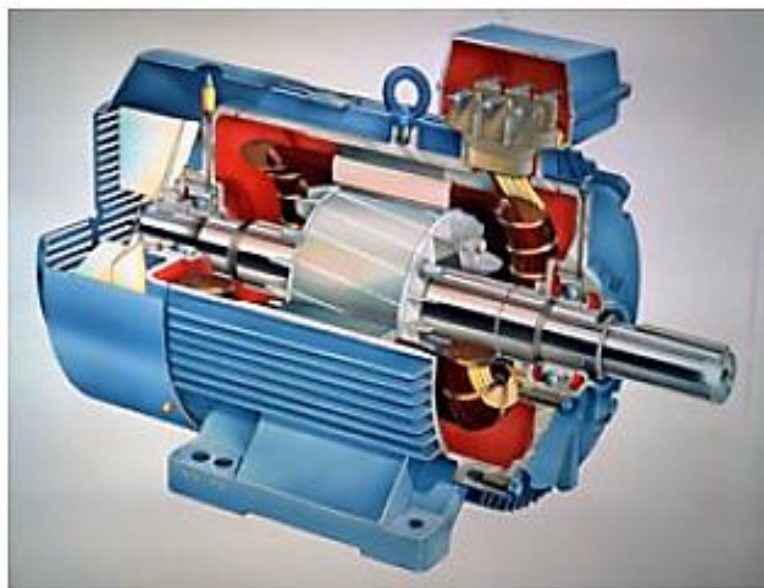


**Figure 2.1** Cutaway diagram of squirrel-cage three-phase AC motor [59].

#### **2.4.1 Stationary Stator**

Several thin laminations of aluminium or cast iron make up the stator of the three-phase induction motor. They are perforated and fastened together to form a resonating cylinder (stator core) with slots as shown in Figure 2.2. Coils of insulated wires are put in into these slots. Each grouping of coils, together with the core it surrounds, forms an electromagnet (a pair of poles) on the application of AC supply. The number of poles of an AC induction motor is hinged on the internal connection of the stator windings. Internally they are connected in such a way that on applying AC supply, a rotating magnetic field is created. To reduce eddy current losses, the

stator core is laminated. In most electrical machines, the axis of rotation is normal to the plane of steel sheets [60-61].



**Figure 2.2** Stator winding of a three-phase induction motor [62].

#### **2.4.2 Rotating Rotor**

For wound rotor induction motors, the rotor comprises a laminated core, rotor windings, shaft, and slip rings as shown in Figure 2.3. The rotor core is made of perforated laminations which are stacked to create a series of rotor slots and provide space for the rotor winding. The two types of rotor windings include:

- I. Conventional windings are made of insulated wire (wound-rotor) like the stator windings. Usually, the ends of the three rotor wires are connected to three slip rings on the rotor shaft using the Y-configuration.
- II. A squirrel-cage shaped rotor formed by aluminium rotor bars shorted together at the ends by two aluminium end rings (squirrel-cage) [62].

Like most motors, an AC induction motor has a fixed external portion called the stator and a rotor that spins inside with a carefully engineered air gap between the former and latter. Virtually all electrical motors use magnetic field rotation to spin their rotor and a three-phase AC induction motor is the only type of motor, where the rotating magnetic field is created naturally in the stator by one set of electromagnets is formed in the stator windings and the alternating nature of the supply voltage induces an electromagnetic force (emf) in the rotor, thus generating another set of electromagnets. Interaction of the magnetic field by the electromagnets generates a twisting force or torque. Thus, the motor rotates in the direction of the resultant torque [63 60].

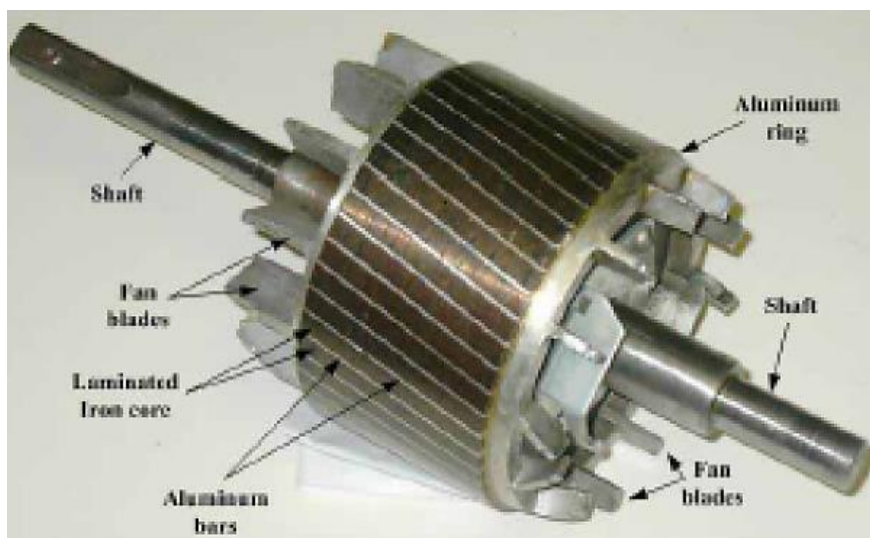


**Figure 2.3** Squirrel cage rotor of a three-phase induction motor [63].

## 2.5 Working Principle of Three-Phase Induction Motor

The fundamental principle of the three-phase induction motor is founded on Faraday's and Lenz's laws of electromagnetic induction. Faraday summed up the laws of electromagnetic induction into two laws known as Faraday's laws of electromagnetic induction. The first law states that when the magnetic flux linked with a circuit changes, an emf is always induced. While the second law states that the magnitude of the induced emf is equal to the rate of change of flux linkages. The induced emf ( $e$ ) is given by equation 2.1:

$$e = -N \frac{d\Phi}{dt} \text{ (webers/second or volts)} \quad 2.1$$

The negative sign is given in equation 2.1 indicates that the induced emf sets up current in such a direction that magnetic effect produced by it opposes that producing it. For an infinitesimal area element  $d\vec{A}$  in a magnetic field  $\vec{B}$ , the magnetic flux  $d\Phi$  through the area is given by equation 2.2;

$$d\Phi = \vec{B} \cdot d\vec{A} = B_{\perp} dA = B dA \cos \Phi \quad 2.2$$

where  $B_{\perp}$  is the component of  $\vec{B}$  perpendicular to the surface of the area element and  $\Phi$  is the angle between  $\vec{B}$  and  $d\vec{A}$ . The total magnetic flux  $\Phi_B$  through a finite area is the integral of the expression over the area in the equation 2.3:

$$\Phi_B = \int \vec{B} \cdot d\vec{A} = \int B dA \cos \Phi \quad 2.3$$

And If  $\vec{B}$  is uniform over a flat area  $\vec{A}$ , then

$$\Phi_B = \vec{B} \cdot \vec{A} = BA \cos \Phi \quad 2.4$$

Lenz's law states that electromagnetically induced current always flows in such direction that the action of the magnetic field set up by it tends to oppose the very cause which produces it. The concept of motional emf for a conductor with any shape, moving in any magnetic field, uniform or not (if the magnetic field at each point does not vary with time) can be generalised. For an element  $d\vec{l}$  of the conductor, the contribution  $d\epsilon$  to the emf is the magnitude  $d\vec{l}$  multiplied by the components of  $\vec{v} \times \vec{B}$  (the magnetic force per unit charge) parallel to  $d\vec{l}$ ; given by equations 2.5 and 2.6 [64-65].

$$d\epsilon = (\vec{v} \times \vec{B}) \cdot d\vec{l} \quad 2.5$$

For any closed conducting loop, the total emf is given by:

$$\epsilon = \oint (\vec{v} \times \vec{B}) \cdot d\vec{l} \quad 2.6$$

Change in the electromechanical energy consists of the interchange of energy between an electrical system and a mechanical system through a coupling magnetic field medium [59, 66].

The induction motor works by inducing a current on the rotor through the small air-gap between the stator and rotor. The stator current generates a rotating magnetic field in the air gap between the stator and rotor. The interaction of the induced rotor current with the rotating magnetic field

generates a torque on the rotor. The induction motor has the advantages of being self-regulating and capable of balancing the torque demand of the load with the output of the motor [58].

For the induction to materialize, the rotor must rotate slower than the stator field. Thus, an induction motor operates at less than synchronous speed using no other power source to excite the rotor's field. Once the synchronous motor's field poles are in step with the stator frequency, the frequency of the applied voltage and the number of poles in the motor determines the synchronous speed of the motor [67]. The speed of the magnetic field's rotation is given by equation 2.7:

$$n_{sync} = \frac{120f_e}{P} \quad 2.7$$

where  $f_e$  is the system frequency in hertz and the number of poles of the machine is represented by  $P$ . Voltage is induced in the rotor bars, when rotating magnetic field ( $B_s$ ) passes over the rotor bars. The voltage induced in each rotor bar is given by the equation 2.8:

$$e_{ind} = (v \times B) \cdot l \quad 2.8$$

where  $v$  is the velocity of the bar relative to the magnetic field,  $B$  is the magnetic flux density vector, and  $l$  is the length of the conductor in the magnetic field.

When the induction motor rotor turns at a synchronous speed, the rotor bars are fixed relative to the magnetic field and no voltage is induced. If  $e_{ind}$  were equal to 0, then there would be no rotor current and no rotor magnetic field generated. With no rotor magnetic field, the induced torque would be zero, and the rotor would slow down because of friction losses. An induction motor can thus speed up to near synchronous speed, but it can never exactly reach synchronous speed. It should be noted that in normal operation both the rotor and stator magnetic fields ( $B_R$  and  $B_S$ ) rotate together at synchronous speed  $n_{sync}$  while the rotor itself turns at a slower speed. The voltage induced in a rotor bar of an induction motor depends on the speed of the rotor relative to the magnetic fields. Since the behaviour of an induction motor depends on the rotor's voltage and current, it is often more logical to talk about this relative speed. Two terms are commonly used to define the relative motion of the rotor and the magnetic fields. The slip speed is defined as the difference between synchronous speed and rotor speed:

$$n_{slip} = n_{sync} - n_m \quad 2.9$$

where  $n_{slip}$  is the slip speed of the machine,  $n_{sync}$  is the speed of the magnetic fields and  $n_m$  is the mechanical shaft speed of the motor.

The relative motion is described by the slip, which is the relative speed expressed on a percentage basis. The slip ( $s$ ) is defined using either equations 2.10 or 2.11 [68].

$$s = \frac{n_{sync} - n_m}{n_{sync}} (\times 100) \quad 2.10$$

$$n_m = (1 - s)n_{sync} \quad 2.11$$

When the rotor is stationary, the frequency of the rotor current is the same as the supply frequency, but when the rotor starts revolving, the frequency depends upon the relative speed or on slip-speed. The frequency ( $f_r$ ) of the rotor induced emf is given by expressions below [57].

$$f_r = \frac{P}{120} (n_{sync} - n_m) \quad 2.12$$

## 2.6 Rotating Magnetic Field Creation Due to Three-Phase Currents

The three-phase induction motor has three identical currents separated from each other across  $120^\circ$ . Three-phase induction motor produces a resultant magnetic flux that rotates like poles actual magnet spinning mechanism [69]. The stator windings of the three-phase induction motor produce a rotating field of a constant magnitude, which rotates at the speed matching the frequency of the supply and the number of poles in the motor. The higher the number of poles the lower the speed of the rotation. The magnetic flux produced by the stator passes through the rotor and cuts the rotor conductors as it rotates. Since the flux has a sinusoidal distribution in space its rotation causes a sinusoidal emf to be induced into the rotor conductors. Hence currents are caused to flow in the rotor conductors due to the emfs that are induced. The EMFs are induced in the rotor by transformer action, which is why the machine is termed an ‘induction motor’ (IM). Since currents now flow in both the stator and the rotor, the rotor conductors will set up local fluxes which interact with the excitation flux from the stator. This interaction causes a torque to be developed on the rotor. If this torque exceeds the torque required by the mechanical load the shaft will begin to rotate and accelerate until these two torques are equal. The rotation will be in the direction of the stator flux since the rotor conductors are being driven by the stator flux [70].

Three-phase of the stator winding (balanced) carry balanced alternating (sinusoidal) currents. A resultant magnetic flux is produced which rotates in space as if actual magnetic poles were

being rotated mechanically when three-phase windings are displaced in space by  $120^\circ$  are fed by three-phase currents displaced in time by  $120^\circ$ . The flux (assumed sinusoidal) due to three-phase windings is shown in Figure 2.4.

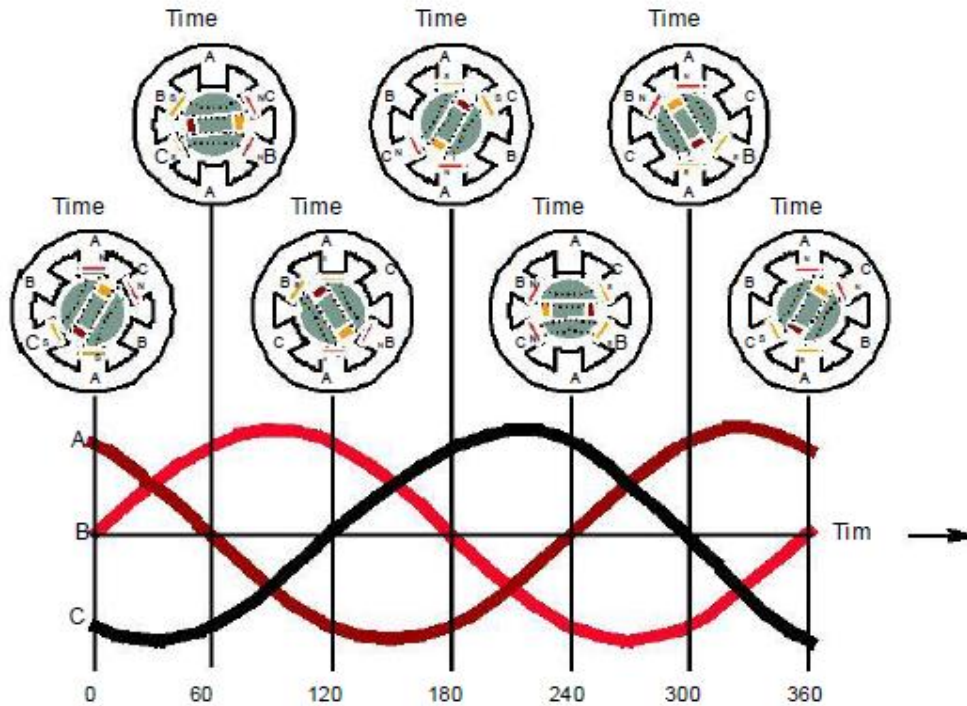


**Figure 2.4** The relationship between three-phase currents and rotating magnetic field over 360 electrical degrees in time [59].

The three-phases  $A$ ,  $B$ , and  $C$  energised from a three-phase current source indicated by  $I_A$ ,  $I_B$ , and  $I_C$ . From Figure 4; the fluxes produced by these currents are given by

$$\Phi_A = \Phi_m \sin \omega t \quad 2.13$$

$$\Phi_B = \Phi_m \sin (\omega t - 120^\circ) \quad 2.14$$

$$\Phi_C = \Phi_m \sin (\omega t - 240^\circ) \quad 2.15$$

If the maximum flux value due to any one of the three phases is  $\Phi_m$ . The resultant flux  $\Phi_r$  at any instant, is given by the vector sum of the individual fluxes,  $\Phi_A$ ,  $\Phi_B$  and  $\Phi_C$  due to the three phases. When  $\theta = 0$ , the current in phase  $B$  is observed to be zero, whereas corresponding currents in phases  $A$  and  $C$  are equal and opposite, with  $\omega t = 0^\circ$  (Figure 2.4). The flux and resultant flux in each phase are given by;

$$\Phi_B = \Phi_m \sin 0^\circ = 0 \quad 2.16$$

$$\Phi_C = \Phi_m \sin (0 - 120^\circ) = \Phi_m \sin (-120) = -\frac{\sqrt{3}}{2} \Phi_m \quad 2.17$$

$$\Phi_A = \Phi_m \sin (0 - 240^\circ) = \Phi_m \sin (-240) = \frac{\sqrt{3}}{2} \Phi_m \quad 2.18$$

$$\Phi_r = 2 \times \left(\frac{\sqrt{3}}{2} \Phi_m\right) \cos \frac{60^\circ}{2} = \frac{3}{2} \Phi_m \quad 2.19$$

When  $\theta = 60^\circ$ , the current in phase A is observed to be zero, whereas corresponding currents in phases B and C are equal and opposite, with  $\omega t = 60^\circ$ . The flux and resultant flux in each phase are given by;

$$\Phi_B = \Phi_m \sin 60^\circ = \frac{\sqrt{3}}{2} \Phi_m \quad 2.20$$

$$\Phi_C = \Phi_m \sin (60^\circ - 120^\circ) = \Phi_m \sin (-60) = -\frac{\sqrt{3}}{2} \Phi_m \quad 2.21$$

$$\Phi_A = \Phi_m \sin (60^\circ - 240^\circ) = \Phi_m \sin (-180) = 0 \quad 2.22$$

$$\Phi_r = 2 \times \left(\frac{\sqrt{3}}{2} \Phi_m\right) \cos \frac{60^\circ}{2} = \frac{3}{2} \Phi_m \quad 2.23$$

It is observed from equation 2.23 that the resultant flux is  $\frac{3}{2} \Phi_m$ , but rotates clockwise through an angle of  $60^\circ$ . When  $\theta = 120^\circ$ , the current in phase C is observed to be zero, whereas corresponding currents in phases A and B are equal and opposite, with  $\omega t = 120^\circ$ . The flux and the resultant flux in each phase are given by;

$$\Phi_B = \Phi_m \sin 120^\circ = \frac{\sqrt{3}}{2} \Phi_m \quad 2.24$$

$$\Phi_C = \Phi_m \sin (120^\circ - 120^\circ) = \Phi_m \sin 0 = 0 \quad 2.25$$

$$\Phi_A = \Phi_m \sin (120^\circ - 240^\circ) = \Phi_m \sin (-120) = -\frac{\sqrt{3}}{2} \Phi_m \quad 2.26$$

$$\Phi_r = 2 \times \left(\frac{\sqrt{3}}{2} \Phi_m\right) \cos \frac{60^\circ}{2} = \frac{3}{2} \Phi_m \quad 2.27$$

The resultant flux is again of the same value ( $\frac{3}{2} \Phi_m$ ), with an additional clockwise rotation through an angle of  $60^\circ$ . When  $\theta = 180^\circ$ , the current in phase B is observed to be zero, whereas

corresponding currents in phases A and C are equal and opposite, with  $\omega t = 180^\circ$ . Hence, the flux and resultant flux in each phase is given by

$$\Phi_B = \Phi_m \sin 180^\circ = 0 \quad 2.28$$

$$\Phi_C = \Phi_m \sin (180^\circ - 120^\circ) = \Phi_m \sin 60^\circ = \frac{\sqrt{3}}{2} \Phi_m \quad 2.29$$

$$\Phi_A = \Phi_m \sin (180^\circ - 240^\circ) = \Phi_m \sin (-60^\circ) = -\frac{\sqrt{3}}{2} \Phi_m \quad 2.30$$

$$\Phi_r = \frac{3}{2} \Phi_m \quad 2.31$$

The resultant flux is observed to be  $\frac{3}{2} \Phi_m$  and has rotated clockwise through an additional angle of  $60^\circ$  or through an angle of  $180^\circ$  from the start. The resultant flux is observed to be of the constant value of  $\frac{3}{2} \Phi_m$ , i.e. 1.5 times the maximum value of the flux due to any phase and the resultant flux rotates around the stator at synchronous speed as given by equation 2.7 [47, 57].

## 2.7 Particle Shadow Velocimetry (PSV)

Humans are very interested in nature observation, as this is and still is of great importance for the survival of humans. Human senses are particularly well adapted to identify moving objects as in many cases they mean ultimate danger. Leonardo da Vinci an artist with outstanding skills and an educated observer of nature was able to make very comprehensive sketches of the structures within a water flow by simple observation. A great stage in the investigation of flows was made, that passive observation of nature could possibly be replaced by experiments cautiously planned to extract information about the flow using visualization methods. Ludwig Prandtl was a well-known promoter of such method, who designed and used flow visualization methods in a water tunnel to study characteristics of unsteady separated flows behind wings and other objects [71-72].

Initial quantitative velocity measurements in fluid flows were obtained using Pitot-static tubes. In the 1920s, a significant development was the subsequent introduction of hot-wire anemometers specifically in terms of probe miniaturization, frequency response, and the ability to measure multiple velocity components. But, these methods (Pitot-static tubes and hot-wire anemometers) required the insertion of a physical probe which can encroach on the flow itself. To enable non-intrusive velocity measurements, laser invention in the 1960s led to the development

of the laser-doppler anemometer which uses a laser probe. Despite the rapid strides in the design of such systems, and the sophistication of the related electronics, the fact remains that all these methods are at best point-wise, i.e. the velocity information obtained is only at the point occupied by the probe. While these methods continue to hold a vital position in experimentalist's arsenal, the ability to make comprehensive velocity measurements has raised particle image velocimetry (PIV) to a special position in fluid mechanics [73].

Multi-dimensional measurements of velocities and the capability to trail the flowing fluid in time provide critical information in many areas of science, engineering and health science [74]. The basics of experimental fluid mechanics are flow visualization and quantitative velocity measurements. They have, with the other pillars of theory and numerical simulations, built up our understanding of the dynamics of complex or turbulent flows [75-78]. Particle image velocimetry (PIV) is an experimental method, based on image cross-correlation methods used for flow velocity fields. The use of PIV for fluid velocities calculation originally emerged in the 1980s. Since then, PIV has played a vital role in various fluid mechanics research. The main advantages of PIV over other methods for the measurement of velocity (e.g. hot-wire velocimetry, Pitot tubes, etc.) are that it is non-intrusive, and it allows for relatively high-resolution measurements over an extended spatial domain [79].

Particle Image Velocimetry (PIV) has been a focus of comprehensive research and development since last three decades due to its capability to provide simultaneous data of the velocity distribution instead of a single point data when compared with other measuring methods. It is a whole field, non-intrusive instantaneous flow field measurement method based on the direct determination of the two fundamental dimensions of the velocity: displacement and time. The particle displacement ( $\Delta x$ ) between two successive recordings is determined through local cross-correlation from which the measured local in-plane velocity ( $V$ ) is obtained as;

$$V(t) = \frac{\Delta x(x,t)}{\Delta t} = \frac{1}{\Delta t} \int_{\Delta t} V(t) dt \quad 2.32$$

where  $V(t)$  is the velocity of the particle's ensemble,  $\Delta x$  is the displacement of the marker particles at time  $t$  over a short period  $\Delta t$  [80-82].

High power light emitting diode (LED) illumination provided an attractive alternative to traditional laser illumination for flow diagnostic and velocimetry. Apart from the theatrically reduced cost of obtaining and considerably longer life of LED, LED provides incoherent light over a wide wavelength range ( $\pm 10-30$  nm) which reduces problems associated with speckle

artifacts found in laser-based illumination. LEDs provide numerous attractive advantages in comparison to laser illumination such as extremely stable pulse to pulse intensity as well as prevention of speckle related artifacts due to their incoherent light emission [83-84].

Volume illumination is an alternative approach, whereby the test section is illuminated by a volume of light. This mode of illumination has been used to measure three-dimensional velocity vectors using a single camera, multiple cameras and a holographic camera. Volume illumination is advantageous when measuring flows through microelectromechanical systems (MEMS) for which optical access is limited to one direction and the length scale is of the order of micrometres [85-86]. Particle shadow velocimetry shares many features of microPIV and forward scatter PIV (fsPIV). It is mostly used for the study of particles, liquid or gases motions. This provides information on the size distribution, shape and particles velocity [87-88].

Particle shadow velocimetry (PSV) is an alternative method to PIV, which permits low-power light sources such as LEDs to be used for PIV in several applications. The PSV method has advantages with respect to laser-based PIV method, as it produces no glare or reflections from surfaces; since LEDs of many monochromatic wavelengths are used. Particle Shadow Velocimetry (PSV) has proven to be an effective substitute to PIV that uses light scattered from seeding particles. The shadows of these particles are recorded using this method. Thus, the light intensity required to detect the location of the particles is reduced. The PSV method employs direct in-line volume illumination and an imaging-optics setup that produces a narrow depth-of-field (DOF) for 2D plane imaging [89].

PSV is an optical method used to measure seeded particle displacement in a plane, comparable to PIV, using images of particle shadows cast by a flashing LED, as an alternative of high-intensity laser light scattered by the particles [86]. In particle shadow velocimetry (PSV), a two-dimensional region of a seeded flow is imaged with a camera and velocity fields are estimated. The flow field is irradiated with pulsed LEDs rather than a laser used in PIV method. This technique can be used with single colour LEDs and a grey-scale camera. [90-91].

The general arrangement of the PSV setup shown in Figure 2.5, the angular offset between the light source and the detection component is zero. A pulsed LED light source is directed through the area of measurement onto an interline transfer or colour camera. This inline arrangement allows for the creation of shadows of the particles suspended in the flowing fluid to be recorded along with their forward scatter. For the most part, the forward scatter is much less than the

extinction caused by the particle. After the recording of the particle images at two separate times, the images are processed using the standard correlation approach to obtain the velocities. To minimize the measurement volume, some pre-processing of the image is necessary. For the precise location of the particle image, multiple pixels are required. It follows that;

$$\frac{d_e}{e} > 1 \quad 2.32$$

where  $d_e$  is the diameter of the image formed by the lens system of the particle and  $e$  is the spacing between adjacent pixels. The diameter of the image formed by the particle located in the object plane can be estimated using equation [87, 92].

$$d_e = \left( (M^2 d_p^2 + (2.44 \lambda f^\# (M + 1))^2 )^{1/2} \right) \quad 2.33$$

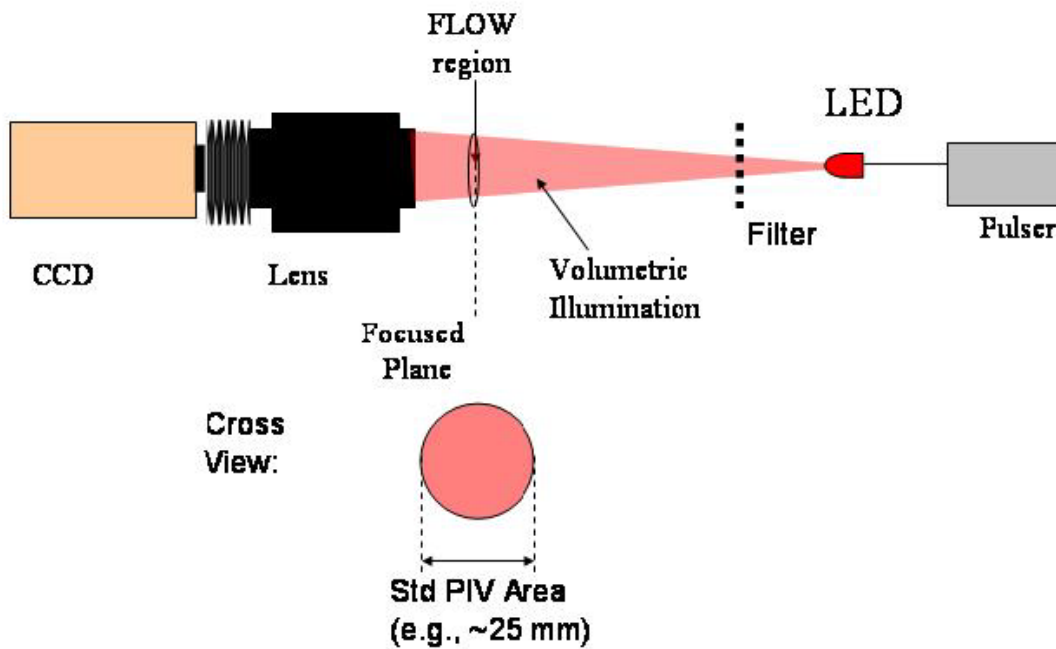


**Figure 2.5** Particle shadow velocimetry setup direct inline LED volume illumination [89]

The particle image recorded by the PSV method can be tacit by examining the diagram in Figure 2.6; which describes the areas associated with the contact of a plane light wave with a hard sphere. Of special interest for PSV is the deep shadow region ( $S$ ), which is the area downstream of the particle. The deep shadow area is slightly smaller than the particle diameter but extends several diameters downstream. The area produces an extinction cross-

section that is twice its geometric cross section. This area (deep shadow) is surrounded by numerous vital areas observed in the PSV images. These include the Fresnel area, the diffraction ring area and the Poisson cone. For a hard sphere, the Poisson cone has the same amplitude as the original waves. But, for a transparent sphere, the amplitude is considerably larger due to the focusing of the wave by the particle [87, 93].

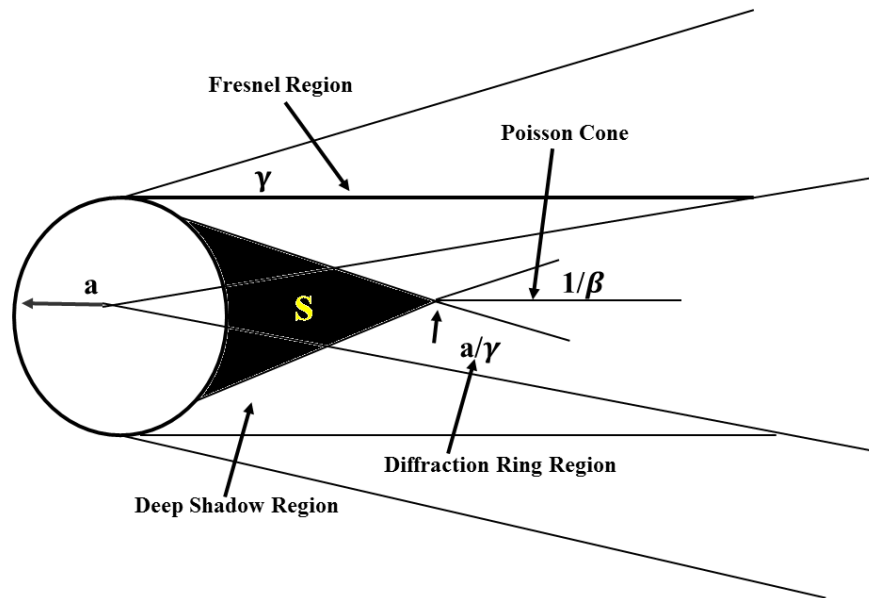


**Figure 2.6** Description of areas associated with the interaction of plane wave associated with a hard sphere, S-deep shadow, a-particle radius,  $\beta$ -size parameter,  $\gamma$ -penumbra width [87].

The tracer particles ability to follow the motions fluid is characterized by the particle response time or the relaxation time. The hypothesis that the particle velocity approaches the flow velocity exponentially is described by equation 2.34:

$$\tau_p = \frac{\rho_p}{\rho} \frac{d_p^2}{18 \nu} \tag{2.34}$$

where  $\rho_p/\rho$  the ratio of the density tracer particles with respect to the density of the fluid the diameter of the tracer particle [94-95].

To determine the displacement of the particle in the PSV method, a PIV-algorithm is used. This essentially works by calculating the cross-correlation function of the image intensity field between two successive images, taken at a short time interval ( $\Delta t$ ). Each image is divided into

rectangular shape regions called interrogation windows. The displacement of each region is determined using the cross-correlation function [96]. The position vector ( $X_i$ ) and image position vector of particle  $i$  in the first exposure ( $x_i$ ) is related by  $X_i = x_i/M$ , where  $M$  is the magnification factor. The image intensity field of the first exposure is expressed as in Figure 2.7;

$$I(\mathbf{x}) = \sum_{i=1}^N V_o(X_i)\tau(\mathbf{x} - \mathbf{x}_i) \quad 2.35$$

where  $V_o(X_i)$  is the transfer function giving the light energy of the image of an individual particle  $i$  inside the interrogation window and its conversion into an electronic signal, and  $\tau(\mathbf{x})$  is the point spread function of the imaging lens, which is Gaussian in both directions of the plane. Between the two exposures all particles inside the interrogation window move with the same displacement vector  $\Delta X$ , the image intensity field of the second exposure is expressed as;

$$J(\mathbf{x}) = \sum_{j=1}^N V_o^t(X_j + \Delta X)\tau(\mathbf{x} - \mathbf{x}_j - \delta\mathbf{x}) \quad 2.36$$

where  $\delta\mathbf{x}$  is the particle image displacement, which can be approximated by  $\Delta X = \delta\mathbf{x}/M$ . The cross-correlation of the two interrogation windows are defined as:

$$P(\mathbf{s}) = \langle I(\mathbf{x})J(\mathbf{x} + \mathbf{s}) \rangle \quad 2.37$$

where  $s$  is the separation factor in the correlation plane, and  $\langle \ \rangle$  is the spatial averaging operator over the interrogation window  $R$  can be broken into three part;

$$P(\mathbf{s}) = P_C(\mathbf{s}) + P_F(\mathbf{s}) + P_D(\mathbf{s}) \quad 2.38$$

where  $P_C$  represents the correlation of the mean image intensities and  $P_F$  is the fluctuating noise component, both of these components relate to  $i \neq j$ .  $P_D$  is the displacement-correlation peak, which represents the component of the cross-correlation function that matches the correlation of images of particles from first exposure with images of identical particles present in the second exposure ( $i = j$ ). This peak reaches a maximum for  $s = \delta\mathbf{x}$ . The determination of the location of the maximum yields  $\delta\mathbf{x}$ , thus  $\Delta X$  [97].

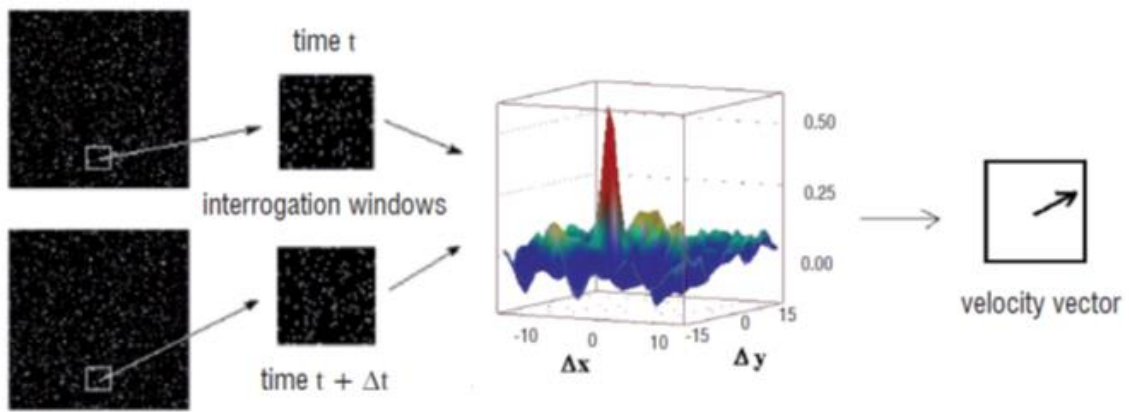


**Figure 2.7** Schematics of cross-correlation procedure [97].

## 2.8 References

- [1] K. R. Reddy, **2008**, Springer Netherlands, 257-274.
- [2] I. S. Yunus, H. A. Kurniawan D. Adityawarman, and A. Indarto, **2012**, Environmental Technology Reviews, 1, 136-148.
- [3] Q. U. Jiuhui, **2008**, Journal of Environmental Sciences 20, 1-13.
- [4] O. B. Akpor, G. O. Ohiobor and T. D. Olaolu, **2014**, Advances in Bioscience and Bio-engineering, 2, 37-43.
- [5] X. Qu, P. J. J. Alvarez and Q. Li, **2013**, Water Research, 47, 3031-3946
- [6] R. D. Ambashta and M. Sillanpaa, **2010**, J. of Hazardous Materials 180, 38-49
- [7] R. Khandanlou, M. B. Ahmad, H. R. F. Masoumi, K. Shameli, M. Basri and K. Kalantari, **2015**, PLOS ONE, 10
- [8] K. Setshedi, M. S. Onyango, F. Otieno, G. Carja and S. Nichetus, **2012**, J. of Hazardous Materials, 61, 278-290.
- [9] M. Yamaura, R. L. Camilo, and M.C.F.C. Felinto, **2002**, J. of Alloys and Compounds 344, 152–156.
- [10] J. F. De Brito, L. De Oliveira Ferreira, M. C. R. Pereira, J. P. Da Silva and T. C. Ramalho, **2012**, Water Air Soil Pollution, 223, 3545–3551
- [11] M. S. Rao and O. Sahu, **2013**, Physics and Materials Chemistry, 1, 34-40.
- [12] N. S. Zaidi, J. Sohaili, K. Muda, and M. Sillanpaa, **2014**, Separation and Purification Reviews, 45, 206-240.
- [13] O. F. G. Vázquez, M. D. R. M. Virgen, V. H. Montoya, R. T. Gómez, J. L. A. Flores, M. A. P. Cruz, and M. A. M. Morán, **2016**, Ind. Eng. Chem. Res., 55, 9323–9331.
- [14] L. Duan, S. Guo, and J. Yang, **2012**, Advances in Chemical Engineering and Science, 2, 101-107.
- [15] X. Hao, H. Liu, G. Zhang, H. Zou, Y. Zhang, M. Zhou, and Y. Gu, **2012**, Applied Clay Science, 55, 177-180.

- [16] L. C. Lipus, A. Hamler, I. Ban and B. Acko, **2015**, *Advances in Production Engineering and Management*, 10, 209-216.
- [17] K. F. Hassan, S. A. Kadhim, N. N. Baqer and E. S. A. Hassan, **2016**, *J. of Life Sciences*, 10, 21-32.
- [18] G. Li, W. Zhu, C. Zhang, S. Zhang, L. Liu, L. Zhu and W. Zhao, **2016**, *Bioresource Technology*, 206, 16-22.
- [19] O. Mosin and I. Ignatov, **2014**, *European J. of Molecular Biotechnology*, 4, 72-85.
- [20] M. F. Ni'am, F. Othman, J. Sohaili and Z. Fauzia, **2006**, *Proceeding of the 1<sup>st</sup> International Conference on Natural Resources Engineering and Technology*, 384-393.
- [21] Y. Ali, R. Samaneh, R. Zohre and J. Mostafa, **2014**, *Current World Environment*, 9, 1008-1016.
- [22] C. J. Quinn, T. C. Molden, and C. H. Sanderson, **1997**, *Iron and Steel Engineer*, 74, 47-52.
- [23] L. Holysz, A. Szezes, and E. Chibowski, **2007**, *J. of Colloid and Interface Science*, 316, 996-1002.
- [24] K. Higashitani, A. Kage, S. Katamura, K. Imai and S. Hatade, **1993**, *J. of Colloid and Interface Science*, 156, 90-95.
- [25] Z. Z. Khater, and M. H. Ibraheim, **2015**, *Int. J. Curr. Res. Aca. Rev.*, 3, 262-279.
- [26] R. R. Mohammed, M. R. Ketabchi and G. Mckay, **2014**, *Chemical Engineering J*; 243, 31-42.
- [27] G. Zhang, X. Yang, Y. Liu, Y. Jia, G. Yu and S. Ouyang, **2004**, *J. of Colloid and Interface Science*, 278, 265-269.
- [28] G. Zhang, Y. Liu, Y. Xie, X. Yang, B. Hu, S. Ouyang, H. Liu, and H. Wang, **2005**, *Applied Clay Science*, 29, 15-21.
- [29] J. Yuan-Yuan, Z. Gao-Ke, H. Bo, and D. Wei, **2004**, *J. of Wuhan University of Technology Material Sci. Ed.*, 19, 52-54.

- [30] F. F. Fondeur, D. T. Hobbs, and S. D. Fink, **2010**, Separation Science and Technology, 45, 1876-1879.
- [31] X. Jiang, J. Qian, I. M. C. Lo, L. Wang, X. Guan, Z. Lu, G. Zhou and C. Xu, **2015**, J. of Hazardous Materials, 283, 880-887.
- [32] J. Li, H. Qin, W. Zhang, Z. Shi, D. Zhao and X. Guan, **2017**, Separation and Purification Technology 176, 40-47.
- [33] L. Liang, X. Guan, Y. Huang, J. Ma, X. Sun, J. Qiao and G. Zhou, **2015**, Separation and Purification Technology, 156, 1064-1072.
- [34] M. Khiadani (Hajian), M. Zarrabi, and M. Foroughi, **2013**, J. of Environmental Health Science and Engineering, 11.
- [35] P. He, X. Zhang, X. Peng, J. Wu, N. Chen and J. Ren, **2015**, Fuel, 162, 211-214.
- [36] A. Eskandarpour, K. Sassa, Y. Bando, M. Okido and S. Asai, **2006**, Materials Transactions, 47, 1822-1837.
- [37] W. Shen, Q. Guo, X. Yang, Y. Liu, Y. Song, and J. Cheng, **2006**, Adsorption Science and Technology, 24, 433-438,
- [38] N. Ahmadinia, **2014**, American J. of Electrical Power and Energy Systems, 3, 71-75.
- [39] M. D. Marko and G. Shevach, **2017**, PLOS ONE, 12, 1-12.
- [40] B. Plangklang, S. Kantawong, and A. Noppakant, **2013**, Energy Procedia, 34, 382 – 389.
- [41] Y. Sumith and J. S. V. Siva Kumar, **2012**, International J. of Engineering Research and Applications, 2, 1668-1674.
- [42] O. Gurdal and O. Cesur, **1999**, J. of Polytechnic, 2.
- [43] J. W. Rengifo-Santana, J. Benzaquen-Suñe, J. M. Aller-Castro, A. A. Bueno-Montilla and J. A. Restrepo-Zambrano, **2015**, Rev. Fac. Ing. Univ. Antioquia, 75, 57-66.
- [44] H. Sarhan, **2011**, Energy and Power Engineering, 3, 107-112.
- [45] T. K. Nagsarkar and M. S. Sukhija, **2011**, Oxford University Press, First Edition.

- [46] R. S. Lodhi and P. Thakur, **2013**, International J. of Emerging Technology and Advanced Engineering, 3, 716-724.
- [47] M. S. Aspalli, R. Asha. and P. V. Hunagund, **2012**, International J. of Advanced Research in Electrical, Electronics and Instrumentation Engineering, 1, 463-469.
- [48] B. Akin and M. Bhardwaj, **2013**, Texas Instrument Incorporated, 1-34.
- [49] G. C. Diyoke, C. Okeke, and U. Aniagwu, **2016**, American J. of Electrical and Electronic Engineering, 4, 62-68.
- [50] Z. Anthony, **2014**, International J. of Engineering Trends and Technology (IJETT), 15, 444-447.
- [51] P. Stekl, **2007**, Freescale Semiconductor Designer Reference Manual DRM092 Rev, 7, 11-15.
- [52] C. Saravanan, J. Sathiswar, and S. Raja, **2012**, International J. of Computer Applications, 46.
- [53] A. Choudhary, A. Chourasia, and V. Srivastava, **2014**, International J. of Electronic and Electrical Engineering, 7, 1-6.92
- [54] D. D. Reljić and D. G. Jerkan, **2014**, International Symposium on Industrial Electronics (INDEL 2014), 106-114.
- [55] Y. Sumith and J. S. V. Siva Kumar, **2012**, International J. of Engineering Research and Applications, 2, 1668-1674.
- [56] J. Murphy, **2012**, Retrieved from <http://www.cmafh.com/WebsiteCatalogs/VendorVideos/TechnicalDropDown/Electrical/Understanding%20Electric%20Motors.pdf>
- [57] K. Ravichandrudu, P. S. P. Kumar, Y. N. V. Kumar and C. Praveen, **2013**, International J. of Computational Engineering Research, 3, 36-48.
- [58] M. G. Nored, J. R. Hollingsworth and K. Brun, **2009**, Gas Machinery Research Council Southwest Research Institute, 4-79.
- [59] F. Giri, **2013**, John Wiley & Sons, Ltd, 17.
- [60] R. Parekh, **2003**, Microchip Technology Inc. 1-24.

- [61] G. Verez, G. Barakat, and Y. Amara, **2014**, Progress in Electromagnetics Research B, 61, 149–168.
- [62] M. P. Singh, **2013**, Dayalbagh Educational Institute, 1-4.
- [63] M. A. Kiseleva, N. V. Kondratyeva, N. V. Kuznetsov and G. A. Leonov, **2015**, IFAC-Papers Online, 48, 700–705.
- [64] B. L. Theraja and A. K. Theraja, **2002**, S. Chand and Company LTD,
- [65] H. D. Young, R. A. Freedman, and A. L. Ford, **2012**, Addison-Wesley (Pearson Education Inc.), Thirteenth Edition, 942-967.
- [66] E. J. Thornton, and J. K. Armintor, **2003**, Proceedings of the 20th International Pump Users Symposium, 20, 95-105.
- [67] J. Parrish, S. Moll, and R. C. Schaefer, **2006**, IEEE Industrial Application Magazine, 61-70.
- [68] S. J. Chapman, **2005**, McGraw-Hill, Fourth Edition, 380-472.
- [69] Z. Anthony, **2013**, International J. of Engineering Trends and Technology (IJETT), 5, 13-16.
- [70] A. L. Sheldrake, **2003**, John Wiley and Sons Ltd, 99-128.
- [71] M. Raffel, C. E. Willert, S. T. Wereley, and J. Kompenhans, **2013**, Springer,
- [72] M. Muste, I. Fujita and A. Hauet, **2008**, Water Resources Research, 44.
- [73] A. K. Prasad, **2000**, Current Science, 79.
- [74] L. Lu and V. Sick, **2013**, Journal of Visualized Experiments, 76, e50559.
- [75] R. J. Adrian, **1991**, Annual Review of Fluid Mechanics 23, 261–304.
- [76] J. Westerweel, G. E. Elsinga, and R. J. Adrian, **2013**, Annual Review of Fluid Mechanics, 45, 409–436.
- [77] C. E. Willert, and M. Gharib, **1991**, Experiments in Fluids, 10, 181–193.
- [78] A. K. Prasad, **2000**, Experiments in Fluids, 29, 103–116.

- [79] Senatore, M. Wulfmeier, I. Vlahinić, J. Andrade, and K. Iagnemma, **2013**, *J. of Teramechanics*, 50, 311-326.
- [80] S. Tomar, S. Chawla, V. Sangwan, R. K. Singh, and A. Dhyani, **2014**,
- [81] J. Soria, **2006**, *Plasmas and Nonlinear Media*, 309-347.
- [82] A. Bichal and A. Altman, **2009**, 47<sup>th</sup> American Institute of Aeronautics and Astronautics.
- [83] N. A. Buchmann, C. Willert and J. Soria, **2010**, Australasian Fluid Mechanics Conference.
- [84] Willert, B. Stasicki, J. Klinner and S. Moessner, **2010**, *Measurement Science and Technology*, 21, 07540.
- [85] D. Meinhart, S. T. Wereley and M. H. B. Gray, **2000**, *Measurement Science and Technology*, 11, 809,
- [86] M. J. McPhail, M. H. Krane, A. A. Fontaine, L. Goss and J. Crafton, **2005**, *Measurement Science and Technology*, 26.
- [87] L. F. Goss, J. Estevadeordal and J. W. Crafton, **2007**, IEEE.
- [88] J. Foldyna, M. Zelenak, J. Klich, P. Hlavacek, L. Sitek and Z. Riha, **2015**, *Tehnicki Vjesnik*, 22, 1441-1446.
- [89] J. Estevadeordal, and L. Goss, **2005**, In 43rd AIAA Aerospace Sciences Meeting and Exhibit, 12355–12364.
- [90] L. Goss, and J. Estevadeordal, **2006**, 5th AIAA Aerodynamics Measurement Technology and Ground Testing Conference,
- [91] L. Goss, J. Estevadeordal, and J. Crafton, **2007**, 37th AIAA Fluid Dynamics Conference and Exhibit.
- [92] R. J. Adrian and C. S. Yao, **1985**, *Appl. Optics*, 33, 7159-7170.
- [93] H. C. Van Da Hulst, **1957**, Wiley New York.

- [94] J. Westerweel, A. A. Draad, J. T. Van der Hoeven, and J. Van Oord, J, **1996**, Experiments in Fluids, 20, 165-177,
- [95] X. Mao and A. J. Jaworski, **2010**, Measurement Science and Technology, 21, 035403-035403.
- [96] L. Sarno, M. N. Papa, Y. C. Tai, A. Carravetta and R. Martino, **2014**, Environmental and Structural Engineering Series.
- [97] Brossard, J. C. Monnier, P. Barricau, F. X. Vandernoot, Y. Le Saint, F. Champagnat and G. Le Besnerais, **2009**, J. of Aerospace Lab, 3

## CHAPTER THREE

### 3.0 Experimental Methods

#### 3.1 Materials

Pyrrrole ( $C_4H_5N$ ), magnetite ( $Fe_3O_4$ ), potassium dichromate ( $K_2Cr_2O_7$ ), congo red (CR) (Chemical formula =  $C_{23}H_{22}N_6O_6S_2Na_2$ , Formula weight =  $696.65g.mol^{-1}$ ), sodium fluoride (NaF), anhydrous ferric chloride ( $FeCl_3$ ), sodium hydroxide (NaOH), hydrochloric acid (HCl) and 1, 5 diphenyl carbazide were purchased from Sigma-Aldrich (South-Africa). All Chemicals used were of analytic grade and freshly distilled prior to use for all experiments. The chemicals were used as they were received without further purification. 1000 mg/L stock solution of chromium (VI), fluoride and congo red were prepared by dissolving 2.83 g of  $K_2Cr_2O_7$ , 2.21 g of NaF and 1 g of congo red powder in deionized water. Desired concentrations of Cr(VI), fluoride and congo red solution were further made by diluting the appropriate stock solution using deionized water.

#### 3.2 Polypyrrole Magnetic Nanocomposite Synthesis and Characterization

In-situ chemical oxidative polymerization technique was used for the preparation of polymer-based magnetic nanocomposite (PPy/ $Fe_3O_4$ ) [1]. 0.4 g of magnetite ( $Fe_3O_4$ ) was added to the 80-mL deionized water in a 250ml Erlenmeyer flask. This was ultrasonicated for 30 minutes to have a proper distribution of the magnetite in the deionized water solution. 0.8 mL of pyrrole was then injected into the ultrasonicated colloid solution. To facilitate polymerization, 6 g of  $FeCl_3$  was subsequently added to the mixture and shaken manually for 5 minutes. For complete polymerization reaction to take place, the mixture is left to stand for three hours. The black powder obtained was vacuum filtered from the reaction medium and washed with deionised water until the filtrate becomes colourless. To stop the reaction within the filtrate and to remove unreacted monomers, acetone was injected. The magnetic nanocomposite was dried under vacuum at  $60^\circ C$  for 24 hours to obtain a constant mass of the product. X-ray diffractometer was used to determine the XRD crystalline structure of the PPy/ $Fe_3O_4$  nanocomposite using SmartLab X-ray diffractometer operating at 45 kV/200 mA with Cu-K $\alpha$  radiation (wavelength ( $\lambda$ ) =  $1.540593 \text{ \AA}$ ). FTIR characterization was performed using FTIR spectrophotometer (Perkin-Elmer Spectrum 100 spectrometer, USA) to determine the functional groups on the PPy/ $Fe_3O_4$  nanocomposite before and after adsorption. High-resolution transmission electron microscopy (JEOL JEM-2100) and Scanning electron microscopy (Leo-Zeiss) coupled with

energy dispersive X-ray (EDX) were used to determine the morphology, size and elementary composition of the PPy/Fe<sub>3</sub>O<sub>4</sub> nanocomposite. The surface area analysis of PPy/Fe<sub>3</sub>O<sub>4</sub> nanocomposite was determined using Brunauer Emmett-Teller (BET) at low-temperature nitrogen adsorption-desorption technique on a Micromeritics ASAP 2020 gas adsorption apparatus (Micromeritics USA). Bruker-Electron Spin Resonance (ESR) spectrometer operating at room temperature was also used to determine the magnetic property of the PPy/Fe<sub>3</sub>O<sub>4</sub> nanocomposite. The magnetic property of the PPy/Fe<sub>3</sub>O<sub>4</sub> nanocomposite was measured at room temperature (300 K) at an interval of -10,000-10,000 Oe using a vibrating sample magnetometer (VSM) of a physical property measurement system (PPMS) (Quantum Design temperature).

### **3.3 Experimental Method**

#### **3.3.1 Experimental Setup: Magnetic Adsorption Device**

The experimental setup comprises of a three-phase induction motor (2-pole and 8-pole induction motor), a power source, a toroidal cleaning chamber, a thermocouple and a fan. The nameplate parameters of the three-phase induction are shown in Table 3.1. The stator windings of the three-phase induction motor have thickness and height of 14.39×160 mm. The rotor was modified to hold an open-top toroidal cleaning chamber used for the magnetic adsorption experiments. The open-top toroidal cleaning chamber was made from perspex plastic with internal, external and height diameters of 66 x 100 x 25 mm. The 10 A variable power supply was used to supply AC power to the three-phase induction motor. A 220 V, 34 W fan mounted on a retort stand and held over the experimental setup was used to dissipate heat generated by the stator windings within the system. The rotating magnetic field generated in the air-gap of the three-phase induction motor was adjustable with the input power supplied to the stator windings, with a maximum magnetic field of 26.94 mT generated. The magnetic field generated was measured by a means of a digital GM07/GM08 gaussmeter.

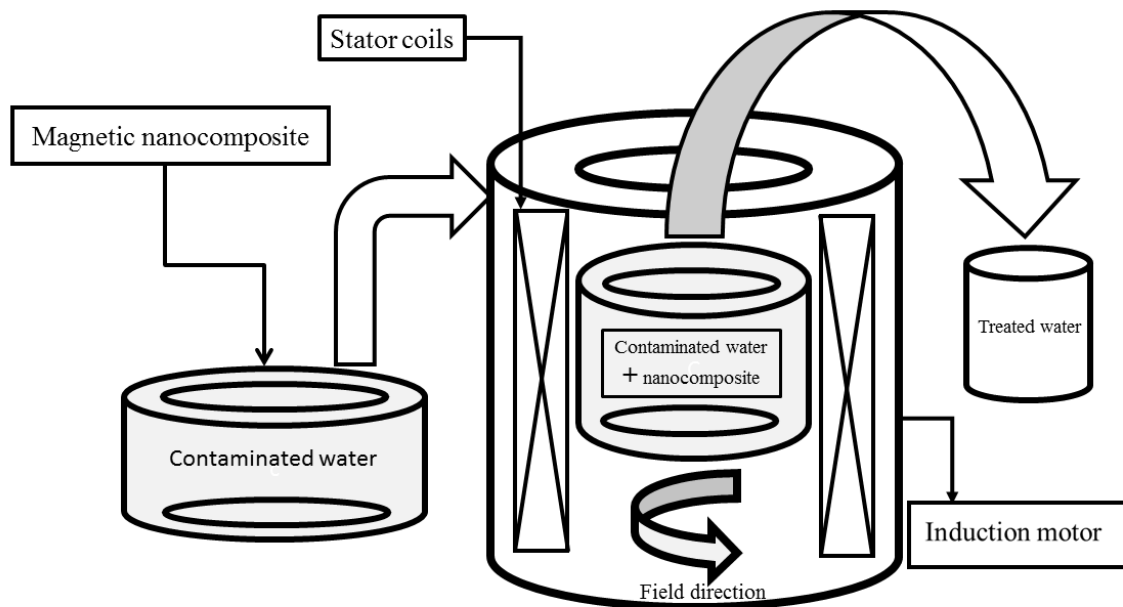


**Figure 3.1** Schematics of the magnetic adsorption device.

**Table 3.1:** Three-Phase Induction Motor Specification

Specification	Value/Unit (2-pole)	Value/Unit (8-pole)
Horsepower	1.5 kW	1.1 kW
Frequency	50 Hz	50 Hz
Synchronous speed	2920 RPM	700 RPM
Voltage	380/400 V	230/400 V
Current	2.19 A	5.5/3.2 A

### 3.3.2 Preparation of Cr(VI), Fluoride and Congo Red Wastewater

Synthetic wastewater containing Cr(VI), fluoride and congo red ions were prepared by dissolving a known mass of  $K_2Cr_2O_7$ , NaF and congo red powder (chemical formula =  $C_{23}H_{22}N_6O_6S_2Na_2$ ) in each volume of deionized water based on the experimental requirements.

### 3.3.3 Adsorption Experiment Influence by Rotating Magnetic Field for Cr(VI) Adsorption using 8-Pole Three-Phase Induction Motor

All adsorption experiments were performed in a three-phase induction motor (Motorelli Industrial Motor, South Africa) under the influence of magnetic field intensity range of 11.84-18.99 mT at 25 °C. To determine the optimal adsorption efficiency of the magnetic nanocomposite under the influence of rotating magnetic field, the following parameters were varied, pH of Cr(VI) solutions (2-10), adsorbent dosage (0.01-0.05 g) and magnetic field (from 11.84-18.99 mT). At the end of each set of experiments, samples are withdrawn with a syringe and filtered through a 0.45 µm syringe filter. To determine the residue concentration of Cr(VI) ions in the samples, PerkinElmer Lambda 1050 UV-Vis spectrophotometer operated at a wavelength of 540 nm was employed with a complexing reagent 1,5 diphenyl carbazide. All experiments were performed in triplicate and the average values reported. The percentage of Cr(VI) ions removed (adsorption efficiency) from the sample solution was evaluated using equation 3.1;

$$\% \text{ removal} = \left( \frac{C_o - C_e}{C_o} \right) \times 100 \quad 3.1$$

where the initial and equilibrium concentration of Cr(VI) in mg/L is denoted by  $C_o$  and  $C_e$ .

The adsorption isotherm data were generated by performing experiments under the influence of a fixed magnetic field at 33 °C. At this temperature, 0.2 g of adsorbent dosage was added to initial Cr(VI) concentration of 200-700 mg/L and spun under the influence of an unsteady magnetic field of 18.99 mT for 24 hours at room temperature. The equilibrium adsorption amounts of Cr(VI) ion adsorbed was calculated using equation 3.2;

$$q_e (\text{mg/g}) = \left( \frac{C_o - C_e}{M} \right) \times V \quad 3.2$$

where  $q_e$  is the amount of Cr(VI) ions absorbed per unit mass of the adsorbent (mg/g),  $V$  is the volume of sample (L) and  $M$  is the adsorbent dosage (g).

Adsorption Kinetic experiments were conducted under the influence of a magnetic field (18.99 mT), by contacting 0.05 g of the adsorbent with initial Cr(VI) concentrations of 50-150 mg/L (50mL) at magnetic exposure time intervals of 5-150 min. The Cr(VI) amount adsorbed by a unit mass of adsorbent at the various time was determined using equation 3.3;

$$q_t(\text{mg/g}) = \frac{(C_o - C_t)}{M} \times V \quad 3.3$$

where the time-dependent amount of Cr(VI) adsorbed per unit mass of adsorbent is denoted by  $q_t$  (mg/g), the bulk phase Cr(VI) concentration (mg/L) at time  $t$  is denoted by  $C_t$ ,  $V$  is the volume of sample (L) and  $M$  is the adsorbent dosage (g).

### 3.3.4 Desorption Experiment

To assess regeneration and the ability to reuse the adsorbent for hexavalent chromium adsorption, adsorption-desorption experiments were performed. For the adsorption cycle experiment, a mass of 0.1 g adsorbent is added to 50 mL of 100 mg/L of hexavalent chromium solution. This was agitated by an unsteady magnetic field of 18.99 mT generated in the air-gap by the stator coils of the induction motor. To desorb the adsorbate from the adsorbent surface (desorption experiments), the adsorbent loaded with Cr(VI) ions was contacted with 0.1 M of NaOH solution in a thermostatic shaker for 60 min. To regenerate adsorption sites on the surface of adsorbent (nanocomposite) after desorption of Cr(VI) ions, the adsorbent is treated with 2 M of HCl. Four successive desorption experiments were performed to evaluate the reuse of the adsorbent for adsorption process.

### 3.3.5 Adsorption Experiment under the Influence of Magnetic Field for Cr(VI) Adsorption using 2-Pole Three-Phase Induction Motor

Adsorption experiments were performed in a 2-pole three-phase induction motor (First electric induction motor) under different magnetic field intensity range of 9.0-13.2 mT at room temperature. For pH effect on the adsorption of Cr(VI) under the influence of magnetic field, pH of Cr(VI) solution was varied from 2-10, which was spun under a constant magnetic field of 13.38 mT. For the adsorbent dosage effect on Cr(VI) adsorption under the influence of a magnetic field, adsorbent dosage was varied from 0.01-0.05 g at a constant pH and magnetic field of 13.38 mT. Magnetic field effect on the adsorption of the Cr(VI) experiments was carried out by varying the magnetic field in clockwise and anticlockwise directions. At the end of all experiments, samples are taken out with a syringe and filtered using 0.45  $\mu\text{m}$  cellulose acetate syringe filter. The residual concentration of Cr(VI) ions in the filtrate were analyzed using a UV/Vis spectrophotometer (PerkinElmer Lambda 1050) at a wavelength of 540 nm by complexing the Cr(VI) with 1,5 diphenylcarbazide reagent. Each experiment was conducted in triplicate and the average values were reported. The percentage of Cr (VI) removal (adsorption efficiency) was calculated according to the following equation 3.4:

$$Cr^{6+} \% \text{ removal} = \left( \frac{C_o - C_e}{C_o} \right) \times 100 \quad 3.4$$

where  $C_o$  and  $C_e$  are the initial and equilibrium concentration of Cr(VI) concentration in mg/L.

### 3.3.6 Adsorption Experiment under the Influence of Magnetic Field for Fluoride Adsorption using 8-Pole Three-Phase Induction Motor

Experiments on the influence of magnetic field on the adsorption of fluoride were conducted at room temperature. Each experiment was conducted in a 100 mL column held into the air-gap of the three-phase induction motor using a rotor. To determine the pH effect on the adsorption of fluoride ions under the influence of magnetic field, fluoride solution pH was adjusted from 2-10 using 0.1 M NaOH or HCl. For effect of adsorbent dosage experiments were performed by contacting varying amount of adsorbent (0.025-0.150 g) with 10 mg/L under the influence of magnetic field. The influence of magnetic field on fluoride ion adsorption was investigated at a magnetic exposure time of 20 and 60 min. At the conclusion of all experiments, samples were withdrawn using a syringe and filtered through 0.45  $\mu$ m syringe filter. The residue concentration of fluoride ions in the samples was determined using the ion selective electrode (Thermo Scientific Orion ISE meter) with a low-level TISAB buffer. The percentage amount of fluoride ions removed was calculated using equation 3.5;

$$\% \text{ removal} = \left( \frac{C_o - C_e}{C_o} \right) \times 100 \quad 3.5$$

where  $C_o$  is the initial concentration of fluoride in the aqueous solution and  $C_e$  is the equilibrium concentration of fluoride in the solution. Experiments were conducted in triplicate, with the average value reported to check for reproductivity of the data points. The standard deviation was calculated and provided in form of error bars.

For initial concentration effect on the adsorption of fluoride ions under the influence of magnetic field experiments, initial fluoride concentrations of 20-100 mg/L were excited with 0.1 g nano-adsorbent using a fixed magnetic field for 24 hours. For kinetics experiments, 0.05 g polypyrrole magnetic nanocomposite were excited with fluoride concentrations of 10, 40 and 60 mg/L at a magnetic exposure time of 5-90 min. The amount of fluoride adsorbed onto the adsorbent ( $q_e$ ) and the amount of fluoride adsorbed by a unit mass of adsorbent at the various time ( $q_t$ ) were determined using equation 3.6 and 3.7:

$$q_e = \frac{(C_o - C_e)V}{m} \quad 3.6$$

$$q_t = \frac{(C_o - C_t)V}{m} \quad 3.7$$

where  $C_o$ , and  $C_e$  are the initial and equilibrium concentration of fluoride solution.  $C_t$ ,  $V$ , and  $m$  represents the bulk phase fluoride concentration (mg/L) at time  $t$ , the volume of fluoride solution (L) and the mass of the adsorbent used (g).

### 3.3.7 Adsorption Experiment under the Influence of Magnetic field for Congo Red Adsorption

To study the effect of pH on congo red adsorption onto magnetic nanocomposite influenced by a rotating magnetic field of 18.99 mT, initial pH of congo red solution was varied from 2-10 by using 0.1 M NaOH or HCl solutions. To evaluate the effect of pH on congo red adsorption, 0.15 g adsorbent dosage was added to 50 mL of 100 mg/L congo red solution spun in a magnetic field of 18.99 mT. Three sets of experiment were performed, and the average value is reported. To separate the dye solution from the adsorbent after adsorption experiments, samples were centrifuged at 4000 rpm for 20 minutes using Lasec Hemle centrifuge. The equilibrium congo red concentrations were evaluated using a calibration curve using a UV/Vis spectrophotometer (PerkinElmer Lambda 1050) at an absorption wavelength ( $\lambda_{max}$ ) at 497 nm. The removal efficiency was determined by computing the percentage sorption from equation 3.8:

$$\% \text{ removal} = \frac{C_o - C_e}{C_o} \times 100 \quad 3.8$$

where the initial and equilibrium concentrations of congo red are represented by  $C_o$  and  $C_e$  (mg/L).

To study the effect of adsorbent dosage on congo red adsorption influenced by a magnetic field was evaluated by contacting varying amounts of adsorbent dose (0.05-0.20 g) with 100 mg/L of congo red solutions adjusted to pH 4 and spun at a fixed magnetic field of 18.99 mT. The residual amount of congo red concentration in the filtrates was used to determine the effect of adsorbent dosage on congo red adsorption under magnetic field influence using equation 3.8.

To study the effects of initial concentrations and adsorption isotherm on congo red adsorption influenced by a magnetic field, experiments were carried out by adding 0.15 g adsorbent dosage to 50 mL of initial congo red concentrations (100-400 mg/L) under the influenced of a magnetic field of 18.99 mT for 24 hours. The equilibrium adsorption capacity was evaluated using equation 3.9 below:

$$q_e = \frac{C_o - C_e}{m} \times V \quad 3.9$$

where  $q_e$  (mg/g),  $V$  (L) and  $m$  (g) represents the amount of congo red absorbed per unit mass of the adsorbent, the sample volume and the mass of the adsorbent

To study the effects of magnetic field applied and the magnetic exposure time on congo red adsorption, each experiment was evaluated by contacting 0.15 g of adsorbent dosage with 50 mL of 100 mg/L congo red solutions spun in varying magnetic field intensity of 11.84-26.94 mT and exposed to magnetic field of 18.99 mT for 10-120 min. For control purpose, magnetic exposure time experiments were also performed to evaluate the effects of no field applied to the adsorption of congo red solutions. The residual amount of congo red solution concentration in the filtrate was used to determine the effects of magnetic field and magnetic exposure time on congo red adsorption onto the adsorbent using equation 3.8.

To study the adsorption kinetics on congo red adsorption induced by the magnetic field of 18.99 mT, kinetics experiments were performed by contacting a fixed adsorbent dosage of 0.05 g to 50 mL congo red solution of initial concentrations (20-80 mg/L) at exposure time intervals of 10-120 min. The time-dependent amount of adsorbate adsorbed by a unit mass of adsorbent at the varying time was determined using equation 3.10;

$$q_t = \frac{C_o - C_t}{m} \times V \quad 3.10$$

where  $q_t$  is the time-dependent amount of adsorbate adsorbed per unit mass of adsorbent (mg/g),  $C_t$  is the bulk phase concentration (mg/L) at any time  $t$ ,  $V$  is the sample volume (L) and  $m$  is the adsorbent mass (g).

### 3.3.8 Adsorption-Desorption Experiment

To evaluate the adsorbent regeneration and recycling for congo red adsorption, adsorption-desorption experiments were performed. For adsorption cycle study, 0.15 g adsorbent dosage was contacted with 100 mg/L of congo red solution at pH 4 and spun at a magnetic field of 18.99 mT. After the adsorption experiments, desorption experiments were performed to desorb the congo red from the adsorbent, by contacting 0.1 M of NaOH solution with the spent adsorbent, spun in the magnetic field of 18.99 mT for 60 min. To regenerate adsorption sites on the adsorbent after the desorption process, the adsorbent was treated with 2 M HCl spun in a magnetic field intensity of 18.99 mT for 60 min. Three successive adsorption-desorption

experiments were performed to test the potential of re-using the adsorbent for congo red adsorption.

### 3.4 Particle Shadow Velocimetry Materials and Methods

#### 3.4.1 Apparatus and Measurements

Cylindrical eight-pole three-phase induction motor with bore dimension as 160 mm height and 105 mm inner diameter was used for the PSV experiments. The nameplate data of the 8-pole induction motor were 50 Hz, 700 rpm, 230/400 V, 1.1 kW, 5.5/3.2 A. The 8-pole induction motor consists of eight identical coil pairs (stator), consisting of several overlapping windings offset by an electrical angle of 120° shown in Figure 3.2(a). The rotor consists of laminated steel in the core with evenly spaced bars of copper or aluminium placed axially around the periphery. To generate rotating magnetic fields (RMF) that rotates with a synchronous speed in the air-gap of the induction motor, a 10 A power supply is used to supply currents to the stator coils. The RMF produces a torque on the particles, resulting from the induction of magnetic field on the particle. The magnetic field induced on the adsorbent causes current to flow in a direction opposite to that creating it (Lenz law). These lead to a twisting motion or torque of the adsorbent particles (magnetic nanocomposite). The voltage induced in the induction coil is a result of fundamental Faraday's induction law given by equation 3.11, where  $\Phi$  is the magnetic flux passing through a coil having an area and number of coils turns  $N$ ,  $B$  is the magnetic flux density,  $H$  is the magnetic field strength and  $\mu_o$  is the core (air) permeability [2]. The magnetic torque,  $\tau$ , applied to the particle scales with the magnetic induction,  $B$ , and the magnetic moment of the particle,  $m$ , is given by equation 3.12:

$$V = -N \frac{d\Phi}{dt} = -\mu_o N \frac{dH}{dt} \quad 3.11$$

$$\tau = \vec{m} \times \vec{B} \quad 3.12$$

In a field gradient, the magnetic force on a particle is given by equation 3.13 [3];

$$F_m = \frac{4}{3} \pi R^3 M \nabla B \quad 3.13$$

where  $R$  is the particle radius,  $M$  is the magnetization of the particle and  $B$  is the magnetic induction. The Lorentz equation describes the force acting on a charge species with charge  $q$  moving with a velocity  $v$  in an electric field  $E$  and a magnetic field  $B$  (equation 3.14):

$$F_{Lorentz} = q(E + v \times B) \quad 3.14$$

In the absence of electric field, the sum of  $qv$  over a unit volume represents the current flux  $J$  and the magnetic body force acting on the unit volume is given by equation 3.15 [4];

$$F_B = J \times B \quad 3.15$$

### 3.4.2 Particle Shadow Velocimetry Measurement

Experiments were carried out in the fluid laboratory in the Mechanical and Industrial Engineering Department of the University of South Africa, using the particle shadow velocimetry technique. The magnetic nanocomposite used for this measurement was synthesized using the in-situ polymerization method. To study the interaction between the rotating particles and the channel wall, the velocity field effects and particle aggregation on the adsorption of contaminants from aqueous solutions, measurements were carried out by varying the intensity of the magnetic field induced on nanocomposite spun in Cr(VI) and fluoride solutions. Experiments on the interaction of particles rotation leading to the adsorption were measured in a cylindrical channel made from clear perspex plastic with external, internal and height dimensions of 100×64×60 mm. The PSV experimental method was used to determine the velocity field, particle interaction and particles aggregation on adsorption of Cr(VI) and fluoride ions onto the nanocomposite. LED Light source (50 W, 1500 Lm brightness) is directed through the measurement area onto an IDT NX-8 CMOS camera (camera resolution of 1600 × 1200 pixel) equipped with a 50 mm Nikon lens with an f-number of 1.4. This in-line arrangement allows shadows formed by the particles suspended in fluids to be recorded. 2000 images were captured at a frame interval of 100 fps at full resolution for all experiments. The images captured were then transferred digitally from the CMOS camera to the image processing computer using Ethernet 100/1000BaseT and stored in a 2-gigabyte external memory drive. A maximum of 25.54 mT magnetic field generated in the air-gap of the induction motor was measured and recorded using a handheld gaussmeter (HMIRS GM08 gaussmeter). The shadows created by the particles rotating (detection of dark objects on bright background) were analyzed using the PIVLab software. The description of the particle's velocity field was computed from the displacement between two image pairs using the PIVLab software. The standard cross-correlation system, which is based on the Fast Fourier transform (FFT) was used to process the PSV images to obtain velocity field profile of the rotating particles using interrogation area of 64

× 32 pixels. Figure 3.2(b) shows the schematics of the PSV experimental setup with the in-line excitation using a LED light.

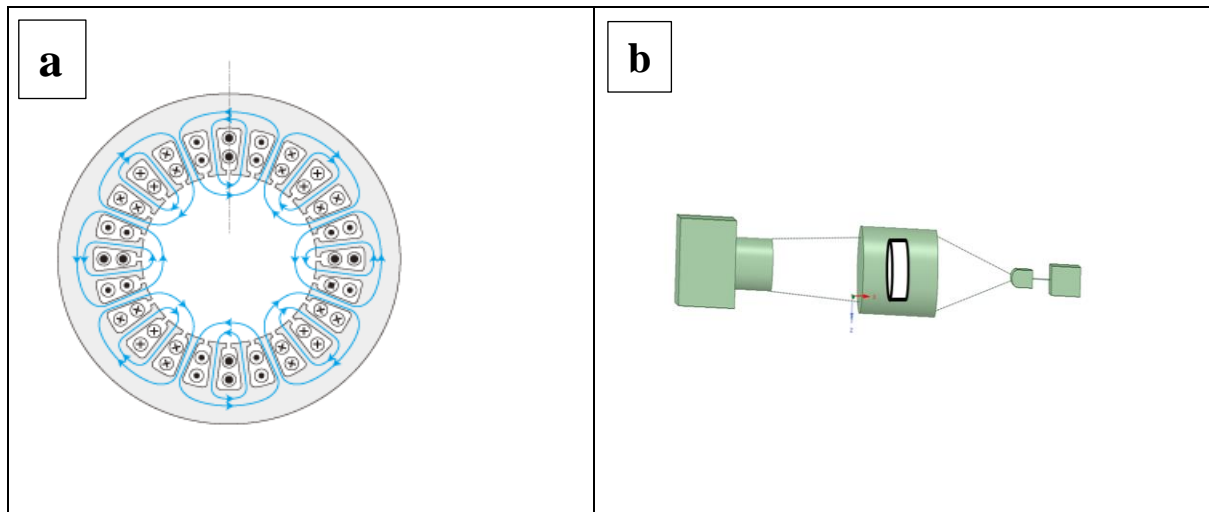


**Figure 3.2(a)** Schematic of the eight-pole three-phase induction motor, **(b)** PSV experimental setup showing inline excitation by LED.

### 3.5 References

- [1] M. Bhaumik, A. Maity, V. V. Srinivasu, and M.S. Onyango, **2011**, *J. Hazard. Mater.* 190, 381–390.
- [2] A. S. Todorovic, and M. D. Jevtic, **2010**, *Facta Universitatis-Series: Electronics and Energetics*, 23, 199-206.
- [3] X. J. A. Janssen, A. Van Reenen, L. J. Van Ijzendoorn, A. M. De Jong, and M. W. J. Prins, **2011**, *Colloids and Surfaces A: Physicochemical and Engineering Aspects*, 373, 88-93.
- [4] N. T. Nguyen, **2012**, *Microfluidics and Nanofluidics*, 12, 1-16.

## CHAPTER FOUR

### 4.0 Results and Discussion

Some of the data presented in this section have not been published; however, they reflect the results already appended in papers I-VI.

**Result I: A Novel Method for Removal of Cr(VI) using Polypyrrole Magnetic Nanocomposite in the Presence of Unsteady Magnetic Fields (<https://doi.org/10.1016/j.seppur.2017.11.057>)**

**Abstract.** A key source for existence on earth is water. Therefore, its conservation is a key issue to all of us. Many purification techniques have been implemented over the years for the advanced treatment of wastewater. The present study highlights on the preparation of polypyrrole (PPy) based magnetic nanocomposite for a fast-adsorptive Cr(VI) ion removal from wastewater using the unsteady electromagnetic field. PPy/Fe<sub>3</sub>O<sub>4</sub> magnetic nanocomposite was prepared via in-situ oxidative polymerization of pyrrole monomer using FeCl<sub>3</sub> oxidant in the presence of suspended Fe<sub>3</sub>O<sub>4</sub> nanoparticles. For physicochemical properties, the resultant magnetic material was characterized using ATR-FTIR, XRD, BET, FE-SEM, HR-TEM, ESR, VSM and zeta sizer. The adsorption capacity and adsorption kinetics were measured by altering the magnetic field intensity, adsorbent dosage, and pH with a maximum adsorption capacity of 208.77 mg/g using the Langmuir isotherm model for the equilibrium Cr(VI) uptake. Results showed a maximum removal up to 99.2% at a magnetic field of 18.99 mT of 50 mg/L Cr(VI) solution at pH 2 with particle aggregation noticed. The results revealed that hexavalent chromium (Cr(VI)) removal induced by a magnetic field, resulted in a higher efficiency of wastewater treatment attributed to increase particles interaction resulting from increased velocity due to Lorentz force.

### 4.1 Introduction

The evolution of society and nations is determined by industrial development, which also comes with severe environmental problems [1]. Globally, the presence of heavy metals in water is a key area of concern due to their adverse effect on human health and the environment [2-3]. Among various toxic metal ions, hexavalent chromium is one of the most hazardous and carcinogenic element in the world to public health. Therefore, their removal from contaminated

wastewater [4-5] is a special concern to us. In aqueous systems, as well in the environment, chromium exists mainly in trivalent chromium and hexavalent chromium oxidative states. In terms of toxicity to humans, Cr(III) is less detrimental compared to Cr(VI). For the metabolic process in living organisms, Cr(III) is a vital micronutrient needed. Due to the mobility of Cr(VI) in the environment, they tend to be toxic, carcinogenic and mutagenic to all living organisms as they move through the food chain [6]. The Cr(VI) concentration of industrial effluents ranges from 0.5 to 270,000 mg/L. Nervous system damage and liver disorder in humans are caused by severe exposure of Cr(VI) at a high level [7]. The allowable maximum concentration of Cr(VI) that can be found in inland, surface and industrial water per the World Health Organization (WHO) are 0.05 mg/L, 0.1 mg/L, and 0.25 mg/L, respectively [8-9].

Standard quality of simple, inexpensive and improved technology for water treatment is a significant growth area [10]. With demand increasing and coupled with escalating cost of energy around the world, energy cannot be consumed more by the water treatment industry. The requirement for water treatment methods that are effective and provide substantial savings in both production time and costs cannot be overemphasised [11]. Techniques such as oxidation-reduction, chemical oxidation, filtration, ion exchange, electrochemical technique, membrane separation, coagulation/flocculation, and adsorption have been applied in the elimination of dissolved toxic substance such as metals from wastewater. However, the use of most of these techniques leads to a partial metal removal, high rate of reagent or energy consumed, generation of sludge and expensive equipment or monitoring system used for water treatment [12]. Adsorption is considered as one of the most effective and economical technique in water purification because of simple to handle and having a straightforward design [13]. For physical and chemical methods of water treatment, a special attention has been focussed on magnetic treatment due to their ecological purity, safety and simplicity [14]. Developing this new technique for water treatment has drawn research interest of scientists worldwide and more frequently the technological systems are presented alongside with physical features [15-16]. The magnetic field changes on the adsorbent or adsorbate in adsorption processes depend on factors like field strength, the direction of applied field, time of the magnetic exposure, the flow rate of the solutions, the additives present in the system and pH of the medium [17,18]. Magnetic enhanced adsorption processes involve the use of a porous material (adsorbent), which not only acts as a magnetic matrix but contributes to the adsorptive component of the adsorption system [19]. Various magnetic effects such as scale prevention, [11,18-20] magnetic field effect on the adsorption of zinc, copper (II), total suspended solids, uranium, strontium and organic dyes have

been reported [16, 21–23]. The presence of magnetic field gradient was shown to enhance the adsorption efficiency of strontium and uranium onto monosodium titanate [24-25]. Use of activated carbon as an adsorbent was also an alternative method to treat contaminated water in the presence and absence of magnetic field [1, 21–23]. It was also reported that magnetic treatment significantly enhances the fraction of adsorption of  $\text{Cu}^{2+}$  using Kaolinite, Ca-rectorite, and  $\text{Zn}^{2+}$  using Na- rectorite.

Influence of magnetic field increases the adsorption process many folds by improvement of the orientation of the adsorbate molecules towards the adsorbent pores. that applied magnetic field significantly affects the zeta potential and size distribution of the particles in the adsorption medium, which was attributed to the Lorentz force ( $\vec{F} = q \cdot \vec{v} \times \vec{B}$ ) exerted on moving ions or the charged solid particles in aqueous solutions [26]. This increases linearly with the charge of the particle, velocity of the particle, and the orthogonal vector component of the magnetic field strength, leading to increased interaction between the adsorbate and the adsorbent in the aqueous solutions [27-28]. The exposure of colloid particles ( $\text{Fe}_3\text{O}_4$ ) to magnetic field combined with electrocoagulation process led to a high electrokinetic movement of the colloid particles, with improved suspended solid removal from waste- water [29-30].

In this study, the influence of induced unsteady magnetic field generated by an induction motor for the adsorption of Cr(VI) onto the adsorbent was explored. Experimental conditions such as magnetic exposure time, magnetic field intensity, pH, the initial concentration and adsorbent dosage on Cr(VI) adsorption were also adjusted to get the maximum Cr(VI) adsorption. The goal is to develop a new water treatment technique which would be valuable in the treatment of waste effluents in every sphere of life.

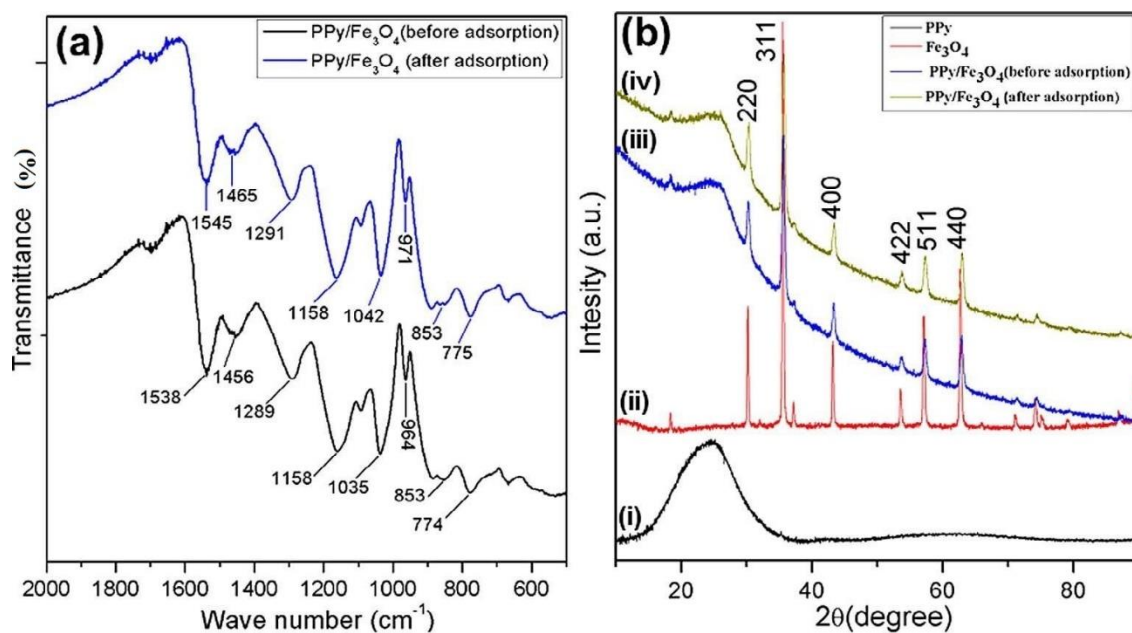
## **4.2 Results and Discussion**

### **4.2.1 PPy/ $\text{Fe}_3\text{O}_4$ Characterization**

The FTIR spectra of the adsorbent at its original state before the adsorbent is used for adsorption studies and subsequently, after adsorption of Cr(VI) are shown in Figure 4.1. The adsorption spectrum of pure PPy/ $\text{Fe}_3\text{O}_4$  comprises of PPy characteristic peaks situated at 1538 and 1456  $\text{cm}^{-1}$ . These peaks are assigned to the symmetric and antisymmetric ring-stretching modes of PPy ring [31]. While characteristic peaks observed at 1035 and 1289  $\text{cm}^{-1}$  are attributed to C-H deformation vibrations and C-N stretching vibrations of PPy, respectively [32]. The two peaks observed at 1158 and 964  $\text{cm}^{-1}$  are assigned to C-H in-plane vibration and out-

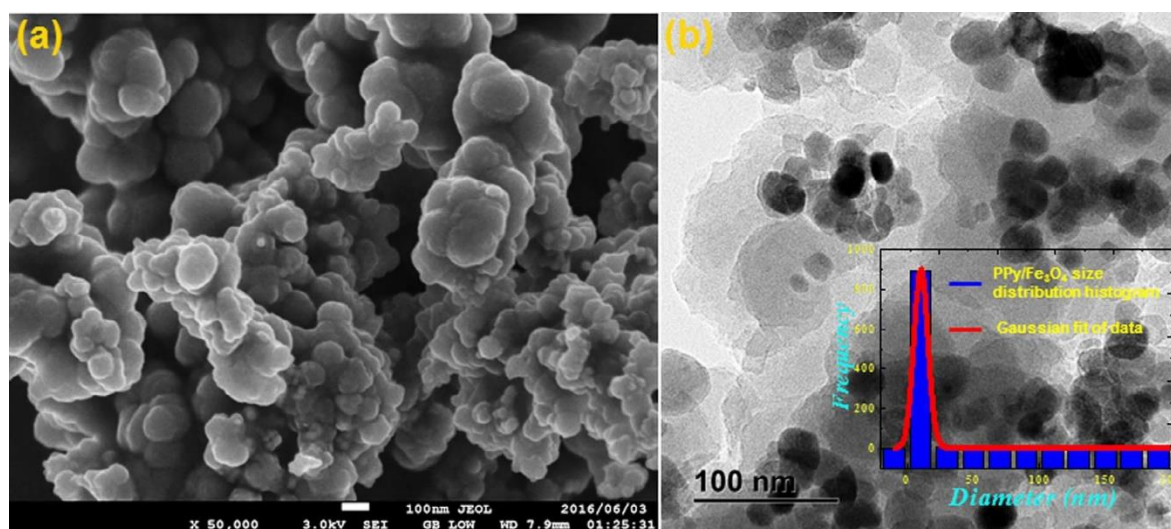
of-plane vibration of PPy, respectively [33-34]. The FTIR spectrum of PPy/Fe<sub>3</sub>O<sub>4</sub> nanocomposite peaks after absorption were observed at 1545, 1465, 1291, 1042, 1158 and 971 cm<sup>-1</sup> which were attributed to the absorption bands of symmetric and antisymmetric ring-stretching, conjugated C-N stretching, C-H deformation and C-H stretching vibration of pyrrole ring, respectively [6, 35]. After adsorption of Cr(VI) ions, the peak values shift to the higher infrared region.

Figure 4.1(b) shows the XRD pattern of the pure PPy, pure Fe<sub>3</sub>O<sub>4</sub> nanoparticles (NPs), and PPy/Fe<sub>3</sub>O<sub>4</sub> before and after Cr(VI) ions adsorption. A broad XRD diffraction peak was observed at  $2\theta = 20.5^\circ$  which is a characteristic peak of the PPy polymer. This indicates the amorphous nature of pure PPy (Figure 4.1b(I)) [36]. The XRD diffraction pattern of pure Fe<sub>3</sub>O<sub>4</sub> NPs with six distinguished sharp diffraction peaks have been shown in Figure 4.1b (II). These characteristic diffraction peaks of pure Fe<sub>3</sub>O<sub>4</sub> were observed at Bragg angles of  $30.3^\circ$ ,  $35.7^\circ$ ,  $43.4^\circ$ ,  $53.6^\circ$ ,  $57.3^\circ$ , and  $62.9^\circ$ . They are assigned to the reflection of (2 2 0), (3 1 1), (4 0 0), (4 2 2), (5 1 1), and (4 4 0) planes of the face-centred cubic (FCC) lattice of Fe<sub>3</sub>O<sub>4</sub> respectively, affirmed by the JCPDS file database (PDF No. 75-0449) [34-37]. In the case of prepared PPy/Fe<sub>3</sub>O<sub>4</sub> before and after adsorption of Cr (VI), all the peaks of Fe<sub>3</sub>O<sub>4</sub> were observed in composites (Figure 4.1(b)(III-IV)) which indicated that after modification as well as adsorption study, Fe<sub>3</sub>O<sub>4</sub> NPs did not change their phases.



**Figure 4.1**(a) FTIR and (b) XRD pattern of (I) PPy, (II) Fe<sub>3</sub>O<sub>4</sub>, PPy/Fe<sub>3</sub>O<sub>4</sub> (III) before and (IV) after adsorption of Cr(VI) ions.

The surface morphology of the PPy/Fe<sub>3</sub>O<sub>4</sub> nanocomposite was observed using both SEM and HR-TEM techniques (Figure 4.2). SEM analysis (Figure 4.2(a)) showed that the developed PPy/Fe<sub>3</sub>O<sub>4</sub> nanocomposite had a regular uniform spherical morphology. The HR-TEM image in Figure 4.2(b) further confirmed that the PPy/Fe<sub>3</sub>O<sub>4</sub> composites had a polydisperse spherical matrix with an average image size of Fe<sub>3</sub>O<sub>4</sub> NPs about  $10.6 \pm 6.3$  nm measured using ImageJ software. The histogram was obtained by analysing (inset of Figure 4.2(b)) more than 900 particles, with 99.6% of the particles distribution size of 10.6 nm. Therefore, it can be concluded from surface analysis results that the Fe<sub>3</sub>O<sub>4</sub> NPs have been completely coated and stabilised by the PPy microspheres in the PPy/ Fe<sub>3</sub>O<sub>4</sub> composite matrix. In addition, the energy-dispersive X-ray analysis (EDX) spectrum of PPy/Fe<sub>3</sub>O<sub>4</sub> confirms the existence of C, O, N, Cl and Fe as the predominant elements into magnetic nanocomposite (Figure S4.1(a), Supporting Information). However, after Cr(VI) adsorption PPy/ Fe<sub>3</sub>O<sub>4</sub> an additional peak of Cr along with C, O, N, Cl and Fe confirmed the adsorption of Cr(VI) ion onto PPy/Fe<sub>3</sub>O<sub>4</sub> surface (Figure S4.1(b), Supporting Information).



**Figure 4.2**(a) SEM and (b) HR-TEM image of PPy/Fe<sub>3</sub>O<sub>4</sub> nanocomposite.

Nitrogen adsorption-desorption isotherm of PPy/Fe<sub>3</sub>O<sub>4</sub> was performed to examine the surface areas (m<sup>2</sup>/g), pore diameter (nm) and pore volume (cm<sup>3</sup>/g) of the prepared magnetic nanocom-

posite (Figure 4.3). The analysis result reflects a typical type-IV adsorption-desorption isotherm curve with the hysteresis loop, indicating the mesoporous characteristics of PPy/Fe<sub>3</sub>O<sub>4</sub> composite [38]. The BET analysis revealed that the specific surface area, BJH cumulative volume of pores and BJH average pore diameter of PPy/Fe<sub>3</sub>O<sub>4</sub> were calculated to be 28.77 m<sup>2</sup>/g, 0.05 cm<sup>3</sup>/g and 15.82 nm, respectively (Figure 4.3).

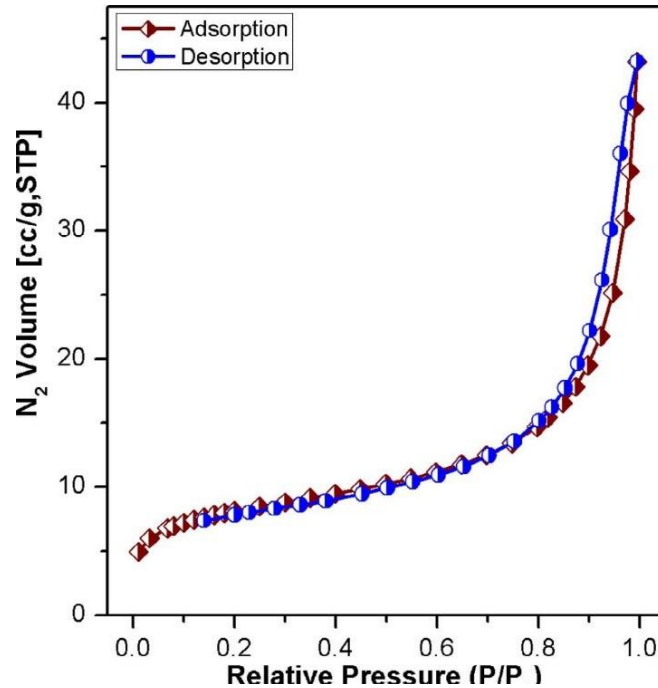


**Figure 4.3** N<sub>2</sub> adsorption-desorption isotherms for PPy/Fe<sub>3</sub>O<sub>4</sub>.

The ESR adsorption spectra of the adsorbent measured at room temperature are shown in Figure 4.4(a). The line shapes and the resonance signal are symmetrical and wide (broad) with a linewidth value of approximately 1400 Gauss. The effective sample g-value of 2.25 G determined from ESR spectra was due to spin interactions of Fe<sup>3+</sup>. Magnetic behaviour characterised by the presence of clusters is shown by such interactions. The shapes and the field position are identical to those of the standard magnetic nanoparticles suspension, which is consistent with ESR spectra of magnetic iron oxide nanoparticles at room temperature [39–41]. The line shape of nanocomposite when fitted to Gaussian and Lorentzian functions shows a line shape of the adsorbent having a Gaussian shape. The Gaussian function had the best fitting of 55% and Lorentzian functions (45%). The dominant Gaussian fit is characteristic of ferromagnetic resonance indicating that the predominant portion of the PPy/Fe<sub>3</sub>O<sub>4</sub> nanocomposite is ferromagnetic as shown in Figure 4.4(b and c) [42-43].

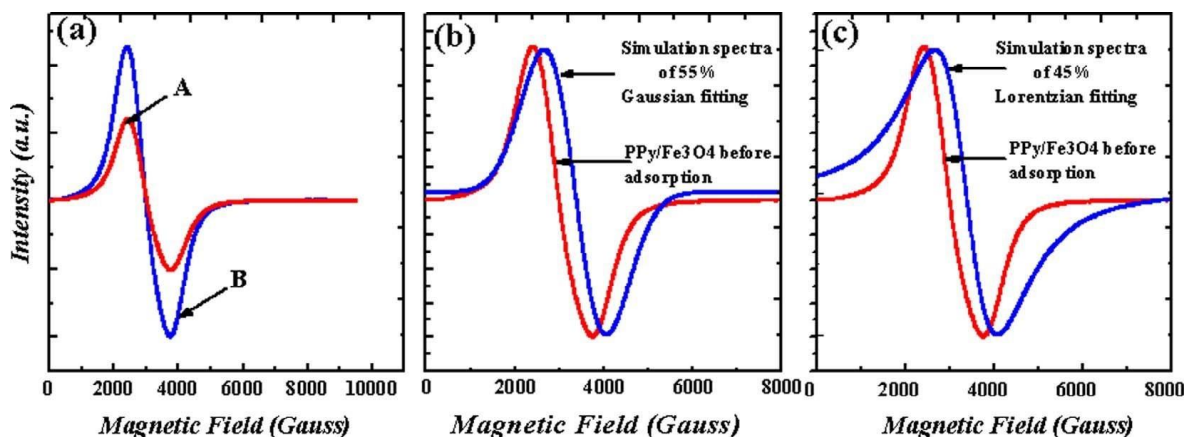


**Figure 4.4**(a) First derivative ESR adsorption signals versus magnetic field ( $H$ ) for (A) PPy/Fe<sub>3</sub>O<sub>4</sub> nanocomposite before and (B) PPy/Fe<sub>3</sub>O<sub>4</sub> nanocomposite after adsorption (b) ESR spectra of PPy/Fe<sub>3</sub>O<sub>4</sub> nanocomposite before adsorption and simulation using Gaussian fitting and (c) ESR spectra of PPy/Fe<sub>3</sub>O<sub>4</sub> nanocomposite before adsorption and simulation using Lorentzian fitting.

To measure the magnetic property of the sample before and after adsorption of Cr(VI), the magnetic moments were determined by vibrating the sample perpendicular to a uniform magnetic field in-between a set of pickup coils [41]. The magnetisation curves of the adsorbent measured in the range of  $-10,000$  Oe to  $10,000$  Oe at room temperature (300 K) are shown in Figure 4.5. A hysteresis loop with a zero coercivity field ( $H_c$ ) and a saturation magnetisation ( $M_s$ ) of 23 and 14 emu/g were observed, which are the characteristic of a ferromagnetic material before and after adsorption of Cr(VI) using PPy/Fe<sub>3</sub>O<sub>4</sub>. The saturation magnetisation of the nanocomposite after adsorption of Cr(VI) is found to be lower than that before adsorption. The surface magnetic anisotropy of the magnetite changes with the addition of Cr(VI) ions to the nanocomposite, which leads to an increase in the surface spins disorientation and results in a decrease of the magnetic moment of the nanocomposite resulting in reduced saturation magnetisation of the adsorbent.

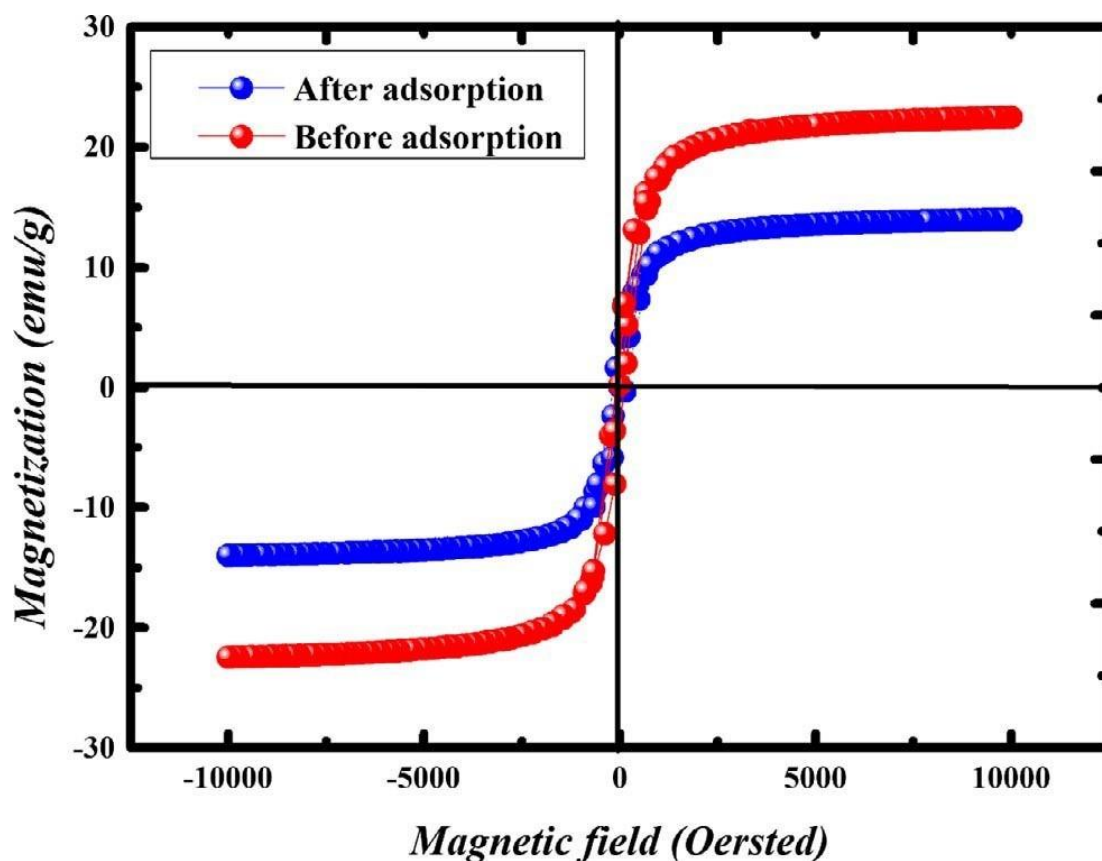


**Figure 4.5** M-H curve at room temperature for PPy/Fe<sub>3</sub>O<sub>4</sub> nanocomposite before and after Cr(VI) adsorption.

### 4.3 Equilibrium Adsorption Studies of Cr(VI)

#### 4.3.1 Influence of Solution pH

In adsorption medium, the solution pH is a significant factor which controlled the metal ions adsorption onto the adsorbent surface [44-45]. The key features for describing the mechanism of adsorption are related to the initial pH of the adsorption medium which influences the ionisation of the adsorptive molecules as well as a surface charge of the adsorbent. The two main forces that act as a vital part of the adsorption processes are chemical interaction and an electrostatic force which corresponding to Coulombic attraction or repulsion between reactive sites and adsorbing ions [46]. The pH effect on Cr(VI) adsorption onto the magnetic nanocomposite was studied under the influence of an unsteady magnetic field of 18.99 mT in the pH range of 2–10. The point-of-zero charge ( $pH_{pzc}$ ) was measured for understanding the electrostatic interactions at the materials surface with charged species of chromium ions in aqueous solution.

The adsorption of the adsorbate (coagulant) on non-specific and specific adsorbents depends on pH, as the surface property of the adsorbate (coagulant) is affected by solution pH [47-48]. The pH<sub>pzc</sub> of PPy/Fe<sub>3</sub>O<sub>4</sub> was determined to be 3.20 shown in Figure S4.2 (Supporting Information). As shown in Figure 4.6(a), the percentage of Cr(VI) ions removed declined with an increase in solution pH. The percentage of Cr(VI) ions removed from the aqueous solution decreased from 99 to 86% with an increase in pH 2–10 and showed a maximum at pH 2. As reported in the literature, hexavalent chromium exists in several species at different pH values like H<sub>2</sub>CrO<sub>4</sub>, HCrO<sub>4</sub><sup>-</sup>, CrO<sub>4</sub><sup>2-</sup>, HCr<sub>2</sub>O<sub>7</sub><sup>-</sup>, and Cr<sub>2</sub>O<sub>7</sub><sup>2-</sup> [49]. In acidic solution (≤2), the most abundant species of Cr(VI) is HCrO<sub>4</sub><sup>-</sup>. The maximum adsorption observed at pH 2 is attributed to the rise in positive charge on the adsorbent surface resulting in attraction between the positively charged adsorbent and the negative monovalent chromate ions (HCrO<sub>4</sub><sup>-</sup>) electrostatically, which is the major species of Cr(VI) at this pH [50]. With increasing pH of the solution, HCrO<sub>4</sub><sup>-</sup> is gradually converted to other Cr(VI) forms like CrO<sub>4</sub><sup>2-</sup> and Cr<sub>2</sub>O<sub>7</sub><sup>2-</sup>. At higher pH value, the competition between the negatively charged OH<sup>-</sup> ions in adsorption medium and CrO<sub>4</sub><sup>2-</sup> species for the adsorbent sites causing a decrease in the efficiency of adsorbent in Cr(VI) ions removal. Zeta potential (Figure S4.2, Supporting Information) confirmed the surface charge of the PPy/Fe<sub>3</sub>O<sub>4</sub> decreases sharply with increasing pH value. Therefore, at higher pH values repulsion between anionic chromium species with a negative surface charged PPy/Fe<sub>3</sub>O<sub>4</sub> also plays a major role in the decreasing the adsorption efficiency.

### 4.3.2 Effect of Adsorbent Dosage

Optimization of adsorbent dosage is crucial to determine the minimum amount required for reaching the maximum adsorption. The adsorbent dosage effect on the sorption of Cr(VI) in an unsteady magnetic field of 18.99 mT was examined and shown in Figure 4.6(b). The experiment was conducted by adding a varying amount of adsorbent dosage (0.01-0.05 g) to 40 mL of 50 mg/L Cr(VI) solution at pH 2, agitated at an unsteady magnetic field of 18.99 mT. The result shows that with increasing amount of adsorbent dosage used from 0.01 to 0.05 g, leads to enhance removal of Cr(VI) from 40.9 to 95.5% respectively. This is associated with more active adsorption sites accessible for the Cr(VI) adsorption which is directly equivalent to the adsorbent mass. At small adsorbent dosage, the low efficiency of Cr(VI) removal was due to insufficient active adsorption sites for the adsorbate molecules to occupy.

### 4.3.3 Effect of Initial Cr(VI) Concentration on Adsorption Studies

The initial concentration effect on the induced sorption of the adsorbate by a magnetic field was examined at five different initial concentrations. With the increase in the initial concentration of Cr(VI) (200-700 mg/L), the adsorption efficiency declines shown in the inset of Figure 4.6(c). The available surface area ratio to the initial concentration of Cr(VI) is high at low concentrations of Cr(VI). The diffusion of Cr(VI) ions from the solution to the adsorbent surface is accelerated as the initial concentration is increased, thereby increasing the driving force of concentration gradient. From the experimental study, the amount of Cr(VI) absorbed per unit mass of the adsorbent increased from 100 to 207 mg/g (Figure 4.7c) with an increase in the initial concentrations of Cr(VI) from 200 to 700 mg/L.

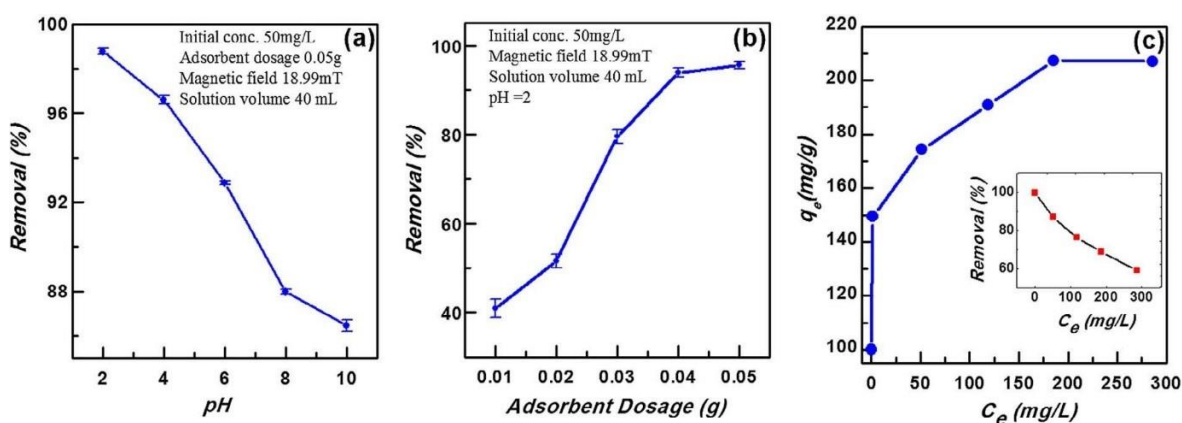


**Figure 4.6** Effect of (a) pH, (b) adsorbent dosage and (c) initial Cr(VI) concentration on the adsorption of Cr(VI) onto PPy/Fe<sub>3</sub>O<sub>4</sub> nanocomposite.

### 4.3.4 Effect of Magnetic Field and Exposure Time

Water treatment by the magnetic field is principally centred on the magnetohydrodynamics. It is assumed that water contains ions and small solid particles having electrostatic charges [16]. Figure 4.8 shows the effect of induced magnetic field and magnetic exposure time on the adsorption of Cr(VI) ions with a magnetic field applied perpendicular to the cleaning chamber containing the Cr(VI) and the adsorbent. It is observed from Figures 4.7(a and b), that Cr(VI) removal efficiency by the adsorbent increased from 91.6 to 99.2% with the increased magnetic field on the system from 11.84 to 18.99 mT. It is obvious that Cr(VI) removal is enhanced from 72.2 to 96.6% with increasing the magnetic exposure from 30 to 60 min. The coagulation of Cr(VI) on PPy/Fe<sub>3</sub>O<sub>4</sub> as a function of magnetic field at pH 2 is described using visual images

obtained from fluid dynamic test shown in Figure S4.3 and Figure S4.4 (Supporting Information). When the surface potential cannot provide enough electrostatic repulsion between particles to stop aggregations, aggregates are formed [51-52]. Image of magnetic nanoparticles aggregation at varying magnetic field is shown in Figure S4.3(a-e). Images of magnetic nanocomposite aggregates were captured at 50 frames rate per second using a CMOS camera in-line with a light source. Enhanced removal of Cr(VI) with increased size of particles aggregates (235-1037 nm) is observed in Figure S4.4, as the induced magnetic field on the magnetic nanocomposite is increased from 10.80 mT (low magnetic field) to 19.01 mT (high magnetic field). Elongated aggregates of particles formed were observed to move in the direction of the field gradient, with their long axis in the local magnetic field direction which is suggestive of the aggregation of particles in chains (Figure S4.3). The sizes of aggregates formed were observed to depend on the magnetic velocity, with fast moving large uniform particles aggregates. Smaller non-uniform particles aggregates travelling with slow drift velocities were also observed at low magnetic field [53]. Chain breakage (aggregates) was noticed to significantly reduces the swimming efficiency of the particles at low magnetic field (Figure S4.3(a)), as the broke segment were unable to rejoin the original chain formation, hence reduced surface area for the adsorption of Cr(VI). The lateral binding of chains driven into contact by magnetic manipulations substantially increases the chain polydispersity as the magnetic field is increased, hence increased chain collision and area of particle interaction (Figure S4.3(e)) [54].

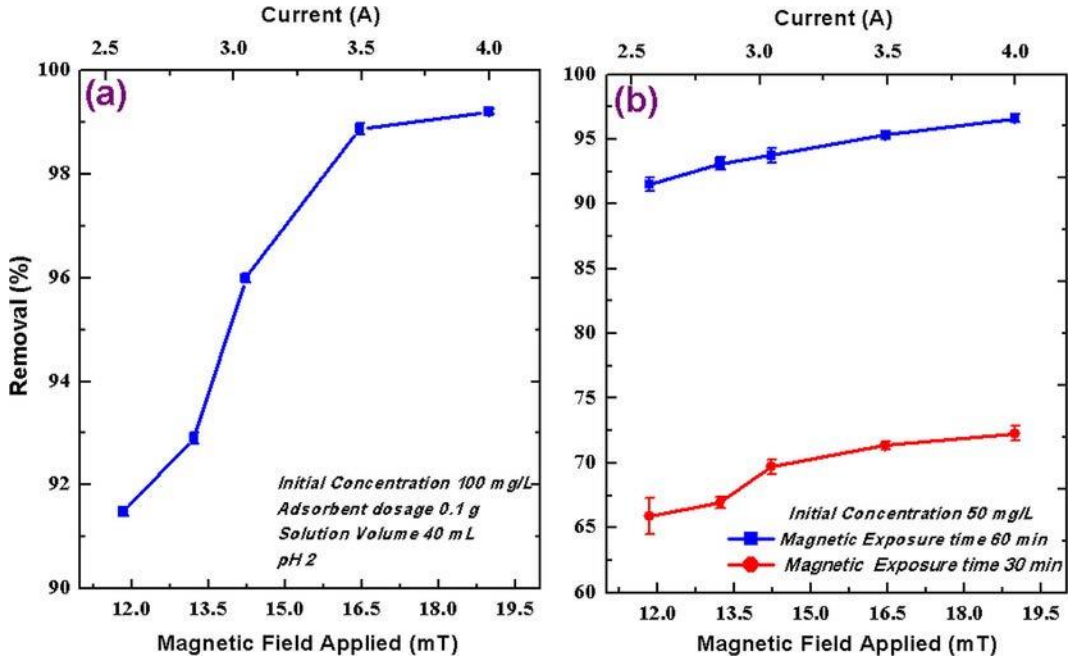


**Figure 4.7** Effect of (a) magnetic field strength and (b) magnetic exposure time on the adsorption of Cr(VI) onto PPy/Fe<sub>3</sub>O<sub>4</sub> nanocomposite.

#### 4.4 Adsorption Isotherms

To describe adsorption processes and mechanisms involved in this Cr(VI) removal studies, different adsorption isotherm models have been used [55]. The obtained experimental data were fitted to the two well-known adsorption isotherm models (Langmuir and Freundlich) to study the mechanism involved during adsorption of Cr(VI) onto PPy/Fe<sub>3</sub>O<sub>4</sub>. Langmuir isotherm model assumes that the adsorption process takes place at the adsorbent surface in a uniform way and that the atoms or ions form a monolayer. The linearized form of the Langmuir equation [56], is represented by equation 4.1;

$$\frac{C_e}{q_e} = \frac{1}{bq_m} + \frac{C_e}{q_m} \quad 4.1$$

The maximum adsorption capacity and the Langmuir constant related to the energy of adsorption are denoted by  $q_e$  (mg/g) and ' $b$ ' (L/mg). A dimensionless equilibrium parameter ( $R_L$ ) is an important characteristic of the Langmuir isotherm, which is defined by equation 4.2;

$$R_L = \frac{1}{1+bC_0} \quad 4.2$$

The initial adsorbate concentration (mg/L) is denoted by  $C_o$  and  $R_L$  values indicate if the adsorption process is irreversible ( $R_L=0$ ), favourable ( $0 < R_L < 1$ ), linear ( $R_L=1$ ), or unfavourable ( $R_L > 1$ ). Adsorption process that occurs on heterogeneous surfaces is described by the Freundlich isotherm model [57]. The postulation that the sorption sites are distributed exponentially with respect to the heat of adsorption results from this model. The Linearize form of Freundlich isotherm [57] can be expressed by the following equation 4.3;

$$\ln q_e = \ln k_F + \frac{1}{n} \ln C_e \quad 4.3$$

The adsorption capacity and intensity of adsorption constants are related by  $k_F$  and  $1/n$ . The related equilibrium parameters for Langmuir and Freundlich isotherms models were determined from the corresponding linear fitting of  $C_e/q_e$  vs.  $C_e$  and  $\ln q_e$  vs.  $\ln C_e$  was shown in Figure 4.8 respectively, at a fluid temperature of  $33 \pm 1$  °C. The results are listed in Table 1. From the regression coefficient values for both isotherm models, the experimental data showed better fitting to Langmuir isotherm model ( $R^2 = 0.9975$ ) with compared to Freundlich isotherm model ( $R^2 = 0.9722$ ). The maximum adsorption capacity using Langmuir model ( $q_m = 208.77$  mg/g at 33 °C) was higher than that obtained from the Freundlich model ( $k_F = 138.29$  mg/g). The Langmuir constant ‘ $b$ ’ (0.2387) obtained from equation 4.1 was used to calculate the feasibility of the adsorption process using the dimensionless separation factor ( $R_L$ ) given by equation 4.2. The calculated  $R_L$  value (Table 4.1) indicates that the Cr(VI) adsorption onto PPy/Fe<sub>3</sub>O<sub>4</sub> nanocomposite is favourable under the Langmuir isotherm model. The adsorption capacity of synthesized PPy/Fe<sub>3</sub>O<sub>4</sub> has been compared with some recently reported adsorbents in Table 4.2. PPy/Fe<sub>3</sub>O<sub>4</sub> composite showed a significantly higher adsorption capacity towards Cr(VI) removal in compare to other reported adsorbents (Table 4.2) [58–61]. Based on the above-reported adsorption capacity values (Table 4.2), PPy/Fe<sub>3</sub>O<sub>4</sub> composite could be considered having a better potentiality for Cr(VI) removal from aqueous medium.

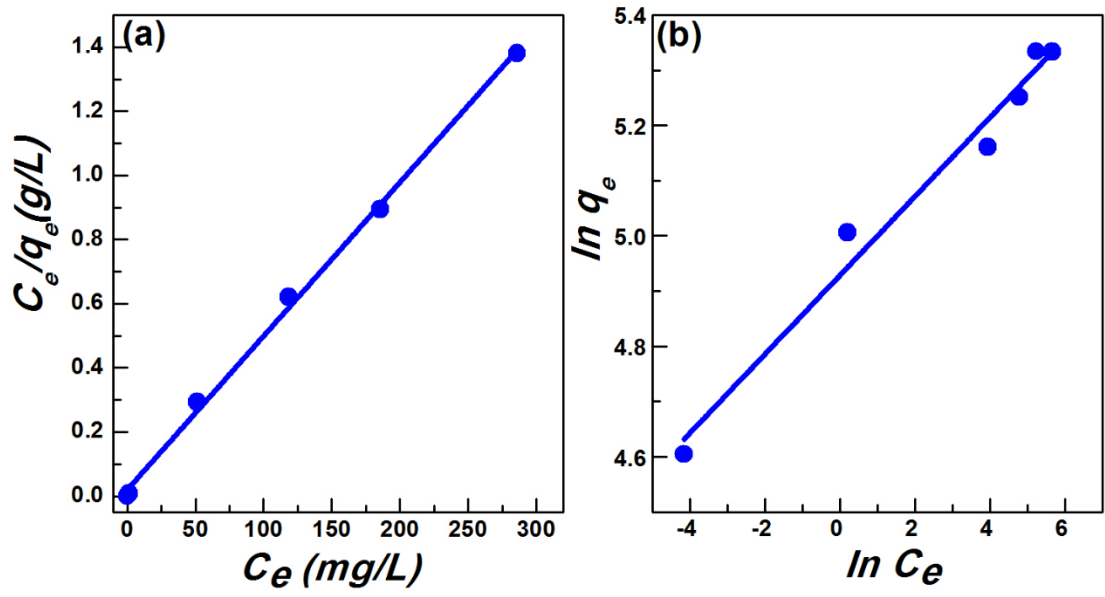


**Figure 4.8** Adsorption isotherm for Cr(VI) removal by PPy/Fe<sub>3</sub>O<sub>4</sub> (a) Langmuir and (b) Freundlich isotherm model.

**Table 4.1** Langmuir and Freundlich constants for adsorption of Cr(VI) ions.

Langmuir isotherm				Freundlich isotherm		
$q_m$ (mg.g <sup>-1</sup> )	$b$ (L.mg <sup>-1</sup> )	$R_L$	$R^2$	$K_F$ (mg.g <sup>-1</sup> )	$n$	$R^2$
208.77	0.2387	0.021	0.9975	138.29	13.99	0.9722

**Table 4.2** Comparison of maximum adsorption capacity of PPy/Fe<sub>3</sub>O<sub>4</sub> against other reported adsorbent for removal of Cr(VI) ion

Adsorbent materials	pH	Adsorption capacity (mg.g <sup>-1</sup> )	References
Magnetic mesoporous carbon incorporated polyaniline (PANI-Fe/OMC)	2.0	172.33	4
Polypyrrole/Fe <sub>3</sub> O <sub>4</sub> magnetic	2.0	200	5
PPY/ $\gamma$ -Fe <sub>2</sub> O <sub>3</sub> MNC	2.0	208.8	8
PANI/ $\gamma$ -Fe <sub>2</sub> O <sub>3</sub> MNC	2.0	195.7	8
Modified Amberlite XAD-4 (MAX-4)	6.9	56.16	9
Nylon 6,6-zirconium(IV)selenite (N6/ZS) fibrous composite	2.0	59.17	45
Halloysite (m-HNTs)	5.0	37.25	49
PANI/humic acid composite	5.0	150	58
SiO <sub>2</sub> -SH/ED3A	1.5–3.0	35	59
Exfoliated polypyrrole-organically modified montmorillonite clay nanocomposite (PPy-OMMT NC)	2.0	119.34	60
Flake-like PANI/montmorillonite NCs	2.0	168	61
PPy/Fe <sub>3</sub> O <sub>4</sub> nanocomposite	2.0	208.77	Present study

## 4.5 Adsorption Kinetics

The performance of an adsorbent is of leading priority of getting an indication of the rate of solute uptake in an adsorption process. The time required for an adsorption process to be completed is determined by the adsorption kinetics. The adsorption dynamics of Cr(VI) to PPy/Fe<sub>3</sub>O<sub>4</sub> composite was evaluated at the unsteady magnetic field of 18.99 mT as well as without any applied magnetic field. The Cr(VI) kinetics sorption on the adsorbent was studied for 150 min and the metal uptake was analysed at different time intervals as shown in Figure 4.9(a). It is observed that the adsorption of Cr(VI) onto the adsorbent increased rapidly in the first 30 min up to equilibrium condition and thereafter adsorption capacity remaining virtually constant up to 120 min of the experimental time. The adsorption dynamic process took 60 min to attain equilibrium without applied magnetic field which is used as a control. The mechanism of Cr(VI) adsorption onto the adsorbent can be understood by using the pseudo-first-order and pseudo-second-order models to fit the kinetics data. The pseudo-first-order [62] and pseudo-second-order [63] kinetics equations can be represented with linearize forms as:

$$\log(q_e - q_t) = \log q_e - \frac{k_1}{2.303} t \quad 4.4$$

$$\frac{t}{q_t} = \frac{1}{k_2 q_e^2} + \frac{t}{q_e} \quad 4.5$$

where  $q_t$  signifies Cr(VI) uptake at time 't',  $k_1$  and  $k_2$  are the pseudo-first and second-order rate constants, respectively. The linear fitting of experimental adsorption data in the pseudo-first-order kinetic [ $\log(q_e - q_t)$  vs  $t$ ] and pseudo-second-order kinetic ( $t/q_t$  vs  $t$ ) equations are shown in Figures 4.9(b and c). All the kinetic parameters of both kinetics models and the correlation coefficient ( $R^2$ ) values are depicted in Table 4.3. The higher correlation coefficients values ( $R^2$  values of 0.9996, 0.9999 and 0.9994) calculated from the pseudo-second-order model indicating that the kinetics is governed by this model. The rate constants ( $k_2$ ) decreases from 0.0106 to 0.0023 mg.g<sup>-1</sup> min<sup>-1</sup> with an increase in the initial concentration of Cr(VI) ions. In addition, the equilibrium Cr(VI) uptake ( $q_e$ ) calculated from the pseudo-second-order model were 50.71, 75.82 and 99.70 mg/g for 50, 100 and 150 mg/L Cr(VI) solution, respectively. On the other hand, without any applied magnetic field (control) the equilibrium Cr(VI) uptake was estimated as only 15.42 mg/g for 50 mg/L Cr(VI) solution. These findings confirm that the Cr(VI) adsorption onto PPy/Fe<sub>3</sub>O<sub>4</sub> nanocomposite is well described using linearize pseudo-second-order model. To identify the importance of diffusion in the adsorption process, the intraparticle diffusion model was applied for the graph plot between amounts of solute adsorbed ( $q_t$ ) against

the square root of the contact time ( $t^{1/2}$ ). The Weber and Morris [64] model for intraparticle diffusion can be expressed using equation 4.6;

$$q_t = k_{id}t^{1/2} + C \quad 4.6$$

where  $k_{id}$  ( $\text{mg g}^{-1} \text{min}^{-1/2}$ ) is an intraparticle diffusion rate constant,  $q_t$  is the amount of Cr(VI) adsorbed at time  $t$  and  $C$  is the thickness of boundary layer, obtained by extrapolation of the linear portion of the plot of  $q_t$  vs  $t^{1/2}$ . If the plot of  $q_t$  versus  $t^{1/2}$  gives a straight line and the straight line passes through the origin, then the sorption process is controlled by intraparticle diffusion only. However, if the data exhibit multi-linear plots, then the sorption process is controlled by two or more steps. The first sharper portion of the curve is the external surface adsorption or instantaneous adsorption stage. The second portion is the gradual adsorption stage, where the intraparticle diffusion is rate limited. The non-linearity of the intra-particle diffusion model in Figure 4.9(d), shows that more than one process is involved in the adsorption process. The intraparticle diffusion model is linked by two straight lines during the Cr(VI) adsorption process, indicating the adsorption process was controlled by both surface and intraparticle diffusion processes. None of the two plots passed through the origin. These shows that intraparticle diffusion was not the only controlling factor in the adsorption of Cr(VI) by PPy/Fe<sub>3</sub>O<sub>4</sub>. The intraparticle diffusion parameters are determined from the Figure 4.9(d) and summarized in Table 4.3.

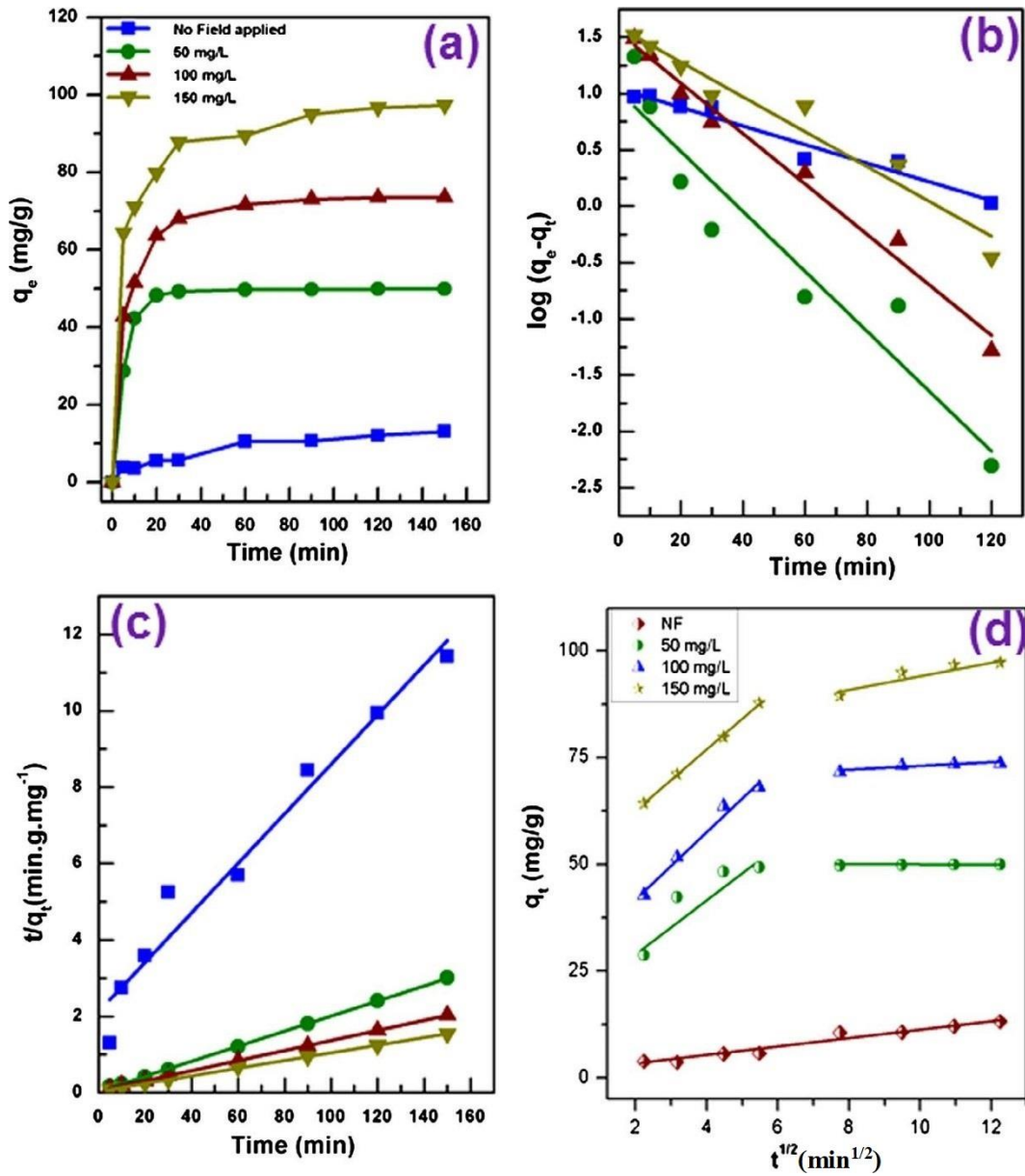


**Figure 4.9**(a) Kinetics for Cr(VI) adsorption onto PPy/Fe<sub>3</sub>O<sub>4</sub>, (b) Pseudo first order (c) Pseudo-second order and (d) intraparticle diffusion model for Cr(VI) adsorption onto PPy/Fe<sub>3</sub>O<sub>4</sub>.

**Table 4.3.** Kinetics parameters for adsorption of Cr(VI) ions from aqueous medium.

Pseudo-first-order kinetic model				Pseudo-second-order kinetic model		
$C_o$ (mg.L <sup>-1</sup> )	$q_e$ (mg.g <sup>-1</sup> )	$k_1$ (min <sup>-1</sup> )	$R^2$	$q_e$ (mg.g <sup>-1</sup> )	$k_2$ (mg.g <sup>-1</sup> .min <sup>-1</sup> )	$R^2$
50	10.45	0.0614	0.8956	50.71	0.0106	0.9996
100	34.80	0.0516	0.9822	75.82	0.0034	0.9999
150	38.92	0.0357	0.9420	99.70	0.0023	0.9994
No Magnetic Field Applied						
50	11.03	0.1905	0.9498	15.42	0.002	0.9576
Weber-Morris model (Intraparticle diffusion model)						
$C_o$ (mg-L <sup>-1</sup> )	$k_{ip1}$ (mg.g <sup>-1</sup> min <sup>-1/2</sup> )	$k_{ip2}$ (mg.g <sup>-1</sup> min <sup>-1/2</sup> )	$C_1$	$C_2$	$(R_1)^2$	$(R_2)^2$
50	6.05	0.039	18.91	49.43	0.7505	0.8299
100	7.97	0.443	25.93	25.93	0.9706	0.7919
150	7.1	1.728	48.27	48.27	0.9984	0.8231
No Magnetic Field Applied						
50	1.017	--	1.058	--	0.9523	--

#### 4.6 Regeneration Study

For a large-scale application, regeneration and recycling are one of the vital features of a progressive adsorbent. The ability to reuse an adsorbent is a crucial parameter for decontaminating process from the economic point of view [65]. Therefore, to perform regeneration study, the adsorbed Cr(VI) on the surface of the PPy/Fe<sub>3</sub>O<sub>4</sub> is initially treated with 0.1 (M) NaOH and subsequently treated with 2M of HCl. After washing, PPy/Fe<sub>3</sub>O<sub>4</sub> composite was dried in a vacuum oven for further use as an adsorbent for Cr(VI) ions removal from aqueous solution.

Four consecutive adsorption-desorption cycles were carried out at pH 2. The results are shown in Figure 4.10. It has been found that PPy/Fe<sub>3</sub>O<sub>4</sub> could preserve high adsorption efficiency up to four consecutive adsorption-desorption cycles, with minimum adsorption capacity of 49.7 mg/g. Thus, it can be concluded that PPy/Fe<sub>3</sub>O<sub>4</sub> magnetic nanocomposite showed excellent recycling ability for the treatment of Cr(VI) from aqueous solution.

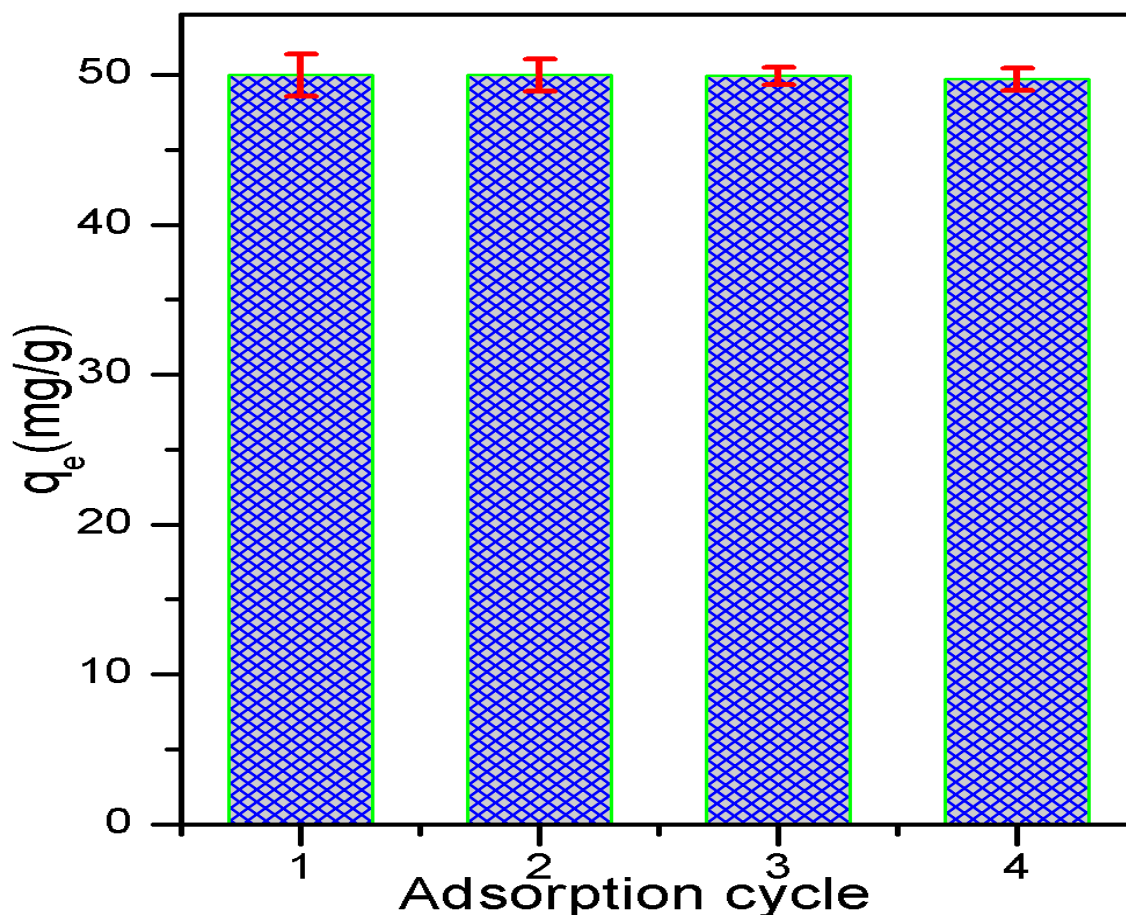


**Figure 4.10** Cr(VI) Adsorption-desorption cycles.

#### 4.7 Conclusion

In this study, the feasibility of Cr(VI) removal from aqueous solutions under the influence of an unsteady magnetic field using synthesized conducting polymer-based magnetic nanocomposite was successfully demonstrated. The synergistic effect of applied magnetic field during adsorption process enhanced the Cr(VI) removal efficiency many-fold. The Cr(VI) removal by PPy/Fe<sub>3</sub>O<sub>4</sub> composite was strongly dependent on initial pH, adsorbent dosage, initial Cr(VI) ion concentration, applied magnetic field strength, and exposure time. The PPy/Fe<sub>3</sub>O<sub>4</sub> composite exhibited a better Cr(VI) removal performance at highly acidic condition (pH=2.0). The

adsorption result was better fitted with pseudo-second-order kinetic model and PPy/Fe<sub>3</sub>O<sub>4</sub> adsorbent follow the Langmuir isotherm with a calculated maximum adsorption capacity of 208.77 mg/g. This study has been found to be a suitable method for eliminating Cr(VI) ions from aqueous solution with the aid of an unsteady magnetic field on magnetic nanoparticles.

## 4.8 References

- [1] J. F. D. Brito, L. D. O. Ferreira, M. C. R. Pereira, J. P. D. Silva and T. Ramalho, **2012**, *Water Air Soil Pollut.* 223, 3545–3551.
- [2] K. Bhattacharya, D. Parasar, B. Mondal, and P. Deb, **2015**, *Sci. Rep.* 5, 1–9.
- [3] J. Hu, D. Zhao and X. Wang, **2011**, *Water. Sci. Technol.* 63, 917–923.
- [4] Y. El-Sherif, J. Y. Farah, E. Girgis, and O. A. Mohamed, **2013**, *J. Appl. Sci. Res.* 9, 1564–1572.
- [5] G. Yang, L. Tang, Y. Cai, G. Zeng, P. Guo, G. Chen, Y. Zhou, J. Tang, J. Chen, and W. Xiong, **2014**, *RSC Adv.* 4, 58362–58371.
- [6] M. Bhaumik, A. Maity, V. V. Srinivasu, and M.S. Onyango, **2011**, *J. Hazard. Mater.* 190, 381–390.
- [7] J. Wang, L. Zhao, W. Duan, L. Han, and Y. Chen, **2012**, *Ind. Eng. Chem. Res.* 51, 13655–13662.
- [8] A. E. Chavez-Guajardo, J. C. Medina-Liomas, L. Maqueira, C. A. S. Andrade, K. G. B. Alves, and C. P. De Melo, **2015**, *Chem. Eng. J.* 281, 826–836.
- [9] A. Bhatti, S. Memon, N. Memon, A. A. Bhatti, and I. B. Solangi, **2017**, *Arab. J. Chem.* 10, S1111–1118.
- [10] G. B. Cotton, H. B. Eldredge, and J. D. Navratil, **2003**, *Nukleonika*, 48, 17–23.
- [11] C. J. Quinn, T. C. Molden, and C. H. Sanderson, **1997**, *Iron Steel Eng.* 47–53.
- [12] L. Duan, S. Guo, and J. Yang, **2012**, *Adv. Chem. Eng. Sci.* 2, 101–107.
- [13] J. Song, H. Kong, and J. Jang, **2011**, *J. Colloid Interface Sci.* 359, 505–511.
- [14] J. Bogatin, N. P. Bondarenko, E. Z. Gak, E. E. Rokhinson, and I. P. Ananyev, **1999**, *Sci. Technol.* 33, 1280–1285.
- [15] R. A. Barrett, and S. A. Parsons, **1998**, *Water Res.* 32, 609–612.
- [16] Y. Ali, R. Samaneh, R. Zohre, and J. Mostafa, **2014**, *Curr. World Environ.* 9, 1008–1016.

- [17] R. R. Mohammed, M. R. Ketabchi, and G. McKay, **2014**, *Chem. Eng. J.* 243, 31–42.
- [18] L. Holysz, A. Szczes, and E. Chibowski, **2007**, *J. Colloid Interface Sci.* 316, 996–1002.
- [19] A. Asfaram, M. Ghaedi, A. Goudarzi, and M. Rajabi, **2015**, *Dalton Trans.* 44, 14707–14723.
- [20] K. Higashitani, A. Kage, S. Katamura, K. Imai, and S. Hatade, **1993**, *J. Colloid Interface Sci.* 156, 90–95.
- [21] E. Sharifpour, H. Z. Khafri, M. Ghaedi, A. Asfaram, and R. Jannesar, **2018**, *Ultrason. Sonochem.* 40, 373–382.
- [22] H. Mazaheri, M. Ghaedi, M. H. Ahmadi Azqhandi, and A. Asfaram, **2017**, *Phys. Chem. Chem. Phys.* 19, 11299–11317.
- [23] E. A. Dil, M. Ghaedi, G. R. Ghezelbash, A. Asfaram, and M. K. Purkait, **2017**, *J. Ind. Eng. Chem.* 48, 162–172.
- [24] F. F. Fondeur, D. T. Hobbs, and S. D. Fink, **2010**, *Sep. Sci. Technol.* 45, 1876–1879.
- [25] P. He, X. Zhang, X. Peng, J. Wu, N. Chen, and J. Ren, **2015**, *Fuel*, 162, 211–214.
- [26] R. Cai, H. Yang, J. He, and W. Zhu, **2009**, *J. Mol. Struct.* 938, 15–19.
- [27] L. Zhao, K. Ma, and Z. Yang, **2015**, *Int. J. Mol. Sci.* 16, 8454–8489.
- [28] N. S. Zaidi, J. Sohaili, K. Muda, and M. Sillanpaa, **2013**, *Sep. Purif. Rev.* 43, 206–240.
- [29] A. A. Tireli, F. C. F. Marcos, L. F. Oliveira, L. D. R. Guimaraes, M. C. Guerreiro, and J. P. Silva, **2014**, *Appl. Clay Sci.* 97, 1–7.
- [30] M. F. Niam, F. Othman, J. Sohaili, and Z. Fauzia, **2006**, *Int. Conf. Nat. Resour. Eng. Technol.* 384–393.
- [31] X. Zhang, J. Zhang, W. Song, and Z. Liu, **2006**, *J. Phys. Chem. B* 110, 1158–1165.
- [32] Y. Ma, S. Jiang, G. Jian, H. Tao, L. Yu, X. Wang, X. Wang, J. Zhu, Z. Hu, and Y. Chen, **2009**, *Energy Environ. Sci.* 2, 224–229.
- [33] H. Zhang, X. Zhong, J. J. Xu, and H. Y. Chen, **2008**, *Langmuir*, 24, 13748–13752.

- [34] W. Chen, X. Li, G. Xue, Z. Wang, and W. Zou, **2003**, *Appl. Surf. Sci.* 218, 215–221.
- [35] E. A. Sanches, S. F. Alves, J. C. Soares, A. M. D. Silva, C. G. D. Silva, S. M. D. Souza, H. O. D. Frota, **2015**, *J. Nanomater.* 16, 301.
- [36] K. Cheah, M. Forsyth, and V.T. Truong, **1998**, *Synth. Met.* 94, 215–219.
- [37] P. Zhang, Z. Mo, L. Han, X. Zhu, B. Wang, and C. Zhang, **2014**, *Ind. Eng. Chem. Res.* 53, 8057–8061.
- [38] J. Wang, P. Wang, H. Wang, J. Dong, W. Chen, X. Wang, S. Wang, T. Hayat, A. Alsaedi, and X. Wang, **2017**, *ACS Sustain. Chem. Eng.* 5, 7165–7174.
- [39] B. Chertok, A. J. Cole, A. E. David, and V. C. Yang, **2010**, *Mol. Pharm.* 7, 375–385.
- [40] Y. Koseoglu, F. Yildiz, D. K. Kim, M. Muhammed, and B. Aktas, **2004**, *Phys. Stat. Sol.* 1, 3511–3515.
- [41] J. B. Mamani, L. F. Gamarra, and G. E. D. S. Brito, **2014**, *Mater. Res.* 17, 542–549.
- [42] M. Bhaumik, T. Y. Leswif, A. Maity, V. V. Srinivasu, and M. A. Onyango, **2011**, *J. Hazard. Mater.* 186, 150–159.
- [43] O. A. Kuznetsov, O. N. Sorokina, V. G. Leontiev, O. A. Shlyakhtin, A. L. Kovarski, and A. A. Kuznetsov, **2007**, *J. Magn. Magn. Mater.* 311, 204–207.
- [44] J. Dui, G. Zhu, and S. Zhou, **2013**, *ACS Appl. Mater. Interface*, 5, 10081–10089.
- [45] R.A.K. Rao, A.A. Khan, and N. Alam, **2016**, *Anal. Methods*, 8, 869–879.
- [46] A. Eskandarpour, K. Sassa, Y. Bando, M. Okido, and S. Asai, **2006**, *Mater. Trans.* 47, 1832–1837.
- [47] Y. Zou, X. Wang, Y. Ai, Y. Liu, J. Li, Y. Ji, and X. Wang, **2016**, *Environ. Sci. Technol.* 50, 3658–3667.
- [48] W. Yao, J. Wang, P. Wang, X. Wang, S. Yu, Y. Zou, J. Hou, T. Hayat, A. Alsaedi, and X. Wang, **2017**, *Environ. Pollut.* 229, 827–836.
- [49] P. Luo, J. Zhang, B. Zhang, J. Wang, Y. Zhao, and J. Liu, **2011**, *Ind. Eng. Chem. Res.* 50, 10246–10252.

- [50] H. Gu, S. B. Rapole, Y. Huang, D. Cao, Z. Luo, S. Wei, and Z. Guo, **2013**, *J. Mater. Chem. A*, 1, 2011–2021.
- [51] X. Liu, J. Li, Y. Huang, X. Wang, X. Zhang, and X. Wang, **2017**, *Environ. Sci. Technol.* 51, 6156–6164.
- [52] J. Wang, Y. Li, W. Chen, J. Peng, J. Hu, Z. Chen, T. Wen, S. Lu, Y. Chen, T. Hayat, B. Ahmad, and X. Wang, **2017**, *Chem. Eng. J.* 309, 445–453.
- [53] G. De Las Cuevas, J. Faraudo, and J. Camacho, **2008**, *J. Phys. Chem. C*, 112, 945–950.
- [54] R. J. Wilson, W. Hu, C. W. P. Fu, A. L. Koh, R. S. Gaster, C.M. Earhart, A. Fu, S. C. Heilshorn, R. Sinclair, and S. X. Wang, **2009**, *J. Magn. Magn. Mater.* 321, 1452–1458.
- [55] B. Nayak, A. Samant, A. K. Naik, and P. K. Misra, **2015**, *Appl. Sci. Adv. Mater. Int.* 1, 215–219.
- [56] Langmuir, **1916**, *J. Am. Chem. Soc.* 38, 2221–2295.
- [57] H. M. F. Freundlich, **1906**, *J. Phys. Chem.* 57, 1100–1107.
- [58] Q. Li, L. Sun, Y. Zhang, Y. Qian, and J. Zhai, **2011**, *Desalination*, 266, 188–194.
- [59] N. Zaitseva, V. Zaitsev, and A. Walcarius, **2013**, *J. Hazard. Mater.* 250–251, 454–461.
- [60] K. Z. Setshedi, M. Bhaumik, S. Songwane, M. S. Onyango, and A. Maity, **2013**, *Chem. Eng. J.* 222, 186–197.
- [61] J. Chen, X. Hong, Y. Zhao, Y. Xia, D. Li, and Q. Zhang, **2013**, *J. Mater. Sci.* 48, 7708–7717.
- [62] S. Lagergren, **1898**, *Sven. Vetenskapsakad. Handl.* 24, 1–39.
- [63] Y. S. Ho, and G. McKay, **1999**, *Process Biochem.* 34, 451–465.
- [64] W. J. Weber Jr., and J. C. Morris, **1963**, *J. Sanit. Div. Am. Soc. Civ. Eng.* 83, 31–59.
- [65] N. Zare, M. M. Lakouraj, and A. Ramezani, **2015**, *Adv. Polym. Technol.*; 34.

## CHAPTER FIVE

### Result II: Removal of Fluoride Ions from Wastewater Influenced by Rotating Magnetic Field

#### 5.1 Results and Discussion

##### 5.1.1 Characterization of adsorbent

The diffraction pattern of the adsorbent before and after adsorption of fluoride (PPy/Fe<sub>3</sub>O<sub>4</sub>), Fe<sub>3</sub>O<sub>4</sub> and PPy is shown in Figure 5.1. A broad diffraction peak, which is a distinctive peak of pure PPy is located at  $2\theta = 24.95$  degree, which shows the amorphous nature of pure PPy Figure 5.1(b) [1]. In Figure 5.1a, the observed diffraction peaks at 18.31(111), 30.09(220), 35.52(311), 43.23(400), 53.67(422), 57.24(511), 62.67(440), 65.90 (440), 71.13 (442), 74.12 (533) and 75.23 (622) confirms that the main phase of the nanocomposite is the crystalline Fe<sub>3</sub>O<sub>4</sub> [2]. The observed diffraction peaks of Fe<sub>3</sub>O<sub>4</sub> (Figure 5.1(a)) are confirmed by the JCPDS file database (PDF No. 75-0449). Figure 5.1(c), it is observed from the XRD result that the Fe<sub>3</sub>O<sub>4</sub> particles exist in the polymer matrix (Figure 5.1(c)). There is no visible change in the XRD crystalline structure of the nanocomposite before and after adsorption of fluoride ions influenced by the magnetic field.

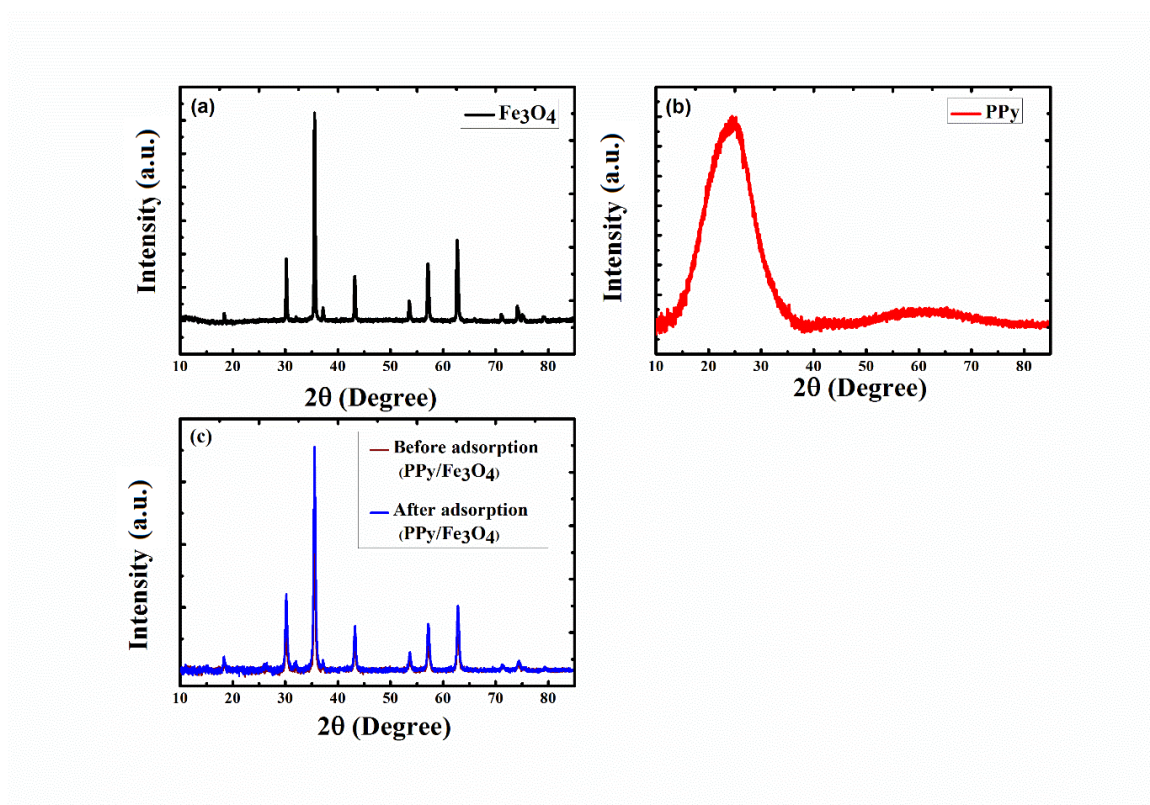


**Figure 5.1** XRD of (a) Magnetite (Fe<sub>3</sub>O<sub>4</sub>), (b) polypyrrole and (c) magnetic nanocomposite before and after adsorption.

Infrared spectroscopy of PPy/Fe<sub>3</sub>O<sub>4</sub> nanocomposite before and after fluoride ions adsorption under the influence of a magnetic field, Fe<sub>3</sub>O<sub>4</sub>, and PPy were performed to determine the functional groups on each material are shown in Figure 5.2. The spectra of the magnetic adsorbent have characteristic peaks of the oxidised PPy and Fe<sub>3</sub>O<sub>4</sub>. The peak observed at 554 cm<sup>-1</sup> was due to the vibration of the Fe-O band, which is a characteristic peak of Fe<sub>3</sub>O<sub>4</sub> (Figure 5.3a) [3]. The adsorption peak observed at 1537 cm<sup>-1</sup>, 1454 cm<sup>-1</sup>, 1288 cm<sup>-1</sup>, 1162 cm<sup>-1</sup>, 1040 cm<sup>-1</sup>, 962 cm<sup>-1</sup> and 777 cm<sup>-1</sup> were characteristic peak of PPy/Fe<sub>3</sub>O<sub>4</sub> nanocomposite before fluoride adsorption. After adsorption, a shift to higher adsorption peaks values for PPy/Fe<sub>3</sub>O<sub>4</sub> nanocomposite was observed, with the peaks of the PPy component shifting to 1545cm<sup>-1</sup>, 1472cm<sup>-1</sup>, 1294 cm<sup>-1</sup>, 1167 cm<sup>-1</sup>, 1040 cm<sup>-1</sup>, 960 cm<sup>-1</sup> and 785 cm<sup>-1</sup>. These were attributed to C=C stretch, C-N stretch, C-H or C-N in-plane deformation, C-C vibration, C-H in-plane deformation, C-C out of plane deformation vibration and out of plane C-H vibration of pyrrole. The characteristic peaks of pure PPy were observed at adsorption peaks of 1568, 1481, 1296, 1198, 1047, 926 and 797 cm<sup>-1</sup>, which is also observed in PPy/Fe<sub>3</sub>O<sub>4</sub> nanocomposite (Figure 5.2(a)). However, the shift in the characteristic peaks to 5-18 cm<sup>-1</sup> when compared

with those of PPy/Fe<sub>3</sub>O<sub>4</sub> before adsorption shows the interaction between the Fe<sub>3</sub>O<sub>4</sub> nanoparticles and polymer matrix [3-5].

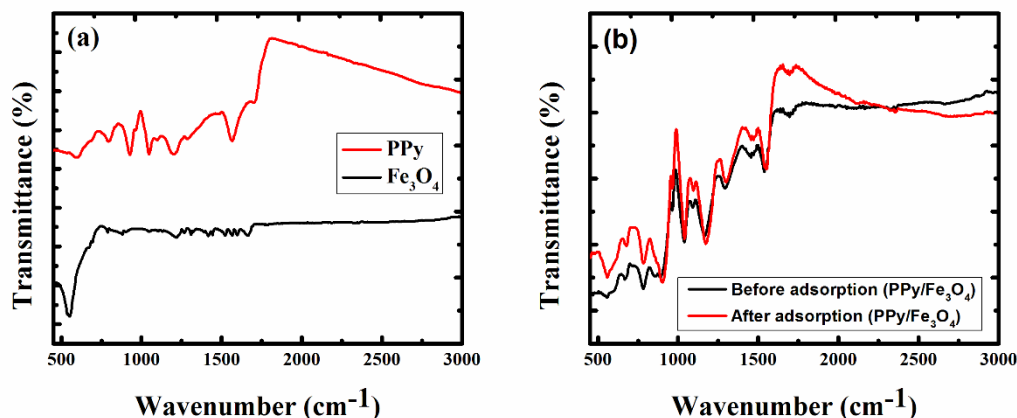


**Figure 5.2** FTIR spectra of (a) PPy and Fe<sub>3</sub>O<sub>4</sub> and (b) Polypyrrole magnetic nanocomposite before and after adsorption of fluoride.

The TEM images of the adsorbent are shown in Figure 5.3(a) and (b). The distribution of the particle size ranges from 5-40 nm, with a predominant average particle size of  $5 \pm 5.7$  nm was determined using ImageJ software shown in the inset of Figure 5.3(a). The average particle size distribution shown in the inset of Figure 5.3(a) was fitted using the Gaussian function. It is observed from the TEM image in Figure 5.3(b), that Fe<sub>3</sub>O<sub>4</sub> nanoparticles (core) is enclosed by the polymer medium of PPy (shell), with the PPy/Fe<sub>3</sub>O<sub>4</sub> nanocomposite being polydispersed. The morphology of the adsorbent shows a core-shell structure with the crystalline Fe<sub>3</sub>O<sub>4</sub> magnetic core being enclosed by the PPy shell. The nanocomposite is observed to be spherical in shape, with a smooth uniform morphology, caused by the deagglomerating effect of the polymer coating the nanoparticles. In addition, the energy-dispersive X-ray analysis (EDX) spectrum of PPy/Fe<sub>3</sub>O<sub>4</sub> confirms the existence of C, O, N, Cl and Fe as the predominant elements into magnetic nanocomposite (Figure 5.3(c)).

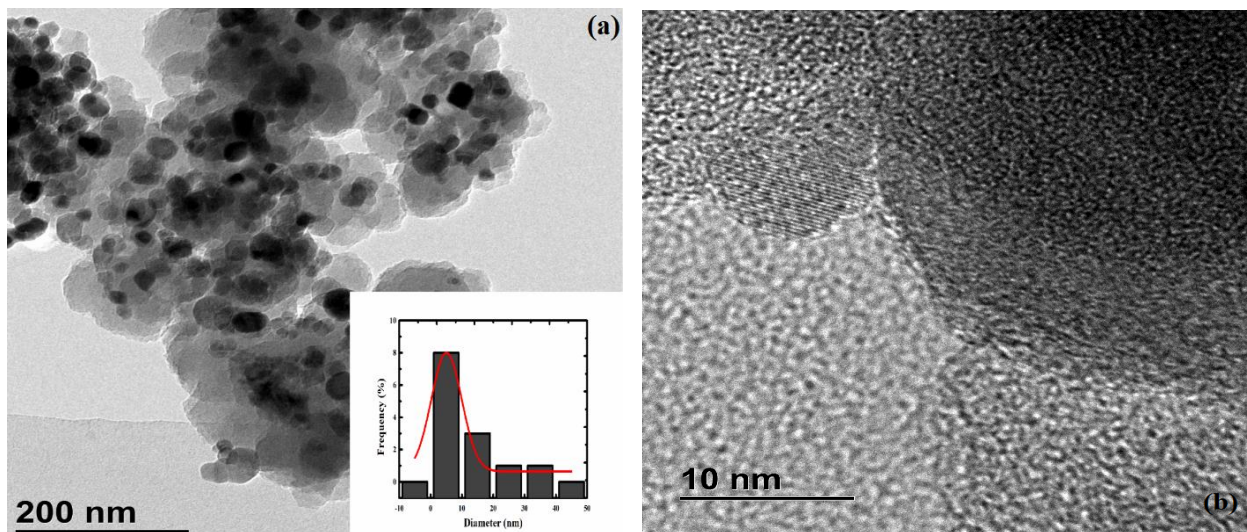


**Figure 5.3** (a) TEM image of polypyrrole magnetic nanocomposite (Inset: Histogram showing the size distribution of the nanocomposite using ImageJ software), (b) TEM image showing the core-shell structure of polypyrrole magnetic nanocomposite and (c) EDX spectrum of PPy/Fe<sub>3</sub>O<sub>4</sub> nanoadsorbent.

Nitrogen adsorption-desorption isotherm of PPy/Fe<sub>3</sub>O<sub>4</sub> was performed to study the surface areas (m<sup>2</sup>/g), pore diameter (nm) and pore volume (cm<sup>3</sup>/g) of the prepared magnetic nanocomposite (Figure 5.4). The result reflects a typical type-IV adsorption-desorption isotherm curve with a hysteresis loop, which indicates the mesoporous characteristics of PPy/Fe<sub>3</sub>O<sub>4</sub> composite

as categorized by IUPAC. The adsorbent has a hysteresis loop that closes at the relative pressure of 0.88 P/P<sub>0</sub> [6-7]. The BET analysis revealed that the specific surface area, BJH cumulative volume of pores and BJH average pore diameter of PPy/Fe<sub>3</sub>O<sub>4</sub> were calculated to be 28.77 m<sup>2</sup>/g, 0.06 cm<sup>3</sup>/g and 15.82 nm, respectively.

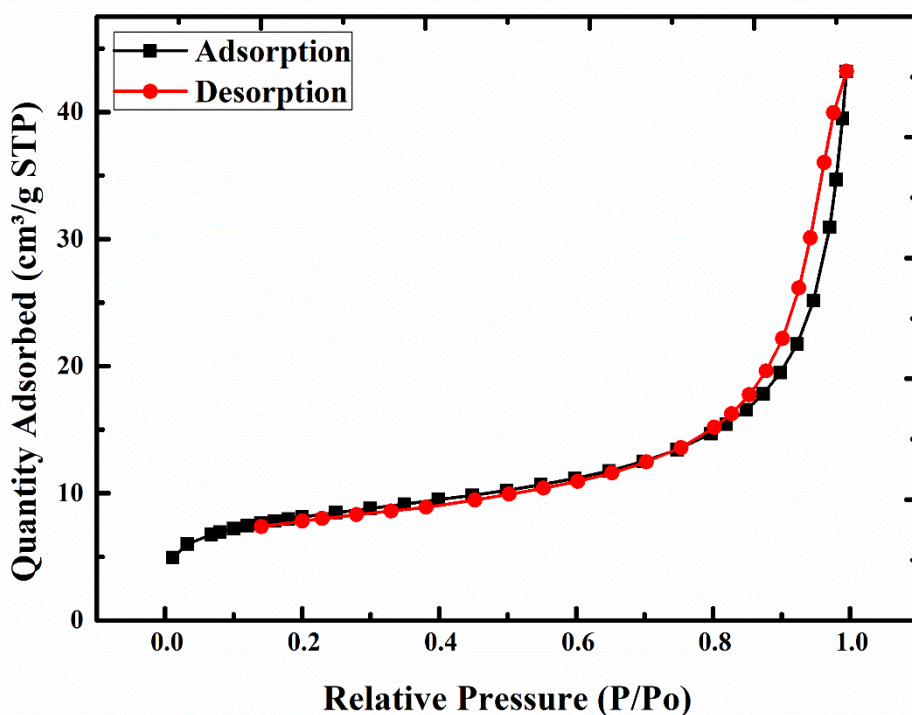


**Figure 5.4** N<sub>2</sub> adsorption-desorption isotherms for PPy/Fe<sub>3</sub>O<sub>4</sub> nano-adsorbent.

Figure 5.5 shows the ESR spectra of the adsorbent carried out at room temperature. The shape of the lines is symmetrical, with a resonance signal that is wide and broad. The linewidth value of about 1200 Gauss is also observed. In the identification of the signal, determining the g-factor of the unknown signal can be of valuable assistance. The g-factor for Fe<sup>3+</sup> is determined to be between 1.4-3.1 for low spin and 2.0-9.7 for high spin complexes. The g-factor of the adsorbent was found to be approximately 2.25 Gauss using  $g = \frac{h\nu}{\beta H_r}$ , which is due to Fe<sup>3+</sup> spin interactions. Such interactions show a superparamagnetic behaviour characterised by the presence of clusters. The shapes and the field location are identical to a standard magnetic nanoparticle suspension and are consistent with ESR spectra of superparamagnetic iron oxide nanoparticles [8-11]. The line shape of nanocomposite when fitted to Gaussian and Lorentzian

functions, the line shape was observed to have a mixture of 59 % Gaussian and 41 % Lorentzian functions. (Figures 5.5(b and c)). The dominant Gaussian fit is characteristic of ferromagnetic resonance indicating that the predominant portion of the PPy/Fe<sub>3</sub>O<sub>4</sub> nanocomposite is magnetic, as this confirms that the predominated fraction of the PPy/Fe<sub>3</sub>O<sub>4</sub> is magnetic [12-13].

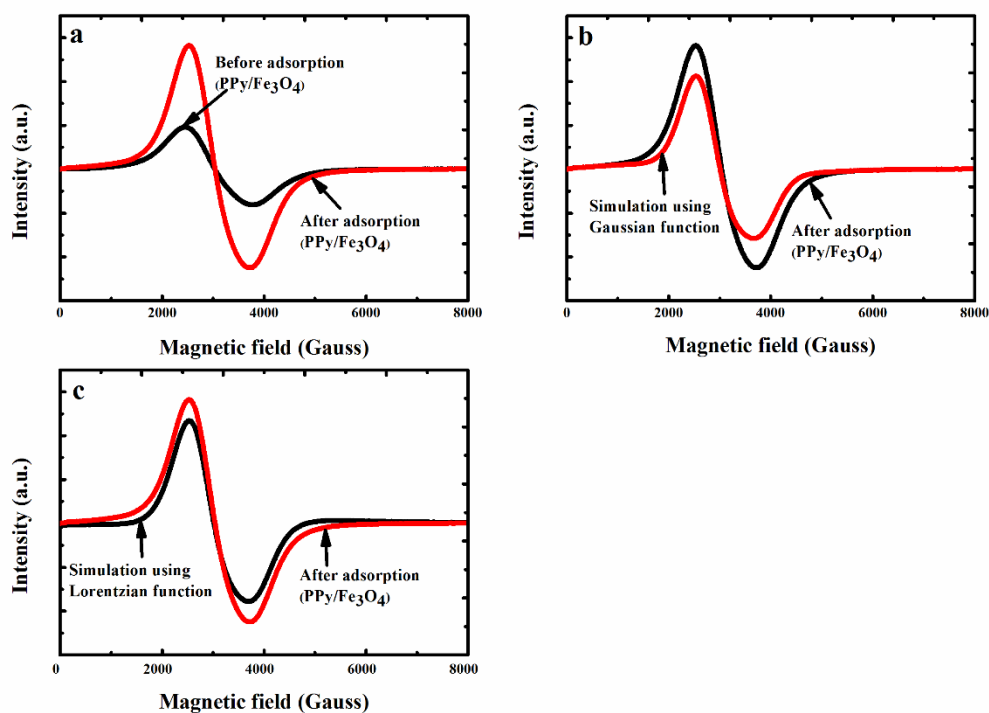


**Figure 5.5** ESR spectra of PPy/Fe<sub>3</sub>O<sub>4</sub> (a) before and after adsorption of fluoride, (b) Simulation of ESR spectra of PPy/Fe<sub>3</sub>O<sub>4</sub> after induced adsorption of fluoride using Gaussian function and (c) Simulation of ESR spectra of PPy/Fe<sub>3</sub>O<sub>4</sub> after induced adsorption of fluoride using Lorentzian function

Figure 5.6 shows the magnetisation curve of the adsorbent measured at 300 K at an interval of -10 000 to 10 000 Oe. A magnetisation hysteresis loop with a zero-remanence magnetisation ( $H_r$ ), zero coercivity field ( $H_c$ ) and a saturation magnetisation ( $M_s$ ) of 23 emu/g was observed. The absent of hysteresis loops with a zero-remanence and coercivity confirms that the adsorbent is superparamagnetic. For such materials, when a magnetic field is applied, there is a free rotation of the magnetic moment of the particles when the blocking temperature is exceeded [14]. The saturation magnetisation of the nanocomposite adsorbent is also observed to be lower than those of magnetite (iron oxide). The surface magnetic anisotropy is changed by the polypyrrole acting as a surfactant, leading to an increase in the disorientation of the

surface spins resulting in a decrease of the magnetic moment of the nanocomposite. The change in the quantum size effects and surface area increase of the nanosized magnetite particles creates the superparamagnetic material [15-17].

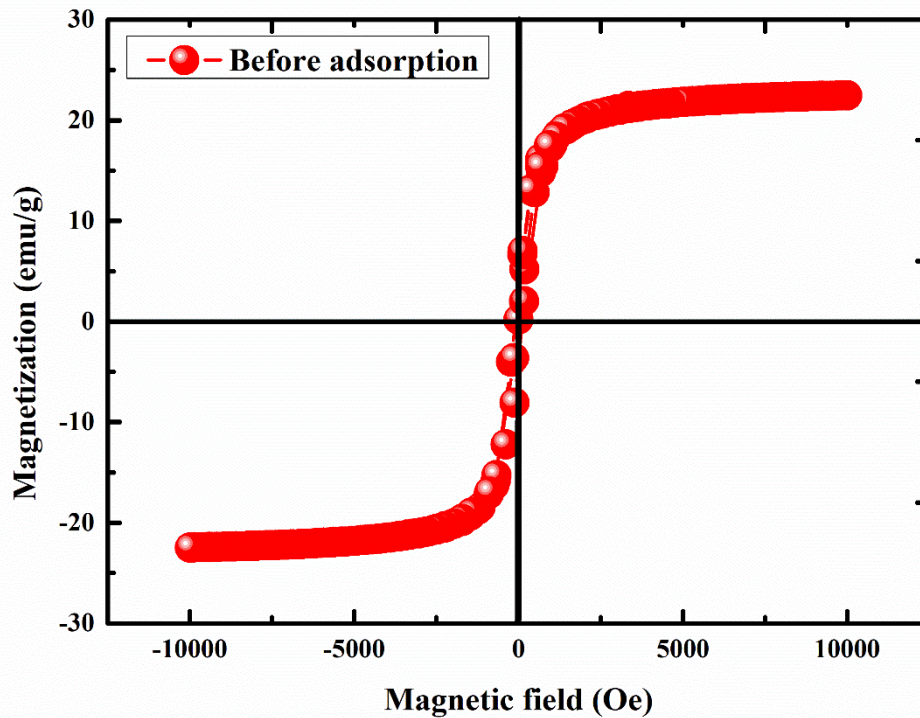


**Figure 5.6** Magnetisation curve of magnetic nanocomposite at room temperature.

## 5.2 Results and Discussion

### 5.2.1 pH Effect on Adsorption of Fluoride

The most important parameter that affects the adsorption process is the solution pH, as it affects speciation of metal ions, the surface charge of adsorbent and the degree of sorbent ionisation [46 18]. The pH effect on the adsorption of fluoride ions from aqueous solution using a rotating magnetic field of 18.99 mT were studied at pH range of 2-10 using 0.1 M NaOH or HCl (Figure 5.7(a)). The surface charge of the adsorbent is affected by the solution pH, which is related directly to the competition ability of  $H^+$  with adsorbate ions for the adsorbent surface sites [19]. Fluoride removal influenced by magnetic field torque on magnetic nanocomposite was observed to increase as the pH of fluoride solution is increased from pH 2-6. A decreased in the amount fluoride removed is subsequently observed as the fluoride pH is increased from pH

6-10, with a maximum fluoride removal of 78.4% observed at pH 6. In acidic medium, the surface of the adsorbent is protonated and hence maximum removal in the acidic medium. This is attributed to the gradual increase in the attractive force between the charged surface and negatively charged fluoride ions [20]. Low removal of fluoride ions at low pH range was due to the reduced availability of free fluoride ions in the solution. The slight reduction of fluoride removal at higher pH results from the competitive interaction between hydroxyl ions and fluoride anions for the adsorption sites on the adsorbent [21].

### **5.2.2 Adsorbent Dosage Effect on Fluoride Adsorption**

The adsorbent dosage effect on the removal of fluoride ions (10 mg/L) was evaluated at an adsorbent dosage range of 0.025-0.150 g, with the excitation of the magnetic nanocomposite at a magnetic field of 18.99 mT is shown in Figure 5.7(b). There is a significant increase in the amount of fluoride ion removed from 34.5-81.5% with an equivalent increase in the adsorbent dosage. This increase removal of fluoride ions is due to increased adsorption sites on the surface of the adsorbent and sorptive surface area as the adsorbent dosage is increased.

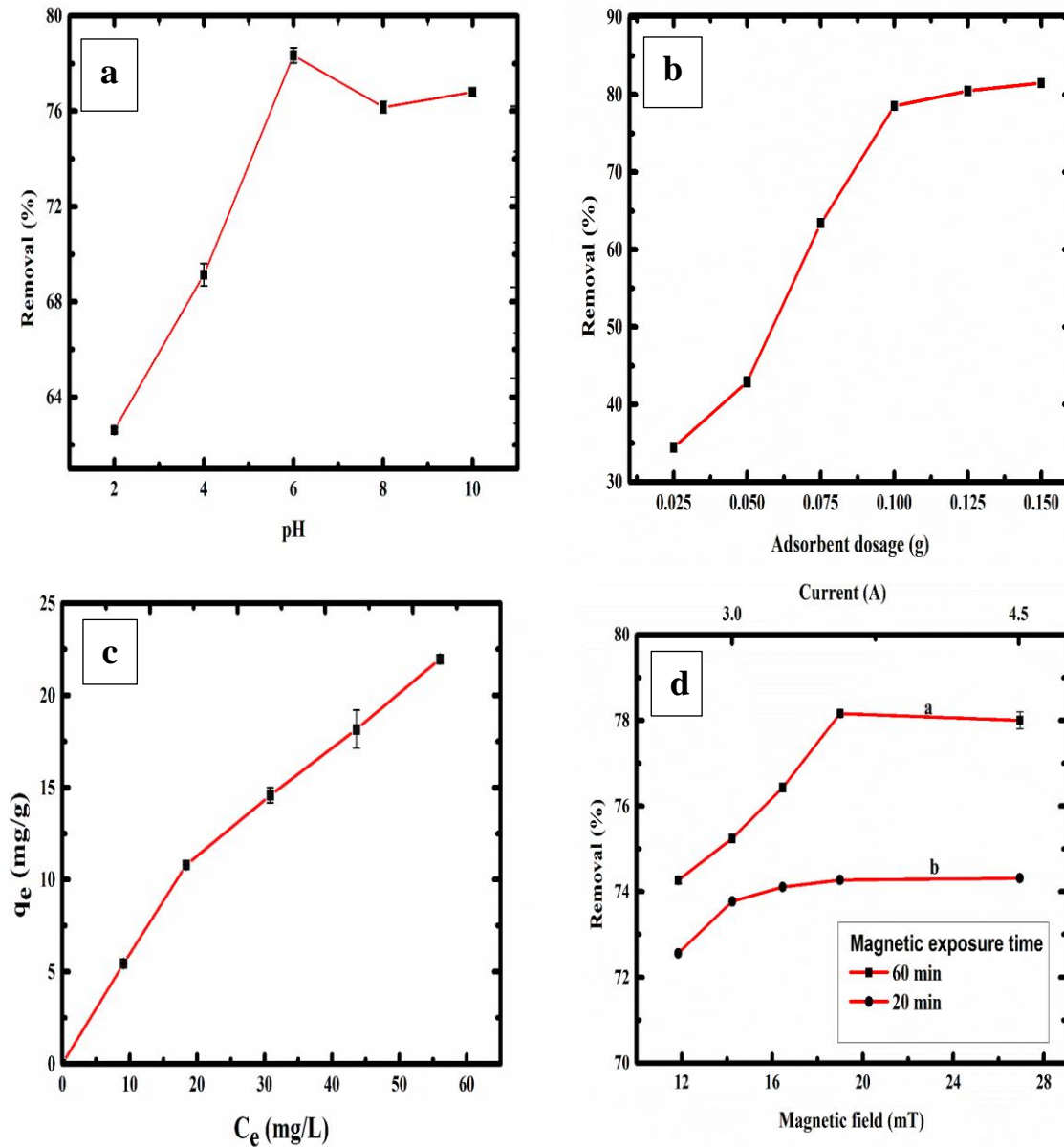
### **5.2.3 Initial Concentration Effect on the Adsorption of Fluoride**

Figure 5.7(c) shows the effect of initial fluoride concentrations range of 20-100 mg/L adsorption by polypyrrole magnetic nanocomposite at a magnetic field of 18.99 mT. The adsorption capacity of the nanocomposite for fluoride removal increased with a rise in the initial fluoride concentrations. The driving force needed to overcome the resistance of the mass transfer of fluoride ion between the aqueous and solid phase is provided by the initial fluoride concentrations, resulting in increased equilibrium sorption until adsorbent saturation is achieved [12].

### **5.2.4 Effect of Magnetic Field on the Fluoride Adsorption at Magnetic Exposure Time**

Figure 5.7(d) shows the effect of magnetic field range of 11.84-26.94 mT on the adsorption of fluoride ions at a magnetic exposure time of 20 and 60 min. An enhanced percentage of fluoride ions adsorbed by the adsorbent is observed as the magnetic field intensity is increased (74.2-78.2%). There is a slight drop in the amount of fluoride ions removal as the magnetic field is increased from 18.99-26.94 mT with the removal of 78% observed. With the increase in the magnetic exposure time from 20 to 60 min, a maximum removal of 74.3 and 78.2% at a fixed magnetic field of 18.99 mT are observed. Increase magnetic field leads to a higher removal of fluoride, which was due to increased force and torque on the particles at high magnetic field.

The aggregation of particles results in increased chain collision and area of particle interaction. Increased fluoride removal is also related to the surface morphology of the adsorbent becoming heterogeneous when exposed to a magnetic field, as this lead to an increase in the surface area of the adsorbent [22-24].



**Figure 5.7** Effect of (a) pH, (b) adsorbent dosage, (c) initial fluoride concentration and (d) magnetic field strength and magnetic exposure time on the adsorption of fluoride onto PPy/Fe<sub>3</sub>O<sub>4</sub> nanocomposite.

### 5.3 Adsorption Isotherms

Information about the surface properties of the adsorbent, behaviour of the adsorbent and isotherm studies were measured in magnetic field presence shown in Figure 5.8, using the Langmuir and Freundlich isotherm models. Both models were fitted to the experimental data.

The Langmuir isotherm describes the adsorption of a solute from a liquid solution, while the Freundlich isotherm is an empirical equation used to describe the adsorption on the heterogeneous surface [25]. The linearized form of both isotherm models are shown in equations 5.1 and 5.2:

$$\frac{C_e}{q_e} = \frac{1}{q_m b} + \frac{C_e}{q_m} \quad 5.1$$

$$\ln q_e = \ln K_F + \frac{1}{n} \ln C_e \quad 5.2$$

where  $q_m$  in mg/g represents the maximum monolayer adsorption capacity,  $C_e$  in mg/L represents the equilibrium fluoride concentration and  $b$  in L/mg represents the Langmuir isotherm constant relating to the affinity of the binding sites at a given temperature.  $K_F$  and  $n$  are the Freundlich isotherm constants related to the adsorption capacity and the adsorption intensity of the adsorbent. The essential characteristics of the Langmuir isotherm model can also be described in terms of a dimensionless constant referred to as the separation factor ( $R_L$ ) defined in equation 5.3;

$$R_L = \frac{1}{(1+bC_o)} \quad 5.3$$

where  $C_o$  in mg/L is the initial concentration of fluoride in the solution. From Figure 5.8, both isotherm models fitted well with the experimental data as shown in Table 5.1. The correlation coefficients ( $R^2$ ) of the Freundlich isotherm model (0.98381) was found to be greater than the Langmuir isotherm model (0.95316). These show that the adsorption of fluoride ion takes place on the heterogeneous surface of the adsorbent. The maximum adsorption capacity for fluoride ions in the presence of magnetic field was found to be 47.99 mg/g based on the Langmuir isotherm model. The adsorption capacity of the adsorbent calculated from the linearized Freundlich isotherm model was 1.11740. The adsorption intensity ( $1/n$ ) value from the Freundlich isotherm model was 0.74532 at 31°C, which shows favourable adsorption of fluoride ions by the magnetic nanocomposite under the influence of magnetic field.

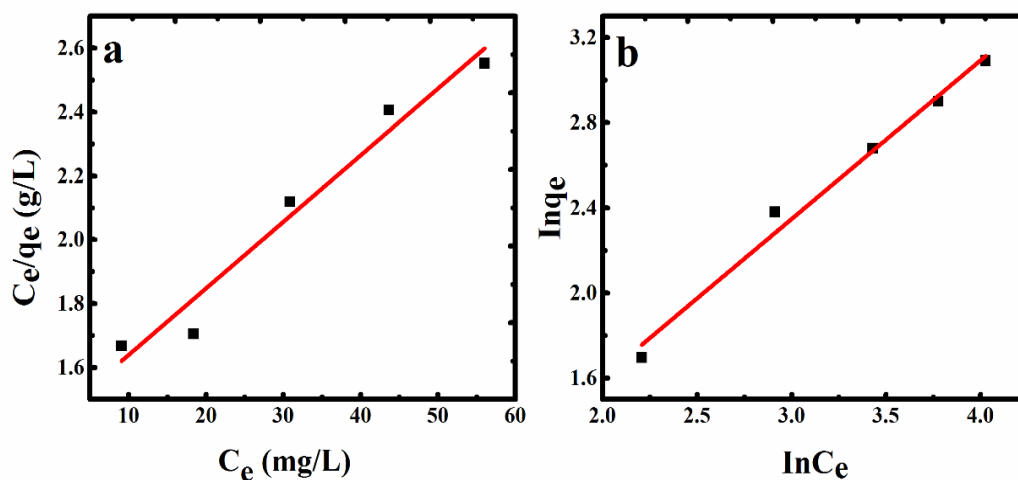


**Figure 5.8** Adsorption isotherm for fluoride removal by PPy/Fe<sub>3</sub>O<sub>4</sub> (a) Langmuir and (b) Freundlich isotherm model.

**Table 5.1:** Langmuir and Freundlich constants for adsorption of Cr(VI) ions.

Langmuir isotherm			Freundlich isotherm		
$q_m$ (mg/g)	$b$ (L/mg)	$R^2$	$K_L$ (mg/g)	$1/n$	$R^2$
47.99	0.0146	0.95316	1.11740	0.74532	0.98381

#### 5.4 Adsorption Kinetics

An important parameter that represents the adsorption efficiency is the adsorption kinetics [53, 26]. The most significant factor in the design of adsorption systems is the estimation of the rate at which adsorption process takes place for certain systems [27]. The rate of fluoride adsorption onto polypyrrole magnetic nanocomposite plotted as a function of initial fluoride concentration is shown in Figure 5.9(a). Adsorption was quite fast, reaching equilibrium at 10 min, as the adsorption capacity of the adsorbent increased with increase in time. The time-dependent adsorption data were analysed using the linearized form of the pseudo-first and second-order kinetic models were used. The linearize forms of the pseudo-first and second-order kinetic models are shown in equations 5.4 and 5.5:

$$\text{Log } (q_e - q_t) = \text{Log } (q_e) - \left(\frac{k_1}{2.303}\right)t \quad 5.4$$

$$\frac{t}{q_t} = \frac{1}{k_2 q_e^2} + \frac{t}{q_e} \quad 5.5$$

where  $k_1$ ,  $k_2$ , are the rate constants of adsorption for the pseudo-first and second-order kinetic models in  $\text{g mg}^{-1}\text{min}^{-1}$ ,  $q_t$  is the number of fluoride ions adsorbed by the adsorbent at time  $t$  in  $\text{mg g}^{-1}$  and  $q_e$  is the adsorption capacity at equilibrium in  $\text{mg.g}^{-1}$ .

The correlation coefficient values ( $R^2$ ) obtained for fluoride removal using the pseudo-second kinetic model were in the range of 0.99933 and 0.99999, with this model best describing the adsorption process taking place in the presence of magnetic field. The results show a decrease in the  $k_2$  values with increase in the  $q_e$  values as the initial fluoride concentrations are increased under magnetic field influence (6.02-24.70  $\text{mg/g}$ ) and 3.70  $\text{mg/g}$  in the absence of magnetic field. The estimated theoretical value of  $q_e$  (second-order model) was in excellent agreement with the  $q_e$  values obtained experimentally. Therefore the adsorption of fluoride ions onto polypyrrole magnetic nanocomposite in the presence of magnetic field is controlled kinetically assuming a pseudo-second-order model rather than the pseudo-first-order model, as the second-order model accounts for chemical adsorption as the rate-limiting process. This suggests that owing to a good degree of mixing and extent dispersion of nanoparticles using a magnetic field, adsorption is only affected by two mechanisms; rapid adsorption due to electrostatic attraction followed by slow gradual adsorption of pollutants onto nanoparticle surface by complexation as seen in Table 5.2 [28].

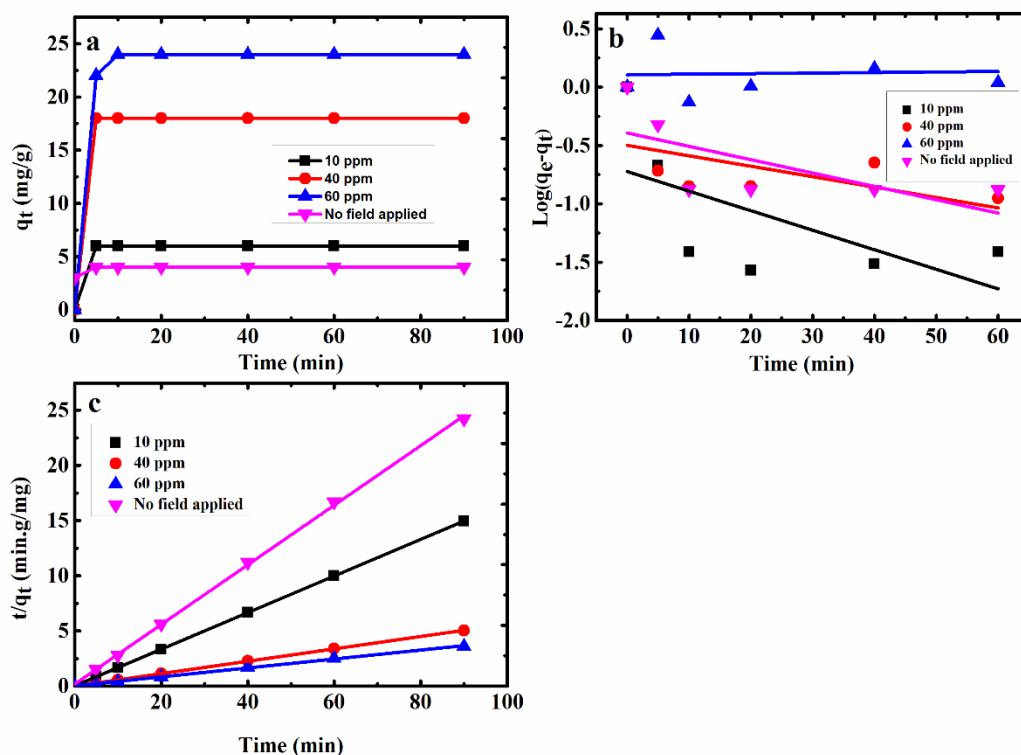


**Figure 5.9**(a) Kinetics for fluoride adsorption onto PPy/Fe<sub>3</sub>O<sub>4</sub>, (b) Pseudo-first-order and (c) Pseudo-second-order

**Table 5.2:** Estimated values of the kinetic parameters of the pseudo-first-order and pseudo-second-order models for the adsorptive removal of fluoride ions onto polypyrrole magnetic nanocomposite at different initial fluoride concentrations. Other experimental parameters are  $T = 301$  K,  $\text{pH} = 6$ , and magnetic field = 18.99 mT.

Conc. (mg/L)	Pseudo-first-order			Pseudo-second-order		
	$q_e$ (mg/g)	$k_1$ (1/min)	$R^2$	$q_e$ (mg/g)	$k_2$ (1/min)	$R^2$
10 (MF)	0.19	0.0395	0.24813	6.02	1.9809	0.99999
40 (MF)	0.33	0.0186	0.11862	17.81	0.4249	0.99996
60 (MF)	1.44	0.0048	0.04730	24.70	0.0573	0.99864
10 (NF)	0.03	0.4037	0.29894	3.70	0.4400	0.99930

## **5.5 Conclusion**

The magnetic field is considered as a potential technology to deal with the harmful effects of fluoride ions in wastewater. From the results obtained, a significant increase in the number of fluoride ions removed increased with the magnetic field and magnetic exposure time, with percentage removal of 74.2-78.2% (60 mins exposure time) and 72.6-74.3% (20 mins exposure time) observed at pH 6. It is also observed from the kinetics and adsorption isotherms models that the magnetic field significantly enhanced adsorption capacity for fluoride ions with the pseudo-second-order and Freundlich isotherm models best describing the adsorption process.

## 5.6 References

- [1] J. Guo, H. Gu, H. Wei, Q. Zhang, N. Haldolaarachchige, Y. Li, D. P. Young, S. Wei, and Z. Guo, **2013**, *J. of Physical Chemistry*, 117, 10191-10202.
- [2] C. Zhang, L. Chen, T. Wang, C. Su, and Y. Jin, **2014**, *Applied Surface Science*, 317, 552-559.
- [3] R. Turcu, O. Pana, A. Nan, I. Craciunescu, O. Chauvet, and C. Payen, **2008**, *J. of Physics D: Applied Physics*, 41, 245002.
- [4] S. Kasisomayajula, N. Jadhav, and V. J. Gelling, **2016**, *RSC. Adv*, 6, 967-977.
- [5] F. Khalilian, M. Rezaee, and M. K. Gorgabi, **2015**, *Analytical Methods*, 7, 2182-2189.
- [6] B. Kakavandi, R. R. Kalantary, A. J. Jafari, S. Nasser, A. Ameri, A. Esrafil, and A. Azari, **2015**, *Clean soil air water*, 43, 1157-1166.
- [7] M. H. Mohamed, M. Pirlot, M. K. Danquah, and L. D. Wilson, **2017**, *J. of Materials Science and Chemical Engineering*, 5, 12
- [8] R. Sivashankar, A. B. Sathya V. Vasatharaj, and V. Sivasubramanian, **2014**, *Environmental Nanotechnology, Monitoring, and Management*, 1, 36-49,
- [9] B. Chertok, A. J. Cole, A. E. David, and V. C. Yang, **2010**, *Molecular Pharmaceutics*, 7, 375-385,
- [10] Y. Koseoglu, F. Yildiz, D. K. Kim, M. Muhammed, and B. Aktas, **2004**, *Phys Stat. Sol;* 12, 3511-3515,
- [11] J. B. Mamani, I. F. Gamarra, and G. E. De Souza Brito, **2014**, *Materials Research*, 17, 542-549.
- [12] M. Bhaumik, T. Y. Leswif, A. Maity, V. V. Srinivasu, and M. A. Onyango, **2011**, *J. of Hazardous Materials*, 186, 150-159,
- [13] O. A. Kuznetsov, O. N. Sorokina, V. G. Leontiev, O. A. Shlyakhtin, A. L. Kovarski, and A. A. Kuznetsov, **2007**, *J. of Magnetism and Magnetic Materials*, 311, 204-207.

- [14] A. Nan, R. Turcu, I. Bratu, C. Leostean, O. Chauvet, E. Gautron, and J. Liebscher, **2010**, *Arkivoc*, 10, 185-198.
- [15] T. Theivasanthi, and M. Alagar, **2014**, arXiv preprint arXiv: 1402-1431.
- [16] M. Muliwa, and M. S. Onyango, **2014**, In *Proceedings of Sustainable Research and Innovation*, 5, 83-90.
- [17] N. Shamim, L. Hong, K. Hidajat, and M. S. Uddin, **2006**, *J. of Colloid and Interface Science*, 304, 1-8.
- [18] L. Lv, N. Chen, C. Feng, J. Zhang and M. Li, **2017**, *RSC Advances*, 7, 27992-28000.
- [19] R. Bhaumik, N. K. Mondal, B. Das, P. Roy, K. C. Pal, C. Das, A. Banerjee, and J. K. Datta, **2012**, *J. of Chemistry*, 9, 1457-1480.
- [20] V. Tomar, S. Prasad, and D. Kumar, **2013**, *Microchemical J.*, 2013, 111, 116-124.
- [21] M. Jokar, R. Foroutani, M. H. Safaralizadeh, and K. Farhadi, **2014**, *Annual Research and Review in Biology*, 4, 3262.
- [22] X. Hao, H. Liu, G. Zhang, H. Zou, Y. Zhang, M. Zhou, and Y. Gu, **2012**, *Applied Clay Science*, 55, 177-180.
- [23] L. I. Bel'chinskaya, N. A. Khodosova, and L. A. Bityutskaya, **2009**, *Protection of Metals and Physical Chemistry of Surfaces*, 45, 203-206.
- [24] W. Shen, Q. Guo, X. Yang, Y. Liu, Y. Song, and J. Cheng, **2006**, *Adsorption Science and Technology*, 24, 433-438.
- [25] G. Li, W. Zhu, C. Zhang, S. Zhang, L. Liu, L. Zhu, and W. Zhao, **2016**, *Bioresources Technology*, 206, 16-22.
- [26] X. Zhao, J. Wang, F. Wu, T. Wang, Y. Cai, Y. Shi, and G. Jiang, **2010**, *J. of Hazardous Materials*, 173, 102-109.
- [27] I. Brnardic, L. Curkovic, T. Sofilic, D. M. Paviovic, G. Matijasic, I. Grcic, and A. Radenovic, **2017**, *Clean-Soil, Air, Water*, 45, 1-9.

- [28] N. N. Nassar, L. A. Arar, N. N. Marei, M. M. A Ghanim, M. S. Dwekat, and S. H. Sawalha, **2014**, Environmental Nanotechnology, Monitoring and Management, 1-2, 14–23.

## CHAPTER SIX

### **Result III: Removal of Hexavalent Chromium from Wastewater using PPy/Fe<sub>3</sub>O<sub>4</sub> Magnetic Nanocomposite Influenced by Rotating Magnetic Field from Two Pole Three-Phase Induction Motor (Accepted for publication by Journal of Physics: Conference Series).**

**Abstract.** The influence of varying rotating magnetic field using a 2-pole three-phase induction motor on the removal of hexavalent chromium ions from wastewater using polypyrrole magnetic nanocomposite was explored in this study. Hexavalent chromium removal in this study was observed to be pH dependent under the influence of rotating magnetic field, as the percentage removal of hexavalent chromium decreased with increase in pH. The percentage amount of hexavalent chromium ions removed from the aqueous solution increased as the rotating magnetic field intensity was increased from 8.96-12.15 mT in the anticlockwise direction and 10.10-13.38 mT in the clockwise direction with maximum removals of 73% and 81% observed.

### **6.1 Introduction**

Water bodies contaminated with toxic materials like heavy metals are prevalent in emerging countries due to increased industrial activities [1]. The occurrence of high concentration of heavy metals like chromium, mercury, cadmium, nickel, cobalt, and lead in natural water supplies and manufacturing wastewater streams is a crucial health and environmental issue due to their high toxicity and bioaccumulation through food chain [2].

Hexavalent chromium is termed a group 'A' human carcinogen owing to its mutagenic and carcinogenic properties. Its concentration in industrial wastewater ranges from 0.5-270,000 mg/L, with the tolerance limit for hexavalent chromium released into the inland surface water and potable water are 0.1 and 0.05 mg/L [3-4]. For the different existing treatment technologies for the removal of toxic heavy metals, adsorption, chemical precipitation, ion exchange, coagulation, reverse osmosis, electrolysis and membrane process are extensively used [5].

To reduce environmental problems resulting from heavy metals contamination, it is necessary to create new residue treatment methods, such that the residue recovery occurs in a faster and efficient way [6]. Magnetic field exposed method have progressively drawn attention to improving the adsorption and separation. Magnetism is an exclusive property that supports water purification as it influences the physical and chemical properties of the contaminants in an aqueous solution. [1, 7-8].

Magnetic field exposure method has shown its capacity for enhancing the removal of contaminants from water as static magnetization is appropriate, simple and cost-effective. Basically, the behaviour and physic-chemical properties of water are affected by a magnetic field. With the application of magnetic field to water, the magnetic field within changes the rates of chemical reactions due to the existence of competing reactions of dissolution and precipitation of dissolved salts facilitates the formation and decomposition of colloidal complexes and improves electro-coagulation followed by sedimentation and crystallization of scaling salts of  $\text{Ca}^{2+}$ ,  $\text{Mg}^{2+}$ ,  $\text{Fe}^{2+}$  and  $\text{Fe}^{3+}$  [9-10].

Increase in the application of an electromagnetic field in different fields including therapeutic and diagnostic medicine, environment management and industrial procedures have been witnessed in recent years [11]. The magnetic field was reported to have significant effects on scale prevention, [12-14], suspended particle separation [15], adsorption of zinc, copper (II), industrial waste, colour removal, total suspended solids, uranium and strontium [16-21].

The motivation for this study is to evaluate the effect of magnetic field on polypyrrole magnetic nanocomposite for the adsorption of Cr(VI) ion. The goal is to develop a water treatment procedure with the information obtained, which would be useful for further application in the treatment of industrial effluents.

## **6.2 Results and Discussion**

### **6.2.1 Characterization of PPy/Fe<sub>3</sub>O<sub>4</sub>**

The size and surface morphology of PPy/Fe<sub>3</sub>O<sub>4</sub> nanocomposite were observed using HR-TEM and SEM (Figure 6.1). The HR-TEM image shown in Figure 6.1(a) confirms that the nanocomposites had a regular uniform spherical morphology with average diameters of  $10.3 \pm 8.3$  nm. The surface analysis results (Figure 6.2(b)), shows that the Fe<sub>3</sub>O<sub>4</sub> nanoparticles are fully covered and stabilised by the PPy microspheres in the PPy/Fe<sub>3</sub>O<sub>4</sub> composite matrix. In addition, the energy-dispersive X-ray analysis (EDX) spectrum of PPy/Fe<sub>3</sub>O<sub>4</sub> confirms the presence of C, O, N, Cl and Fe as the major elements in the polypyrrole magnetic nanocomposite (Figure 6.1(c)). After Cr(VI) adsorption, an additional Cr peak along with C, O, N, Cl and Fe is observed. This confirms the adsorption of Cr(VI) ion onto PPy/Fe<sub>3</sub>O<sub>4</sub> nanocomposite surface (Figure 6.1(d)).

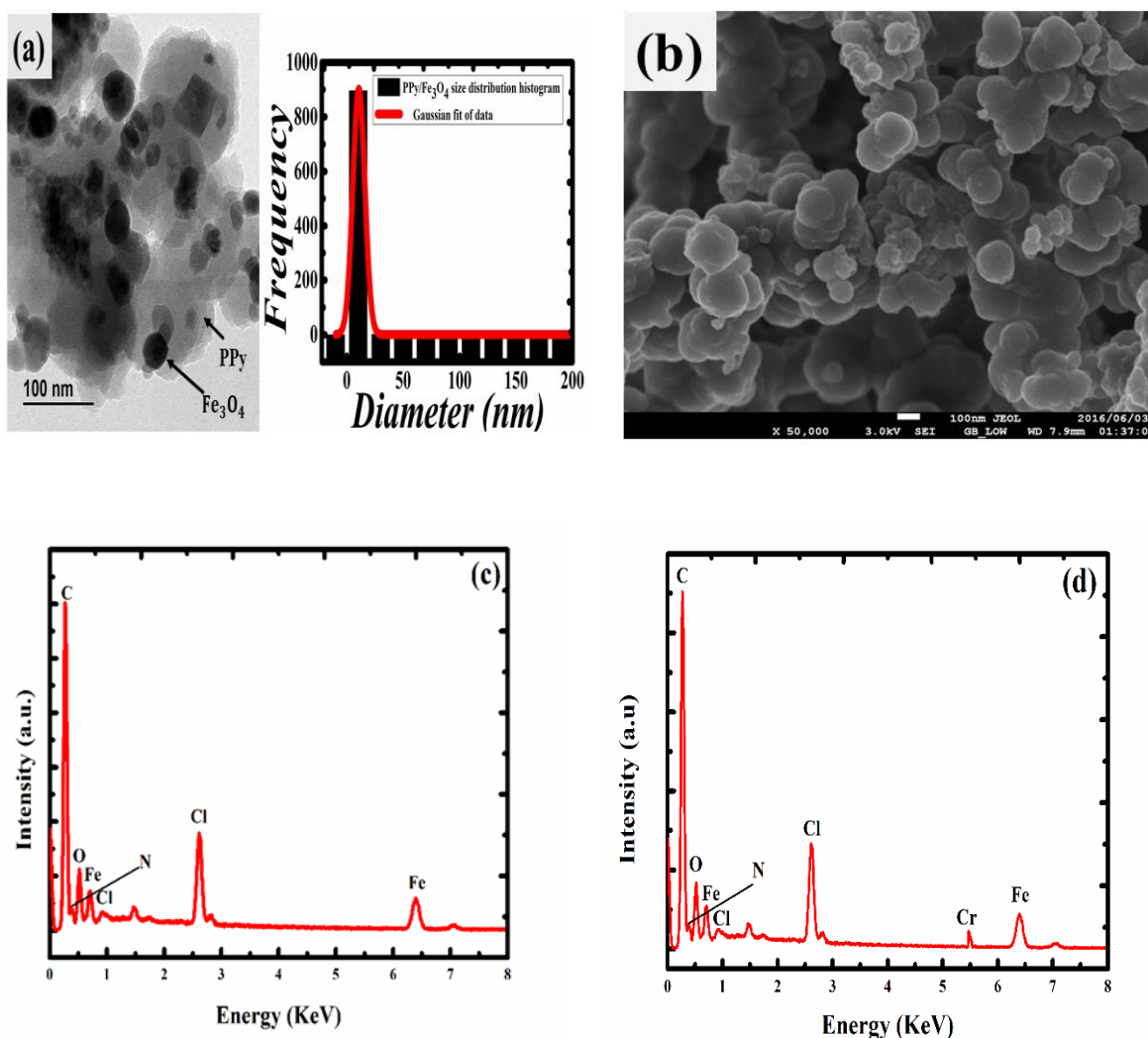


**Figure 6.1**(a) HR-TEM image of polypyrrole magnetic nanocomposite (b) SEM image of polypyrrole magnetic nanocomposite (c) EDX spectrum of PPy/Fe<sub>3</sub>O<sub>4</sub> nanocomposite before hexavalent chromium adsorption and (d) EDX spectrum of PPy/Fe<sub>3</sub>O<sub>4</sub> magnetic nanocomposite after hexavalent chromium adsorption.

The nitrogen adsorption-desorption isotherm for the nanocomposite is shown in Figure 6.2. The result reveals a hysteresis loop that closes near a relative pressure of 0.82. This is indicative of mesoporous characteristics of the nanocomposite. The adsorption-desorption isotherm shape indicates a typical type-IV, which agrees with the nature of mesoporous adsorbents according to IUPAC [22]. The specific surface area of the nanocomposite was 28.77 m<sup>2</sup>/g, while the BJH cumulative volume of pores and BJH average pore diameter were determined to be 0.06 cm<sup>3</sup>/g and 15.82 nm, respectively.

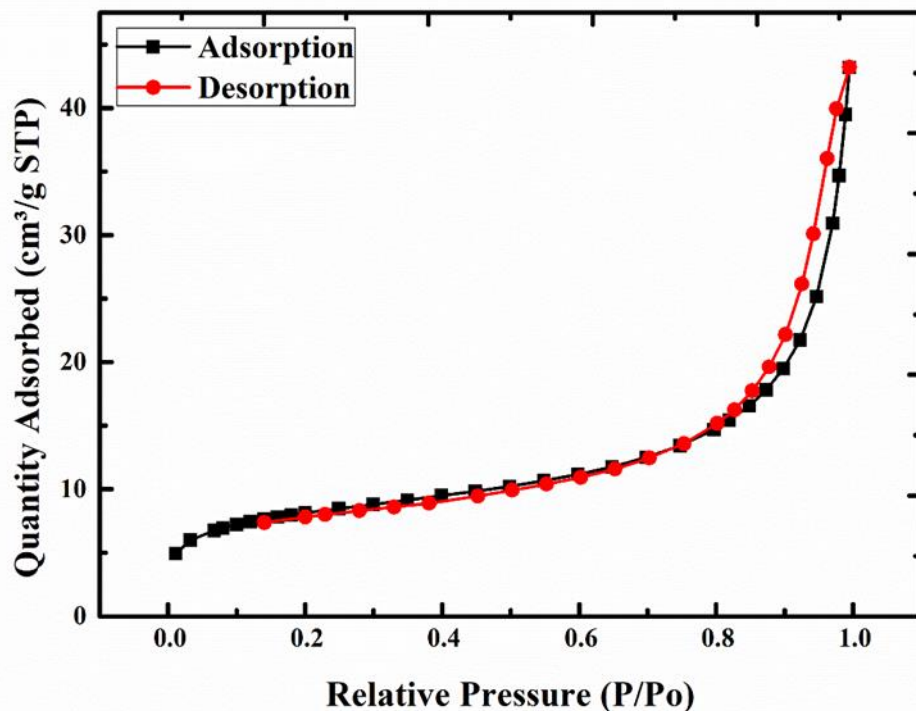


**Figure 6.2** N<sub>2</sub> adsorption-desorption isotherms for PPy/Fe<sub>3</sub>O<sub>4</sub> nanocomposite.

The XRD patterns of PPy, Fe<sub>3</sub>O<sub>4</sub> nanoparticles, and the polypyrrole magnetic nanocomposite before and after adsorption of Cr(VI) is shown in Figure 6.3. A broad peak (Figure 6.3a) observed at  $2\theta = 24.6^\circ$ , is a characteristic peak of amorphous PPy [23]. The characteristic diffraction peaks of Fe<sub>3</sub>O<sub>4</sub> observed at  $2\theta = 30.3^\circ, 35.7^\circ, 43.4^\circ, 53.6^\circ, 57.3^\circ,$  and  $62.9^\circ$  are assigned to (220), (311), (400), (422), (511), and (440) planes of Fe<sub>3</sub>O<sub>4</sub> [24-27]. Peaks of Fe<sub>3</sub>O<sub>4</sub> were observed in the nanocomposites before and after adsorption of Cr(VI) (Figure 6.3(c)). This shows that after modification of Fe<sub>3</sub>O<sub>4</sub> nanoparticles, their phases were not modified. The XRD study clearly shows that the Fe<sub>3</sub>O<sub>4</sub> nanoparticles are successfully incorporated into the polypyrrole network.

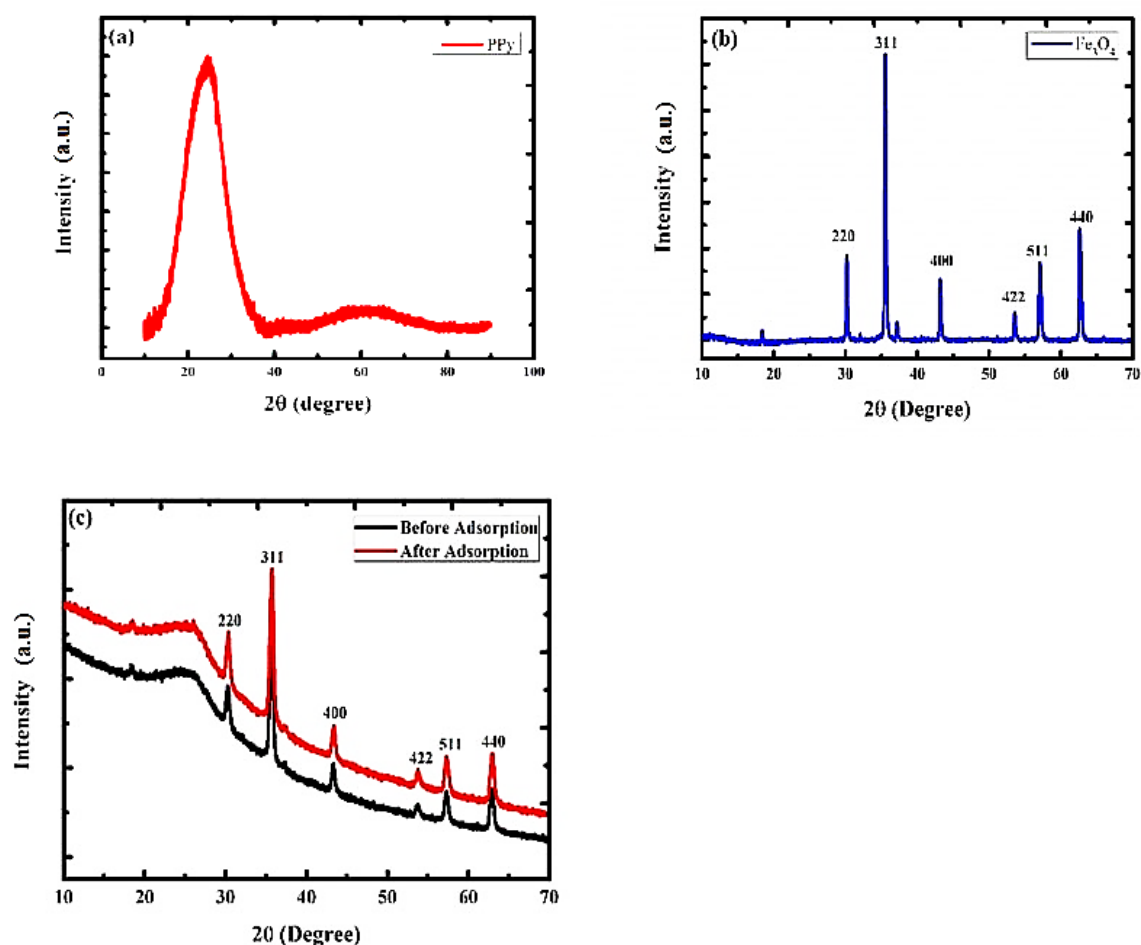


**Figure 6.3** XRD pattern of (a) polypyrrole, (b) magnetite ( $\text{Fe}_3\text{O}_4$ ), and (c) polypyrrole magnetic nanocomposite before and after adsorption of hexavalent chromium using 2-pole three-phase induction motor.

The FTIR spectra of  $\text{Fe}_3\text{O}_4$ , PPy, polypyrrole magnetic nanocomposite before and after Cr(VI) adsorption obtained from  $500\text{--}2800\text{ cm}^{-1}$  is shown in Figure 6.4. The characteristic peak of  $\text{Fe}_3\text{O}_4$  nanoparticles appears at  $549\text{ cm}^{-1}$  (Figure 6.4(b)), which is due to the stretching vibration mode associated to the metal-oxygen adsorption band (Fe-O bonds in the crystalline lattice of  $\text{Fe}_3\text{O}_4$ ) [28]. The bands observed at  $1534$  and  $1449\text{ cm}^{-1}$  relate to the fundamental vibration of the pyrrole rings [29-30]. The bands at  $1040$  and  $1157\text{ cm}^{-1}$  corresponds to =C-H out of plane vibration [31]. Peaks observed at  $967\text{--}853\text{ cm}^{-1}$  are attributed to C-H deformation [2]. After adsorption of chromium (VI) ions, there were clear shifts in the peak's values to the higher infrared region. The FTIR spectrum of PPy/ $\text{Fe}_3\text{O}_4$  nanocomposite after adsorption peaks were observed at  $1537$ ,  $1460$ ,  $1159$ ,  $1042$ ,  $971$  and  $895\text{ cm}^{-1}$ , which were attributed to the absorption

bands of symmetric and antisymmetric ring-stretching, conjugated C-N stretching, C-H deformation and C-H stretching vibration of pyrrole ring, respectively. The shift in the adsorption peaks (after adsorption) indicated that there was a metal binding process taking place at the adsorbent surface [2, 32].

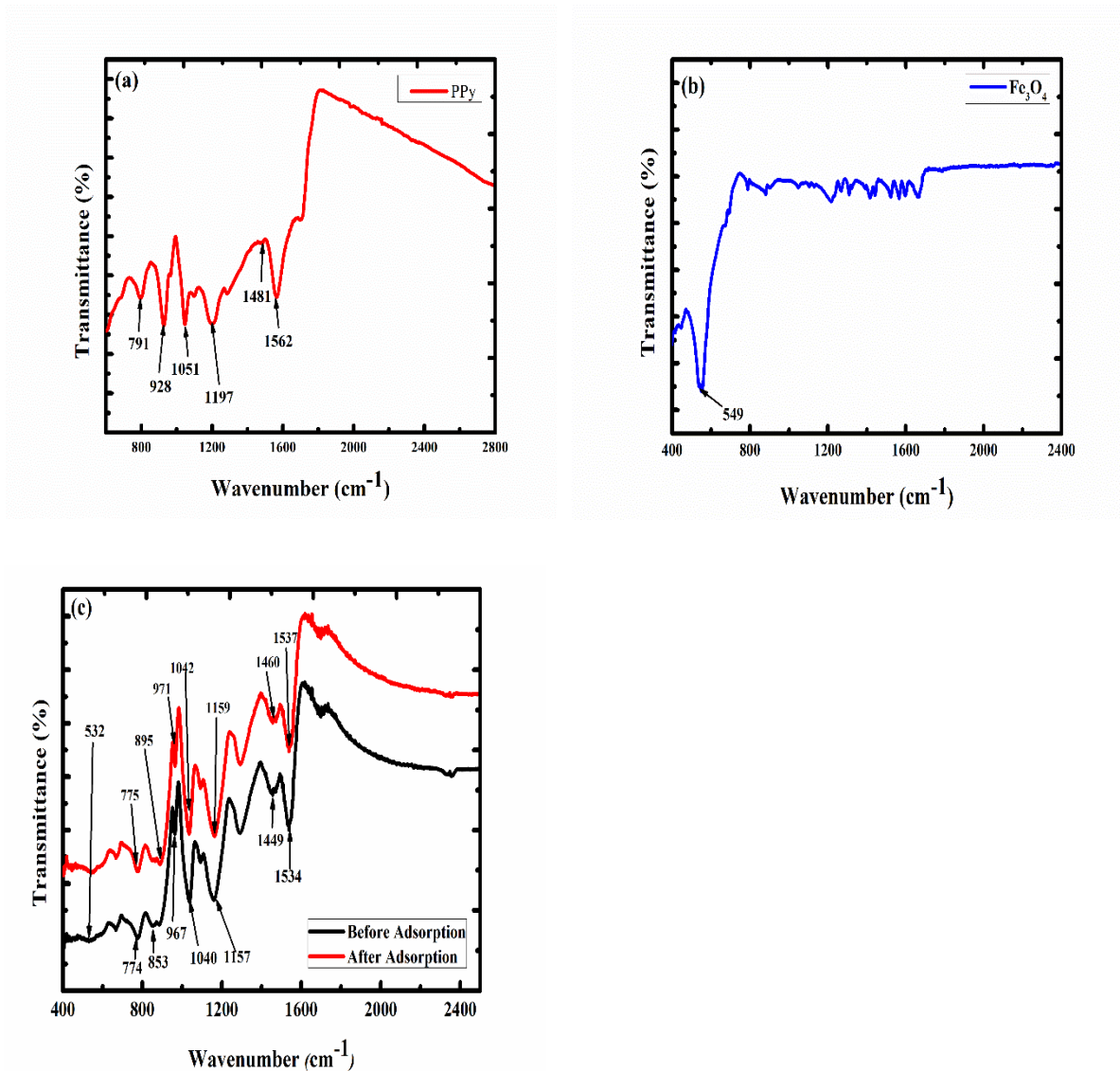


**Figure 6.4** FTIR spectra of (a) PPy, (b) Fe<sub>3</sub>O<sub>4</sub> and (c) polypyrrole magnetic nanocomposite before and after adsorption of hexavalent chromium using 2-pole three phase induction motor.

The ESR adsorption spectra for polypyrrole magnetic nanocomposite before and after adsorption of Cr(VI) at room temperature is shown in Figure 6.5. The line shapes were detected to be symmetrical. The resonance signal was also observed to be wide and broad with a linewidth value of 1400 Gauss. The effective g-value of the nanocomposite was determined to be 2.25

G, which was attributed to  $\text{Fe}^{3+}$  spin interactions. Such interactions show a superparamagnetic behaviour characterized by the presence of clusters. The shapes and the field position are identical to those of the standard magnetic nanoparticles suspension and are consistent with ESR spectra of superparamagnetic iron oxide nanoparticles at room temperature [33-35]. The line shape of polypyrrole magnetic nanocomposite when fitted to Gaussian and Lorentzian functions, showed a line shape having a combination of 55% Gaussian and 45% Lorentzian functions. The dominant Gaussian fit is characteristic of ferromagnetic resonance indicating that the main percentage of the polypyrrole magnetic nanocomposite is magnetic as shown in Figure 6.5(b and c), as this confirms that the dominated fraction of the PPy/ $\text{Fe}_3\text{O}_4$  is magnetic [36-37].

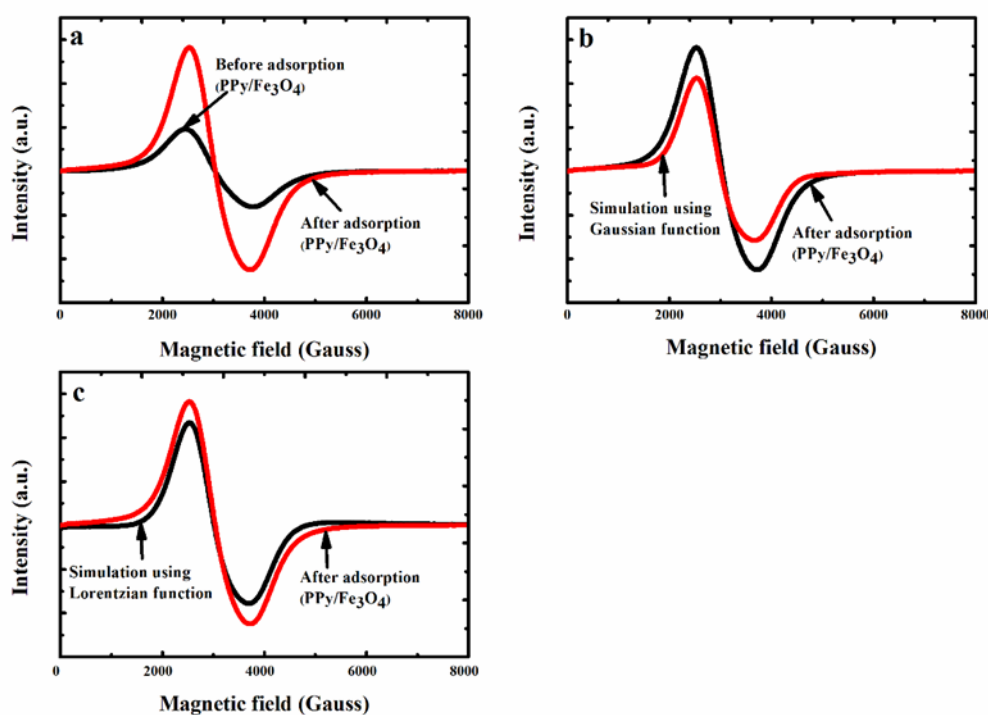


**Figure 6.5** ESR spectra of PPy/ $\text{Fe}_3\text{O}_4$  (a) before and after adsorption of hexavalent chromium, (b) PPy/ $\text{Fe}_3\text{O}_4$  nanocomposite after Cr(VI) adsorption (b) ESR spectra of PPy/ $\text{Fe}_3\text{O}_4$  nanocomposite after hexavalent chromium adsorption fitted with Gaussian function and (c) ESR spectra of PPy/ $\text{Fe}_3\text{O}_4$  nanocomposite after hexavalent chromium adsorption fitted with Lorentzian function

The magnetization hysteresis loop of polypyrrole magnetic nanocomposite at room temperature (300 K) was measured at intervals of -10 000 to 10 000 is shown in Figure 6.6. The saturation magnetization was determined to be 23 emu/g, with a zero-remanence magnetization and coercivity field, which is typical of a superparamagnetic material. The superparamagnetic behaviour is mostly generated by the magnetite core in the sample [38].

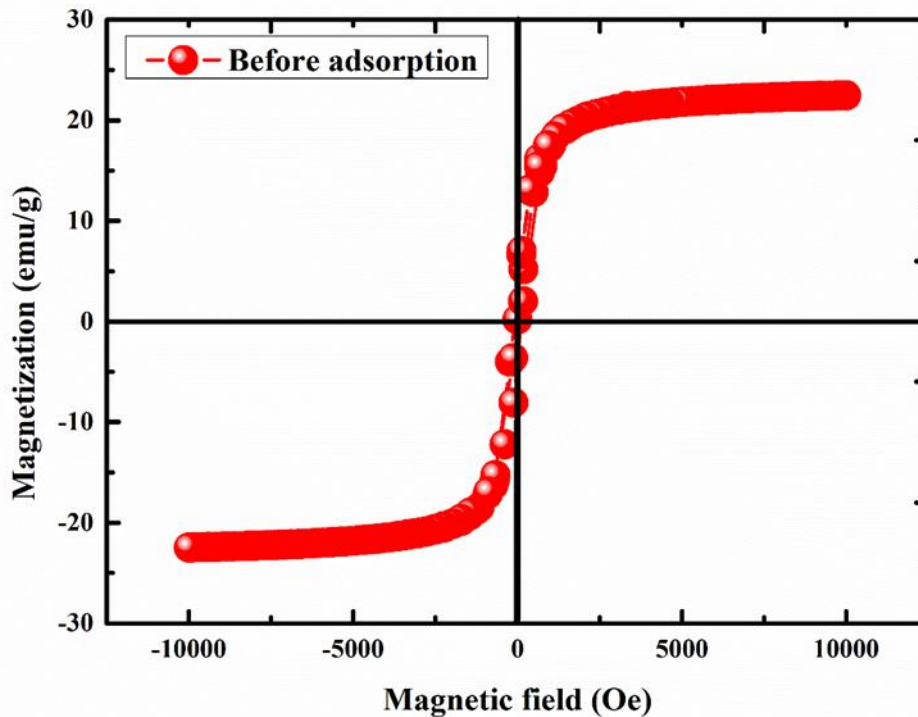


**Figure 6.6** Magnetization curve of polypyrrole magnetic nanocomposite at room temperature.

### 6.2.2 Effect of pH on Adsorption of Hexavalent Chromium Under the Influence of Magnetic Field

Determining the point of zero charge where the net surface charge of a material is zero is vital for understanding the electrostatic interactions at the materials surface, mostly for charged species. The adsorption of the adsorbate on non-specific and specific adsorbents depends on pH, as the surface property of the adsorbate is affected by solution pH [22, 39]. In adsorption medium, the pH of any solution is an important factor which controlled the metal ions adsorption onto the adsorbent surface [40-41].

The surface charge and the protonation degree of the adsorbent are significantly influenced by the pH value [42]. For electrostatic adsorption the zeta potential and its devolution with changing pH are important. For adsorption process, the pH is adjusted in a way that both components have opposed surface charges. By changing the pH-value and hence the zeta potential of one component repulsive interaction forces occurs and the molecules detach from the surface of the carrier particles. One of the most important parameters that influence adsorption of metals ions is the solution pH, which influences the surface properties the adsorbents and ionic forms of the chromium solutions [43].

Increase in the percentage of Cr(VI) removed as the pH is increased from 2-10 is observed, with a maximum removal observed at pH 2 is shown in Fig. 8a. It is remarkable that Cr(VI) removal curve can be explained by the surface properties of the polypyrrole magnetic nanocomposite and the relative distribution Cr(VI) species under a wide range of pH value [44]. The  $\text{pH}_{\text{pzc}}$  of the nanocomposite was found to be 3.20 as shown in Figure 6.7. The surface of the magnetic nanocomposite was mainly negative charged when the  $\text{pH} > \text{pH}_{\text{pzc}}$  (3.20) and mainly positive charged when  $\text{pH} < \text{pH}_{\text{pzc}}$  (3.20). When the solution pH was below the  $\text{pH}_{\text{pzc}}$  ( $< 3.20$ ), Cr(VI) ions were electrostatically attracted to the positively charged magnetic nanocomposite, as the Cr(VI) exists as  $\text{HCrO}_4^-$  in anionic species at acidic pH, hence the enhanced Cr(VI) removal at the acidic condition. With the increase in solution pH, low percentage of Cr(VI) removed was due to the electrostatic repulsion between the anionic species of Cr(VI) ( $\text{CrO}_4^{2-}$ ) and negative charged  $\text{OH}^-$  ions on the surface of the polypyrrole magnetic nanocomposite, causing a decrease in the efficiency of the adsorbent for Cr(VI) ions removal.

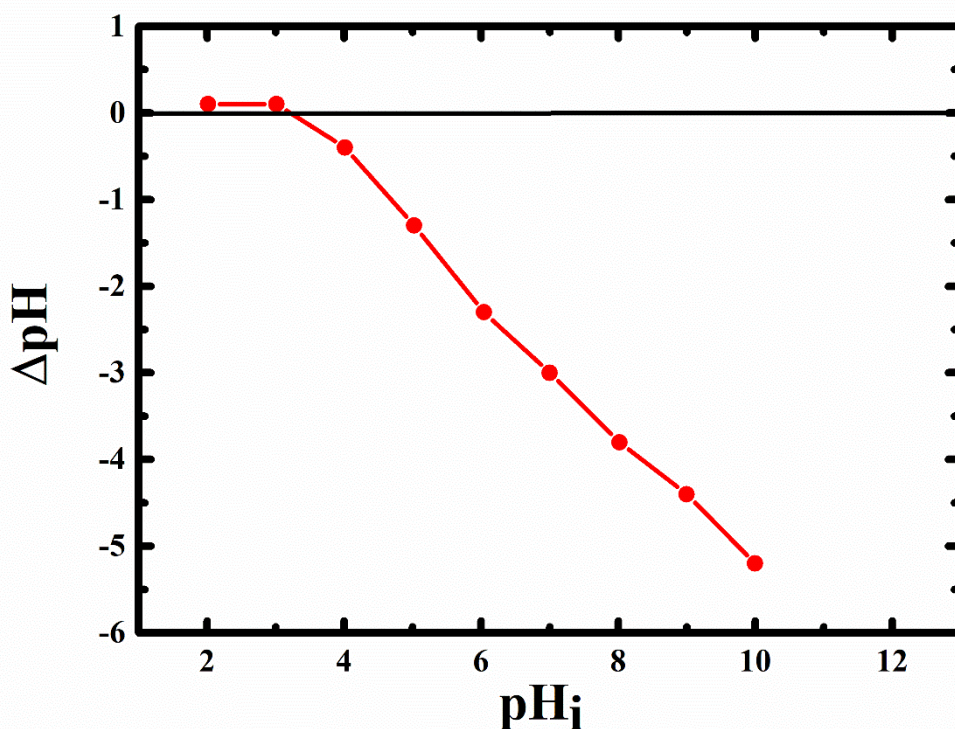


**Figure 6.7** Point of zero charge of polypyrrole magnetic nanocomposite.

### 6.2.3 Effect of Adsorbent Dosage on Adsorption of Hexavalent Chromium Under the Influence of Magnetic Field

The effect of adsorbent dosage on the removal of hexavalent chromium by the magnetic nanocomposite was investigated under the influence rotating magnetic field from a two-pole induction motor at room temperature. The results indicated in Figure 6.8(b) shows that the percentage of Cr(VI) removed using the magnetic nanocomposite under the influence of rotating magnetic field increased with increase in the nanocomposite dosage. Precisely, the range of Cr(VI) removed from 40 mL of 50 mg/L Cr(VI) solution increased from 27.9% at a dosage of 0.01 g to 77.8% at a dosage of 0.05 g. Increase in the amount of hexavalent chromium removed from aqueous solution with an increase in the adsorbent dosage was due to increase in the number of active adsorption sites for a constant concentration of hexavalent chromium. At low adsorbent dosage, the active adsorption sites were insufficient for the adsorbate (Cr(VI)) to occupy. However, at the high adsorbent dosage, the active adsorption sites are sufficient for the adsorbate to occupy. Similar results have been reported in the study of Cr(VI) adsorption [43, 45].

#### **6.2.4 Effect of Magnetic Field on Adsorption of Hexavalent Chromium**

The effect of the induced magnetic field in anticlockwise and clockwise direction on the adsorption of Cr(VI) ions onto polypyrrole magnetic nanocomposite are shown in Figure 6.8(c and d). It is observed that percentage of Cr(VI) removed onto polypyrrole magnetic nanocomposite under the influence of rotating magnetic field increased from 72-81% and 68-73% with the increase in magnetic field range of 8.96-13.38 mT in the clockwise and anti-clockwise directions. Improved removal of Cr(VI) ions under magnetic field were attributed to the increased size of particles aggregates as the induced magnetic field on the polypyrrole magnetic nanocomposite was increased from low magnetic field to high magnetic field. The sizes of aggregates formed were observed to depend on the magnetic velocity, with fast moving uniform particles aggregates with a large surface area for adsorption process were observed at the high magnetic field. Smaller non-uniform particles aggregates travelling with slow drift velocities were also observed at the low magnetic field, with a reduced surface area for the adsorption process. Chain breakage in the aggregates was also noticed to significantly reduces the swimming efficiency of the particles at the low magnetic field, as the segment of the chain broken were incapable to rejoin the original chain formation, leading to the reduced surface area for the adsorption of Cr(VI) ions. The lateral binding of chains driven into contact by magnetic manipulations substantially increases the chain polydispersity, hence increased chain collision and area of particle interaction [46-47].

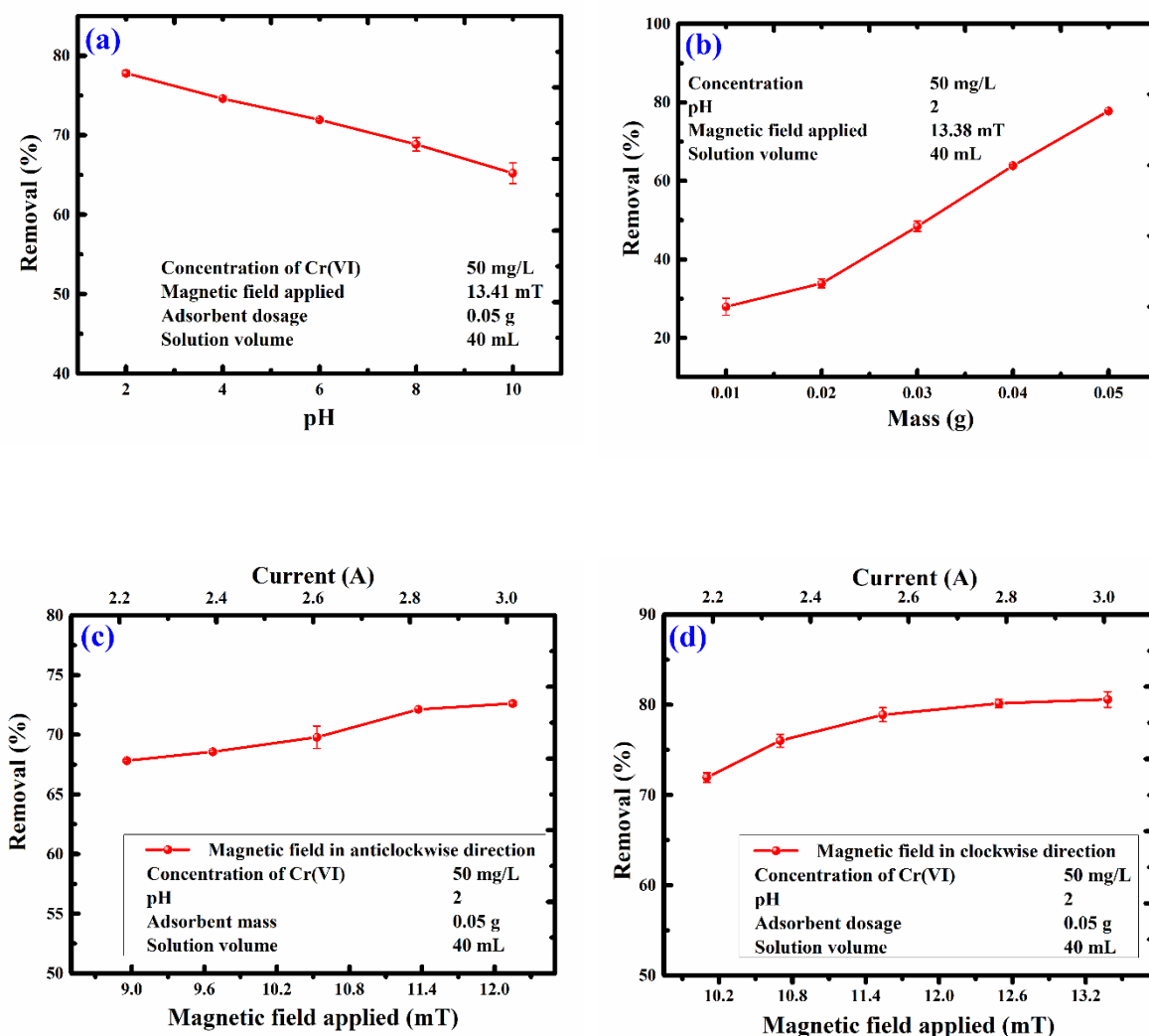


**Figure 6.8** Effect of (a) pH on the adsorption of hexavalent chromium onto PPy/Fe<sub>3</sub>O<sub>4</sub> nanocomposite, (b) adsorbent dosage on the adsorption of hexavalent chromium onto PPy/Fe<sub>3</sub>O<sub>4</sub> nanocomposite, (c) magnetic field strength on the adsorption of hexavalent chromium onto PPy/Fe<sub>3</sub>O<sub>4</sub> nanocomposite (anticlockwise direction) and (d) magnetic field strength on the adsorption of hexavalent chromium onto PPy/Fe<sub>3</sub>O<sub>4</sub> nanocomposite (clockwise direction).

### 6.3 Conclusion

The effect of rotating magnetic field on the adsorption of Cr(VI) onto polypyrrole magnetic nanocomposite was explored in this study. The study showed that Cr(VI) adsorption onto the polypyrrole magnetic nanocomposite under the influence of magnetic field was dependent on the solution pH, adsorbent dosage and the magnetic field direction. Enhanced percentage of

Cr(VI) ions removed was observed at pH 2, at an adsorbent dosage of 0.05 g and magnetic field of 12.15 mT (anticlockwise direction) and 13.38 mT (clockwise direction). Increased in the magnetic field was also observed to enhance Cr(VI) ions removal. These were due to increased aggregation of particles. The size of aggregates formed depended on the magnetic velocity, with fast moving large uniform particles aggregates observed. Smaller non-uniform particles aggregates travelling with slow drift velocities were also observed at the low magnetic field.

## 6.4 References

- [1] O. F. G. Vazquez, M. M. Virgen, V. H. Montoya, R. T. Gomez, J. L. A. Flores, M. P. Cruz and M. A. M Moran, **2016**, *Industrial and Engineering Chemistry Research*, 55, 9323-9331.
- [2] M. Bhaumik, A. Maity, V. V. Srinivasu, and M. S. Onyango, **2011**, *J. of Hazardous Materials*, 190, 381-390.
- [3] A. Attia, S. A. Khedr, and S. A. Elkholy, **2010**, *Brazilian J. of Chemical Engineering*, 27, 183-193.
- [4] S. Nethaji, A. Sivasamy, and A. B. Mandal, **2013**, *Bioresource Technology*, 134, 94-100.
- [5] N. Ilankoon, **2014**, *J. of Engineering Research and Application*, 4, 55-63.
- [6] J. F. De Brito, L. De Oliveira Ferreira, M. C. R Pereira, J. P. Da Silva and T. C. Ramalho, **2012**, *Water, Air, and Soil Pollution*, 223, 3545-3551.
- [7] X. Hao, H. Liu, G. Zhang, H. Zou, Y. Zhang, M. Zhou, and Y. Gu, **2012**, *Applied Clay Science*, 55, 177-180.
- [8] L. Duan, Guo S, and Yang J, **2012**, *Advances in Chemical Engineering and Science*, 2, 101-107.
- [9] G. Li, W. Zhu, C. Zhang, S. Zhang, L. Liu, L. Zhu and W. Zhao, **2016**, *Bioresource Technology*, 206, 16-22.
- [10] O. Mosin and I. Ignatov, **2014**, *European J. of Molecular Biotechnology*, 2, 72-85.
- [11] Y. Ali, R. Samaneh, R. Zohre and J. Mostafa, **2014**, *Current World Environment*, 9, 1008-1016.
- [12] C. J. Quinn, T. C. Molden and C. H. Sanderson, **1997**, *Iron and Steel Engineer*, 74, 47-52.
- [13] L. Holysz, A. Szczes, and E. Chibowski, **2007**, *J. of Colloid and Interface Science*, 316, 996-1002.
- [14] K. Higashitani, A. Kage, S. Katamura, K. Imai and S. Hatade, **1993**, *J. of Colloid and Interface Science*, 156, 90-95.
- [15] Z. Z. K. Khater and M. H. Ibraheim, **2015**, *International J. of Current Research and Academic Review*, 3, 262-279.
- [16] G. Zhang, X. Yang, Y. Liu, Y. Jia, G. Yu, and S. Ouyang, **2004**, *J. of Colloid and Interface Science*, 278, 265-269.
- [17] G. Zhang, Y. Liu, Y. Xie, X. Yang, B. Hu, S. Ouyang, H. Liu and H. Wang, **2005**,

- Applied Clay Science, 29, 15-21.
- [18] J. Yuan-Yuan, Z. Gao-Ke, H. Bo and D. Wei, **2004**, J. of Wuhan University of Technology-Mater. Sc. Ed, 19, 52-54.
- [19] R. R. Mohammed, M. R. Ketabchi, and G. Mckay, **2014**, Chemical Engineering J; 243, 31-42.
- [20] M. S. Rao and O. Sahu, **2013**, Physics and Material Chemistry, 1, 34-40.
- [21] F. F. Fondeur, D. T. Hobbs and S. D. Fink, **2010**, Separation Science and Technology, 45, 1876-1879.
- [22] M. H. Mohamed, M. Pirlot, M. K. Danquah, and L. D. Wilson, **2017**, J. of Materials Science and Chemical Engineering, 5, 12-24.
- [23] J. Azadmanjiri, P. Hojati-Talemi, G. P. Simon, K. Suzuki, and C. Selomulya, **2011**, Polymer Engineering and Science, 51, 247-253.
- [24] D. Shi, H. Yang, S. Ji, S. Jiang, X. Liu, and D. Zhang, **2015**, Procedia Engineering, 102, 1555-1562.
- [25] A. J. Silva, P. L. Andrade, M. P. C. Silva, L. D. L. S. Valladares, and J. A. Aguiar, **2013**, J. of Magnetism and Magnetic Materials, 343, 138-143.
- [26] J. K. Mathad, and R. M. V. G. K. Rao, **2011**, Polymer Composites, 32, 1416-1422.
- [27] W. Peng, X. Hu, and D. Zhang, **2011**, J. of Magnetism and Magnetic Materials, 323, 2064-2069.
- [28] G. Qiu, Q. Wang, and M. Nie, **2006**, Macromolecular Materials and Engineering, 291, 68-74.
- [29] S. Li, X. Lu, Y. Xue, J. Lei, T. Zheng, and C. Wang, **2012**, PLoS One, 7, e43328.
- [30] M. Tanzifi, and K. Karimipour, **2017**, J. of Water and Environmental Nanotechnology, 2, 265-277.
- [31] W. Chen, X. Li, G. Xue, Z. Wang, and W. Zou, **2003**, Applied Surface Science, 218, 215-221.
- [32] E. A. Sanches, S. F. Alves, J. C. Soares, A. M. D. Silva, C. G. D. Silva, S. M. D. Souza, and H. O. D. Frota, **2015**, J. of Nanomaterials, 16, 301.
- [33] B. Chertok, A. J. Cole, A. E. David, and V C. Yang, **2010**, Mol. Pharm., 7, 375-385.
- [34] Y. Koseoglu, F. Yildiz, D. K. Kim, M. Muhammed, and B. Aktas, **2004**, Phys. Stat. Sol., 1, 3511-3515.
- [35] J. B. Mamani, L. F. Gamarra, and G. E. D. S. Brito, **2014**, Mat. Res; 17, 542-549.
- [36] M. Bhaumik, T. Y. Leswifi, A. Maity, V.V. Srinivasu, and M. A. Onyango, **2011**, J. of Hazardous Materials, 186, 150-159.

- [37] O. A. Kuznetsov, O. N. Sorokina, V. G. Leontiev, O. A. Shlyakhtin, A. L. Kovarski, and A. A. Kuznetsov, **2007**, *J. of Magnetism and Magnetic Materials*, 311, 204-207.
- [38] A. J. Silva, P. L. Andrade, M. P. C. Silva, L. D. L. S. Valladares, and J. A. Aguiar, **2013**, *J. of Magnetism and Magnetic Materials*, 343, 138-143.
- [39] Y. Zou, X. Wang, Y. Ai, Y. Liu, J. Li, Y. Ji, and X. Wang, **2016**, *Experimental Science and Technology*, 50, 3658-3667.
- [40] J. Dui, G. Zhu, and S. Zhou, **2013**, *ACS Appl. Mater. Interfaces*, 5, 10081-10089.
- [41] R. A. K. Rao, A. A. Khan, and N. Alam, **2016**, *Anal. Methods*, 8, 869-879.
- [42] M. Anbia, K. Kargosha, and S. Khoshbooei, **2015**, *Chemical Engineering Research and Design*, 93, 779-788.
- [43] E. Mekonnen, M. Yitbarek and T. R. Soreta, **2015**, *S. Afr. J. Chem*, 68, 45-52,
- [44] K. Zhu, C. Chen, H. Xu, Y. Gao, X. Tan, A. Alsaedi, and T. Hayat, **2017**, *ACS Sustainable Chemistry and Engineering*, 5, 6795-6802.
- [45] R. Zhang, H. Ma, and B. Wang, **2010**, *Ind. Eng. Chem. Res.* 49, 9998-10004.
- [46] U. O. Aigbe, R. Das, W. H. Ho, V. Srinivasu, and A. Maity, **2017**, *Separation and Purification Technology*. 194, 377-387.
- [47] D. Kim, J. Kim, and W. Choi, **2011**, *J. of Hazardous Materials*, 192, 928-931,

## CHAPTER SEVEN

### **Result IV: Congo Red Dye Removal Under the Influence of Rotating Magnetic Field by Polypyrrole Magnetic Nanocomposite (Paper under Review with Desalination and Water Treatment Journal).**

**Abstract.** Magnetic field and magnetic exposure time effects on congo red dye adsorption were examined in this study. A maximum removal of 94% removal was observed for the adsorption of 100 mg/L of the adsorbate using 0.15 g of adsorbent at a magnetic field and exposure time of 18.99 mT and 120 min. From magnetic exposure time experiment, the percentage amount of congo red removed increases with an increase in the magnetic exposure time with the removal of 79-94% observed. When a magnetic field was not applied to congo red solution at the same magnetic exposure time, removal of 5-15% was observed. The increased removal owing to increase magnetic field is attributed to the magnetic force which is applied in moving the charged solid particle placed in the region of magnetic field. The magnetic force exerted on the charged solids particles leads to increase adsorption of congo red due to an increase in the velocity and reorientation of the charged particles. The Langmuir isotherm model had the highest correlation coefficient value and fitted well with the experimental data. The maximum adsorption capacity of 119.76 mg/g was observed using this isotherm model.

### **7.1 Introduction**

Water is essential for all forms of life on earth. It is also a valuable resource for human development. Providing clean affordable water to meet human needs is a 21st-century problem, as potable water for human use for drinking, cooking, and industrial purpose should be clean. However, the purity of water bodies is affected by civilisation and industrialisation resulting in pollution of water bodies with toxic substances like heavy metals, pigments, dyes, which are prevalent in developing countries [1-3]

Colour is the first contaminant to be acknowledged in wastewater [4]. Dyes are organic compounds that have the capability to imparts specify colours to the substance which it is being applied. Effluents with colour contamination including azo dyes have received huge severe concerns due to their potential carcinogenic effect [5-6]. A major ecological concern around the world is the discharge of coloured effluents from manufacturing and textile dyeing mills [7].

Wastewater produced by the textile industries contains substantial amounts of non-fixed dyes, precisely azo dyes and inorganic salts [8]. Azo dyes are characterized by vivacious colour and by the presence of one or more azo groups ( $-N=N-$ ) aromatic rings in their structure. Over

60% of the total dyes used are represented by azo dyes, being the major and the most versatile class of dyes for commercial use. Therefore, their direct release into the environment from effluents containing azo dyes, including congo Red (CR), causes serious environmental, ecological and health problems. Because of the high stability against light, temperature, chemicals and microbial attack, azo dyes are difficult to decompose and eliminate from water using traditional wastewater technique methods [9-10]

To reduce their impact on the environment, a variety of removal methods have been developed. These techniques include adsorption of dye contaminants onto mineral or carbon-based matrices, photo-catalysis or oxidation processes, microbiological or enzymatic decomposition, etc. Amongst the water treatment techniques available, adsorption is regarded as more effective because of its design simplicity and ease of operation [11]. Owing to a broad spectrum of magnetic field application such as therapeutic and diagnostic medicine, environmental management and industries over the years [12], solving environmental problems using magnetic technique has received substantial consideration in recent years [12-14].

Application of the magnetic field in water treatment has been known to be effective in most instance [15]. Due to their ecological purity, safety, and simplicity of magnetic field method, it has been shown to have the capacity to enhance the removal of contaminants from water [16-17]. Magnetism is a unique property that independently helps in the water purification process, influencing the physical and chemical properties of contaminants in water [18]. The physicochemical properties of water, aqueous solutions, and suspension are influenced by a magnetic field, as it causes a redistribution of flow energy due to momentum changed of the charged particles [16, 19].

Duan et al [19] reported an increased removal of Pb (II) using modified chitosan in the presence of magnetic field, which resulted in the viscosity and surface tension of solutions being reduced. This increase in Pb(II) removal was associated with the resonance effect, which occurs when the magnetic field and the oscillating frequency of the molecules are in tune. When energy was imparted to the system for activation, changes in the structure and nature of the material was observed, thus promoting the adsorption of the Pb(II) ions. Brito et al [20] and Foroughi et al [21] showed that magnetic field significantly increased the adsorption of aromatic compound and treatment of urban runoff. This was attributed to breaks in the hydrogen bond between water molecules by the magnetic force, facilitating the adsorption process as adsorbate molecules will be freer in solution and more active adsorption sites released.

Hao et al [22] reported that the surface morphology of the organo-bentonite used for methyl blue adsorption was observed to become heterogeneous under the effect of magnetic field, leading to an increase in the surface area of the adsorbent with improving adsorbent affinity for the adsorption of methyl blue onto organo-bentonite under magnetic field exposure. Mohamed et al [18] and Bel'chinskaya et al [23] also reported that the adsorbent surface changes when exposed to a magnetic field, which leads to grain orientation and improved adsorption of the adsorbate. The adsorption sites are apparently activated by favourably oriented dipoles facilitating the adsorptive process and resulting in a gain in the adsorption time.

The zeta potential and size distribution of the particles formed in solution were also observed by Cai et al [24] to be significantly influenced by a magnetic field. This was attributed to Lorentz force ( $\vec{F} = q \cdot \vec{v} \times \vec{B}$ ) exerted on moving ions or the charged solid particles placed in a magnetic field, as it was observed to improve the adsorption process. The force was observed by Zaidi et al [25] to increase linearly with particle charge, the particle velocity, and the orthogonal vector component of the magnetic field strength. Magnetic field effect on the adsorption of adsorbate was shown by Fondeur et al [26] to increase the mobility of molecules being adsorbed (sorbative) or already adsorbed (sorbate), with magnetic field providing a higher rate of adsorbate or adsorbent transportation in the volume of transport pores.

Khiadani (Hajian) et al [27] reported that the magnetic force caused an increase in electrostatic interaction between the negatively charged ions (lead, zinc and cadmium) with the adsorbent surface which was followed with an increase in metals adsorption capacity, due to release of free electrons from the adsorbent surface bonding with the metal ions. It was reported by Bhatnagar et al [28] that adsorption is influenced by the magnetic field when the sum of the molecular susceptibilities of the final product of the reactants is greater than the sum of the molecular susceptibilities of initial reactants. Besides magnetic field influencing adsorption, variations in temperature, the surface of tubes and unequal stirring also influence the adsorption process.

In this study, developing magnetic techniques for water treatment using polypyrrole magnetic nanocomposite as an adsorbent is reported to evaluate the magnetic field effect created by an induction motor for congo red dye adsorption. Other parameters like magnetic exposure time, pH, initial concentration and adsorbent dosage effects on congo red adsorption are also evaluated. The goal is to create a water treatment technique, which would be useful for further application in the removal of congo red dye from industrial waste effluents.

## 7.2 Results and Discussion

### 7.2.1 Characterization of PPy/Fe<sub>3</sub>O<sub>4</sub> Magnetic Nanocomposite

The XRD pattern of the adsorbent (PPy/Fe<sub>3</sub>O<sub>4</sub>) before and after adsorption, magnetite (Fe<sub>3</sub>O<sub>4</sub>) and PPy which were normalized to [0, 100] are shown in Figure 7.1. A broad diffraction peak located at  $2\theta = 24.5$  degree, which is a characteristic peak of amorphous PPy is observed in Figure 7.1(b) [29]. Diffraction peaks observed at  $2\theta$  value of 18.35(111), 30.14(220), 35.54(311), 43.18(400), 53.62(422), 57.06(511) and 62.68(440) corresponds to the cubic Fe<sub>3</sub>O<sub>4</sub> phase (Figure 7.1(a)) [35 30]. The diffraction peaks of Fe<sub>3</sub>O<sub>4</sub> observed are confirmed by the JCPDS file database (PDF No. 75-0449). It is also observed from the XRD result in Figure 7.1 (c), that the Fe<sub>3</sub>O<sub>4</sub> particles exist, and it is incorporated into the nanocomposite. The XRD pattern of the nanocomposite before and after adsorption of congo red was not affected by the induced magnetic field, as the crystalline structure of the nanocomposite did not change graphically after congo red adsorption.

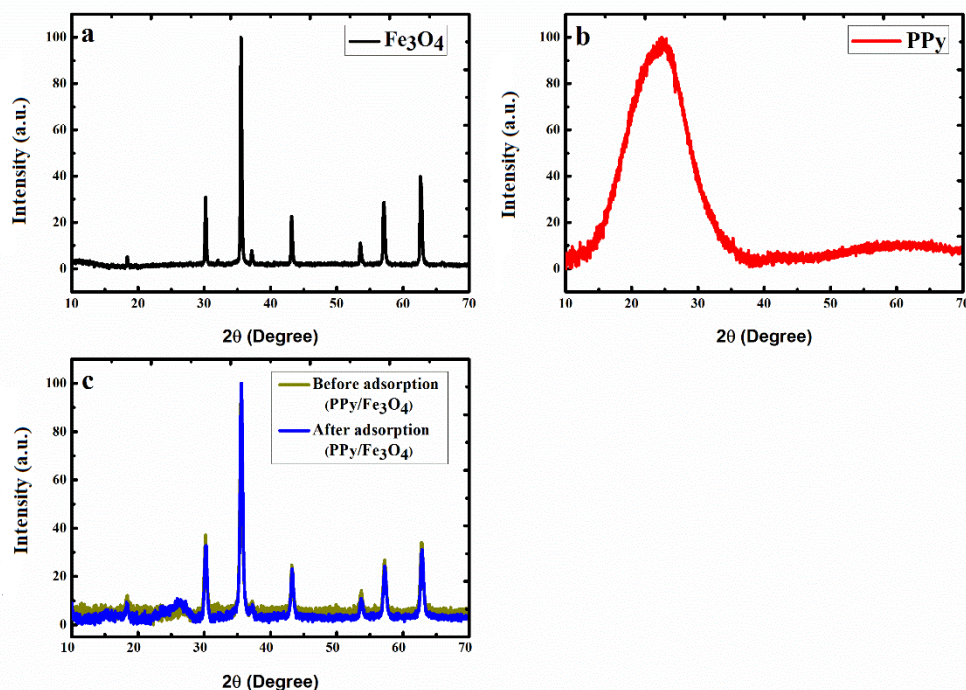


**Figure 7.1** XRD diffraction pattern of (a) Fe<sub>3</sub>O<sub>4</sub>, (b) PPy and (c) PPy/Fe<sub>3</sub>O<sub>4</sub> nanocomposite before and after congo red adsorption.

FTIR spectra before and after adsorption of congo red by PPy/Fe<sub>3</sub>O<sub>4</sub>, Fe<sub>3</sub>O<sub>4</sub>, and PPy are shown in Figure 7.2. The spectra of the magnetic adsorbent have characteristic peaks of the oxidised PPy and Fe<sub>3</sub>O<sub>4</sub>. Characteristic adsorption peak observed at 554 cm<sup>-1</sup> is due to the vibration of the Fe-O band, which is a characteristic peak of Fe<sub>3</sub>O<sub>4</sub> (inset of Figure 7.2(a)) [31]. Adsorption peaks observed at 1543 cm<sup>-1</sup>, 1458 cm<sup>-1</sup>, 1290 cm<sup>-1</sup>, 1173 cm<sup>-1</sup>, 1034 cm<sup>-1</sup>, 968 cm<sup>-1</sup> and 787 cm<sup>-1</sup> were the characteristic peak of PPy in the nanocomposite before congo red adsorption. A shift to low adsorption values of the characteristic peak of PPy is observed after adsorption of congo red by the PPy/Fe<sub>3</sub>O<sub>4</sub> nanocomposite, with the PPy characteristic peaks shifting to 1537cm<sup>-1</sup>, 1454 cm<sup>-1</sup>, 1286 cm<sup>-1</sup>, 1159 cm<sup>-1</sup>, 1030 cm<sup>-1</sup>, 957 cm<sup>-1</sup>and 785 cm<sup>-1</sup>. The adsorption peaks of PPy before and after adsorption of congo red corresponds to C=C stretch, C-N stretch, C-H or C-N in-plane deformation, C-C vibration, C-H in-plane deformation, C-C out of plane deformation vibration and out of plane C-H vibration of pyrrole (Figure 7.2). From the FTIR analysis, it is confirmed that PPy moiety is incorporated into the PPy/Fe<sub>3</sub>O<sub>4</sub> nanocomposite [29, 32-33].

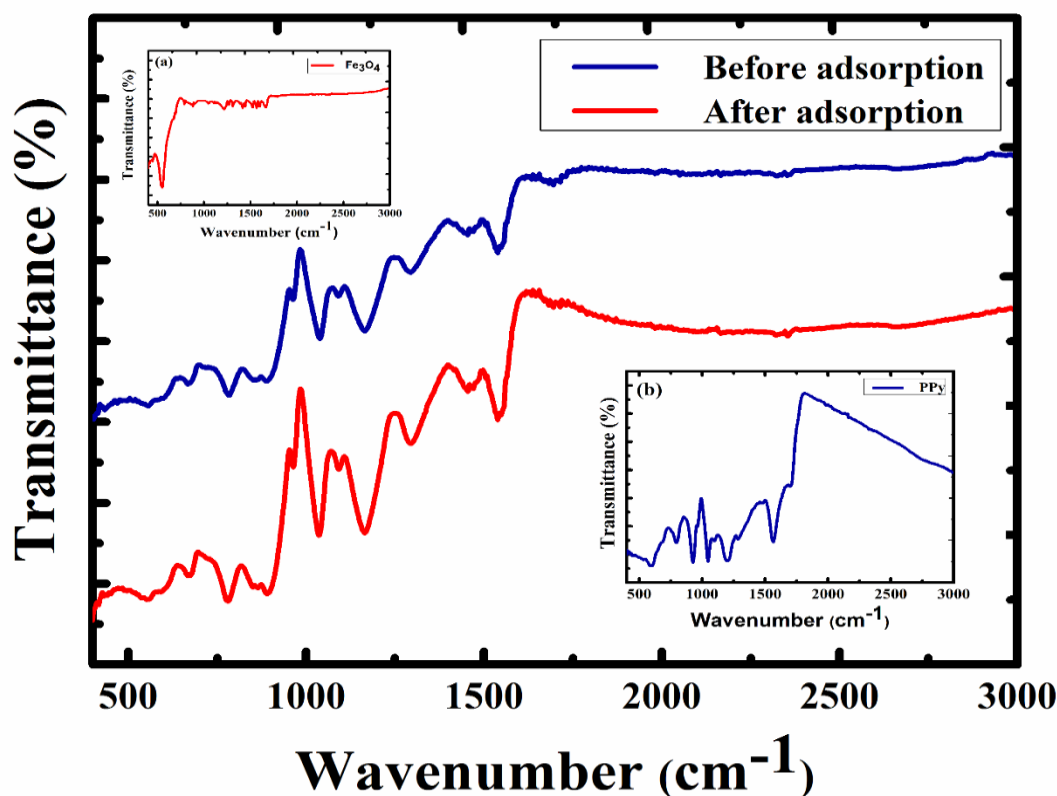


**Figure 7.2** FTIR spectra of PPy/Fe<sub>3</sub>O<sub>4</sub> nanocomposite before and after adsorption, (Inset (a) Fe<sub>3</sub>O<sub>4</sub>, and (b) PPy).

TEM and SEM images of the PPy/Fe<sub>3</sub>O<sub>4</sub> nanocomposite is shown in Figure 7.3. The PPy/Fe<sub>3</sub>O<sub>4</sub> nanocomposite in SEM image shows spherical shape particles with a smooth uniform morphology caused by the deagglomerating effect of the polymer coating the nanoparticles. The particle size diameter ranges from 10-30 nm, with particle average size of  $10.6 \pm 6$  and  $10.4 \pm 10$  nm for TEM and SEM image analysis shown in Figures 7.3(a-b). The average particle size distribution obtained were fitted with the Gaussian function using ImageJ software. From TEM images, Fe<sub>3</sub>O<sub>4</sub> nanoparticles are observed to be encapsulated by the polymer matrix PPy, with the PPy/Fe<sub>3</sub>O<sub>4</sub> nanocomposite being polydispersed. The morphology of the adsorbent also shows a core-shell structure with the Fe<sub>3</sub>O<sub>4</sub> crystalline magnetic core being covered by the PPy shell (Figure 7.3(a)). The EDX spectra (Figure 7.3(c)) confirms the existence of C, O, N, Cl and Fe as the predominant elements in PPy/Fe<sub>3</sub>O<sub>4</sub> nanocomposite with peaks observed at 0.27 keV, 0.51 keV, 0.36 keV, 2.61 keV and 0.69 and 6.39 keV. This confirms the incorporation of Fe<sub>3</sub>O<sub>4</sub> into the polypyrrole polymer. The EDX analysis also shows that the PPy/Fe<sub>3</sub>O<sub>4</sub> structure is composed of 58.54% carbon, 14.55% nitrogen, 5.71% chloride, 10.35% oxygen and 10.85% iron.

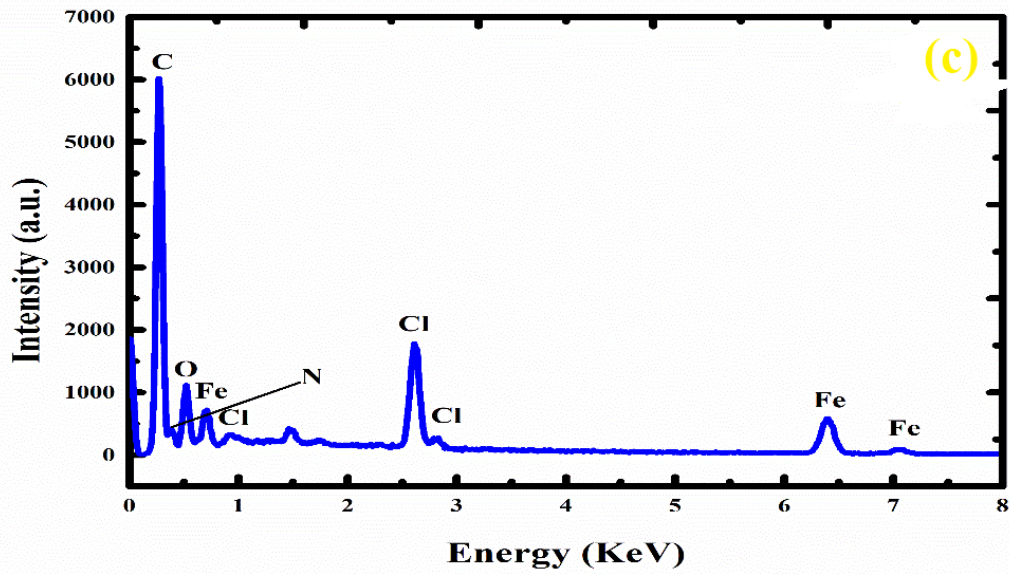
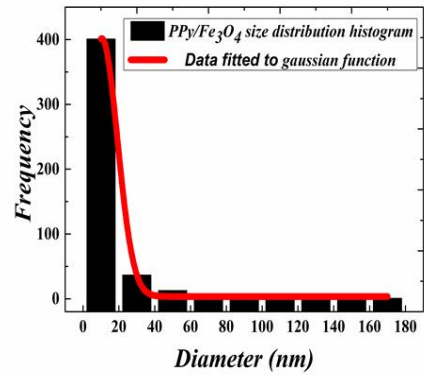
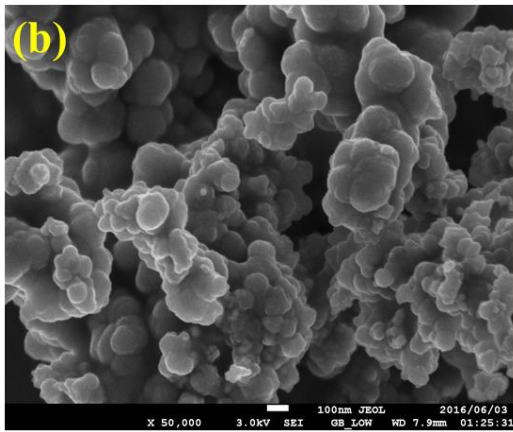
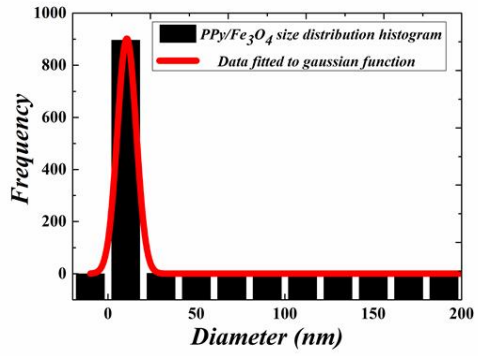
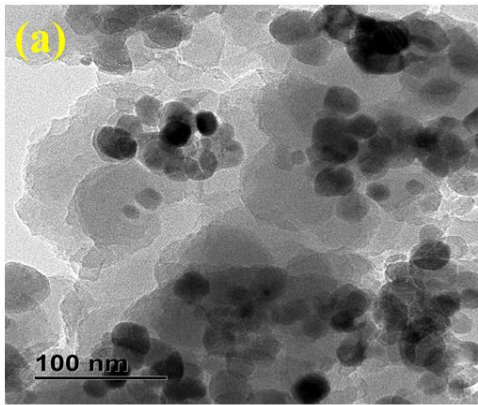


**Figure 7.3**(a) TEM image of polypyrrole magnetic nanocomposite, with histogram obtained from TEM showing the size distribution of the MNC fitted with a Gaussian fitting (b) SEM image of polypyrrole magnetic nanocomposite, with histogram obtained from TEM showing the size distribution of the MNC fitted with Gaussian fitting and (c) EDX spectra of PPy/Fe<sub>3</sub>O<sub>4</sub> nanocomposite before adsorption.

The Nitrogen adsorption-desorption isotherm of PPy/Fe<sub>3</sub>O<sub>4</sub> is shown in Figure 7.4. The curve of the magnetic nanocomposite is a characteristic type IV nitrogen adsorption-desorption isotherm, which describes a mesoporous material as categorized by IUPAC. The PPy/Fe<sub>3</sub>O<sub>4</sub> nanocomposite has a hysteresis loop that closes at the relative pressure of 0.88 P/P<sub>0</sub>. The BET surface area, BJH cumulative volume of pores and BJH average pore diameter of the magnetic nanocomposite were found to be 28.77 m<sup>2</sup>/g, 0.06 cm<sup>3</sup>/g and 15.82 nm. The tabulated values from the BET analysis is shown in Table 7.1 for polypyrrole magnetic nanocomposite. [34-36].

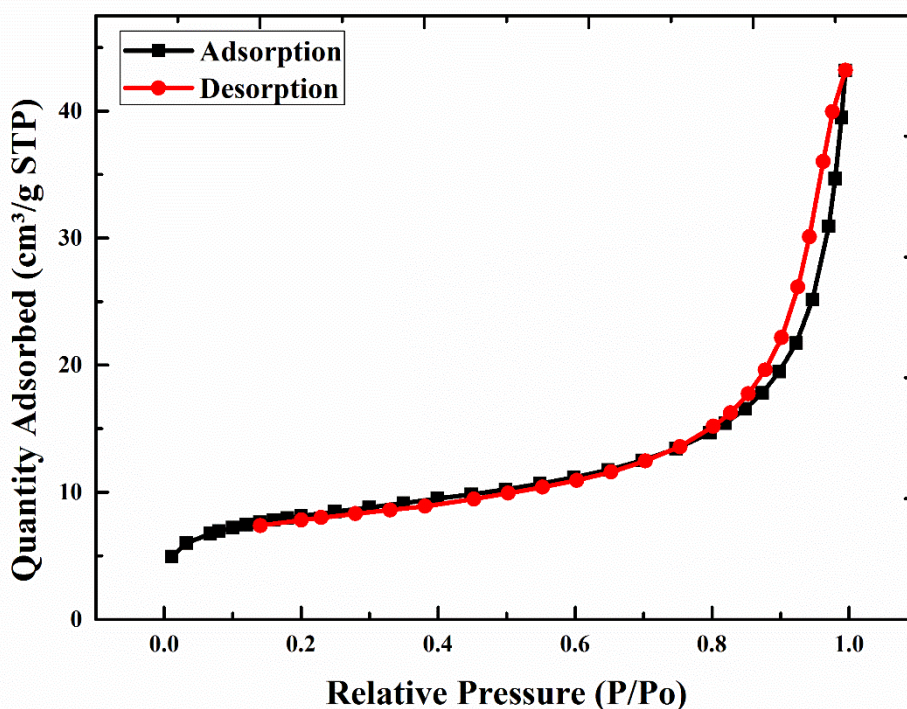


**Figure 7.4** N<sub>2</sub> adsorption-desorption isotherms of polypyrrole magnetic nanocomposite.

**Table 7.1:** Surface parameters of PPy/Fe<sub>3</sub>O<sub>4</sub> nanocomposite sample

Sample	BET surface area (m <sup>2</sup> .g <sup>-1</sup> )	BJH cumulative pore of volume (cm <sup>3</sup> .g <sup>-1</sup> )	BJH average pore diameter (nm)
PPy/Fe <sub>3</sub> O <sub>4</sub> nanocomposite	28.7688	0.063102	15.8235

The ESR spectra for magnetic nanocomposite before and after adsorption of congo red evaluated at room temperature is shown in Figure 7.5. The line shapes are observed to be symmetrical and the resonance signal is wide and broad with a linewidth value of about 1400 Gauss. The g-factor measurement of the unknown signal can be of valuable help in identifying a signal. For Fe<sup>3+</sup>, the g-factor is determined to be 1.4-3.1 for low spin and 2.0-9.7 for high spin complexes. The g-factor of the synthesized magnetic nanocomposite was found to be  $\approx 2.25$  Gauss using  $g = \frac{h\nu}{\beta H_r}$  ((where  $h$  is the Planck constant ( $6.626 \times 10^{-27}$  ere/s),  $\beta$  is a universal constant ( $9.274 \times 10^{-21}$  Erg/G),  $\nu$  is frequency ( $9.44 \times 10^9$  Hz) and  $H_r$  is the resonance of magnetic field (3000 G)), which is due to Fe<sup>3+</sup> low spin interactions. Such interactions show a superparamagnetic behaviour characterised by the presence of clusters. The shapes and the field location are identical to standard magnetic nanoparticle suspension and are consistent with ESR spectra of superparamagnetic iron oxide nanoparticles [37-40]. The line shape of the adsorbent after congo red adsorption was simulated with Gaussian and Lorentzian functions, with the line shape of the adsorbent fitting better to the Gaussian function, with a 67% compared to 31% for Lorentzian functions (Figure 7.5(B and C)). A characteristic of ferromagnetic resonance (FMR) is because of the dominant Gaussian function fitting (Figure 7.5(B)). The predominated part of the PPy/Fe<sub>3</sub>O<sub>4</sub> been magnetic is confirmed by this [41-42]

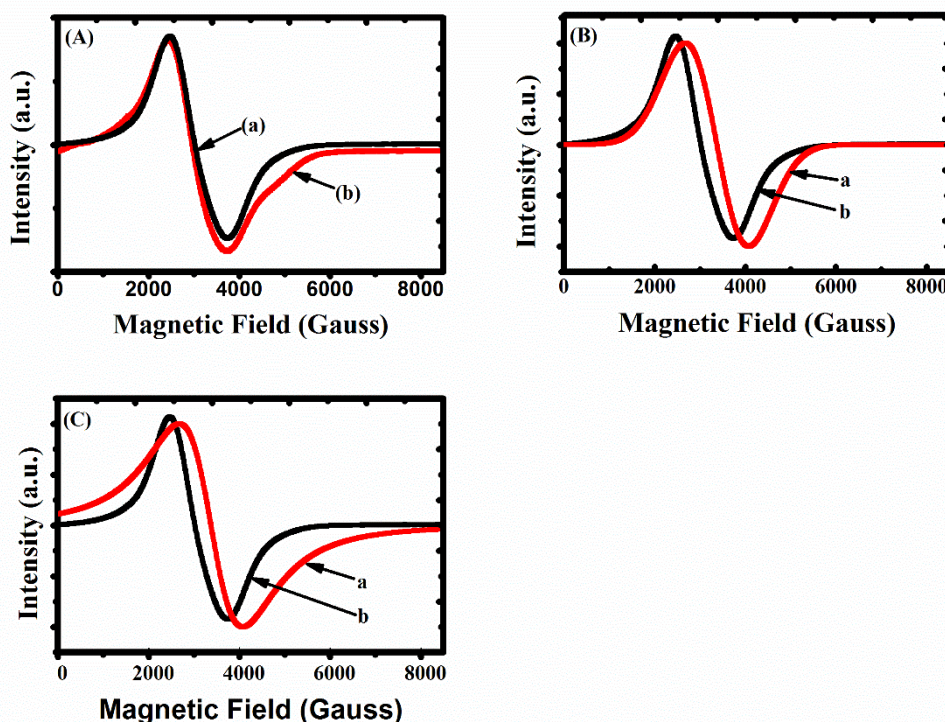


**Figure 7.5**(A)(a) ESR spectra of PPY/Fe<sub>3</sub>O<sub>4</sub> nanocomposite after congo red adsorption and (b) before congo red adsorption, (B)(a) ESR spectra of PPY/Fe<sub>3</sub>O<sub>4</sub> nanocomposite after congo red adsorption fitted to Gaussian fitting and (b) ESR spectra of PPY/Fe<sub>3</sub>O<sub>4</sub> nanocomposite after congo red adsorption and (C)(a) ESR spectra PPY/Fe<sub>3</sub>O<sub>4</sub> nanocomposite after congo red adsorption fitted to Lorentzian fitting and (b) ESR spectra PPY/Fe<sub>3</sub>O<sub>4</sub> nanocomposite after congo red adsorption.

A plot of magnetisation (emu/g) vs magnetic field (Oe) measured at 300 K (Figure 7.6) shows a magnetisation hysteresis loop with a zero-remanence magnetisation ( $H_r$ ), coercivity field ( $H_c$ ) and a saturation magnetization ( $M_s$ ) of 23 emu/g. The absence of hysteresis loops, remanence, and coercivity confirms that the polypyrrole magnetic nanocomposite is superparamagnetic. The saturation magnetisation of the nanocomposite is lower than those of magnetite, as the surface magnetic anisotropy is changed by the polypyrrole acting as a surfactant, which leads to an increase of the surface spins disorientation resulting in a decrease of the magnetic moment. This change is due to quantum size effects and increases in the surface area of the nanosized magnetite particles create superparamagnetic [43-45].

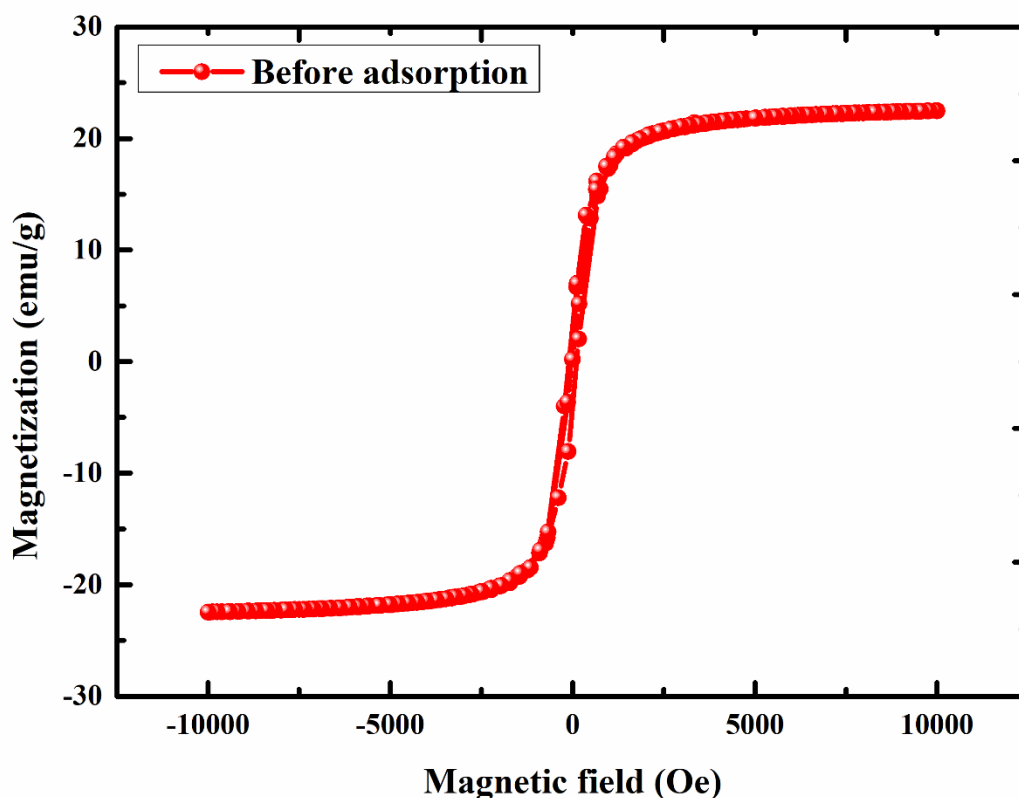


**Figure 7.6** M-H curve at room temperature for PPy/Fe<sub>3</sub>O<sub>4</sub> nanocomposite.

### 7.2.2 Effect of pH on Congo Red Adsorption Influenced by Magnetic Field

The key factor affecting the adsorption process is pH, as wastewater from textile industries has a range of pH values. The degree of ionisation of dye is also affected by pH. At pH 7, the colour of congo red in aqueous solution is solid red. This changes to blue-black at acid pH and red at alkaline pH (10-12). This red colour is slightly different from the original red colour of congo red dye at neutral pH [46-49]. The two main forces that play a role in the adsorption process are electrostatic forces and chemical interaction of the adsorbent and adsorbate [50]. The congo red percentage removal increased as the pH value was increased from pH 2-4, subsequently decreasing as the pH is increased from pH 6-10 (Figure 7.7(a)). At pH 2, increase concentration of hydrogen ions in the solution promotes the build-up of H<sup>+</sup> ions on the nanocomposite adsorption sites (PPy/Fe<sub>3</sub>O<sub>4</sub>). This increase in protonation caused a strong repulsion between H<sup>+</sup> ions on the surface of PPy/Fe<sub>3</sub>O<sub>4</sub> and the protonated congo red. Competition between protons (H<sup>+</sup>) from the aqueous medium and congo red species for the adsorption site of PPy/Fe<sub>3</sub>O<sub>4</sub>,

leads to a suppressed removal of congo red at pH 2 [51-52]. The optimal pH for adsorption/removal of congo red onto PPy/Fe<sub>3</sub>O<sub>4</sub> nanocomposite from aqueous solution induced by a magnetic field was found at pH 4. This is attributed to the increasing H<sup>+</sup> ions on the adsorbent surface, resulting in electrostatic attraction between the positively charged adsorbent surfaces with the negatively charged adsorbate, which allows for the adsorption of congo red onto the nanocomposite. As the pH is increased above pH 4, an increase in OH<sup>-</sup> ions on the adsorbent surface results in electrostatic repulsion between the negatively charged adsorbent with the negative congo red ions, as congo red has the property to aggregate in aqueous and organic solution. The aggregation phenomenon is important for high congo red concentrations at low pH. The protonation of the functional groups from congo red at a low pH been restricted is responsible for this [53].

### **7.2.3 Effect of Adsorbent Dosage on Congo Red Adsorption under Magnetic Field Influence**

A vital parameter that ascertains the capacity of an adsorbent for a given initial concentration of an adsorbate is adsorbent dosage. The size and amount of adsorbent must be optimised for adsorption process. The adsorbent dosage is the most critical parameters for rapid and efficient dye removal [54, 47]. The effect of adsorbent dosage on the adsorption of congo red influenced by magnetic field intensity of 18.99 mT was studied at room temperature. It is observed from Figure 7.7(b), that the amount of congo red adsorbed by the adsorbent increased from 7-99% as the adsorbent dosage is increased from 0.05-0.20 g. This increase in removal efficiency is related to the availability of more active adsorption sites for congo red adsorption, which is directly related to the adsorbent mass. At low adsorbent dosage, the active adsorption sites are insufficient for the adsorbate to occupy. At high adsorbent dosage, the active adsorption sites are sufficient for the adsorbate to occupy, which leads to an increase in adsorption attributed to the increased adsorbent surface area and adsorption sites available.

### **7.2.4 Effect of Initial Concentration on Congo Red Adsorption under Magnetic Field Influence**

The initial concentration effect on congo red adsorption under the influence of a magnetic field was examined at five different initial concentrations. As shown in Figure 7.7(c), increased in the initial congo red concentration (100-400 mg/L) leads to a decrease in the adsorption efficiency (100-88%). The ratio of available surface area to initial concentration of congo red is

high at low concentrations; thereby adsorption efficiency tends to increase, as the initial concentration of the adsorbate is inversely related to the adsorption efficiency. As the initial concentration increases, efficiency decreases. The quantity of congo red absorbed per unit mass of the adsorbent increased from 33-117 mg/g as the equilibrium concentration of the adsorbate increased from 0.3-50 mg/L for initial concentrations of 100-400 mg/L. The high driving force for mass transfer in high dye concentrations causes an increase in the adsorption capacity as the initial concentration is increased [55].

### **7.2.5 Effect of Magnetic Field and Exposure Time on Congo Red Adsorption**

Results from the adsorption of congo red ions onto polypyrrole magnetic nanocomposite influenced by magnetic field of different intensity and magnetic exposure time are shown in Figure 7.7(d-e). An increase is observed in the removal percentage of congo red ions adsorbed onto polypyrrole magnetic nanocomposite under the influence of increasing magnetic field, with increased removal percentage from 55-94% as the intensity of magnetic field is increased from 11.84-18.99 mT. A maximum removal percentage of congo red is observed at 18.99 mT magnetic field. For magnetic exposure time and no applied fields are experimental results (used as a control), an increase in the removal percentage of congo red ions as the magnetic exposure time is increased from 10-120 min is observed, with removals of 79-94% at a constant magnetic field of 18.99 mT. when exposure time experiment is compared to no field applied experimental results (control) at the same exposure time, the removal percentage of congo red ions adsorbed by the adsorbent was 5-15%. Increase in the removal percentage might be due to the magnetic field promoting the movement of the molecules on a macroscopic scale, as well enhancement in the reorientation of the magnetic moment of the adsorbent or the adsorbate, which increases the number of active sites of the adsorbent released. An increase in the collision/interaction between the congo red molecules and the adsorbent leads to an increase in the proportion of congo red adsorbed onto the active sites on the adsorbent [18, 22-23, 26].

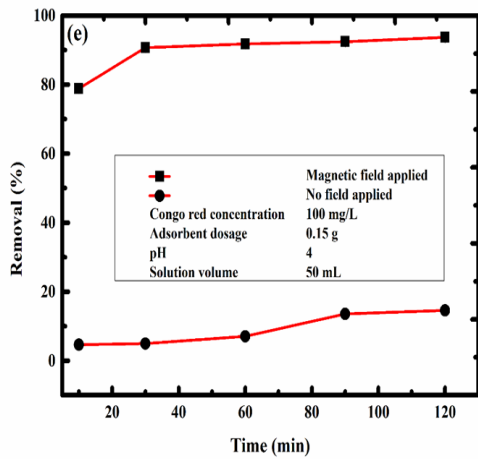
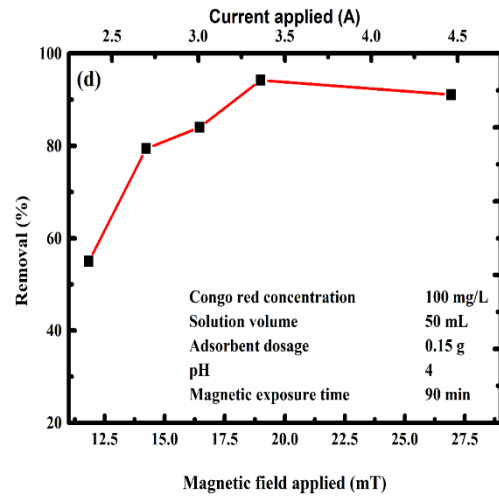
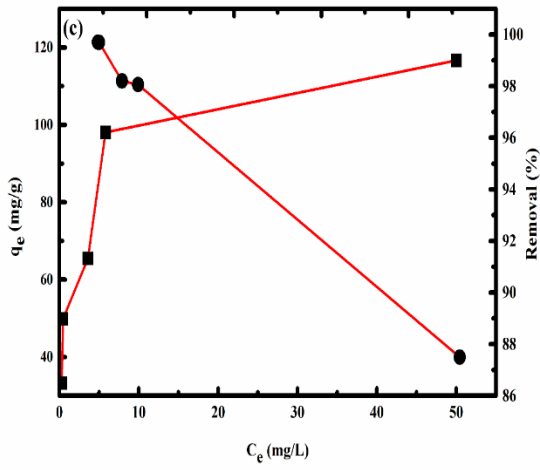
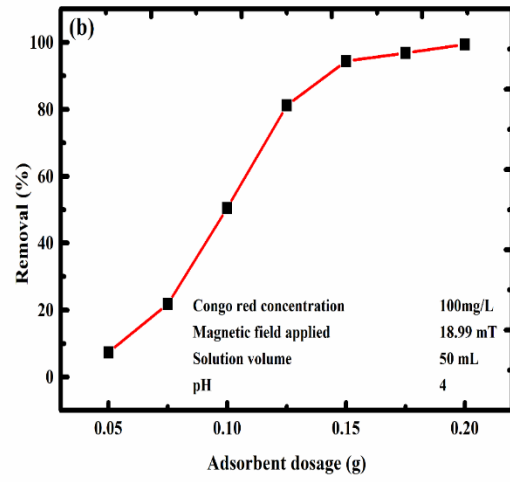
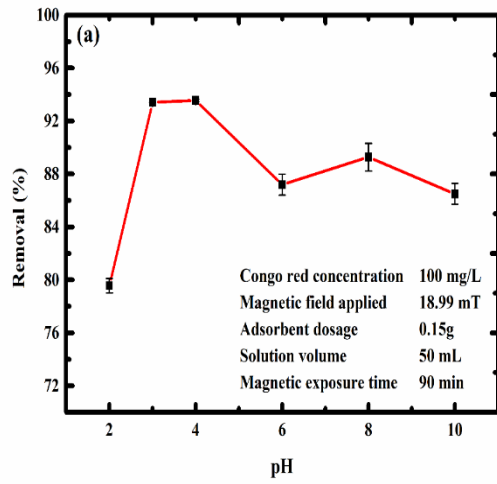


**Figure 7.7**(a) pH effect on congo red adsorption under the influence of MF (b) adsorbent dosage effect on CR adsorption under MF influence (c) initial concentration effect on CR adsorption under MF influence (d) effect of magnetic field intensity on the adsorption of CR and (e) effect of magnetic exposure time on adsorption of CR.

### 7.3 Adsorption Isotherms

The interaction between the adsorbate molecules and the adsorbent surface is best described by adsorption isotherm models. To optimise the design of adsorption systems, a suitable correlation for equilibrium curves is essential [55-56]. Thus, congo red adsorption onto polypyrrole magnetic nanocomposite is ascertained as a function of congo red equilibrium concentration ( $C_e$ ) and the related adsorption isotherm is plotted in Figure 7.8. To study the adsorption of the adsorbate onto the adsorbent, Langmuir and Freundlich isotherm models are adjusted with the isotherm data. The Langmuir adsorption isotherm model assumes that the adsorptions occur at specific homogeneous sites on the adsorbent. It is successfully used in many monolayer adsorption processes. The nonlinear and linearize form of the Langmuir equation are represented by the following equations:

$$q_e = \frac{q_m b C_e}{1 + b C_e} \quad 7.1$$

$$\frac{C_e}{q_e} = \frac{1}{q_m b} + \frac{C_e}{q_m} \quad 7.2$$

The maximum monolayer adsorption capacity, the equilibrium dye concentration and the Langmuir isotherm constant related to the affinity of the binding sites are represented by  $q_m$  (mg/g),  $C_e$  (mg/L) and  $b$  (L/mg). An additional analysis of the Langmuir equation is made on the fundamentals of a dimensionless equilibrium parameter ( $R_L$ ), also known as the separation factor, which is defined as;

$$R_L = \frac{1}{1 + b C_o} \quad 7.3$$

where  $C_o$  is initial adsorbate concentration (mg/L),  $R_L$  values indicate whether the adsorption process is irreversible ( $R_L = 0$ ), favourable ( $0 < R_L < 1$ ), linear ( $R_L = 1$ ), or unfavourable ( $R_L > 1$ ) [57].

Freundlich isotherm is an empirical model based on the assumption of the heterogeneous surface with a non-uniform adsorption heat distribution over the surface of the adsorbent. The non-linearize and linearize form of Freundlich isotherm is given by the following equations:

$$q_e = k_f C_e^{\frac{1}{n}} \quad 7.4$$

$$\ln q_e = \ln k_f + \frac{1}{n} \ln C_e \quad 7.5$$

The adsorption capacity and intensity of adsorption constants are associated with  $k_f$  and  $1/n$  [16, 58]. Figures 7.8(a-b) shows the linearized forms of Langmuir and Freundlich isotherms models. Parameters for Langmuir and Freundlich isotherms models were estimated from plots for  $\frac{C_e}{q_e}$  vs.  $C_e$  and  $\ln q_e$  vs.  $\ln C_e$  respectively at a solution temperature of  $31 \pm 1^\circ\text{C}$ . Based on the correlation coefficient values for the two models, the higher correlation coefficient value for Langmuir isotherm model ( $R^2 = 0.99977$ ) fitted well to the experimental data very well when compared to Freundlich isotherm model ( $R^2 = 0.85488$ ). This indicates a homogeneous distribution of the active sites on the surface of the polypyrrole magnetic nanocomposite and the chemical adsorption between congo red and the nanocomposite. The values of the Langmuir equilibrium coefficient, 'b', Langmuir maximum monolayer adsorption capacity  $q_m$  and the dimensionless separation factor ' $R_L$ ' were estimated to be 0.72 L/g, 119.76 mg/g and 0.014 respectively, with the dimensionless separation factor ' $R_L$ ' signifying that the adsorption process is favourable. The Freundlich parameters  $k_f$  and  $n$  values are 52.52 and 4.34. The intensity of adsorption constant (n) from the Freundlich isotherm is greater than 1, which shows a favourable adsorption. The Langmuir and Freundlich isotherm parameters calculated from the slope and intercept of the linear equations is shown in Table 7.2. Table 7.3 shows the comparison of congo red adsorption capacity of PPy/Fe<sub>3</sub>O<sub>4</sub> nanocomposite with other reported adsorbents.

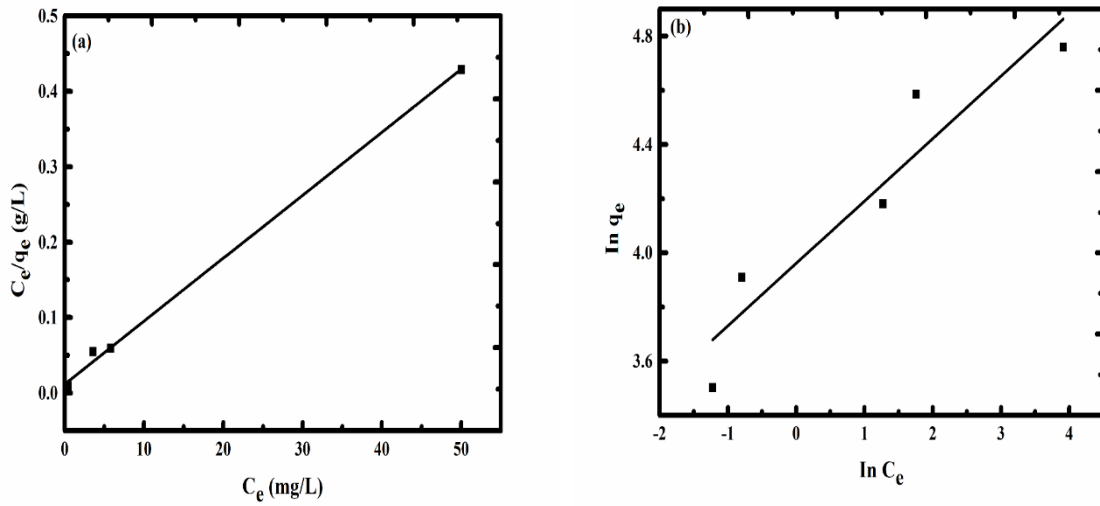


**Figure 7.8**(a) Fit of equilibrium data to Langmuir isotherm model and (b) Fit of equilibrium data to Freundlich isotherm model.

**Table 7.2:** Langmuir and Freundlich isotherm constants for adsorption of congo red dye on 0.15 g PPy/Fe<sub>3</sub>O<sub>4</sub> nanocomposite

Temperature	Langmuir constant				Freundlich constant		
	$q_m$	$b$	$R_L$	$R^2$	$k_f$	$n$	$R^2$
$31 \pm 1$ °C	119.76	0.72	0.014	0.99977	52.52	4.34	0.85488

**Table 7.3:** Comparison of congo red adsorption capacity of PPy/Fe<sub>3</sub>O<sub>4</sub> nanocomposite with other reported adsorbents.

Adsorbent	q <sub>m</sub> (mg/g)	Optimum pH	Reference
SPS/MNPs	71.429	7	10
PAn/TiO <sub>2</sub> nanocomposite	80.645	6	59
Iron oxide/carbon nanocomposites	105.3	-	60
Leucaena leucocephala (Subabul) seed pods	4.4131	5	54
Al <sub>2</sub> O <sub>3</sub> /Ni <sub>0.5</sub> Zn <sub>0.5</sub> Fe <sub>2</sub> O <sub>4</sub> Microfibers	75.5	6.5	61
Magnetic iron oxide nanopowder	54.46	6	9
Chitosan/montmorillonite nanocomposite	54.52	4	62
PPy/Fe <sub>3</sub> O <sub>4</sub> nanocomposite	119.76	4	Present Study

#### 7.4 Adsorption Kinetics

The rate of solute uptake governs the adsorption reaction residence time, best described by the adsorption kinetics [63]. The dynamics of congo red sorption onto polypyrrole magnetic nanocomposite was evaluated at a magnetic field of 18.99 mT. The exposure time was varied from 10-120 min with initial congo red concentrations of 20-80 mg/L. The congo red dyes uptake was analysed at different exposure time intervals as shown in Figure 7.9(a). Congo red adsorption is fast, increases with an increase in exposure time and initial concentration, with equilibrium been attained from 40-120 min under the influence magnetic field is observed. To understand the mechanism of congo red adsorption onto the adsorbent, the pseudo-first-order and pseudo-second-order model were used to fit the kinetics data. The linearize forms of the pseudo-first-order and pseudo-second-order kinetics equations are:

$$\log(q_e - q_t) = \log q_e - \frac{k_1}{2.303} t \quad 7.6$$

$$\frac{t}{q_t} = \frac{1}{k_2 q_e^2} + \frac{1}{q_e} t \quad 7.7$$

The congo red uptake at time  $t$ , the pseudo-first and second order rate constants are represented by  $q_t$  (mg/g),  $k_1$  and  $k_2$  (1/min). The linear plot of equations (7.6) and (7.7) are shown in Figure 7.9(b-c). From the plot, the rate constants and the correlation coefficients were determined given in Table 4. The correlation coefficients of the pseudo-second-order model gave a better explanation of the congo red dye adsorption onto PPy/Fe<sub>3</sub>O<sub>4</sub> ( $R^2 = 0.99959, 0.99936$  and  $0.99347$ ) when equated to the pseudo-first order model ( $R^2 = 0.96798, 0.95031$  and  $0.95280$ ), which indicates that the kinetics congo red dye adsorption onto PPy/Fe<sub>3</sub>O<sub>4</sub> is governed by this model (pseudo-second order), with the rate constants ( $k_2$ ) decreasing from 0.024-0.003 g.min/mg with an increase in congo red dye initial concentration. The equilibrium sorption uptake were 18.66, 29.79 and 39.05 mg/g for the linear pseudo-second-order model under a magnetic field applied influence. Thus, the adsorption capacity ( $q_e$ ) from the experimental values fits very well with the theoretical adsorption capacity ( $q_e, \text{cal}$ ) values calculated from the pseudo-second-order model. The trend of equilibrium sorption uptake ( $q_e$ ) values obtained from the linear fit of the pseudo-second-order model showed an increase with an increase in initial concentration, which is attributed to adsorption being a passive process, driven specifically by concentration gradient as a driving force [64]. These results confirm that congo red adsorption kinetics can be better defined by the pseudo-second-order model. Table 7.4 shows the kinetics parameters for adsorption of congo red ions from aqueous medium.

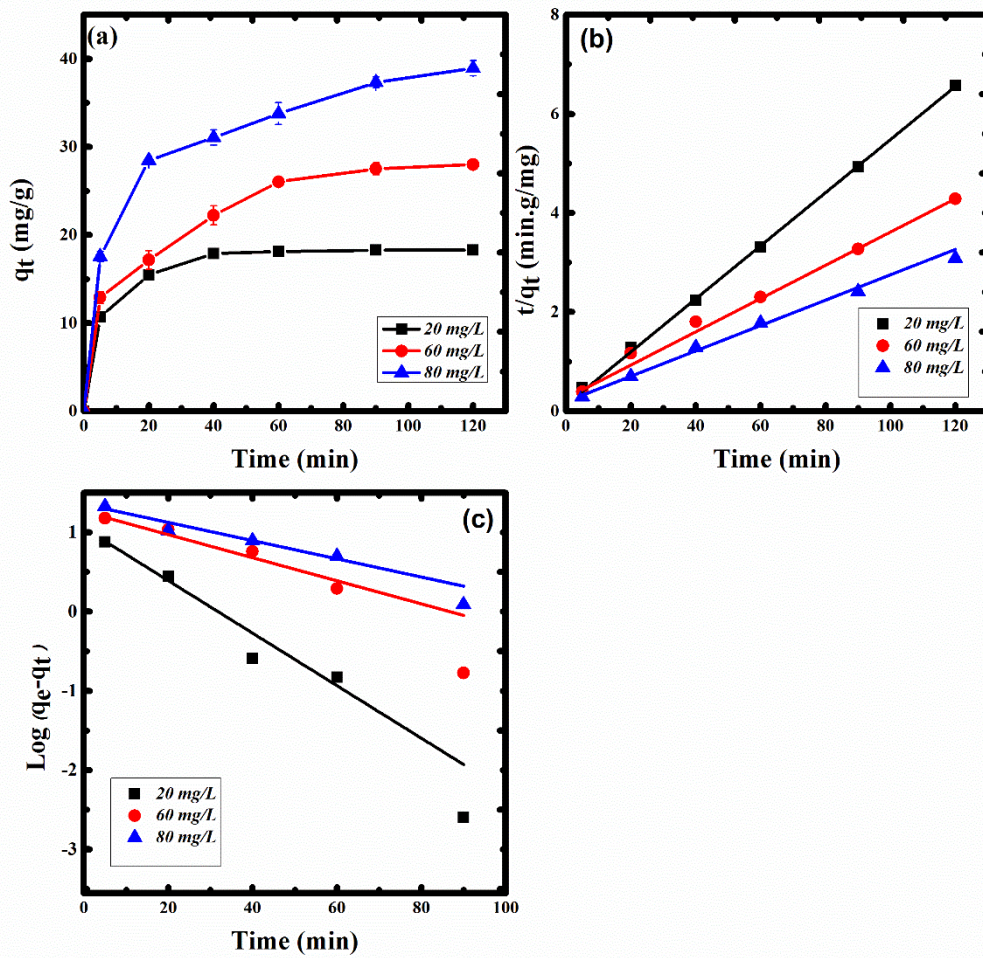


**Figure 7.9**(a) Kinetics data for CR adsorption onto PPy/Fe<sub>3</sub>O<sub>4</sub>, (b) Pseudo-first-order model for adsorption of CR onto PPy/Fe<sub>3</sub>O<sub>4</sub>, and (c) Pseudo-second-order model for adsorption of CR onto PPy/Fe<sub>3</sub>O<sub>4</sub>.

**Table 7.4:** Kinetics parameters for adsorption of congo red ions from aqueous medium.

Pseudo-first-order model				Pseudo-second-order model		
$C_e$ mg/L	$k_1$ (1/min)	$q_e$ (mg/g)	$R^2$	$k_2$ (g/mg/min)	$q_e$ (mg/g)	$R^2$
20	0.076	11.34	0.96798	0.024	18.66	0.99959
60	0.034	18.31	0.95031	0.004	29.79	0.99936
80	0.027	22.67	0.95200	0.003	39.05	0.99347

### 7.5 Reuse of Pre-treated PPy/Fe<sub>3</sub>O<sub>4</sub>

The potential for recycling of adsorbent is a very important parameter to assess their practicability. If strong base such NaOH can desorb the dye, it can be said that the attachment of the dye onto the adsorbent is ion exchange [65]. NaOH was used for the elution of congo red dyes from PPy/Fe<sub>3</sub>O<sub>4</sub> for three cycles to desorb congo red adsorbed on the surface of PPy/Fe<sub>3</sub>O<sub>4</sub> after adsorption. To regenerate adsorption sites after desorption of congo red dye with NaOH, the adsorbent is subsequently treated with 2M HCl. The results of the adsorption-desorption process using NaOH is shown in Figure 7.10. It is observed that congo red removal remains constants (96%) up to the second cycle and that there is a slight drop in the congo red removal at the third cycle (94%). The slight decrease in removal may be due to breakage of the polymer chain by repeated acid/base treatment of the nanocomposite during the regeneration process [66].

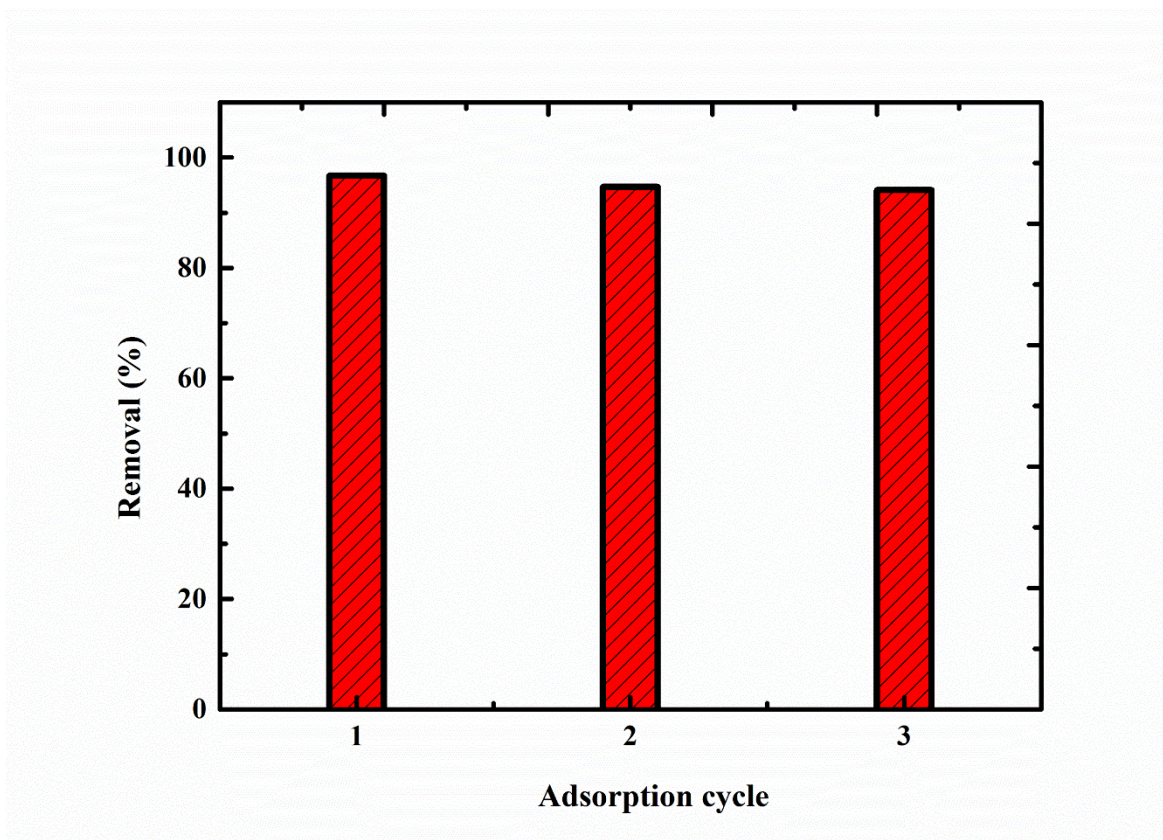


**Figure 7.10** Adsorption-desorption cycles.

## 7.6 Conclusion

Using magnetic field to overcome the harmful effect of water pollution is considered as a potential technology. Enhanced removal of congo red from aqueous solutions onto polypyrrole magnetic nanocomposite under the influence of magnetic field and magnetic exposure time was observed, with percentage removal of 94 % under the influence of magnetic field. When no field was applied at the same magnetic exposure time, the percentage removal was 15 %. This increase in removal efficiency is due to the magnetic force applied when a charged particle passes through a magnetic field, thereby realigning the magnetic moment of either the adsorbent or adsorbent for quick adsorption. From kinetics and adsorption isotherm models, it is observed that there was significantly enhanced adsorption of congo red, as the initial concentration is increased. The pseudo-second model best describes the adsorption of congo red onto the adsorbent. The equilibrium adsorption capacity obeys the Langmuir isotherm with a maximum adsorption capacity of 119.76 mg/g.

## 7.7 References

- [1] F. Ferrarini, I. R. Bonetto, J. S. Crespo and M. Giovanela, **2016**, *Water Science, and Technology*, 73, 2132-2142.
- [2] A. A. Tireli, F. C. F. Marcos, L. F. Oliveira, L. Do Rosario Guimaraes, M. C. Guerreiro and J. P. Silva, **2014**, *Applied Clay Science*, 97, 1-7.
- [3] O. F. G. Vazquez, M. M. Virgen, V. H. Montoya, R. T. Gomez, J. L. A. Flores, M. P. Cruz and M. A. M. Moran, **2016**, *Industrial, and Engineering Chemistry Research*, 55, 9323-9331.
- [4] A. Afkhami, and R. Moosavi, **2010**, *J. of Hazardous Materials*, 174, 398-403.
- [5] H. Kaur, S. Kaur, and R. Kaur, *Kinetic*, **2014**, *Chemical Science Transactions*, 3, 1300-1309.
- [6] W. B. Mbarek, M. Azabou, E. Pineda, N. Fiol, L. Escoda, J. J. Sunol and M. Khitouni, **2017**, *RSC Advances*, 7, 12620–12628.
- [7] A. Mittal, L. Kurup, and J. Mittal, **2007**, *J. of Hazardous Materials*, 146, 243-248.
- [8] H. R. Pouretedal and M. H. Keshavarz, **2011**, *International J. of Physical Sciences*, 27, 6268-6279.
- [9] O. Paşka, R. Ianoş, C. Păcurariu and A. Brădeanu, **2014**, *Water Science & Technology*, 69, 1234-1240.
- [10] A.M. Al-Sabagh, Y.M. Moustafa, A. Hamdy, H.M. Killa, R.T.M. Ghanem, and R.E. Morsi, **2017**.
- [11] O. V. Makarchuk, T. A. Dontsova and I. M. Astrelin, **2016**, *Nanoscale Research Letters*, 11, 161.
- [12] Y. Ali, R. Samaneh, R. Zohre, and J. Mostafa, **2014**, *Current World Environment*, 9, 1008-1016.
- [13] R. A. Barrett and S. A. Parsons, **1998**, *Water Resources*, 32, 609-612.
- [14] P. L. Hariani, M. Faizal, R. Seliabudidaya, M. Seliabudidaya and D. Setiabudidaya, **2013**, *J. of Environmental Science and Development*, 4, 336-340.
- [15] M. M. K. Alkhazan and A. A.N. Saddiq, **2010**, *J. of Evolutionary Biology Research*, 2, 7-14.
- [16] G. Li, W. Zhu, C. Zhang, S. Zhang, L. Liu, L. Zhu and W. Zhao, **2016**, *Bioresource Technology*, 206, 16-22.
- [17] J. Bogatin, N. P. Bondarenko, E. Z. Gak, E. E. Rokhinson, and I. P. Ananyev, **1999**, *Environ. Sci. Technol*, 33, 1280-1285.

- [18] R. R. Mohammed, M. R. Ketabchi and G. Mckay, **2014**, *Chemical Engineering J.*, 234, 31-42
- [19] L. Duan, S. Guo, and J. Yang, **2012**, *Advances in Chemical Engineering and Science*, 2, 101-107.
- [20] J. F. De Brito, L. De Oliveira Ferreira, M. C. R. Pereira, J. P. Da Silva and T. C. Ramalho, **2012**, *Water, Air, and Soil Pollution*, 223, 3545-3551.
- [21] M. Foroughi, M. Khiadani (Hajian), M. M. Amin, H. R. Pourzamani and M. V. Dastjerdi, **2013**, *International J. of Environment Health Engineering*, 2, 31.
- [22] X. Hao, H. Liu, G. Zhang, H. Zou, Y. Zhang, M. Zhou, and Y. Gu, **2012**, *Applied Clay Science*, 55, 177-180.
- [23] L. I. Bel'chinskaya, N. A. Khodosova and L. A. Bityutskaya, **2009**, *Protection of Metals and Physical Chemistry of Surface*, 45, 203-206
- [24] R. Cai, H. Yang, J. He and W. Zhu, **2009**, *J. of Molecular Structure*, 938, 15-19.
- [25] N. S. Zaidi, J. Sohaili, K. Muda and M. Sillanpaa, **2013**, *Separation and Purification Reviews*, 43, 206-240.
- [26] F. F. Fondeur, D. T. Hobbs and S. D. Fink, **2010**, *Separation Science and Technology*, 45, 1876-1879.
- [27] M. Khiadani (Hajian), M. Zarrabi and M. Foroughi, **2013**, *J. of Environmental Health Science and Engineering*, 11, 43.
- [28] S. S. Bhatnagar, P. L. Kapur, and A. N. Kapur, **1937**, *The London, Edinburgh, and Dublin Philosophical Magazine*, 23, 256-264.
- [29] J. Guo, H. Gu, H. Wei, Q. Zhang, N. Haldolaarachchige, Y. Li, D. P. Young, S. Wei, and Z. Guo, **2013**, *J. of Physical Chemistry*, 117, 10191-10202.
- [30] K. Suri, S. Annapoorni and R. P. Tandon, **2001**, *Bulletin of Materials Science*, 24, 563-567.
- [31] R. Turcu, O. Pana, A. Nan, I. Craciunescu, O. Chauvet and C. Payen, **2008**, *J. of Physics D: Applied Physics*, 41, 245002.
- [32] S. Kasisomayajula, N. Jadhav, and V. J. Gelling, **2016**, *RSC. Adv*, 6, 967-977.
- [33] F. Khalilian, M. Rezaee, and M. K. Gorgabi, **2015**, *Analytical Methods*, 7, 2182-2189.
- [34] K. Zhu, C. Chen, H. Xu, Y. Gao, X. Tan, A. Alsaedi, T. Hayat, **2017**, *ACS Sustainable Chemistry and Engineering*, 5, 6795-6802,
- [35] B. Kakavandi, R.R. Kalantary, A.J. Jafari, S. Nasser, A. Ameri, A. Esrafil, and A. Azari, **2015**, *Clean Soil Air Water*, 43, 1157-1166,

- [36] M. H. Mohamed, M. Pirlot, M. K. Danquah, and L. D. Wilson, **2017**, *J. of Materials Science and Chemical Engineering*, 5, 12-24.
- [37] R. Sivashankar, A. B. Sathya V. Vasatharaj and V. Sivasubramanian, **2014**, *Environmental Nanotechnology, Monitoring, and Management*, 1, 36-49.
- [38] B. Chertok, A. J. Cole, A. E. David and V. C. Yang, **2010**, *Molecular Pharmaceutics*, 7, 375-385.
- [39] Y. Koseoglu, F. Yildiz, D. K. Kim, M. Muhammed and B. Aktas, **2004**, *Phys Stat. Sol;* 12, 3511-3515.
- [40] J. B. Mamani, I. F. Gamarra and G. E. De Souza Brito, **2014**, *Materials Research*, 17, 542-549.
- [41] M. Bhaumik, T. Y. Leswif, A. Maity, V. V. Srinivasu and M. A. Onyango, **2011**, *J. of Hazardous Materials*, 186, 150-159.
- [42] O. A. Kuznetsov, O. N. Sorokina, V. G. Leontiev, O. A. Shlyakhtin, A. L. Kovarski and A. A. Kuznetsov, **2007**, *J. of Magnetism and Magnetic Materials*, 311, 204-207.
- [43] T. Theivasanthi and M. Alagar, **2014**, arXiv preprint arXiv, 1402-1431.
- [44] A. M. Muliwa and M. S. Onyango, **2014**, In *Proceedings of Sustainable Research and Innovation*, 5, 83-90.
- [45] N. Shamim, L. Hong, K. Hidajat, and M. S. Uddin, **2006**, *J. of Colloid and Interface Science*, 304, 1-8.
- [46] Z. Hu, H. Chen, F. Ji, and S. Yuan, **2010**, *J. of Hazardous Materials*, 173, 292-297.
- [47] M. Ghaedi, S. Ramazani, and M. Roosta, **2011**, *Indian J. of Science and Technology*, 4, 1208-1217.
- [48] L. Dong, Z. Zhipeng and D. Yigang, **2016**, *J. of Dispersion Science and Technology*, 37, 73-79.
- [49] S. Kaur, S. Rani, and R. K. Mahajan, **2012**, *J. of Chemistry*, 2013.
- [50] A. Eskandarpour, K. Sassa, Y. Bando, M. Okido, and S. Asai, **2006**, *Materials Transactions*, 47, 1832 – 1837.
- [51] R. Satheesh, K. Vignesh, M. Rajarajan, A. Suganthi, S. Sreekantan, M. Kang and B. S. Kwak, **2016**, *Materials Chemistry, and Physics*, 180, 53-65.
- [52] T. V. Toledo, C. R. Bellato, C. H. Ferreira de Souza, J. T. Domingues, D. D. C. Silva, C. Reis, and P. F. Fontes, **2014**, *Quimica Nova*, 37, 1610-1617.
- [53] B. Gurunathan, D. Viswanathan, S. Rajasekar and G. B. George, **2016**, *Management of Environmental Quality*, 27, 45-58.

- [54] V. S. Shrivastava, **2012**, International J. of Chem. Tech Research, 4, 1038-1043.
- [55] H. Chen and J. Zhao, **2009**, Adsorption, 15, 381-389.
- [56] B. Saha, S. Das, J. Saiki and G. Das, **2011**, J. of Physical Chemistry, 115, 8024-8033.
- [57] W. C. Wanyonyi, J. M. Onyari, and P. M. Shiundu, **2014**, Energy Procedia, 50, 862-869.
- [58] A. Shojamoradi, H. Abolghasemi, M. Esmaili, M. Foroughi-Dahr and H. Fatoorechi, **2013**, J. of Petroleum Science and Technology, 3, 25-34.
- [59] M. Tanzifi, K. Karimipour, M. Najafifard, S. Mirchenari, **2016**, International J. of Engineering, 29, 1659-1669.
- [60] T. Hao, X. Rao, Z. Li, C. Niu, J. Wang, and X. Su, **2014**, J. of Alloys and Compounds, 617, 76-80.
- [61] X. Yang, Z. Wang, M. Jing, R. Liu, L. Jin, and X. Shen, **2014**, Water Air Soil Pollut, 225, 1819.
- [62] L. Wang, and A. Wang, **2007**, J. Hazard. Mater. 147, 979-985.
- [63] M. Ghaemi, G. Absalan, and L. Sheikhan, **2014**, J. of Iranian Chemical Society, 11, 1759-1766.
- [64] K. Parashar, N. Ballav, S. Debnath, K. Pillay and A Maity, **2016**, J. of Colloid and Interface Science, 476, 103-118.
- [65] H. Wang, Y. Shen, C. Shen, Y. Wen and H. Li, **2012**, Desalination, 284, 122-127.
- [66] M. Bhaumik, R. McCrindle, and A. Maity, **2013**, Chemical Engineering J., 228, 506-515.

## CHAPTER EIGHT

### **Result V: Velocity Measurement of Rotating Particles in Cylindrical Channel Using Particle Shadow Velocimetry**

#### **8.1 Introduction**

In the development of magnetic nanoparticles used in a broad range of applications that extend both in fundamental and applied research, there is substantial and growing interest. The study of vital physical phenomena like superparamagnetism, magnetic dipolar interactions, single electron transfer and magnetoresistance is related to the fundamental research. While the applied research is associated with the integration of magnetic nanoparticles in numerous commercial applications like ferrofluids and data storage [1]. Magnetic interaction is an important phenomenon that governs the behaviour of materials in a magnetic field. The manipulation, recovery and removal of magnetic nanoparticles using the inhomogeneous magnetic field (magnetophoresis) have emerged as a great area of interest in research and technological area. A spectrum of applications that are novel has been developed based on this concept from environmental applications like wastewater treatments and pollutant removal, to a biomedical application like protein isolation, drug delivery, magnetic hyperthermia for cancer treatment and magnetic particle imaging [2-3].

In environmental application, magnetic microspheres are tailored to adsorb target solutes or pollutants. The critical step in the different applications is the removal of the magnetic particles (plus adsorbed pollutants) using inhomogeneous magnetic fields (magnetophoresis) [4]. The magnetic force is induced into a fluid by the introducing of magnetic particles. The ability to manipulate magnetic particles using external field leads to additional applications like tagging target entities to the magnetic particles. The ability to control magnetic particles using an external magnetic field offers the choice of wireless manipulation, which leads to the opportunity for drug delivery, water decontamination using magnetic particles [5].

For the characterization and colloidal particles separation, including industrial and environmental particles and living cells, developing new measurement methods for the physical and chemical properties of these particles is required highly in several fields. The general concept of electromagnetophoresis was first studied by Kolin (1953), involves the application of the Lorentz force for migration analysis. A force is said to exert on both fluid and the particles

when the electric current is applied through the conductive fluid with particles in a homogeneous magnetic field perpendicular to the current. When the force exerted on the fluid is not equal to that working on the particles, migration of the particles is triggered [6].

In a nonuniform magnetic field, magnetic particles experience a force which comes from the interaction between the external magnetic field and the induced moment inside the magnetic particles. This is known as magnetophoresis, which has been exploited in various industrial and commercial process for separation and beneficiation of suspended solids in liquids [7]. Crystal alignment, levitation, separation, flow control of electrically conductive fluid, etc are useful functions of the magnetic field. On the other hand, electrically conductive fluid such as liquid metal, iron oxide can be controlled by the magnetic field used and a second phase motion affected through the reaction of the Lorentz force generated by the interaction between fluid or solid motion and the magnetic field [8].

Recently, colloidal suspensions of magnetic nanoparticles (MNP) have prompted a lot of research, basically due to their size and magnetic properties of the magnetic nanoparticles dispersed, allowing for their manipulation at a distance using the external magnetic field. Due to this, magnetic nanoparticles have been used in several applications where mixing at a micro-scale is a critical issue. Rotating magnetic field has remarkable potential in mixing applications. This potential comes from the fact that the external magnetic field forces the alignment of the magnetic nanoparticles with the direction of the field by exerting a magnetic torque on the magnetic moments of the magnetic nanoparticles suspended in liquids or fluids [9-10].

The time-varied magnetic field induces a rotating electric field around the nanoparticles according to Faraday's law of electromagnetic induction. For electrostatically stabilized nanoparticles, the colloidal electric double layers interact with the rotating electric field, thereby deforming the electric double layers and weaken the colloidal stability, thus leading to the amorphous aggregation of small particles [11]. The particle of magnetisable suspension interacting with a wall in electromagnetic fields influences their flow properties. To study this influence, it is essential to determine the force acting on the particle in a liquid near the boundary of the liquid [12-13]. The magnetic torque which acts against the mechanical rotation generated by the flow is caused by the shear-flow induced rotation of particles that moves the magnetic moment of the particle out of the direction of the external magnetic field. Measuring velocity experimentally is essential in understanding the fluid dynamics of complex fluids [14-15].

To give insight on the instantaneous velocities, sizes and shapes of observed particles, an in-situ diagnostic of particles in heterogeneous flow are used. The in-situ approach is an optical technique since the minimization of the impact of the observation is required to study flows representatively [16]. Volume illumination is an alternative approach, where the test section is illuminated by a volume of light. This mode of illumination has been used to measure three-dimensional velocity vectors using a single camera, multiple cameras, and a holographic camera. A novel technique that shares the attributes of micro-PIV and forward scatter PIV is the particle shadow velocimetry (PSV). PSV is an optical technique used to measure seed particle displacement in a plane, like PIV, using images of particle shadows cast by a flashing LED, instead of high-intensity laser light scattered by the particles. Fluid displacements are estimated by cross-correlation of particle image fields acquired successively at a prescribed time delay [17-18].

The particle images recorded using the PSV technique is best understood by examining the diagram shown in Figure 1; which shows regions associated with a plane light wave interacting with a hard sphere, with regions downstream of the particle being called “deep shadow region”, which of special interest for PSV technique. This region is smaller slightly than the diameter of the particle but extends several diameters downstream. An extinction cross section produced is twice its geometric cross section (extinction paradox) by the deep shadow [19-20]. The purpose of this study is to set up and validate a low-cost PSV system to estimate the appropriate particle velocity field of magnetic nanocomposite excited by rotating magnetic field for the adsorption of hexavalent chromium and fluoride ions from aqueous solution. The analysis of the interaction of the magnetic nanocomposite with the aqueous solution of hexavalent chromium and fluoride under magnetic field influence is needed in a broad range of different sector application for water decontamination.

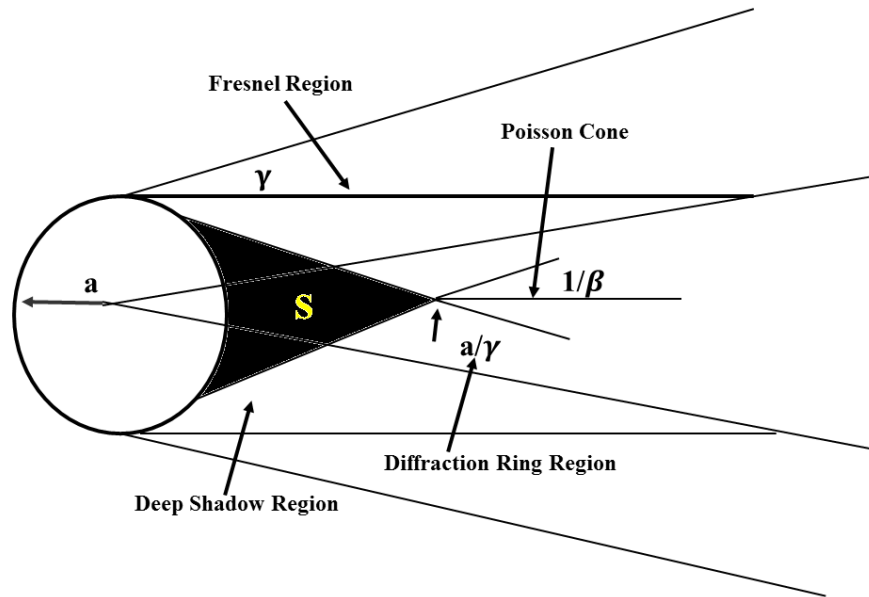


**Figure 8.1** Description of the regions associated with the plane wave interaction with hard sphere,  $S$ -deep shadow,  $a$ -particle radius,  $\beta$ -size parameter,  $\gamma$ -penumbra width from Nussenzweig [20].

## 8.2 Results and Discussion

To compare with the predictions of the analysis of rotating particle movement in a multipole stator winding, velocity profile measurements were obtained in a series of experiments. The experimental observations were analyzed by considering the force acting on the particles and the medium. To determine the velocity of the rotating particles inside the cylindrical channel, chains of rotating particles were traced in hexavalent chromium and fluoride solutions, with no flow applied at different magnetic fields intensity. In the absence of magnetic field applied (Figures 8.2 and 8.3(a)), the net spin vector is equal to zero due to the randomized magnetic particles moments being in all directions. Under sufficient large magnetic field, the dipolar interaction between particles serves to drive colloidal particles to form chain-like structures. Particles chains align with the external magnetic field for the inhomogeneous magnetic field. After the removal of the external magnetic field, the chains rapidly disaggregate, and the initial particles dispersion is recovered. When external magnetic field is applied to the particles, the dipole interaction between the superparamagnetic particles, a secondary minimum in the energy landscape is generated which enables the particles to bind to each other forming chains or

other structures. But, the magnetic interaction must be large enough to overcome thermal agitation, which tends to destroy them. The application of magnetic field on the particles induces structuration (aggregation or chain formation), as the particles lack no magnetic dipole in the absence of an external magnetic field. The interaction between the particles in the solution under a high magnetic field will lead to aggregate head to tail to minimize the magnetic energy, forming chain-like structures. For large magnetic fields, the particles structures are observed to become more stable, with former particles aligning and leading most robust and straight chain [9, 21].

Application of external magnetic field perpendicular to the channel-wall result in a chain formation, with micro size chains formed along the direction of the external magnetic field. In the absence of an external magnetic field on the particles, the magnetic interaction energy between the nanocomposite in the solution medium was smaller than the thermal energy ( $K_B T$ ), hence no particles aggregation was observed, and the particles remain in the solution medium [Figures 8.2 and 8.3(a)]. When external magnetic field is applied to the particles, the particles magnetic moment orient along the external magnetic field and the magnetic energy contribution dominates the thermal energy. Structures that are ordered are formed due to this interaction (Figures 8.2 and 8.3(b-e)) [22].

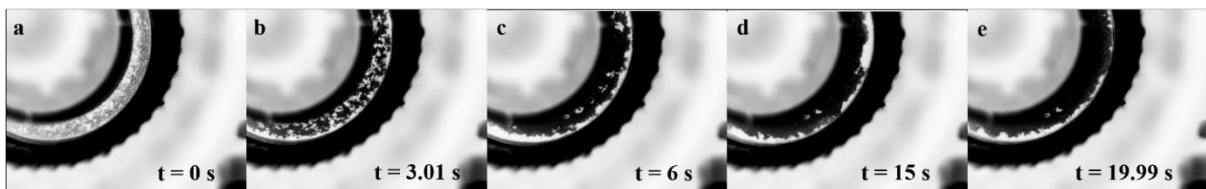


**Figure 8.2** Sequence of inverted image of particles in chromium six solution at magnetic field of 15.48 (a) no field is applied, (b) 3.01 s (RMF), (c) 6 s (RMF), (d) 15 s (RMF) and (e) 19.99 s (RMF).

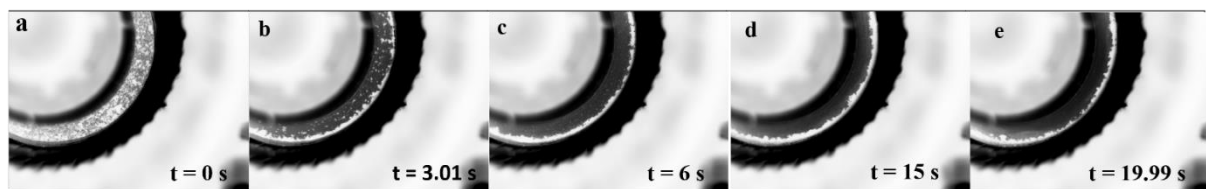


**Figure 8.3** Sequence of inverted image of particles in chromium six solution at magnetic field of 25.54 mT (a) no field is applied, (b) 3.01 s (RMF), (c) 6 s (RMF), (d) 15 s (RMF) and (e) 19.99 s (RMF).

The particles migration towards the channel walls is immediately observed after the introduction of the external induced rotating magnetic field. Elongated aggregates of particles formed with their long axis in the local magnetic field direction move in the direction of the field gradient, which is the radial direction as shown in Figures 8.4. The particle's velocity was reported by [4] to depend on the size of aggregates formed during the rotation of the particles, with larger particles aggregates moving faster, while smaller particles aggregate travelling with slow drift velocities. Chain breakage of aggregates at low external magnetic field was observed to significantly reduces the spinning efficiency of the particles, as the broken segment may not rejoin to the original chain formation (Figure 8.4). Under the influence of strong magnetic field, a stable chain was observed in a less viscous environment (Figure 8.4(b and d)).

Rotating particle velocity depends on the length of the chain formed, as long chains move over a larger distance per cycle compared to short chains, as increase interaction between the rotating particles and the aqueous solutions are observed at high external magnetic field applied. Hence, increasing the external magnetic field applied to the particles leads to the particles moving twice as fast as at low external magnetic field and particles are observed to perform more steps per time interval, as the particles align with the field line rotating at the same rotational frequency (Figure 8.4) [23].

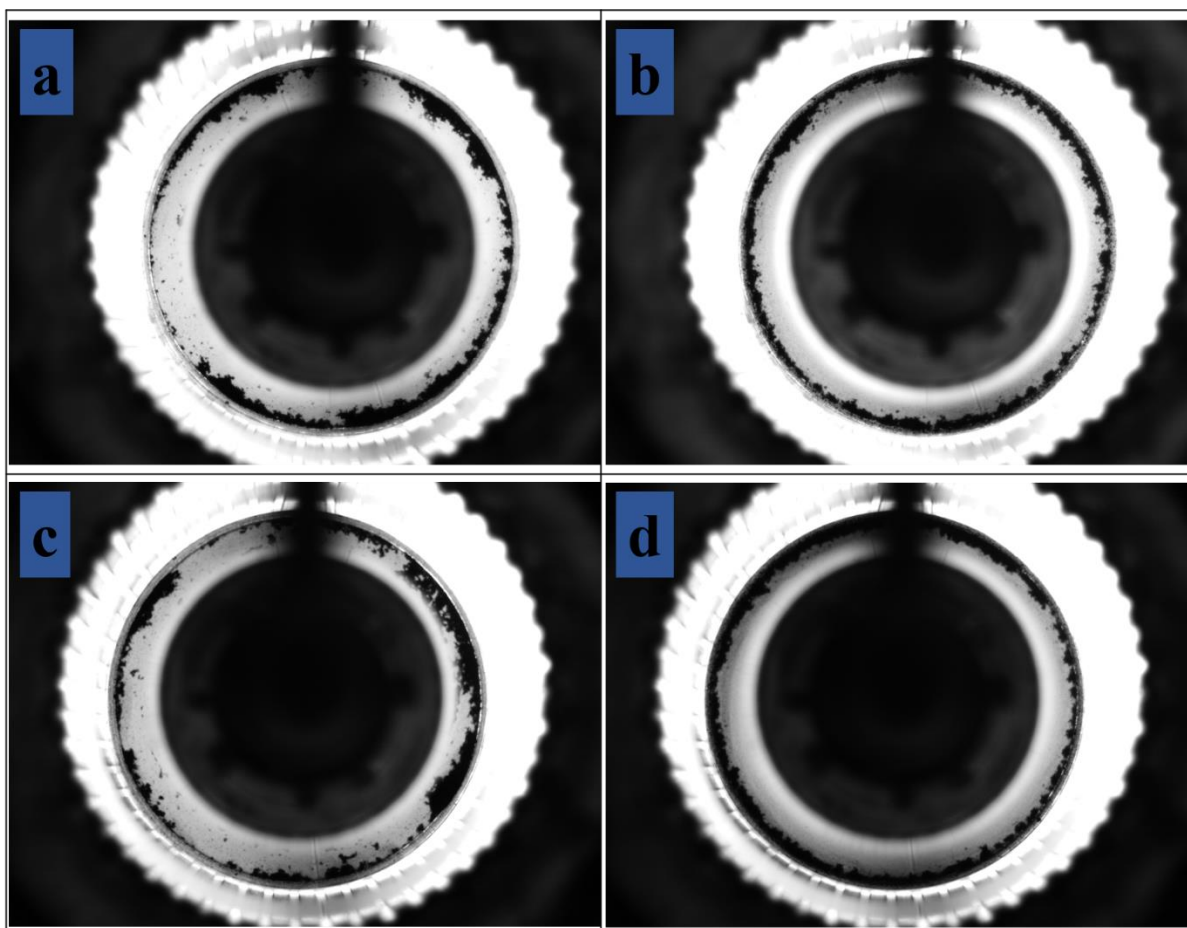


**Figure 8.4** Aggregation of particles in magnetic field of (a) 11.84 mT in fluoride solution, (b) 19 mT in fluoride solution, (c) 11.84 mT in hexavalent chromium solution and (d) 19 mT in hexavalent chromium solution.

The instantaneous and mean velocity field sequence with their corresponding colour bars (on the right) for each pair of images captured by the camera for fluoride solution at the different magnetic field are shown in Figures 8.5 and 8.6. The arrow indicates the direction of the velocity vectors and the increasing value of the instantaneous and average velocity field is represented by a colour change from blue to red in each panel are also shown in Figures 8.4 and 8.5. The mean velocity field of the rotating particles is observed to increase from 0.0068-0.0145 m/s and 0.0085-0.0145 m/s as the induced external magnetic field on the particles is increased from 15.48-25.54 mT in a fluoride solution and 16.54-25.54 mT in hexavalent chromium solution. The particles trajectories show the different dynamics in each solution. High particles velocities were observed close to the channel wall, as the induced magnetic field from the stator windings is stronger and tends to affect the particle motion. For low induced magnetic field, the particles trajectories were observed to interact more with the channel wall, with drop-in

particle velocity as the particle tries to overcome frictional force and high density of particles numbers close to the channel wall (Figure 8.5(a-d)). Particles motion was also observed to be dense at low magnetic field, which was dominated by particle-particle collisions, which resulted in less deflection of particles due to little free space between the particles [24]. The particle-wall interaction was reported to depend on the inertia of the particle. Particles colliding with the wall rebounds from the channel wall, with kinetic energy loss due to friction and inelasticity effects. The effect of particle size on the mainstream particle velocity distribution is minimal once the particles strike the solid surface. The rebounding phenomena indicate that the particle size has a significant effect on the motion of the rebounding particles. The region of a high percentage of rebounding particles can be identified by particles size. This may be attributed to the variation of pressure gradient/magnetic field gradient around the back end of the cylindrical channel close to the stator windings [25-26].

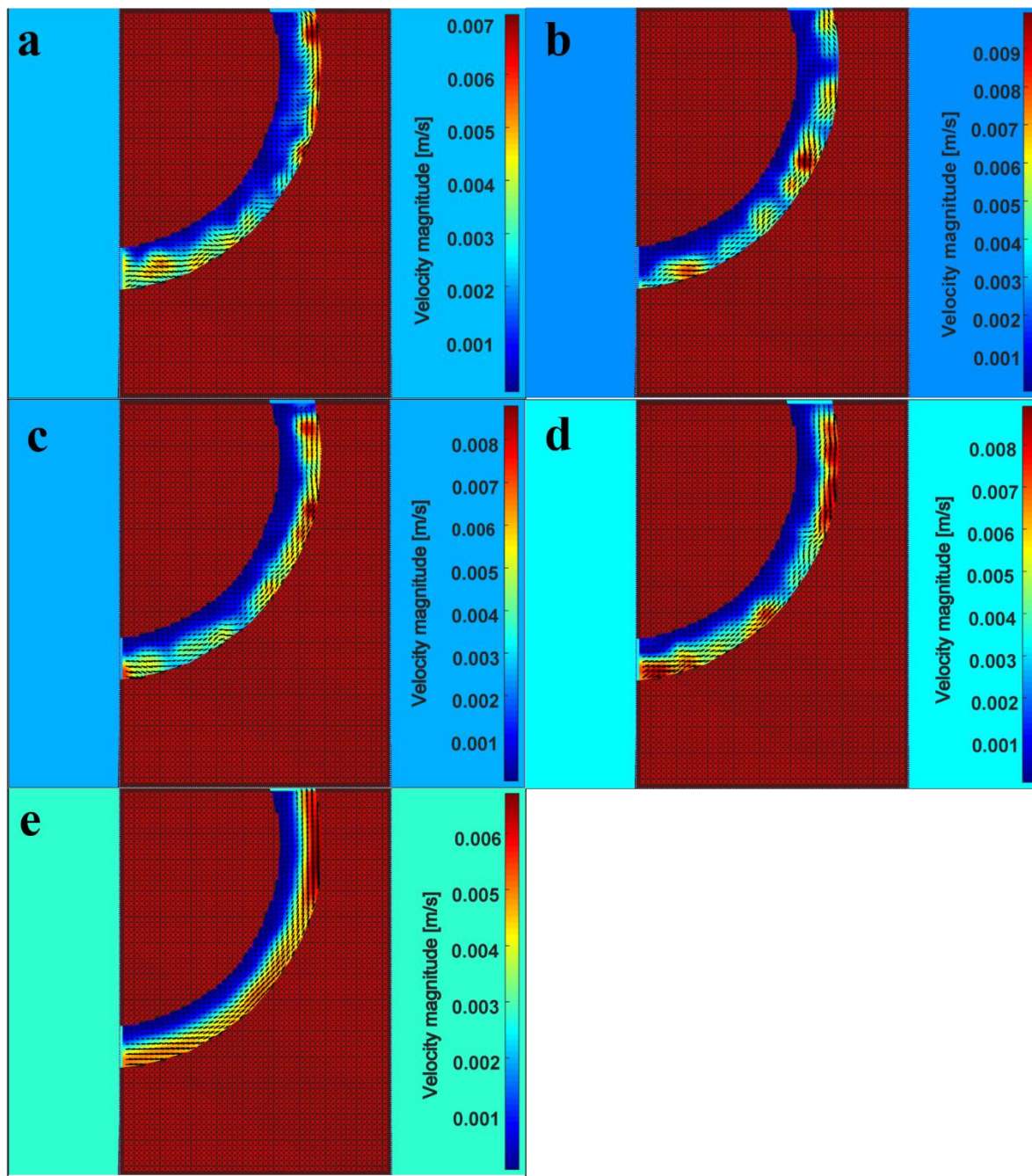


**Figure 8.5** Instantaneous and mean velocity measurement of particles in fluoride solution at magnetic field of 15.48 mT (a) instantaneous velocity of particles at time interval of 3.06 s (b) resulting instantaneous velocity of particles at time interval of 6.01 s, (c) resulting instantaneous velocity of particles at time interval of 13 s, (d) resulting instantaneous velocity of particles at time interval of 14 s, and (e) resulting average velocity field of particles.

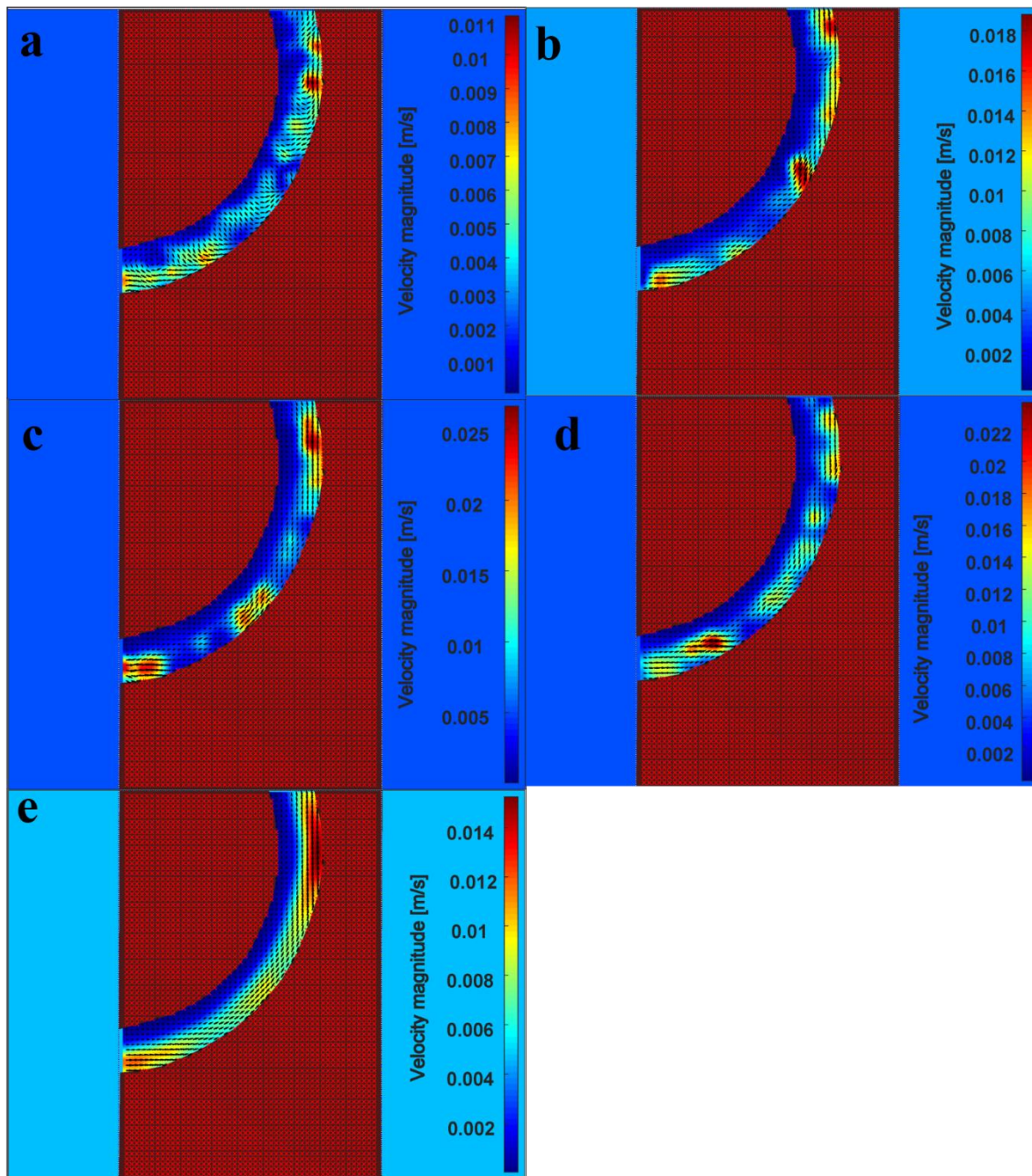


**Figure 8.6** Instantaneous and mean velocity measurement of particles in fluoride solution at magnetic field of 25.54 mT (a) instantaneous velocity of particles at time interval of 3.06 s (b) resulting instantaneous velocity of particles at time interval of 6.01 s, (c) resulting instantaneous velocity of particles at time interval of 13 s, (d) resulting instantaneous velocity of particles at time interval of 14 s, and (e) resulting average velocity field of particles resulting average velocity field of particles.

The induced chain rotation and broad magnetic velocity distributions lead naturally to chain collisions as reported by [27]. The lateral binding of chains driven into contact by magnetic

manipulations was observed to substantially increases the chain polydispersity as the magnetic field is increased, which depends on the vertical orientation of the magnetic field. The strong increases in the magnetic torque and forces, produced assemblies containing thousands of nanoparticles, leading to enhanced magnetophoretic velocities [27]. The rotating magnetic field yields strong enough torque on the individual magnetic nanoparticles to overcome Brownian thermal agitation and hydrodynamic torque, a rotational reorientation underwent by the magnetic nanoparticles lead them to spin almost parallel to the flow direction. It can be hypothesized that at the magnetic nanoparticles level, a mixed fluid zone is formed around each spinning magnetic particle where the molecular transport phenomenon is supported meaningfully with kinetic energy spread out from particle spin [28]. Increase in the magnetic field induced on the particles over a magnetic exposure time, the rotating particles were observed to forms aggregates due to the increased magnetic force and torque on the particles leading to increased chain collision and area of particle interaction as shown in Figure 8.6, with the particle's aggregates increasing from 235-1037 in hexavalent chromium solution and 76-408 in fluoride solution as the magnetic field is increased.

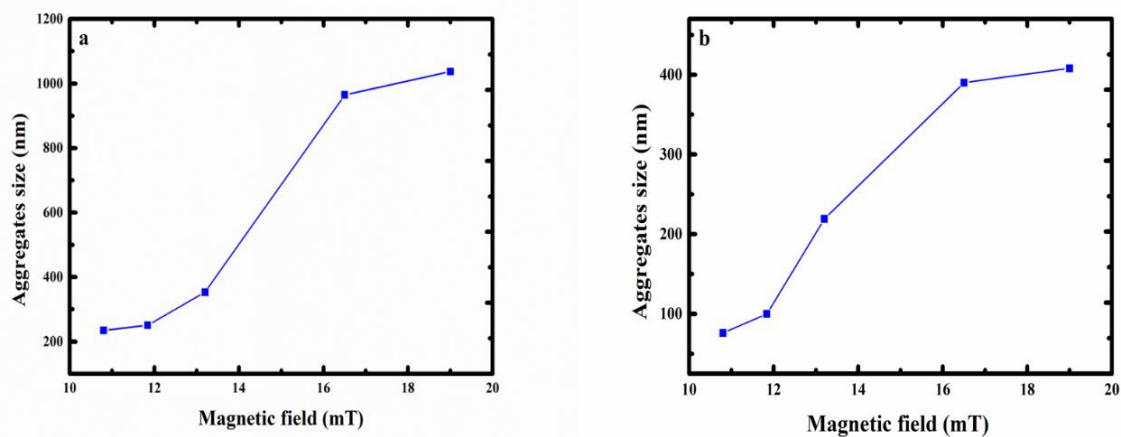


**Figure 8.7** Aggregation of particles in the magnetic field of (a) 16.55 mT and (b) 25.54 mT.

### 8.3 Conclusion

Using the particle shadow velocimetry technique, rotating particles actuated by a rotating magnetic field for chromium six and fluoride adsorption from aqueous solution were observed. Increase in the magnetic field induced by the particles led to enhanced magnetic force and torque on the particles, thereby causing the particles to rotate and form aggregates. Induced

chain rotation and broad magnetic velocity distributions were observed to lead to chain collisions. The lateral binding of chains driven into contact by magnetic manipulations substantially increases the chain polydispersity as the magnetic field is increased leading to an enhanced adsorption process.

## 8.4 References

- [1] Y. Sahoo, A. Goodarzi, M. T. Swihart, T. Y. Ohuichanskyy, N. Kaur, E. P. Furlani, and P. N. Prasad, **2005**, *J. of Physical Chemistry*, 109, 3879-3885.
- [2] Z. Sun, M. Guo, F. Verhaeghe, J. Vieugels, O. Van Der Biest, and B. Blanpain, **2010**, *Progress in Electromagnetics Research*, 103, 1-16.
- [3] M. Benelmekki, and L. M. Martinez, **2013**, *Nanotechnology*, 7.
- [4] G. De Las Cuevas, J. Faraudo, and J. Camacho, **2008**, *J. of Physical Chemistry C*, 112 (4), 945-950.
- [5] G. P. Zhu, and N. T. Nguyen, **2012**, *Lab Chip*, 12, 4772–4780.
- [6] Y. Iiguni, and H. Watarai, **2003**, *Analytical Sciences*, 19, 33-37.
- [7] Y. Gao, Y. C. Jian, L. F. Zhang, and J. P. Huang, **2017**, *The J. of Physical Chemistry C*, 111, 10785-10791.
- [8] K. Iwai, J. Akiyama, M. G. Sung, I. Furuhashi, and S. Asai, **2006**, *Science and Technology of Advanced Materials*, 7, 365-368.
- [9] O. Gravel, J. Lauzon-Gauthier, C. Duchesne, and F. Larachi, **2015**, *Chemical Engineering J.*, 260, 338-346.
- [10] N. T. Nguyen, **2012**, *Microfluidics and Nanofluidics*, 12, 1-16.
- [11] J. Sun, Y. Zhang, Z. Chen, J. Zhou, and N. Gu, **2007**, *Angewandte Chemie International Edition*, 46, 4767-4770
- [12] V.A Naletova, V. A. Turkov, V. V. Sokolov, and A. N. Tyatyuskin, **2005**, *J. of Magnetism and Magnetic Materials*, 289, 367-369.
- [13] M. Karle, J. Wohrle, J. Miwa, N. Paust, G. Roth, R. Zengerie, and F. V. Stetton, **2011**, *Microfluid Nanofluid*, 10, 935-939.
- [14] S. Thurm, and S. Odenbach, **2002**, *J. of Magnetism and Magnetic Materials*, 252, 247-249.
- [15] A. Mirsepassi, and D. D. Rankin, **2012**, *16th International Symposium on Application of Laser Technologies to Fluid Mechanics*.
- [16] P. Toth, A. B. Palotas, T. A. Ring, and E. G. Eddings, **2013**, *8th US National Combustion Meeting*.
- [17] C. D. Meinhart, S. T. Wereley, and M. H. B. Gray, **2000**, *Measurement Science and Technology* 11, 809.
- [18] M. J. McPhail, M. H. Krane, A. A. Fontaine, L. Goss, and J. Crafton, **2005**, *Meas. Sci. Technol.* 26, 045301.

- [19] A. Bichal, A. Altman, A. M. Briones, and S. Stouffer, **2009**, 47th AIAA Aerospace Sciences Meeting Including the New Horizons Forum and Aerospace Exposition, 884.
- [20] L. P. Goss, J. Estevadeordal, and J. W. Crafton, **2007**, Instrumentation in Aerospace Simulation Facilities, 22nd International Congress on. IEEE, 1-8.
- [21] J. A Segura, **2013**, PhD Thesis in Material Science, 15-17.
- [22] C. Pai, H. Muthurajan, N. Momin, S. Radha and R. Nagarajan, **2015**, arXiv preprint arXiv:1509.04923.
- [23] F. Wittbracht, A. Weddemann, A. Auge, and A. Hutten, **2010**, In Quantum, Nano and Micro Technologies, ICQNM'10. Fourth International Conference, IEEE.102-106.
- [24] T. Hagemeier, C. Roloff, A. Buck and E. Tsotsas, **2014**, 17<sup>th</sup> International Symposium on Application of Laser Techniques to Fluids Mechanics.
- [25] B. Ghosh, and M. Poshtan, **2011**, Canadian Journal of Pure and Applied Sciences, 5, 1657-1664.
- [26] Y. S. Morsi, J. Y. Tu, W. W. Yang, and D. D. Atapattu, **1998**, 13<sup>th</sup> Australasian Fluid Mechanics Conference, 199-202.
- [27] R. J. Wilson, W. Hu, C. W. P. Fu, A. L. Koh, R. S. Gaster, C. M. Earhart, A. Fu, S. C. Heilshorn, R. Sinclair, and S. X. Wang, **2009**, Journal of Magnetism and Magnetic Materials, 321, 1452-1458.
- [28] P. Hajiani and F. Larachi, **2013**, Chemical Engineering Journal, 223, 454-466.

## CHAPTER NINE

### 9.1 Conclusion

The study demonstrates the application of an external magnetic field generated from a prototype on polypyrrole magnetic nanocomposite for the adsorption of extremely toxic hexavalent chromium, fluoride and congo red dye from synthetic wastewater. The polypyrrole magnetic nanocomposite used for the magnetic assisted adsorption process was synthesized using the in-situ polymerization process, with an average particle size of 10 nm determined using TEM and SEM characterization. The energy dispersive X-ray analysis (EDX) of the magnetic nanocomposite confirmed the existence of carbon (58.5%), nitrogen (14.55%), chloride (5.71%), oxygen (10.35%) and iron (10.85%) as the predominant elements in the magnetic nanocomposite. It is established from the X-ray diffraction characterization that the magnetic nanocomposite has a crystalline and amorphous structure of  $\text{Fe}_3\text{O}_4$  and polypyrrole. FTIR characterization confirms that the spectra of the adsorbent comprise of characteristics peaks of polypyrrole and  $\text{Fe}_3\text{O}_4$  with functional groups. The BET analysis of polypyrrole magnetic nanocomposite reflects a typical type VI adsorption-desorption isotherm curve with a hysteresis loop signifying a mesoporous material. The surface area and the BJH average pore diameter of the nanocomposite were determined to be  $28.77 \text{ m}^2/\text{g}$  and  $15.82 \text{ nm}$ . The magnetic properties of the adsorbent were determined using ESR and VSM at room temperature, which revealed that the nanocomposite was superparamagnetic with an effective g-value of 2.25 and saturation magnetization of 23 and  $14 \text{ emu/g}$  before and after adsorption.

Under the influence of external magnetic field, an enhanced removal of hexavalent chromium, fluoride and congo red dye was observed. Results also showed enhanced removal under other experimental conditions like pH, adsorbent dosage, initial adsorbate concentration and magnetic exposure time. Results show 99% of hexavalent chromium ions adsorb onto the magnetic nanocomposite at pH 2 using a rotating magnetic field of 18.99 mT at a magnetic exposure time of 60 min. The percentage of adsorbate ions (hexavalent chromium) adsorbed was observed to increase from 91.6-99.2% and 72.2-96.6% at varying magnetic field and magnetic exposure time. Results showed improvement in the percentage of fluoride ions adsorbed, which was observed to be pH dependent and it increased with an increase in the magnetic field and magnetic exposure time. Results showed that the external magnetic field significantly enhances the percentage of congo red dye adsorbed, with a maximum removal of 94% congo red dye removed at pH 4 and at an external magnetic field of 18.99 mT.

From the particle shadow velocimetry (PSV) results, particle aggregation, particle-wall interaction and particle velocity field were observed to play a role in the adsorption process. The sizes of aggregates formed were observed to be elongated and magnetic velocity dependent, with fast moving large uniform particles aggregates observed at the high magnetic field. Smaller non-uniform particles aggregates travelling with slow drift velocities were also observed at the low magnetic field. Chain breakage in particles aggregates was noticed, which significantly reduced the swimming efficiency of the particles at the low magnetic field, hence reduced surface area for adsorption to take place was also observed. The lateral binding of chains driven into contact by magnetic manipulations substantially increases the chain polydispersity as the magnetic field is increased, hence increased chain collision and area of particle interaction. Based on the above results it is conclusive to say that the technology of using an external magnetic field from a three-phase induction motor is a very promising wastewater treatment technique which would enhance the efficiency of contaminants extraction.

## **9.2 Future Research**

Future research work needs to be carried out using real wastewater to gather more reliable information regarding the system's ability to treat water. To redesign and optimize the prototype magnetic adsorption device to improve its treatment capacity for industrial and synthetic waste. It is further recommended that  $\text{Fe}_3\text{O}_4$  core nanoparticles be replaced with other iron oxides cores for performance comparison purposes.

## Appendix I

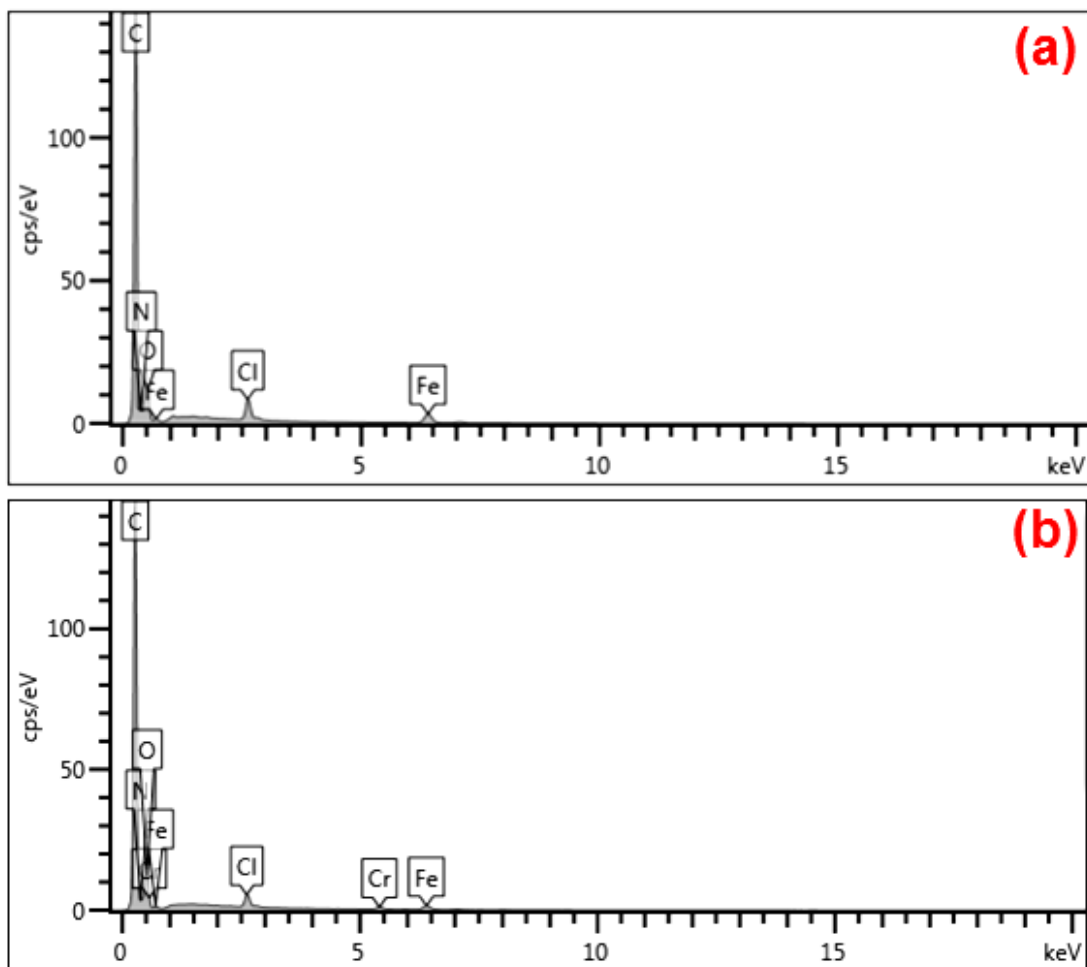


**Figure S4.1** EDX spectra of PPy/Fe<sub>3</sub>O<sub>4</sub> (a) before and (b) after Cr(VI) adsorption

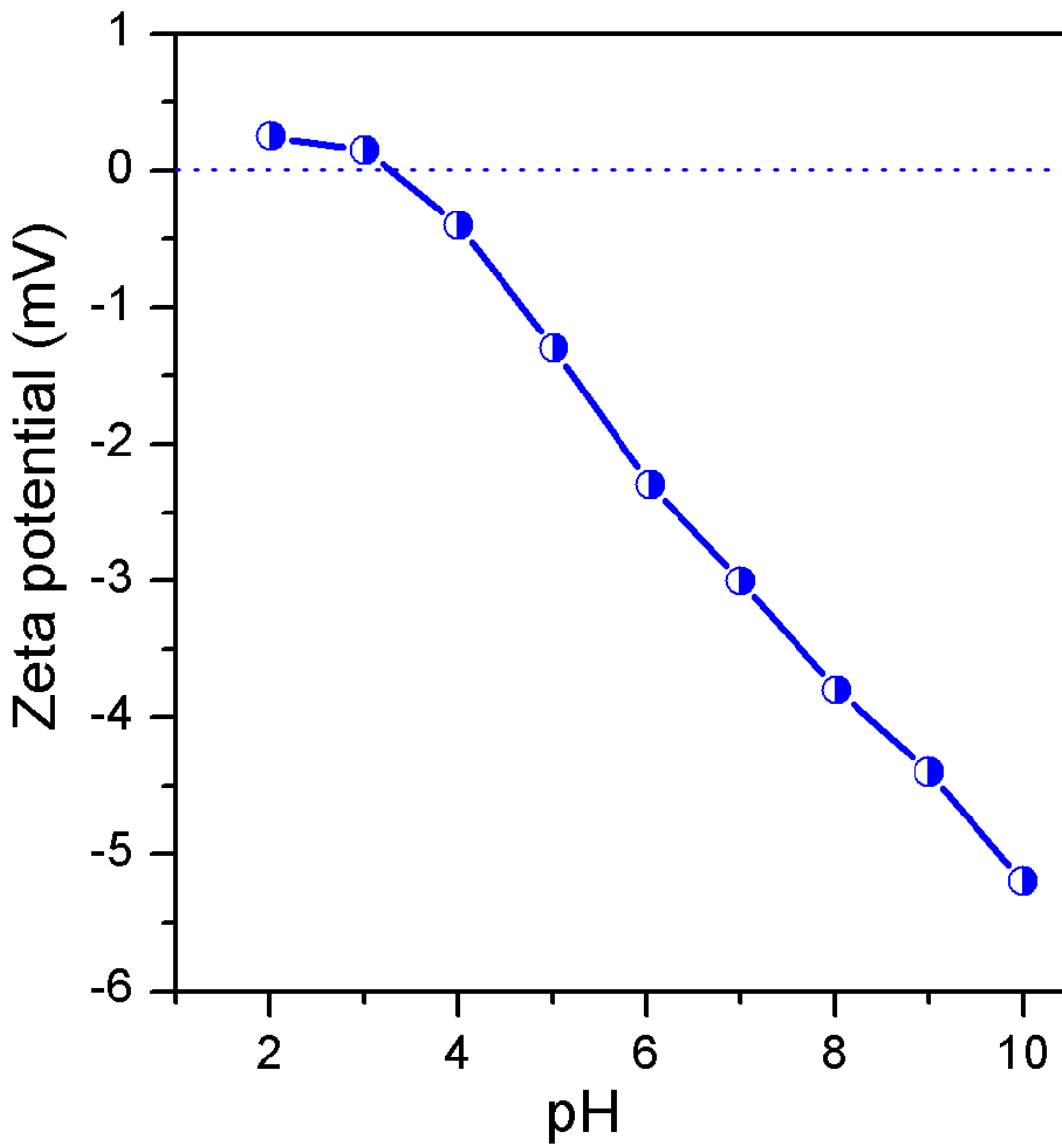


**Figure S4.2** Zeta potential of adsorbent (PPy/Fe<sub>3</sub>O<sub>4</sub>) at different pH

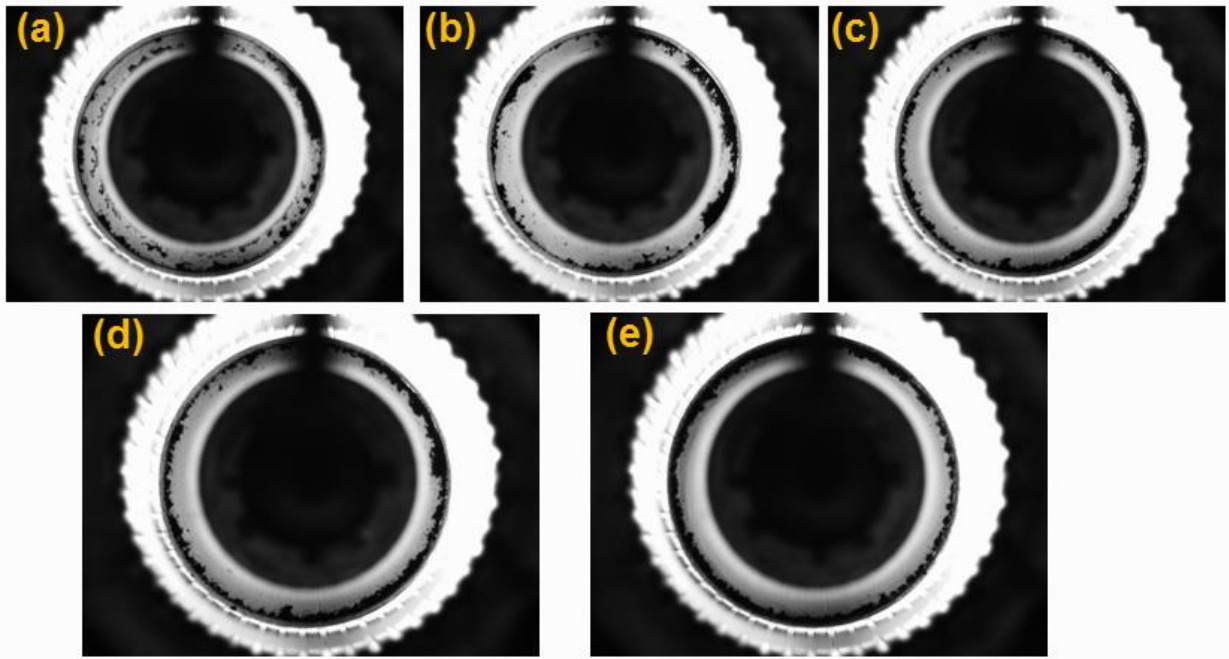


**Figure S4.3** Images of particles aggregation of PPy/Fe<sub>3</sub>O<sub>4</sub> nanocomposite at different magnetic field of (a) 10.80, (b) 11.84, (c) 13.20, (d) 16.46 and (e) 19.01 mT

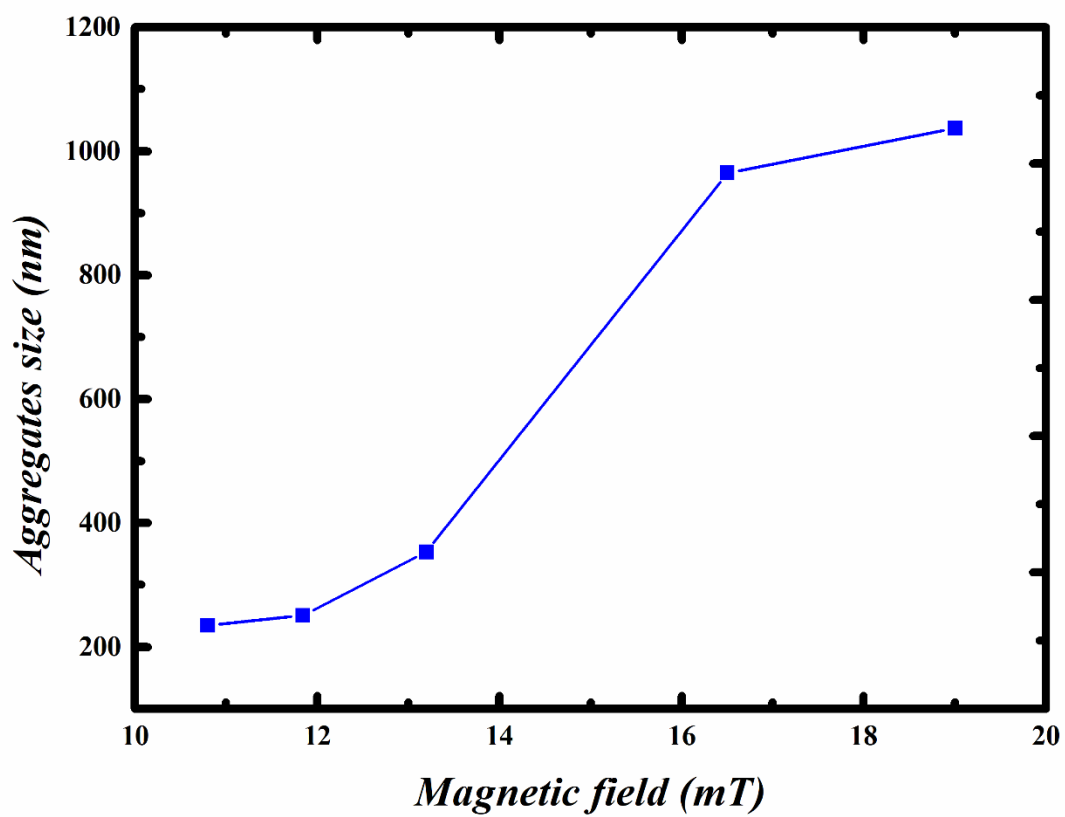


**Figure S4.4** Effect of magnetic field on particle aggregation for Cr(VI) adsorption.

## Appendix II

### List of Publications

#### Journal Papers

- I A Novel Method for Removal of Cr(VI) using Polypyrrole Magnetic Nanocomposite in the Presence of Unsteady Magnetic Fields (<https://doi.org/10.1016/j.seppur.2017.11.057>) (Paper Accepted and Published 2018).
- II Removal of Hexavalent Chromium from Wastewater using PPy/Fe<sub>3</sub>O<sub>4</sub> Magnetic Nanocomposite Influenced by Rotating Magnetic Field from Two Pole Three-Phase Induction Motor (Accepted for Publication by Journal of Physics: Conference Series, 2018).
- III Congo Red Dye Removal Under the Influence of Rotating Magnetic Field by Polypyrrole Magnetic Nanocomposite (Paper under Review with Desalination and Water Treatment Journal, 2017).

